RÉPUBLIQUE FRANÇAISE
Liberté Égalité Fraternité

Université de Toulouse

Doctorat de l'Université de Toulouse

préparé à l'ISAE-SUPAERO

Conception de filtres vibratoires absolus par le design de guides d'ondes lattices périodiques.

Thèse présentée et soutenue, le 23 juin 2026 par

Théo BONNEVAL

École doctorale
MEGEP - Mécanique, Energétique, Génie civil, Procédés

Spécialité
Génie mécanique, mécanique des matériaux

Unité de recherche
ICA - Institut Clément Ader

Thèse dirigée par
Guilhem MICHON et Adrien PELAT

Composition du jury
M. Nicolas DAUCHEZ, Rapporteur, Université de Technologie de Compiègne
M. Kerem EGE, Rapporteur, INSA Lyon
Mme Anne-Christine HLADKY-HENNION, Présidente, CNRS/ISEN
M. Fabrice LEMOULT, Examinateur, ESPCI Paris - PSL
M. Guilhem MICHON, Directeur de thèse, ISAE-SUPAERO
M. Adrien PELAT, Co-directeur de thèse, Le Mans Université

Membres invités
M. Léonardo SANCHES, Airbus
M. Maxime LANOY, Co-encadrant, Le Mans Université

Acknowledgements

Ces trois années de doctorat ont été extrêmement enrichissantes, tant sur le plan scientifique qu'humain. Elles m'ont permis de développer de nombreuses compétences, de progresser dans plusieurs domaines, mais aussi de faire de très belles rencontres. Certaines de ces personnes sont devenues de véritables amis et collègues, avec qui j'espère continuer à travailler et à partager encore de nombreux moments.

Je tiens tout d'abord à remercier l'Université du Mans, et en particulier l'ensemble des personnes travaillant à l'ENSIM, pour leur accueil chaleureux, ainsi que toute l'équipe de chercheurs, post-doctorants et doctorants du LAUM. Je pense plus particulièrement à mes collègues du bureau des doctorants de l'ENSIM — Alex, Elie, Wala, Eliott, Kyu, Alexandre, Lionel, Patrick, Amar et Stepan avec qui j'ai partagé de très bons moments.

Je remercie également l'ISAE-SUPAERO et l'Institut Clément Ader, qui m'ont eux aussi accueilli, et ce depuis déjà plusieurs années, à commencer par mon stage de fin d'études. Je pense à toute l'équipe VIB, à Jean-Benoît, et Louis, ainsi qu'à tous les doctorants, ingénieurs et stagiaires de l'équipe.

Je souhaite adresser mes sincères remerciements à mes encadrants, Guilhem, Adrien et Maxime, pour leur bienveillance et leur disponibilité. Vous m'avez accompagné et soutenu tout au long de ces travaux, tout en me formant avec exigence et confiance. Grâce à vous, j'ai énormément appris et j'ai pu faire évoluer en profondeur mes méthodes de travail.

Je remercie également Caroline, Rémy et Jules, de l'IRT, qui m'ont accompagné tout au long de ce doctorat et ont toujours été très présents.

Je souhaite remercier mon ami et ancien collègue Léonardo, qui a suivi ce projet du côté d'Airbus et avec qui j'ai le plaisir de collaborer depuis plusieurs années.

Je remercie tout particulièrement Louis, Dorian, Stepan, Mustapha et Gauthier, qui sont devenus bien plus que de simples collègues : de très bons amis.

Je remercie aussi mes parents et mon frère pour leur soutien. Les week-ends passés à la maison, en Corrèze, à vos côtés, m'ont toujours permis de réellement décompresser et de repartir plus sereinement.

Enfin, je souhaite remercier Lucie, avec qui je partage mon quotidien, pour son soutien constant dans chacun de mes projets. C'est une chance immense de t'avoir à mes côtés, et ce soutien est bien entendu pleinement réciproque.

Résumé

Le confort des passagers constitue un enjeu majeur dans la conception des cabines d'avion. Parmi les différentes sources d'inconfort, les vibrations transmises par la structure occupent une place importante, en particulier celles dues au balourd des turbines, généralement situées sous les ailes. Ces vibrations se propagent à travers la structure de la cabine jusqu'aux sièges et peuvent altérer sensiblement le confort perçu. Cette problématique devient encore plus critique avec l'émergence de nouvelles architectures de propulsion, comme les open rotors, dont les vitesses de rotation plus faibles déplacent les excitations vibratoires vers des fréquences plus basses, précisément dans la gamme où le corps humain est le plus sensible. En cas d'exposition prolongée, ces vibrations peuvent engendrer, au-delà de l'inconfort, des effets néfastes sur la santé. Cette thèse porte sur l'atténuation de la transmission vibratoire au sein de la cabine d'un aéronef, plus précisément au niveau du rail supportant les sièges passagers, qui constitue un chemin de transmission critique. En raison de la complexité des sous-ensembles traversés, cette transmission conduit à une excitation multipolarisée. L'objectif est de concevoir ce rail de façon à préserver ses performances statiques tout en lui conférant une fonction de filtrage vibratoire absolu, indépendante de la polarisation de l'excitation. L'approche repose sur le développement de structures lattices, c'est-à-dire d'architectures périodiques formées d'un réseau de poutres, offrant un excellent compromis entre masse et rigidité. Employées comme guides d'ondes, ces structures périodiques peuvent générer des bandes interdites, c'est-à-dire des plages de fréquences dans lesquelles les ondes élastiques ne se propagent plus. Deux mécanismes physiques sont exploités : les interférences de Bragg, liées à la périodicité de la structure, et les résonances locales, obtenues par l'ajout de résonateurs capables de localiser l'énergie vibratoire autour de leur fréquence propre et d'en limiter la propagation. L'ambition de ce travail est ainsi de développer un filtre vibratoire absolu, efficace à basse fréquence et compatible avec les contraintes industrielles de l'aéronautique. La démarche combine conception, modélisation, optimisation et validation expérimentale. Elle aboutit à la fabrication et à la caractérisation expérimentale, à l'échelle laboratoire, d'un démonstrateur représentatif de l'application visée, afin d'évaluer concrètement le potentiel de cette approche pour les futures cabines d'avion.

Abstract

Passenger comfort is a major issue in aircraft cabin design. Among the various sources of discomfort, structure-borne vibrations play an important role, particularly those caused by turbine imbalance, with the engines generally located beneath the wings. These vibrations propagate through the cabin structure to the seats and can significantly affect perceived comfort. This issue becomes even more critical with the emergence of new propulsion architectures, such as open rotors, whose lower rotational speeds shift the dominant excitations toward lower frequencies, precisely within the range to which the human body is most sensitive. Under prolonged exposure, such vibrations may cause not only discomfort but also adverse health effects. This thesis focuses on mitigating vibration transmission within an aircraft cabin, more specifically through the rail supporting the passenger seats, which constitutes a critical transmission path. Owing to the complexity of the substructures crossed by the vibrations, this transmission results in a multi-polarized excitation. The objective is to design this rail so as to preserve its static performance while endowing it with an absolute vibration-filtering function, independent of the polarization of the excitation. The proposed approach is based on the development of lattice structures, that is, periodic architectures made of a network of beams, offering an excellent compromise between mass and stiffness. When used as waveguides, these periodic structures can generate band gaps, that is, frequency ranges in which elastic waves can no longer propagate. Two physical mechanisms are exploited: Bragg interference, related to the structural periodicity, and local resonances, obtained by adding resonators capable of localizing vibrational energy around their natural frequency and limiting its propagation. The ambition of this work is therefore to develop an absolute vibration filter that is effective at low frequencies and compatible with the industrial constraints of aeronautics. The methodology combines design, modeling, optimization, and experimental validation. It leads to the fabrication and experimental characterization, at laboratory scale, of a demonstrator representative of the targeted application, in order to assess concretely the potential of this approach for future aircraft cabins

Contents

Acknowledgements . . . . . **iii**

Résumé . . . . . **v**

Abstract . . . . . **vii**

List of Figures . . . . . **xiii**

List of Tables . . . . . **xxv**

1 Introduction **1**

1.1 Context 2

1.2 Vibration control strategies 5

1.3 State of art on the periodic structures 7

1.3.1 Key Concepts 8

1.3.2 Phononic Crystals 10

1.3.3 Lattice structures 11

1.3.4 Absolute bandgap in 1D elastic wave guide 18

1.4 Outline of the thesis 21

2 Dispersion analysis in a 3D lattice elastic waveguide for the design of an absolute filter 25

2.1 Introduction 26

2.2 System under study 27

2.2.1 Geometry of the investigated structure 27

2.2.2 Example of configurations 28

2.3 Spectral Element Method (SEM) in a three-dimensional assembly of beams . . 29

2.3.1 Spectral stiffness matrices 29

2.3.2 Application of Periodicity Conditions 32

2.3.3 Dispersion of the reference structure 33

2.4 Mode decomposition and dispersion analysis 34

2.5 Parametric study of the unit cell geometry 36

2.5.1 Mechanisms governing the band gap characteristics 38

2.6 Experimental demonstration 42

2.6.1 Material characterization . . . 42
2.6.2 Experimental setup . . . 42
2.6.3 Experimental results . . . 42
2.7 Conclusions . . . 46

3 Analysis of the trade-off between bending stiffness and absolute bandgap width based on the dispersion relations of a periodic lattice sandwich beam . . . 47
3.1 Introduction . . . 48
3.2 Semi-analytical model . . . 49
3.2.1 Spectral model of a free-edge plate element . . . 49
3.2.2 Plate–beam coupling formulation . . . 53
3.2.3 Extension to XBS structure . . . 56
3.2.4 Periodic condition . . . 56
3.2.5 Numerical validation . . . 57
3.2.6 Classification of modes . . . 58
3.3 Trade-off analysis . . . 60
3.4 Experimental validation . . . 63
3.5 Conclusion . . . 64

4 From Bragg lattices to locally resonant vibration filters . . . 67
4.1 Introduction . . . 68
4.2 Undamped periodic resonator chain . . . 69
4.2.1 Unit-cell model and equations of motion . . . 69
4.2.2 Non-dimensional parameters . . . 70
4.2.3 Floquet–Bloch analysis and dispersion relation . . . 70
4.2.4 Mass–bandwidth trade-off . . . 72
4.3 Damped periodic resonator chain . . . 74
4.3.1 Damped unit cell and complex dispersion . . . 75
4.3.2 Attenuation band of a finite chain . . . 75
4.3.3 Influence of damping and number of cells . . . 77
4.3.4 Mass–attenuation trade-off . . . 77
4.4 Nonlinear resonator chains . . . 78
4.4.1 Nonlinear unit cell . . . 79
4.4.2 Nonlinear dispersion . . . 83
4.4.3 Attenuation performance . . . 85
4.5 Design guidelines . . . 87
4.6 Structural modeling of the resonant filter . . . 88
4.6.1 Waveguide definition . . . 89

4.6.2 Dispersion analysis . . . 89
4.6.3 Resonator design . . . 90
4.6.4 Mass–bandwidth trade-off . . . 92
4.6.5 Mass–attenuation trade-off . . . 93
4.7 Experimental validation of the resonant waveguide filter . . . 97
4.7.1 Prototype design and experimental setup . . . 97
4.7.2 Linear regime . . . 98
4.7.3 Nonlinear regime . . . 99
4.8 Conclusion . . . 102

5 Design of an absolute resonant vibration filter . . . 103
5.1 Introduction . . . 103
5.2 Definition of the lattice waveguide . . . 104
5.2.1 Dispersion analysis . . . 105
5.2.2 Reference frequencies . . . 106
5.3 Definition of the local resonators . . . 106
5.4 Mass–bandwidth trade-off . . . 108
5.4.1 Illustrative scenarios for a fixed mass fraction . . . 109
5.4.2 Parametric sweep . . . 110
5.4.3 Influence of resonant mass distribution . . . 112
5.5 Performance limits of the damped absolute resonant filter . . . 114
5.6 Design guidelines . . . 115
5.7 Development of an applied demonstrator . . . 117
5.7.1 System-level demonstrator and interfaces . . . 119
5.7.2 Numerical model . . . 120
5.7.3 Performance indicators . . . 122
5.7.4 Role of the x-oriented resonator . . . 124
5.7.5 Experimental analysis . . . 125

6 Conclusion and perspectives . . . 129
6.1 Summary . . . 129
6.2 Conclusion . . . 131
6.3 Perspectives . . . 133
6.3.1 Promising configuration: 2-DOF resonators . . . 133
6.3.2 The filtering periodic lattice waveguide as a cable HUB . . . 135
6.3.3 Controlling resonator nonlinearities . . . 136

Appendices . . . 137
A Spectral beam matrices . . . 137

B Beam orientation 139
C Symmetry-based condensation 140
D Full complex solution corresponding to Figure 2.12 143
E Spectral formulation of a free-edge plate element 144
F Plate–beam coupling formulation 154

Bibliography **163**

List of Publications **185**

List of Figures

1.1 a) Mechanisms for sound generation in an aircraft b) An overview on external and internal noise sources. Figures extracted from [3] 2

1.2 Used aircraft cabin seat bench on the vibration platform at Carl von Osszietzky University from the front (a) and the back showing the accelerometer on the seat rail (b). (c) Mean pleasantness ratings (with verbal anchors) as a function of vibration frequency f vib averaged across all (N = 40) participants divided by acceleration levels (re. 1 lm/s2) at the seat rail (left) and averaged across all acceleration levels divided by gender (right). Error bars show 95 % confidence intervals. Figures extracted from [14] 3

1.3 a) View from below of the inside an aircraft fuselage, extracted from [21]. b) View from above of the upper floor inside an aircraft fuselage, extracted from the cover of [22]. 4

1.4 a) CAD model plot of cabin passenger extraded from [21] b) reduced vibration problem 7

1.5 a) Discretization of a rod into a spring-mass lattice (b) Dispersion relation and (c) phase velocity of the 1D spring-mass lattice (solid line) and of the continuous rod (dashed line). All the 3 sub-figures are extracted from [80] 8

1.6 (a) Periodic bi-layered continuum medium which thickness of alternating layers are h1 and h2, respectively. (b) Bi-atomic chain representation of the bi-layered medium extrated from [57] (c) Dispersion curves for the 1D diatomic spring-mass lattice showing real (solid line) and imaginary (dashed line) parts of the propagation constant extracted from [80] 10

1.7 FEM numerical study of the wave coupling band gap and resulting double filtering effect. (a) Comparison of the dispersion relations of a periodic symmetric (blue triangles) and non-symmetric (brown circles) beam; (b) Flexural and longitudinal components of the forced displacement of a 8-cell beam, symmetrical (top line) or nonsymmetrical (bottom line), excited by a flexural (left column) or longitudinal (right column) unit point force (pink arrow) at the coupling frequency f = 2780 Hz. Extraded from [103] 11

1.8 Extract from [144] : a) 3D model of the periodic lattice. b) unit structure. c) unit band structure analysis. Vibration modes of the unit band structure at four boundary points. d), e) is the vibration mode of the first bandgap edge points 1, 2, and f), g) is the vibration mode of the second bandgap edge points 3, 4 13

1.9 Extract from [141] : (a) Unit cell of a phononic sandwich beam with an asymmetric hourglass core; (b) dispersion diagram showing only the branches associated with flexural motion; (c) simulated transmissibility; (d–f) simulated displacement fields for an excitation outside the bandgaps (5160 Hz) and within the two bandgaps (3650 Hz and 1830 Hz) 14

1.10 Extract from [169] :(a) Schematic of truss beam structures with cruciform resonators. (b) Dispersion relations (c) 7-cell configuration.(d) Transmission varying with the damping coefficient η 17

1.11 Extract from [159] : (a) Considered 1D periodic sandwich with a lattice core beam. (b) Construction of a beam-type metastructure by attaching periodic local resonators. The lattice constant of the metastructure is given by a = nh, where n is an integer dependent on design. (c) Comparison of dispersion relations of the host truss beam (red dashed lines) and those of the metastructure (blue solid lines) 18

1.12 Extract from [188] : (a) Images of the manufactured crystal phononic pipe implemented in an experimental setup. The structure consists of five cells, introducing an alternation between an aluminum beam and a nylon beam. Numerical analysis and experimental characterisation of the optimal PC pipe: (b) real part and imaginary part of the complex dispersion relation obtained by the Floquet–Bloch method and considering the viscoelastic losses (blue) Longitudinal, (red) flexural, and (green) torsional; measured (light line) and simulated (dark line) acceleration transfer functions in the (c) flexural, (d) longitudinal, and (e) full loading cases; with the 3D views of the simulated total displacement in the full loading case at (f) 900 Hz where all wave types propagate, (g) 2500 Hz where only the flexural bandgap is opened, and (h) 4500 Hz within the absolute bandgap. 19

1.13 Extract from [133] : (a) Two chiral units. Unit-cells for b) isotactic and c) syndiotactic configuration. Band structures of 3D chiral mechanical metamaterial for (d) Isotactic configuration and (e) Syndiotactic configuration (Band gaps are highlighted in grey and the lowest four band branches are colored). 20

1.14 Extract from [191] : Metabeam design. (a) Photograph of the metamaterial beam. (b) Schematic of the top view of the unit cell. The gray region is aluminum, and the inner white areas are holes. The unit-cell geometry comprises a frame, an inner mass, and several ribs. (c) Acoustic dispersion relation for axial propagation in the metabeam; k and a are the wavevector and unit-cell length, respectively. The solid red, dotted blue, dashed green, and dashed-dotted pink curves correspond to compressional (C), shear-horizontal (SH), shear-vertical (SV), and torsional (T) modes, respectively. (d)–(e) Geometries used for the models. The blue regions and red ribs act as masses and springs, respectively, shown for the following modes: (d) compressional (C, motion along the axial direction), (e) shear-horizontal (SH, motion along the width direction), (f) shear-vertical (SV, out-of-plane flexural motion), and (g) torsional (T, rotation about the axis along the axial direction). (h)–(k): simulated kinetic- and strain-energy distributions for the lowest four eigenmodes, respectively. The green arrows show the displacements. 21

1.15 Structure of the thesis 23

2.1 Investigated structure displayed at three different scales. (a) Mesoscopic scale, consisting of 11 unit cells, (b) a single unit cell, and (c) the elementary beam pattern from which the unit cell can be constructed by applying mirror symmetry operations with respect to all three planes: $(\mathbf{x}, \mathbf{y})$, $(\mathbf{x}, \mathbf{z})$ and $(\mathbf{y}, \mathbf{z})$. 27

2.2 Seven different unit cells derived from the default structure for different values of the parameters vector $\mathbf{p}_S = \left[\hat{z}_A, \hat{y}_B, \hat{z}_C, \hat{y}_C, \hat{x}D\right]$. The $\mathbf{p}_{S0} = \left[0, 0, 0, 0, 0\right]$ unit cell (a) is considered as our reference. (b) $\mathbf{p}_S = \left[1, 0, 0, 0, 0\right]$, (c) $\mathbf{p}_S = \left[0, 1, 0, 0, 0\right]$, (d) $\mathbf{p}_S = \left[0, 0, 1, 0, 0\right]$, (e) $\mathbf{p}_S = \left[0, 0, 0, 1, 0\right]$, (f) $\mathbf{p}_S = \left[1, 1, 1, 1, 0\right]$ and (g) $\mathbf{p}_S = \left[1, 1, 1, 1, 1\right]$ 28

2.3 Schematic representation of a single beam element of length L, connecting two arbitrary points P and Q. The beam's deformation at any position s, can be described with 3 translational (U_1, U_2, U_3) and 3 rotational (θ_1, θ_2, θ_3) degrees of freedom. These are associated with three components for the internal force (F_1, F_2, F_3) and moment (M_1, M_2, M_3). 30

2.4 a) Dispersion graph obtained for the reference structure S_0 (sketched in the inset) with the SEM Matlab® code (blue symbols) and with Comsol® Solid Module (dashed line in gray). Here we adopt the reduced coordinates $K = ka_x/\pi$ and $\Omega = fa_x/c_t$. b) and c) show the deformed shapes of the unit cell computed with Comsol® Solid Module for $K = 0$ at $\Omega = 0.079$ and $\Omega = 0.018$, respectively. The normalized U_y-component is represented by a color gradient ranging from blue (negative) to red (positive). . . . 34

2.5 (a) Sketch of the reference unit cell displaying, in blue and yellow, the two planes considered to examine the eigenmodes symmetries. (b) Representation of deformed unit cells using the total displacement $\left(U_x^2 + U_y^2 + U_z^2\right)^{1/2}$ for the first twelve eigenmodes of the structure. The color is indicative of the sign of the longitudinal displacement U_x. (c) Dispersion diagram for the reference structure and (d) the same data sorted in four different diagrams according to the symmetries of U_x. The colormap indicates the dominant polarization of the total displacement; green (respectively black) for a transverse (respectively longitudinal) polarization. The red symbols refer to the solutions sketched in (b). (e) Inverse of the determinant of $\mathbf{S}_p$ at Ω_t versus $\mathrm{Re}(K)$ and $\mathrm{Im}(K)$, (f) Inverse of the determinant of condensed matrices $\mathbf{S}_p^{\mathrm{SS}}, \mathbf{S}_p^{\mathrm{SA}}, \mathbf{S}_p^{\mathrm{AS}}, \mathbf{S}_p^{\mathrm{AA}}$ at the same Ω_t. 36

2.6 Reduced bandgap width $\Delta\Omega/\Omega_0$ of the absolute bandgaps exhibited from 2.757 structures selected from a starting pool of 16.000. The results are displayed as a function of all seven tuning parameters of the investigated system; with (a-b) the parameters governing the unit cell's aspect ratio and (c-g) the parameters setting the elementary beam pattern structure. Three clusters of structures showing strong geometrical similarities are identified and highlighted in blue, cyan and red. Among each cluster, the structures S_1^*, S_2^* and S_3^*, associated with the broadest total bandgaps are depicted with dark-edged diamond symbols. 38

2.7 Unit cells of the three optimal structures S_1^* (top), S_2^* (middle) and S_3^* (bottom) along with their respective dispersion diagrams. The absolute band gaps are indicated by the grey-shaded area. 39

2.8 Evolution of the dispersion diagrams as structure S_0 (a) is continuously transformed into structure S_1 (c) by sweeping parameters $\hat{y}_B$ and $\hat{y}_C$, simultaneously (*i.e.* setting $\hat{y}_B = \hat{y}_C$) from 0 to 1. Right column: reduced bandgap width plotted as a function of $\hat{y}_C$. The coloured region indicates the bandgap extension as well as its nature (blue for a partial bandgap, pink for an absolute bandgap). 40

2.9 Evolution of the dispersion diagrams as structure S_1 (a) is continuously transformed into structure S_3 (c) by varying parameters $\hat{z}_A$ and $\hat{z}_C$, simultaneously (*i.e.* setting $\hat{z}_A = \hat{z}_C$) from 0 to 1. Right column: reduced bandgap width plotted as a function of $\hat{z}_C$. The coloured region indicates the bandgap extension as well as its nature (blue for a partial bandgap, pink for an absolute bandgap). 41

2.10 Characterization of the constitutive material (PLA): (a) photograph of the experimental setup. (b) Experimental frequency response function (black) and SEM prediction using a Zener model (red). (c) Frequency dependence of the real part of the Young modulus E' (blue) and of the loss factor η (red). 43

2.11 Experimental setup: (a) Finite-size 3D-printed structure S_3. (b) Experimental configuration with the lattice structure mounted in a configuration corresponding to an excitation along the **z** direction. (c-d) Same experimental setup but with the excitation along **x** and **y**. 44

2.12 Experimental demonstration of the filtering effect: (A.1) Theoretical dispersion diagram of the unit cell S_3 with a complex Young's modulus $E = 3.2(1 + i0.011)$ GPa (coloured points between green and black) and a real Young's modulus $E = 3.2$ GPa (red points) . The sizes of the points corresponding to the case where E is complex are determined by the value $1 - Z = 1 - |k_i|/\sqrt{k_r^2 + k_i^2}$. The shaded areas highlight the theoretical expectations for the bandgap extension where $Z > 0.95$ for all points in the area. (A.2) Theoretical (blue) and experimental (black) transmissions of the γ_T $/\gamma_B$ ratio whose components are shown in (B.2), (C.2) and (D.2) when the finite-size structure is excited in the **x**, **z** and **y** directions respectively. (B.1), (C.1) and (D.1) are the theoretical scatter plots classified into the SS, SA and AS mode families respectively. 45

3.1 (a) Unit cell of the X-Beam Plate (XBP). (b) Unit cell of the X-Beam Sandwich (XBS), consisting of two XBP layers (red) connected by a lattice core (blue). 49

3.2 Coordinate system and notation for translations, rotations, forces, and moments of a thin plate. 50

3.3 (a) Coordinate system and notation of displacements and forces involved in the coupling between plate edges and beam nodes. (b) Diagram of the complete plate–beam assembly. 54

3.4 (a) Three-dimensional FEM unit cell with Floquet–Bloch periodicity imposed on the plate cross-section. (b) Equivalent unit cell reduced to plate and beam elements in the semi-analytical model. (c) Dispersion curves computed using the 3D FEM model in COMSOL (Black lines) and predicted by the proposed semi-analytical formulation (Blue dots). 58

3.5 (a) Complete XBS unit cell. (b) Half XBS model with symmetric boundary conditions imposed on the $y = 0$ plane (red-highlighted elements). (c) Half XBS model with antisymmetric boundary conditions imposed on the $y = 0$ plane (blue-highlighted elements). (d) Dispersion relation computed on the complete unit cell. (e) Dispersion branches obtained from the symmetric half-model. (f) Dispersion branches obtained from the antisymmetric half-model. In (e) and (f), the color of each branch indicates the mode polarization, ranging from predominantly in-plane deformation (blue) to predominantly out-of-plane deformation (yellow). (g) shows the propagation of a symmetric out-of-plane–polarized mode and (h) shows an antisymmetric out-of-plane–polarized mode. 59

3.6 (a), (b), and (c) show dispersion diagrams computed using the semi-analytical plate+beam model for three unit cells: (a) homogeneous plate, (b) X-beam Plate (XBP), and (c) X-beam Sandwich (XBS). Dispersion branches are color-coded using two gradients to distinguish four wave polarizations: z-bending/compression (green $\rightarrow$ black) and y-bending/torsion (red $\rightarrow$ blue). The bar charts display, in green, the value of C_{RIG} (bending stiffness-to-mass ratio) and, in grey, the value of C_{ABG} (absolute band gap percentage below Ω_5) for each unit cell. 61

3.7 Column (a): (a.1) schematic of the X-Beam Plate (XBP); (a.2) absolute band gap ratio C_{ABG} and (a.3) specific flexural stiffness C_{RIG}, as functions of beam width e_s and span L_s. Columns (b) and (c): performance maps for X-Beam Sandwich (XBS) structures using skins corresponding to the two selected points in (a), showing variation of C_{ABG} and C_{RIG} with core diameter d_c and height H_c. (d): Pareto fronts comparing all configurations studied. 62

3.8 (a–c) Photographs of the experimental setup under x-, y-, and z-axis excitation, respectively. Subfigures (a.1), (b.1), and (c.1) show the corresponding measured FRFs (black) and COMSOL simulations (blue). (d) Dispersion relation predicted by the semi-analytical model; grey bands indicate the predicted absolute band gaps. 64

4.1 (a) Lumped resonator unit cell. (b) Finite periodic resonator chain. 70

4.2 Dispersion diagram of the undamped periodic resonator chain ($\mu_2 = 0.5$ and $\alpha = 0.6$). (a) Imaginary part of the Floquet multiplier λ. (b) Real part of the reduced wavenumber qa. (c) Imaginary part of qa. The shaded region indicates the resonant bandgap . . . 72

4.3 Mass–bandgap trade-off for the undamped resonator chain. (a) Relative bandgap width β as a function of the resonator mass fraction μ_2 for different α. Each curve corresponds to a distinct value of α and is distinguished by a colour gradient. (b) Trade-off function $\Phi = (1 - \mu_2)\beta$ for the same set of parameters. For each value of α, the black dot marks the optimal operating point, defined as the maximum of Φ; the corresponding optimal mass fractions are also indicated in (a). 74

4.4 Damped unit cell of the periodic resonator chain. Viscous dampers c_1 and c_2 are added in parallel with k_1 and k_2 to the undamped unit cell of Fig. 4.1a). 75

4.5 Effect of viscous dissipation on the dispersion and finite-chain response of the resonator chain. (a) Real part $\mathrm{Re}(qa)$ and (b) imaginary part $\mathrm{Im}(qa)$ of the propagation constant for different loss factors. (c) Frequency response function H in dB for a finite chain of $N_c = 10$ cells. The grey region recalls the undamped bandgap, while the filled areas below $H_{\mathrm{lim}} = -6$ dB define the attenuation bands. 76

4.6 Relative attenuation bandwidth $\beta_{6\mathrm{dB}}$ as a function of damping and number of cells. (a) Influence of the waveguide loss factor ξ_1 for $\xi_2 = 10^{-3}$. (b) Influence of the resonator loss factor ξ_2 for $\xi_1 = 10^{-3}$. Curves are colour-coded by the number of cells N_c. . . . 77

4.7 Mass–attenuation trade-off for a finite resonator chain with damping ($\xi_1 = \xi_2 = 0.01, N_c = 5$). (a) Relative attenuation bandwidth $\beta_{6\mathrm{dB}}$ as a function of the resonator mass fraction μ_2 for different value of α, distinguished by a colour gradient. (b) Trade-off function $\Phi = (1 - \mu_2)\beta_{6\mathrm{dB}}$ for the same set of parameters. For each value of α, the black dot marks the optimal operating point, defined as the maximum of Φ. 78

4.8 Nonlinear extension of the damped unit cell shown in Fig. 4.4, obtained by adding a cubic stiffness k_3 to the local resonator. 80

4.9 Complex nonlinear dispersion relation of the damped periodic resonator chain under Floquet–Bloch conditions computed for $N_h = 1$. (a) Imaginary part and (b) real part of the complex wavenumber qa as functions of the reduced frequency Ω. Enlarged views around the onset of the attenuation band ($\Omega \in [0.98, 1.03]$) are shown in (a.1) and (b.1). The linear dispersion is reported in green. Nonlinear branches are shown for softening ($\kappa_3 < 0$, blue) and hardening ($\kappa_3 > 0$, orange-to-brown) nonlinearities; lighter to darker shades correspond to increasing prescribed vibration amplitudes $A^\star$. Solid lines denote stable solutions, while dashed lines indicate unstable branches. Results are obtained for $\alpha = 0.25$, $\mu_2 = 0.25$ and $\xi = 0.01$. 84

4.10 Nonlinear frequency response of a finite resonator chain composed of $N_c = 8$ unit cells computed for $N_h = 1$. Transfer function magnitude H as a function of the reduced frequency Ω. Enlarged views highlight the onset of attenuation ($\Omega \in [0.95, 0.98]$) and the attenuation region ($\Omega \in [0.98, 1.04]$). The linear response is shown in green. For hardening nonlinearities ($\kappa_3 = +0.75$), orange and brown curves correspond to excitation amplitudes $U_{\text{in}} = 4 \times 10^{-3}$ and 5×10^{-3}, respectively. For softening nonlinearities ($\kappa_3 = -0.75$), light and dark blue curves correspond to the same amplitudes. Solid lines denote stable solutions, while dashed lines indicate unstable branches. Results are obtained for $\alpha = 0.25$, $\mu_2 = 0.25$ and $\xi = 0.01$. 86

4.11 Schematic design workflow for the optimisation of a periodic resonant vibration filter based on a resonator chain. 88

4.12 Beam-lattice waveguide. (a) Unit cell (frame) and node numbering. (b) Cross-sections of the longitudinal (green) and transverse (blue) beams. (c) Periodic waveguide composed of five unit cells. 89

4.13 Dispersion of the beam-lattice waveguide. (a) Full dispersion diagram of the frame. (b)–(e) Dispersion diagrams for the SS, SA, AS and AA symmetry families. Colours indicate the dominant polarization of the mode (green: x, red: y, blue: z). Representative mode shapes are shown above each sub-figure and correspond to the black star markers positioned on the dispersion branches. 90

4.14 Resonant waveguide. (a) Resonant unit cell and node numbering. (b) Cross-sections of the resonator beams (red/black/violet). (c) Periodic waveguide composed of five resonant unit cells. 91

4.15 Dispersion of the resonant unit cell (AS family) for $\mu_2 = 0.25$ and (a) $\alpha = 0.5$, (b) $\alpha = 1.1$, (c) $\alpha = 1.7$. Colours indicate the dominant polarization of the propagating mode (green: x, red: y). Grey rectangles highlight the AS-polarized bandgap. 92

4.16 Mass–bandwidth trade-off for the undamped resonant waveguide. (a) Colormap of the effective relative bandgap width β as a function of μ_2 and α. (b) Classification of bandgap closure scenarios: case 1 (pure resonant bandgap), case 2 (closure by a cut-off branch), and case 3 (no effective bandgap). Evolution of (c) β and (d) Φ. Red markers indicate the results for case 1 ($\alpha = 0.05$), while the black dashed curve recalls the Pareto front of the lumped mass–spring model in the limit $\alpha \to 0$. 93

4.17 Complex dispersion and finite-chain response of the damped resonant waveguide for $\mu_2 = 0.5$ and $\alpha = 0.5$. The AS-family dispersion of the unit cell is shown through (a) the imaginary part $\mathrm{Im}(kL_x)$ and (b) the real part $\mathrm{Re}(kL_x)$ of the complex wavenumber in the undamped case ($\xi = 0$). (c) Corresponding frequency response function H_y (in dB) of a finite chain composed of $N_c = 5$ unit cells. s.1) and s.2) respectively show the mode shape associated with the complex solution within the bandgap and the edge mode at the resonance frequency. Sub-figures (a.1), (b.1) and (c.1) present zoomed views over $\Omega \in [0.9,\ 1.45]$ for increasing loss factors: $\xi = 0$ (black), $\xi = 0.05$ (red) and $\xi = 0.1$ (green) 96

4.18 Comparison of the damped mass–bandwidth trade-off for $\alpha = 0.1$ and $\xi = 0.01$. (a.1) Evolution of the attenuation bandwidth $\beta_{6\mathrm{dB}}$ with μ_2 for the beam-lattice model. (b.1) Corresponding evolution for the lumped mass–spring model. (a.2) Trade-off function $\Phi = (1 - \mu_2)\beta_{6\mathrm{dB}}$ for the beam-lattice model. (b.2) Corresponding trade-off for the lumped model. Curves correspond to increasing numbers of cells N_c (from blue to yellow); black dots indicate the optimal points corresponding to the maximum of each trade-off function Φ 97

4.19 Experimental validation of the resonant waveguide filter. (a) Photograph of the experimental setup showing the five-cell resonant filter clamped at the base and excited by a shaker, with a laser vibrometer measuring the response at the free end. (b) Imaginary part $\mathrm{Im}(kL_x)$ and (c) real part $\mathrm{Re}(kL_x)$ of the AS eigenvalues of the damped unit cell, computed using the beam-lattice model; the colour scale from green to red indicates the dominant polarization from x- to y-motion. (d) Experimental FRF H^y_{exp} (black) compared to numerical FRFs from the beam-lattice model (blue) and the lumped mass–spring model (yellow). The grey rectangle indicates the undamped bandgap, and the horizontal line at -6 dB defines the attenuation bandwidth $\beta_{6\mathrm{dB}}$. . . 100

4.20 Characterisation of the geometric nonlinearity of a single resonator. (a) Finite-element model used to compute the static force–displacement relation. (b) Photograph of the experimental setup for dynamic testing of a single unit cell. (c) Static force–displacement relation obtained from finite-element simulations (red markers) and cubic polynomial fit (black line). (d) Measured frequency response function of the single resonator for increasing base excitation amplitudes. 101

4.21 Measured frequency response function H of the five-cell resonant filter, obtained from the same experimental configuration as in Fig. 4.19(a), but for higher excitation levels. The curves correspond to base acceleration amplitudes of $0.5\,g$ (dark blue), $0.8\,g$ (light blue), $1.2\,g$ (green), and $1.4\,g$ (yellow). Zoomed views highlight the amplitude-dependent shift of the attenuation band around 130 Hz 101

5.1 Cube-lattice waveguide. (a) Beam layout and node numbering of the unit cell. (b) Periodic lattice waveguide composed of five unit cells in series. (c) Cross-sections of the different beams 105

5.2 Dispersion of the beam-lattice waveguide. (a)–(d) Dispersion diagrams for the SS, SA, AS and AA symmetry families. Colours indicate the dominant polarization of the mode (green: x, red: y, blue: z). Representative mode shapes are shown above each sub-figure. 106

5.3 Multi-resonant cubic unit cell for the absolute filter. (a) Cube-lattice waveguide with attached local resonators. (b) Details of the resonator integration: (b.1) external face carrying the z-resonators, (b.2) external face carrying the y-resonators, and (b.3) internal face carrying the x-resonator. 107

5.4 Successive addition of resonators to the cube lattice: (a) two y-oriented resonators, (b) two y-oriented plus two z-oriented resonators, and (c) two y-oriented plus two z-oriented plus one x-oriented resonator. Columns 1)–4) report the dispersion curves for the SS, SA, AS, and AA mode families, respectively. Branches are coloured according to the dominant modal polarization along the x- (green), y- (red), and z-axes (blue). Polarized bandgaps are highlighted by grey shaded regions, while the absolute bandgap is indicated by the black shaded region. The modal deformations associated with the starred black markers R_{SS}, R_{SA}, R_{AS}, and R_{AA} are shown above the corresponding panels. 108

5.5 Dispersion diagrams of the four symmetry families for a cubic resonant lattice with resonant mass fraction equal to $\mu_2 = 0.7$. The three rows correspond to different frequency location of the resonance: $\alpha = 0.5$ (green box), $\alpha = 1.05$ (red box) and $\alpha = 1.5$ (black box). Columns (a)–(d): SS, SA, AS and AA families, respectively. For each family, the locally resonant bandgap is shaded in grey, and the overlap between the four families defines the absolute bandgap (black rectangle). 110

5.6 Mass–bandwidth trade-off for the undamped absolute resonant filter. (a) Absolute bandgap width β_{abs} in the (μ_2, α)-plane, shown using a colour map ranging from dark blue ($\beta_{abs} = 0$) to red ($\beta_{abs} = 0.1$). (b) Classification of the closure scenarios of Fig. 5.5: case 1 in green (absolute bandgap limited by SS), case 2 in red (closure driven by SA/AS cut-off branches), and case 3 in black (no absolute bandgap). (c) Relative width β_{abs} as a function of μ_2 restricted to case 1; the resonance placement α is encoded by the point colour using a colour map ranging from dark blue ($\alpha = 0.05$) to yellow ($\alpha \simeq 1.12$). 111

5.7 Influence of γ_{SS} (resonant mass share of the x-oriented resonator) on the undamped absolute bandgap. For $\mu_2 = 0.5$ and $\alpha = 0.05$: (a) dispersion diagram for $\gamma_{SS} = 1/3$; (b) upper bandgap edges versus γ_{SS} (AA: violet, SA/AS: red, SS: green), with the resulting absolute bandgap shaded in grey; (c) dispersion diagram for $\gamma_{SS} = 1/2$. For $\mu_2 \in [0.05, 0.95]$ and $\alpha = 0.05$: (d) absolute bandgap width β_{abs} versus μ_2 for $\gamma_{SS} = 1/5$ (black) and $\gamma_{SS} = 1/3$ (cyan); (e) trade-off function $\Phi = (1 - \mu_2)\beta_{abs}$ versus μ_2 for the same cases, with the optimal points marked. 113

5.8 Damped dispersion diagram for $\mu_2 = 0.5$, $\alpha = 0.1$, $\gamma_{SS} = 1/3$ and $\xi = 0.005$. (a) Imaginary part $\mathrm{Im}(kL_x)$ and (b) real part $\mathrm{Re}(kL_x)$. Only the most propagative solutions are shown, corresponding to compression (green), bending in y and z (red), and torsion (violet). (c) FRFs of a finite chain of $N_c = 5$ unit cells: $H_{x,y,z}$ (black) for an oblique excitation with equal components along x, y and z, and $H_{y,z}$ (red and blue dashed curves) for an excitation restricted to the y and z directions. The black dashed line indicates the -6 dB level. In all panels, the grey band denotes the absolute bandgap predicted by the undamped dispersion relation. 115

5.9 Four-step design for the absolute resonant filter. (1) Bare lattice waveguide is sized to meet static stiffness, mass, and strength constraints (FE stress check under representative loading). (2) Dimensionless parameters are defined from the bare-waveguide design and the target filtering frequency. (3) The absolute mass–attenuation bandwidth trade-off is optimised. (4) FRFs of the bare waveguide and the optimised filter are compared to confirm the attenuation band and identify potential side effects. 117

5.10 Design and assembly of the printed cube-lattice unit cell. (a) CAD view of the face carrying the z-resonators. (b) CAD view of the face carrying the y-resonators. (c) CAD view of the face carrying the x-resonator. (d) Assembled unit cell (e) Example of a four-cell filter obtained by assembling four unit cells in series. 118

5.11 Applicative demonstrator inspired by the passenger-cabin floor assembly of an aircraft. a) CAD model plot of cabin passenger extraded from [21] (b) Schematic of the reduced problem: the seats (beige) is periodically connected, via interface parts (cyan), to a long rail (dark blue), which is itself periodically attached to the aircraft structure through additional interface parts (green). The aircraft structure is here reduced to a multi-axial vibration source. The black dashed box indicates the size of the manufactured demonstrator relative to this schematic. (c) CAD model of the demonstrator using the same colour code: Norcan aluminium beam (beige, representing one seat), two resonant lattice filters (dark blue, representing the rail), and interface parts connecting the filters to the beam (cyan, zoomed in c.2) and to the support brackets (green, zoomed in c.1). 120

5.12 Numerical modelling of the printed unit cell. (a) COMSOL model of the bare cube-lattice cell, (b) COMSOL model of the unit cell with three identical resonators ($\gamma_{SS} = 1/5$, $\mu_2 = 0.5$, $\alpha = 0.157$). (c) Reference frequencies of the four symmetry families (SS, SA, AS, AA) for the bare waveguide cell. (d) Dispersion diagrams: coloured curves from the beam spectral-element model and black dots from the 3D COMSOL model. The dark grey rectangle indicates the absolute bandgap; the light grey rectangle shows the SA/AS-polarised bandgap. 121

5.13 Numerical response of the full demonstrator. (a) Resonant structure: full FE model including the resonant elements. (b) Reference structure: same model without the resonant elements. The blue lines indicate the excitation areas and the red point indicate where the response is evaluated. (c) Global transmission T_1 (in dB) at the observation red point on the Norcan beam for the filtered (solid black) and reference (dashed black) configurations. (d) Insertion loss for each acceleration component: IL_x (green), IL_y (red) and IL_z (blue). Positive/negative values indicate that, at a given frequency, the response of the resonant configuration is attenuated/amplified relative to the reference configuration. Dark grey rectangle: predicted absolute bandgap; light grey rectangle: predicted SA/AS-polarised bandgap. 123

5.14 Influence of the x-oriented resonator on the demonstrator performance. (a) Dispersion diagrams of the periodic unit cell with all five resonators (a.1) Dispersion diagrams of the unit cell without the x-resonator (b) Global transmission T_1 at the observation point for the full demonstrator with (solid line) and without (dashed line) the x-resonator. Dark grey rectangle: absolute bandgap of the five-resonator case; light grey rectangle: SA/AS-polarised bandgap. 125

5.15 Experimental and numerical transfer functions of the demonstrator. (a) Photograph of the test set-up: the demonstrator is bolted to the top plate of a tri-axial shaker; the reference accelerometer on the shaker table and the three accelerometers mounted on the Norcan beam are indicated. (1)–(3) Transfer functions T_1 (mid-span), T_2 (right) and T_3 (left): experiments (black) and corresponding numerical predictions (blue). Dark grey bands denote the predicted absolute bandgap and light grey bands the SA/AS-polarised bandgap. Insets (Z.1)–(Z.3) provide zoomed views over [90, 140] Hz. 126

6.1 Alternative multi-resonator layouts for the cubic beam-lattice unit cell and preliminary numerical comparison. (a) Transmitted-to-input acceleration norm ratio for five-cell filters : actual configuration (red) and new configuration (blue). (b) Actual configuration with five single-degree-of-freedom resonators: two z-oriented resonators, two y-oriented resonators, and one internal x-oriented resonator. (c) New configuration with four external two-degree-of-freedom resonators: on each face, a primary resonator polarized along x is coupled to a secondary resonator polarized along y or z. 134

6.2 Three-functional passenger seat rail prototype: (1) a load-bearing rail enabled by its lattice architecture, (2) a rail capable of filtering elastic waves through the integration of periodically distributed resonators, and (3) a cable-routing rail, where the cables may provide additional damping and thereby further enhance the vibration filtering performance. 135

6.3 Concepts for exploiting nonlinear effects in local resonators. (a) Example of a resonator designed to exhibit a softening geometric nonlinearity through inclined slender supporting beams. (b) Example of an impact-based resonator, in which the mass displacement is limited by two stops, leading to repeated impacts under resonance. (c) Alternative impact-based concept relying on a ball embedded within the resonator mass. 136
B.1 Direction cosines for an 3D oriented beam 139
D.1 Full complex dispersion of figure 2.12 (including the imaginary part of the wave vector) and frequency responses for the unit cell S_3 in the presence of damping: (A.1), (B.1), (C.1), and (D.1) display the real part of the complex wavenumber K computed for a complex Young's modulus $E = 3.2(1 + 0.011\mathrm{i})$ GPa (colored points) and a purely real one $E = 3.2$ GPa (red points). These results are identical to those shown in Figure 12. (A.1.I), (B.1.I), (C.1.I), and (D.1.I) display the imaginary part of the complex wavenumber. (D.1.I.1) and (D.1.1) provide close-up views of Figures D.1.I and D.1, respectively, highlighting the bandgap broadening induced by material damping. (A.2), (B.2), (C.2), and (D.2) present the frequency responses of the γ_T/γ_B ratio, obtained from the SEM model (blue curves) and from experimental measurements (black curves), for excitations along the **x**, **z**, and **y** directions. 143
E.1 Coordinate system and notation for translations, rotations, forces, and moments of a thin plate. 144
F.1 (a) Coordinate system and notation of the displacements and forces involved in the coupling between plate edges 1 and 2 and beam node 1. (b) Schematic representation of the complete plate–beam assembly. 154

List of Tables

2.1 Summary of the relevant configurations and the associated structural and lattice parameters. 29

6.1 Main contributions of the thesis. 132

CHAPTER 1

Introduction

Contents

1.1 Context 2
1.2 Vibration control strategies 5
1.3 State of art on the periodic structures 7
1.3.1 Key Concepts 8
1.3.2 Phononic Crystals 10
1.3.3 Lattice structures 11
1.3.4 Absolute bandgap in 1D elastic wave guide 18
1.4 Outline of the thesis 21

1.1 Context

Passenger comfort is a central issue in aircraft cabin design, both for the user experience and the acceptability of future designs [1]. After a long flight, it is not uncommon for passengers to report an uncomfortable experience. Bouwens et al. [2] ranked the main environmental factors affecting cabin comfort: anthropometry (space), noise, odor, climate, vibration, and light. Among these, noise and vibration — often co-present and physically linked — play a major role in the overall perception of comfort.

Fig. 1.1 a), extracted from [3], highlights (in red) the main contributors, while Fig. 1.1 b) provides a more detailed classification. These sources include radiation from onboard subsystems (ventilation, landing gear deployment/retraction, etc.), the aerodynamic flow around the aircraft, and excitations primarily associated with engine components, usually located under the wings. In the acoustic case, these disturbances are transmitted to the fuselage through air-borne and/or structure-borne paths, and then generate sound radiation into the cabin via the fuselage panels [4–6]. Although these acoustic and vibro-acoustic issues are widely documented in the literature [7–11], they are not addressed further in this work.

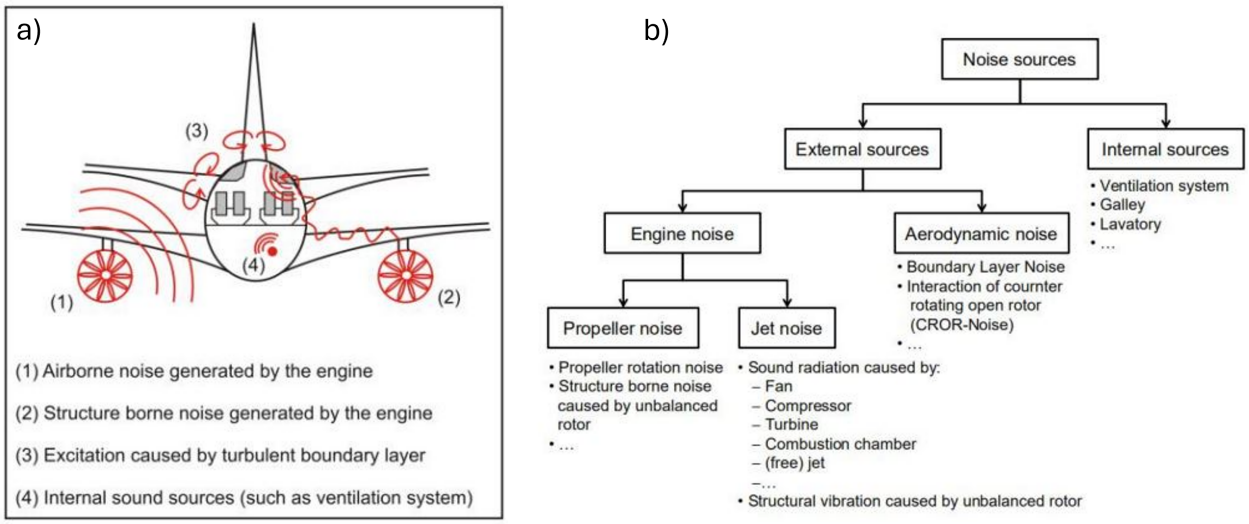

Figure 1.1: a) Mechanisms for sound generation in an aircraft b) An overview on external and internal noise sources. Figures extracted from [3]

This work focuses on the purely vibratory excitation induced by turbine imbalance, which primarily propagates through the structure to the seats. For current turbofans, the dominant frequency associated with this imbalance—linked to the rotation speed—typically ranges from 40 to 90 Hz [12, 13]. In this same frequency range, Krause et al. [14] performed comfort tests (Fig. 1.2), evaluating passenger perception while seated on an aircraft seat for different vibration amplitudes (see 1.2a) and 1.2b)). The curves in 1.2c) indicate a critical vibration amplitude beyond which discomfort becomes pronounced, and show that this threshold decreases as the excitation frequency decreases. According to Hostens et al. [15], such low-frequency excitations can resonate with the human body, potentially leading to muscle fatigue and back hurting.

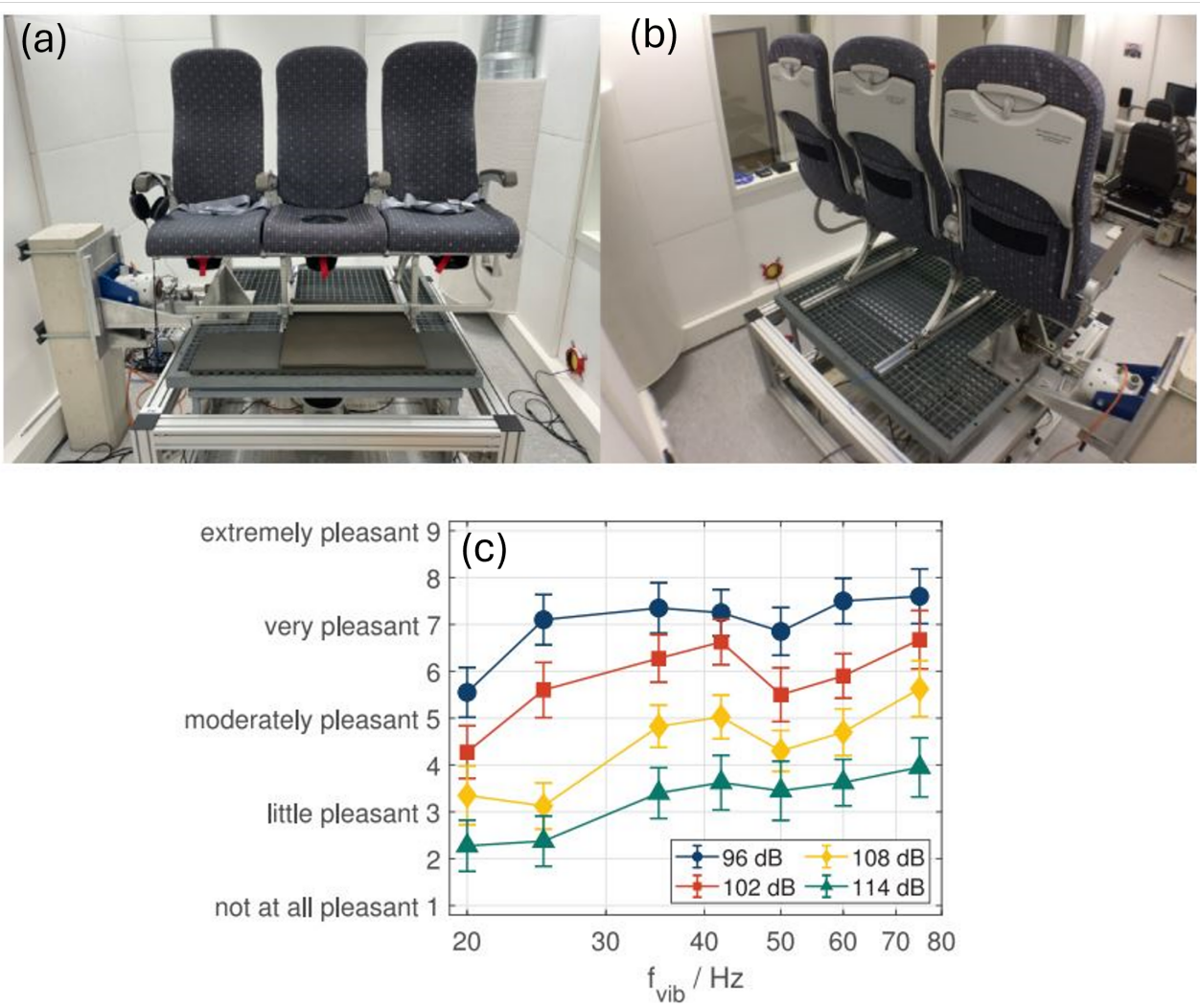

Figure 1.2: Used aircraft cabin seat bench on the vibration platform at Carl von Osszietzky University from the front (a) and the back showing the accelerometer on the seat rail (b). (c) Mean pleasantness ratings (with verbal anchors) as a function of vibration frequency f vib averaged across all (N = 40) participants divided by acceleration levels (re. 1 lm/s2) at the seat rail (left) and averaged across all acceleration levels divided by gender (right). Error bars show 95 % confidence intervals. Figures extracted from [14]

In the context of reducing aviation's ecological impact by 2050 [16, 17], more efficient propulsion architectures are being investigated, such as the *open-rotor turbofan* [18, 19]. Because these concepts operate at lower rotational speeds, they tend to shift the dominant excitations toward lower frequencies—precisely in the range where passenger tolerance to vibratory amplitude decreases (see Fig. 1.2c). It therefore becomes crucial for future cabin designs to implement effective low-frequency vibration control solutions, while limiting added mass and keeping costs reasonable to meet environmental objectives [20].

To better understand the problem, it is necessary to examine the cabin floor supporting architecture, which forms the mechanical interface between the aircraft structure and the seats. Fig. 1.3 (extracted from [21] and [22]) shows the bare interior of an aircraft fuselage—floor panels and seats removed—from a bottom view (a) and a top view (b), highlighting the main load-carrying elements. The floor is supported by *floor beams*, connected to the fuselage by inclined *struts*. Longitudinal *rails* attached to the *floor beams* then provide the passenger *seat* attachment points.

This configuration suggests a critical transmission path to passengers: turbine → wings → fuselage → *struts* → floor beams → rails → seats. Effective vibration control must therefore target one or more of these components to reduce vibration reaching the seats. However, transmission takes place through a complex geometry, marked by discontinuities (assemblies, cross-section changes, joints) that promote mode conversions between bending, longitudinal, and shear/torsional waves [23–25]. As a result, the vibration experienced at seat level is potentially multi-polarized, calling for an absolute vibration control system able to simultaneously attenuate all this polarizations within the critical frequency range.

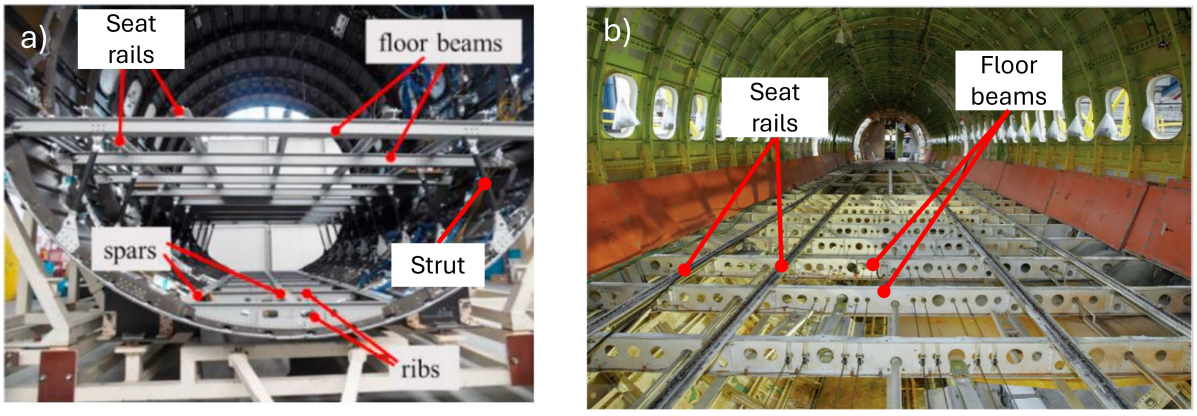

Figure 1.3: a) View from below of the inside an aircraft fuselage, extracted from [21]. b) View from above of the upper floor inside an aircraft fuselage, extracted from the cover of [22].

1.2 Vibration control strategies

Several vibration control strategies have been reported in the literature, typically classified as passive, active, or hybrid [26, 27]. Active approaches rely on distributed sensing and actuation, often using piezoelectric films bonded to the structure [28–33]. Hybrid solutions combine passive and active mechanisms to maintain performance under temperature or frequency variations [34–37]. Yet, both active and hybrid systems require many components, increasing cost and maintenance and thus limiting industrial uptake. This thesis therefore focuses on passive vibration mitigation, which is simpler and more robust. Most passive vibration-control solutions reported in the literature rely on three physical mechanisms: dissipation, absorption, and filtering of vibratory energy [38, 39].

Regarding dissipative strategies, two main types of treatments are generally distinguished. Viscoelastic treatments [40–43] dissipate vibratory energy through the deformation (often shear) of a polymer layer integrated into the structure. This mechanism allows for an increase in effective damping with relatively simple implementation (bonded layers, inserts, sandwiches). However, their properties are sensitive to operating conditions (temperature, deformation level, aging), which can lead to performance variability and require careful characterization. On the other hand, friction devices [44–47] dissipate energy through controlled sliding between two surfaces, generating large hysteresis loops. However, their applications are mainly limited by their nonlinear nature, which is difficult to predict, and the uncertainties associated with contact (variability of the coefficient of friction, *stick–slip* phenomena, wear), which may impose additional maintenance requirements.

Regarding absorption strategies, two main families are generally distinguished: Tuned Mass Dampers (TMD) and Nonlinear Energy Sinks (NES). TMDs [48, 49] are passive attachments that use a secondary mass tuned to a targeted resonance of the primary structure. They can be highly effective over a narrow frequency band, but this performance typically comes with a noticeable mass penalty and strong sensitivity to detuning or broadband excitation. In practice, TMDs often require on the order of 5–10% of the primary mass, which can be prohibitive. NES [50–52] are conceptually similar attachments, but intentionally introduce strong nonlinearity so that vibratory energy is transferred from the primary structure to the absorber through targeted energy transfer. This nonlinearity can enable mitigation over a broader range of frequencies and improve robustness to changes in the primary dynamics, often with a substantially smaller attached mass than a TMD for comparable vibration reduction. However, the nonlinear response is inherently amplitude-dependent: the dominant operating regime (e.g., activation threshold, energy pumping, saturation) is governed by the excitation level. Consequently, achieving reliable performance requires careful tuning of the NES parameters—particularly the damping—which strongly conditions the onset and efficiency of energy transfer

The strategy we will focus on in this thesis is vibration filtering. In industry, filtering is most often implemented by inserting a compliant interface—such as elastomeric pads or spring–damper mounts—between the protected structure and the excitation source [53, 54]. This configuration introduces an isolation resonance governed by the supported mass and the mount stiffness. Below this frequency, the structure remains effectively coupled to the source and attenuation is limited; above it,

transmissibility decreases with frequency, with performance strongly governed by damping. Such isolators have shown promising performance for helicopter and aircraft seat applications [55, 56]. Yet, while they provide broadband attenuation above the isolation frequency, they also introduce a low-frequency resonant mode and allow relative motion between subsystems, which can degrade mechanical integrity and functional tolerances.

To address these limitations, an alternative is to act directly on the load path by tailoring the structural architecture to reduce vibration transmission through the supporting structure. By adjusting geometry and material distribution, elastic-wave propagation can be shaped and attenuated over targeted frequency ranges [57], without relying on a compliant interface between subsystems. Among architectural solutions, periodic structures are especially promising for controlling elastic waves [22, 58]. Periodic networks have been extensively studied across wave physics—electromagnetic, acoustic, and elastic—for applications such as guiding, trapping, and filtering [59–65]. In mechanics, periodicity can passively induce destructive interference, leading to frequency intervals where waves cannot propagate (band gaps) and thus to an effective filtering action [66–68].

Based on the vibration transmission path identified earlier (see Fig. 1.2), the most relevant component to architect is the *seat rail*. Unlike the floor beams and the struts, the rail is not a primary contributor to the global stiffness of the fuselage or the cabin floor, which makes it a good candidate for design modifications with limited impact on the overall structure. Its main role is to carry the static loads associated with the seats and occupants.

Figure 1.4a) shows a CAD view of the cabin interior, while Fig. 1.4b) introduces a simplified vibro-acoustic model of the floor system. The rail is modeled as a beam, periodically connected along its length to the floor beams. Each passenger seat is attached to the rail through two attachment points located on the top face of the beam, positioned on either side of a floor-beam connection. This layout creates a *staggered* pattern between the seat attachment points and the floor-beam fixations. Elastic waves transmitted by the floor beams therefore propagate into the rail and then reach the seat attachment points.

The objective of this thesis is to redesign the rail as a periodic structure that simultaneously satisfies two requirements: (i) ensure the necessary static load-bearing capability for seats and occupants, and (ii) filter the elastic waves propagating between floor-beam connections and seat attachment points, thereby reducing the vibration spectrum transmitted to the passenger.

To assess the feasibility of this approach, the next section presents the state of the art on periodic structures, focusing on understanding the associated physical principles, their effectiveness, and identifying the potential limits of the trade-off between stiffness and filtering performance.

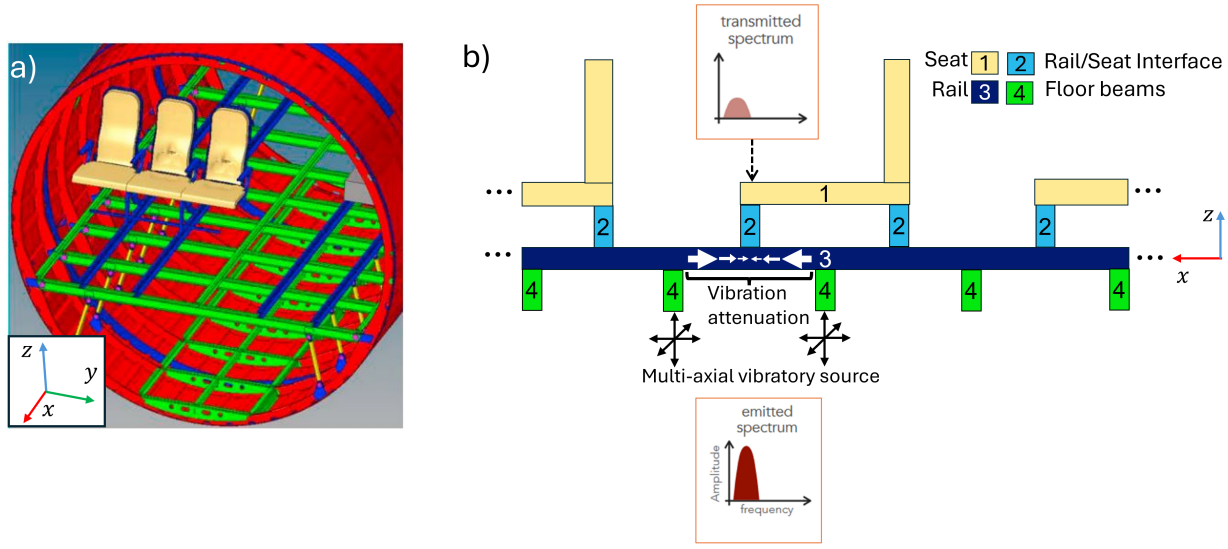

Figure 1.4: a) CAD model plot of cabin passenger extraded from [21] b) reduced vibration problem

1.3 State of art on the periodic structures

The study of periodic structures and their effects on wave propagation has a long history. Early roots can be traced to Newton's attempt to model sound propagation in air [69] and to Rayleigh's investigations of continuous periodic systems [70]. Over the eighteenth and nineteenth centuries, analyses of periodic chains and lattices progressively highlighted the hallmark of periodicity: *dispersion*, i.e., the dependence of wave velocity on frequency, later formalized in the general framework of wave motion in periodic media and crystal lattices [71, 72].

During the twentieth century, these ideas were consolidated and widely adopted in engineering mechanics, notably for periodic layered composites and repeated structural components, where unit-cell and matrix-based formulations naturally yield dispersion curves and pass/stop-band behavior [73, 74]. A major turning point occurred in the late 1980s with *photonic crystals*, which stressed the role of lattice symmetry and Brillouin-zone band diagrams in generating forbidden frequency ranges [75, 76]. Soon after, analogous concepts were transposed to acoustics and elastodynamics through *phononic crystals*, i.e., periodic composites or geometries engineered to create band gaps via *Bragg interference* [66, 77].

In the early 2000s, the emergence of *acoustic/elastic metamaterials* introduced local resonances as a route to *subwavelength* band gaps, alleviating the low-frequency scaling constraints of Bragg scattering [78]. Today, periodic media are commonly described through band structures and associated band gaps, providing a compact framework for wave filtering, guiding, and vibration mitigation.

In the remainder of this bibliographic study, we focus on *one-dimensional periodicity*. We first introduce the core notions required throughout—periodic conditions, the dispersion relation, and the concepts of pass and stop bands—and we define *phononic crystals* in the context of elastic-wave control. We then narrow the scope to a particularly relevant subclass, *lattice (truss-like) structures*, and review how they can be exploited for wave filtering, first via Bragg-type band gaps and then

through the integration of local resonant features. Finally, we survey the strategies that can yield *absolute* band gaps, i.e., stop bands that simultaneously affect multiple wave polarizations, with the aim of identifying architectures suitable for absolute vibration filtering.

1.3.1 Key Concepts

Dispersion relations and periodic conditions

The central quantity for characterizing an *elastic bandgap material* is the *dispersion relation*, i.e., the link between the angular frequency ω and the wavenumber associated with a harmonic wave. In a homogeneous medium, this relation is usually simple and leads to phase and group velocities, $c_\mathrm{p} = \omega/k$ and $c_\mathrm{g} = \mathrm{d}\omega/\mathrm{d}k$, that are only weakly dependent on frequency. In a periodic medium, however, the relevant quantity is no longer the "classical" wavenumber k but the *Bloch wavenumber* q, defined by the Floquet–Bloch theorem [79]: for a spatial period a, a harmonic field reproduces from one unit cell to the next up to a phase factor,

$$u(x + a) = u(x), e^{iqa}, \tag{1.1}$$

where q may be complex. This formulation implies that the dispersion diagram is *periodic in reciprocal space*: since e^{iqa} is invariant modulo the reciprocal lattice vector $G = 2\pi/a$, the branches $\omega(q)$ repeat with period $2\pi/a$, so it is sufficient to represent them over the *first Brillouin zone* $q \in [-\pi/a, \pi/a]$ [71].

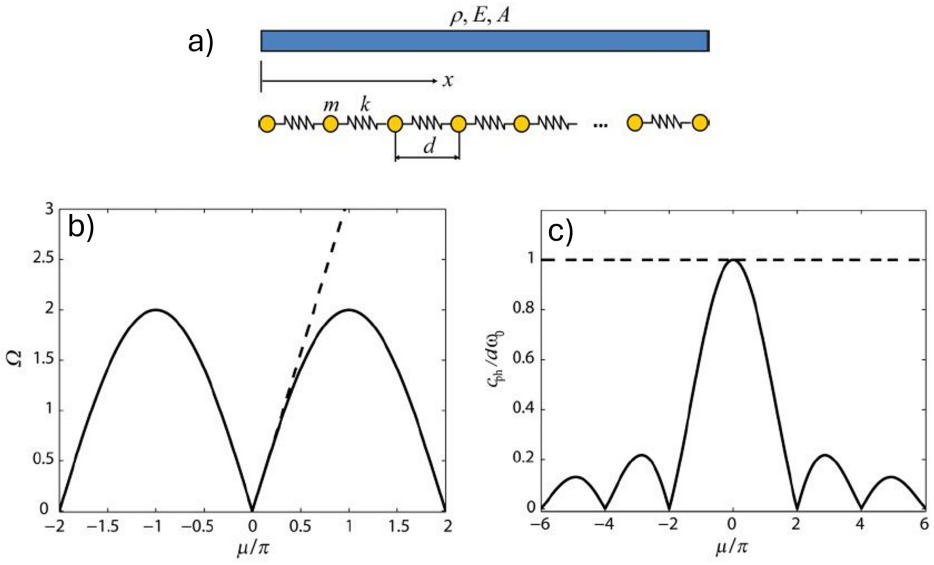

Figure 1.5: a) Discretization of a rod into a spring-mass lattice (b) Dispersion relation and (c) phase velocity of the 1D spring-mass lattice (solid line) and of the continuous rod (dashed line). All the 3 sub-figures are extracted from [80]

Fig. 1.5 (reproduced from [80]) illustrates the most immediate effect of periodicity on dispersion by comparing a continuous medium (a rod) with its periodic/discretized counterpart (a mass–spring chain). While the continuous rod exhibits an $\omega(k)$ relation with an almost constant slope over the frequency range considered (constant phase velocity), the mass–spring chain displays a nonlinear $\omega(q)$ law: the slope varies with q, reflecting a pronounced frequency dependence of both phase and group velocities. The figure also highlights the *quasi-continuum* limit at long wavelengths: when $qa \ll 1$, the lattice dispersion converges toward that of the continuous medium, which supports interpreting the periodic network as a "micro-structured" representation of an effective low-frequency continuum [81].

In practice, two main computational routes are used to extract dispersion relations. *Direct* approaches (e.g., transfer-matrix methods) prescribe ω and determine $q(\omega)$, which is particularly convenient for 1D modulated structures and periodic multilayered stacks [82–84]. By contrast, *inverse* approaches sweep q over the Brillouin zone to compute $\omega(q)$ [76, 85].

Band diagram

In a periodic structure, the wave interacts in each unit cell with heterogeneities (material interfaces, cross-section variations, connection conditions, etc.). The resulting sequence of internal reflections and transmissions can, over certain frequency ranges, lead to interference that is globally unfavorable to propagation. Within the Bloch–Floquet framework, this is captured in a unified manner by allowing a complex Bloch wavenumber q: when $q = \Re(q) + i\Im(q)$, solutions with $\Im(q) = 0$ correspond to *propagating* waves (pass bands), whereas solutions with $\Im(q) \neq 0$ describe *evanescent* waves whose amplitude decays exponentially along the periodic direction, thereby characterizing a *stop band* [71, 79].

Historically, these phenomena were identified early and exploited in the study of *stratified media*, where the periodic alternation of two layers naturally structures wave propagation into pass bands and attenuation bands. Such 1D models are widely used to describe wave motion in multilayered stacks, including laminated composites, for which periodicity lends itself to analytical and numerical unit-cell-based treatments [86–88]. An important point for physical intuition is that these continuous bi-layer systems can be *discretized* and *approximated* by a *diatomic* mass–spring model (two masses per unit cell), which qualitatively reproduces the separation into two branches and the emergence of an attenuation region between them [89].

As an illustration, Fig. 1.6 (reproduced from [80] and [57]) presents the canonical case of a *diatomic mass–spring lattice*. The dispersion diagram highlights an *acoustic branch* (low frequency) and an *optical branch* (high frequency), separated by a frequency interval in which no propagating solution exists: the real part $\Re(q)$ alone can no longer describe propagation, and the emergence of an imaginary part $\Im(q) \neq 0$ reflects spatial decay. Plotting $\Re(q)$ (propagation) together with $\Im(q)$ (evanescence) therefore provides a direct reading of the "stop-band" nature: within the band gap, the Bloch solution becomes evanescent, which explains the attenuation observed in a finite structure composed of a limited number of cells.

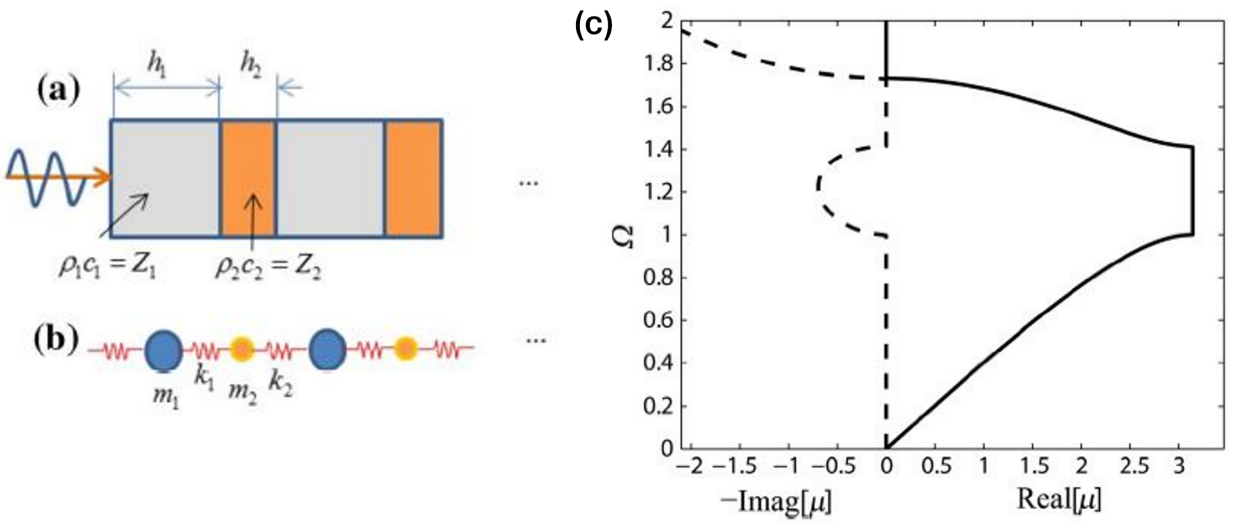

Figure 1.6: (a) Periodic bi-layered continuum medium which thickness of alternating layers are h1 and h2, respectively. (b) Bi-atomic chain representation of the bi-layered medium extrated from [57] (c) Dispersion curves for the 1D diatomic spring-mass lattice showing real (solid line) and imaginary (dashed line) parts of the propagation constant extracted from [80]

1.3.2 Phononic Crystals

Definition

Building on the notions introduced above (dispersion, periodicity, and the emergence of stop bands), phononic crystals can be defined. By analogy with photonic crystals, which are designed to control the propagation of electromagnetic waves [90, 91], phononic crystals are periodic media whose unit cell is engineered to control the propagation of acoustic or elastic waves. In their most common form, periodicity arises either (i) from a periodic distribution of scatterers (inclusions) embedded in a host medium, or (ii) from an intrinsically periodic geometry (e.g., cross-section modulation, ribs, corrugations), without necessarily changing the material [92–94]. In both cases, the signature is a band-structured dispersion relation featuring band gaps, whose most classical physical origin is the Bragg mechanism: when the wavelength becomes of the order of the period ($\lambda \sim 2a$), reflections from cell to cell lead to destructive interference of the transmitted wave, opening a frequency interval where propagation is strongly inhibited [95]. On dispersion diagrams, this opening typically occurs at the edges of the first Brillouin zone ($q = \pm\pi/a$). At these values, the Bloch wavelength is of the order of $2a$, corresponding to an alternating phase shift from one cell to the next: the field then tends to form standing-wave patterns and Bragg reflection becomes maximal, preventing propagation over the associated frequency range.

In the remainder of this study, we focus more specifically on controlling elastic waves through one-dimensional periodicity. Within this scope, phononic-crystal-type solutions include multilayer stacks (stratified media) and a wide range of structural waveguides, such as periodically supported, periodically loaded, or periodically modulated beams, as well as beam assemblies named as lattice structure, whose pass/stop behavior follows directly from the periodicity conditions [96–99]. Early

analyses of periodic beams notably showed how cutoff frequencies and band structuring can be related to the unit-cell dynamic characteristics and to the inter-cell coupling, providing a direct lever to shift and tune a stop band through local modifications of mass and/or stiffness [100–102]. Finally, when multiple wave polarizations interact, bandgap physics can be enriched by coupling phenomena that generate additional attenuation regions, or gaps wider than the primary Bragg gap [103, 104]. Fig. 1.7 provides a representative example for a periodically corrugated beam: geometric asymmetry induces flexural–longitudinal coupling, opening a coupling-induced stop band and resulting in strongly attenuated displacement fields in a finite structure.

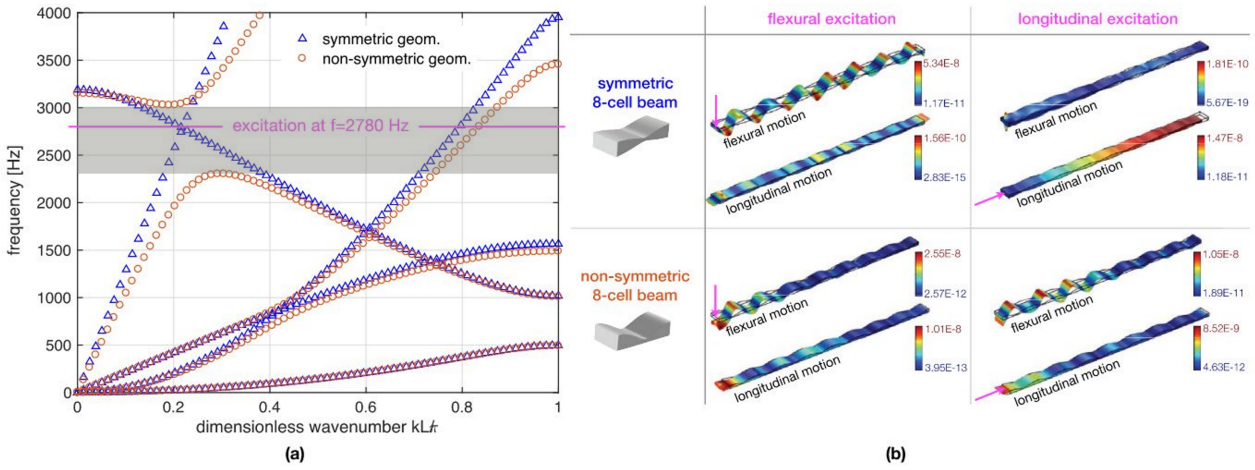

Figure 1.7: FEM numerical study of the wave coupling band gap and resulting double filtering effect. (a) Comparison of the dispersion relations of a periodic symmetric (blue triangles) and non-symmetric (brown circles) beam; (b) Flexural and longitudinal components of the forced displacement of a 8-cell beam, symmetrical (top line) or nonsymmetrical (bottom line), excited by a flexural (left column) or longitudinal (right column) unit point force (pink arrow) at the coupling frequency f = 2780 Hz. Extraded from [103]

From a methodological standpoint, the analysis of 1D phononic crystals relies on well-established tools to extract dispersion relations, notably the Transfer Matrix Method [105, 106], as well as frequency-domain approaches such as Plane Wave Expansion [107, 108] and numerical formulations tailored to waveguides, including the Waveguide Finite Element method [109, 110]. In addition, although the remainder of this work focuses on architectures that are periodic along a single direction, 2D and 3D phononic crystals extend these concepts to multiple propagation directions, with band gaps that are strongly governed by the unit-cell topology and lattice symmetry [111–114]. Structural counterparts have also been developed for periodic surfaces supporting Rayleigh waves and for periodic plates supporting Lamb waves [115–117].

1.3.3 Lattice structures

Among the phononic crystals introduced above, a class of particular interest here is lattice (truss-like) structures. Industrial interest in these architectures is currently very strong: they have been developed and optimized for lightweighting and multifunctionality in aerospace applications, for

energy absorption under impact/crash loading, and for the integration of thermo-fluidic functions enabled by their high specific surface area and internal connectivity [118–122].

From a structural standpoint, lattices are widely recognized for their mechanical efficiency: by distributing material at the unit-cell scale, they can achieve high specific stiffness and a static response that can be tuned through the topology, the cell size, and the relative density [123–125]. From a wave-propagation perspective, the beam network that forms a lattice naturally involves multiple degrees of freedom and multiple wave polarizations. This promotes mode coupling and can enrich band-structure features compared with simpler periodic systems such as 1D chains or bi-layer media.

Taken together, these two aspects make lattices a natural platform for a dual-function design strategy: (i) preserving mechanical performance (stiffness, stability, anisotropy) while (ii) configuring the architecture as a filtering waveguide by exploiting periodicity to generate stop bands [126, 127].

Bragg band gaps in lattice structures

Lattice structures are periodic assemblies of interconnected beams that can be tailored to control elastic-wave propagation. As the architecture becomes more complex, the number of degrees of freedom increases, which in turn enables a larger variety of wave polarizations to travel through the network. The coexistence of multiple polarizations promotes modal interactions and conversions, opening stop band.

This idea is central to origami-inspired lattice [128, 129]. While classical origami relies on complex folds, the mechanical counterpart is encoded here in the angles between lattice beams, which reproduce “fold-like” kinematics. By shaping these angles, the architecture can support a wider set of wave polarizations and, importantly, provides a direct geometric lever to tune waves coupling and therefore the resulting band-gap configuration for vibration filtering.

Another effective route to enhance coupling consists in breaking lattice symmetries, for instance through chiral motifs [130–134]. Chirality refers to geometries that are not superposable with their mirror image (as with human hands). In a lattice, this asymmetry modifies how translational and rotational motions interact, thereby enriching the band structure and potentially creating coupling-induced attenuation regions.

Coupling-driven stop bands are often observed in the mid- to high-frequency range. To shift Bragg-type effects toward lower frequencies, several strategies aim at increasing the effective wave path (tortuosity). Using curved beams lengthens the travel distance and reduces the apparent phase velocity, which can push the Bragg band gap downward [135–138]. A similar mechanism occurs in zigzag architectures, where the folded geometry enables low-frequency attenuation within compact, dense designs [139, 140].

A different approach is to modify connectivity by introducing multi-beams junctions. This is the case for hourglass-shaped lattices [141–143], where several beams converge toward a central node. Such configurations tend to concentrate compliance at specific locations, creating a periodic contrast in local stiffness that strengthens Bragg scattering. Figure 1.8, adapted from Chen et al. [144], illustrates this mechanism. The unit cell is a beam-based hexagonal frame that is stiff in bending. Periodicity is introduced by connecting successive hexagonal frames with slender beams of low bending stiffness.

This periodic alternation between stiff hexagonal cells and compliant interconnections creates a strong contrast in flexural impedance along the propagation direction, which enhances Bragg scattering and leads to the stop bands observed in Fig. 1.8 c).

Overall, these band-gap-opening mechanisms typically come with a structural cost. Increasing the number of degrees of freedom, introducing pronounced member angles, or locally reducing stiffness can degrade load-bearing capability, making the trade-off between vibration filtering performance and mechanical stiffness a central design constraint for lattice-based filters

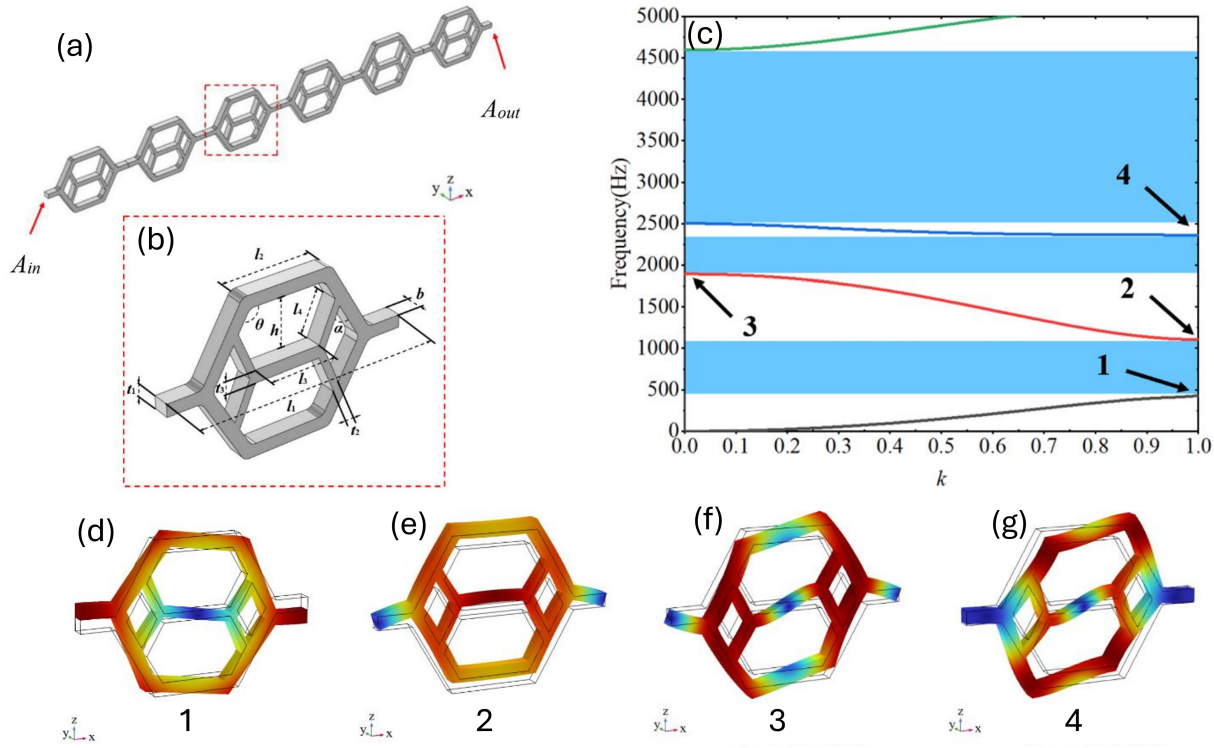

Figure 1.8: Extract from [144] : a) 3D model of the periodic lattice. b) unit structure. c) unit band structure analysis. Vibration modes of the unit band structure at four boundary points. d), e) is the vibration mode of the first bandgap edge points 1, 2, and f), g) is the vibration mode of the second bandgap edge points 3, 4

To mitigate the mechanical limitations of some highly filtering lattice topologies, an alternative is to integrate lattices into sandwich structures, where the periodic network forms the core between two thin face sheets. This configuration provides higher overall static stiffness—especially in bending—thanks to the load-carrying role of the outer skins. In this setting, stop-band formation arises from the interaction between the face-sheet modes (mainly flexural) and the modes of the lattice core, whose geometric heterogeneities promote Bragg-type scattering.

A variety of core geometries have been investigated, including pyramidal, hourglass, octahedral, and nested architectures, with the aim of maximizing mechanical and vibratory performance simultaneously [145–150]. A representative example is provided by Guo et al. [141], who propose a sandwich beam with an asymmetric hourglass core.

Their design relies on the band-folding principle, which consists in introducing an extended

periodicity through the use of supercells. As illustrated in Fig. 1.9, the unit cell is made of two hourglass sub-cells with different stiffness levels. This asymmetry, while preserving the compactness of the module, folds the dispersion branches into a smaller Brillouin zone, thereby promoting additional destructive interference and leading to extra stop bands.

However, because the outer face sheets impose a high flexural stiffness, the resulting band-gap frequencies typically remain relatively high. In addition, these mechanisms mainly affect flexural or torsional waves, whereas compressional waves—largely guided by the stiff face sheets—are only marginally disturbed.

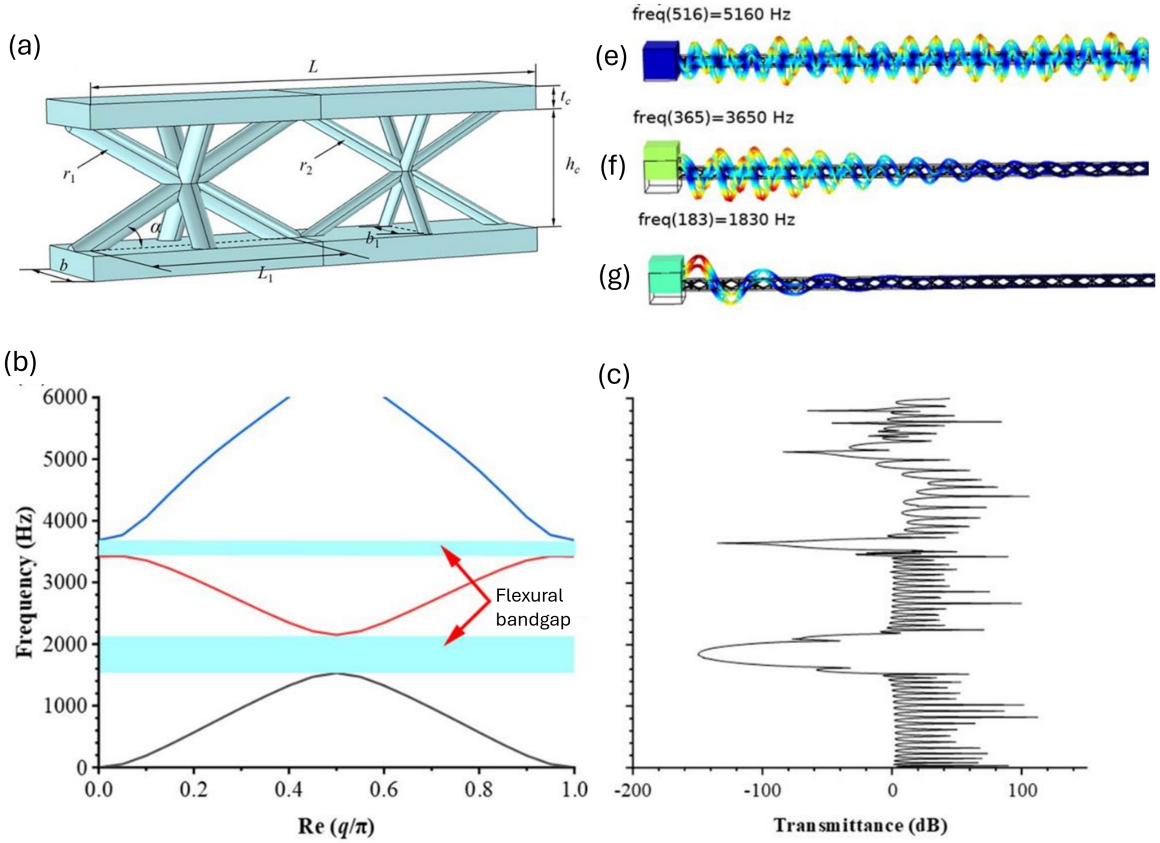

Figure 1.9: Extract from [141] : (a) Unit cell of a phononic sandwich beam with an asymmetric hourglass core; (b) dispersion diagram showing only the branches associated with flexural motion; (c) simulated transmissibility; (d–f) simulated displacement fields for an excitation outside the bandgaps (5160 Hz) and within the two bandgaps (3650 Hz and 1830 Hz)

To characterize wave mechanisms in these architectures, several modeling frameworks can be employed depending on geometric complexity and the desired accuracy. The spectral element method is a semi-analytical approach based on exact shape functions derived from the governing beam differential equations. It is particularly efficient for regular lattice networks, enabling dispersion extraction at a very low computational cost [151–154]. For more intricate structures or designs involving singularities, the finite element method provides greater flexibility—especially to capture nonlinear effects, property gradients, or complex interfaces—at the expense of higher computational effort [135, 141, 155]. Finally, when the unit-cell geometry allows it, analytical models based on Timoshenko beam theory or homogenization can establish direct links between network topology and effective dynamic properties [156, 157].

These tools have enabled the optimization of lattice vibratory responses at the unit-cell level. Nevertheless, Bragg-type band gaps remain subject to a fundamental scaling constraint: they emerge when the wavelength becomes comparable to twice the period ($\lambda \sim 2a$), which ties their spectral location to the geometry and the effective stiffness of the periodic medium. Shifting them to lower frequencies therefore requires either increasing the period—at the cost of compactness—or drastically reducing the phase velocity, which generally implies structural softening that is often incompatible with the static stiffness requirements of most industrial applications.

Local resonance in latttice structure

To overcome the intrinsic limitations of Bragg band gaps, a major trend in recent research is to embed local resonators within truss lattices—secondary elements designed to vibrate at targeted frequencies—in order to generate subwavelength stop bands. The underlying physics can be interpreted through the analogy of a mass–spring oscillator attached to a host structure: near the resonator's natural frequency, the internal mass oscillates strongly and, through phase opposition, imposes an anti-resonance on the host. This produces a sharp drop in transmitted response and turns the wavenumber into a predominantly imaginary quantity, thereby preventing wave propagation over the corresponding frequency range [158, 159].

In practice, several implementations have been proposed. One of the most common approaches is to connect a local resonator—often well approximated by a lumped mass–spring system—at specific locations within the lattice [160–168]. A representative example is shown in Fig. 1.10, adapted from Liu et al. [169]. The waveguide is a 3D periodic truss built by repeating cube-like unit cells along one direction (Fig. 1.10(a)). A locally resonant stop band is created by integrating resonators on the top and bottom faces of each unit cell. Each resonator consists of a cross-shaped central mass connected to the surrounding frame by four slender beams. By adjusting the beam length and the mass geometry, the target resonance frequency can be tuned.

The associated dispersion relation (Fig. 1.10(b)) highlights a flexural band gap opening at the local resonance frequency, characterized by a nearly flat branch. Over this frequency interval, flexural-wave propagation becomes impossible, while other polarizations are not affected.

The impact on a finite structure is evaluated on a waveguide made of seven cells (Fig. 1.10(c)): a transverse displacement is imposed at the input and the response is measured at the output, yielding a

frequency-dependent transmission curve. The results (Fig. 1.10(d)) show a clear transmission drop over the range predicted by the dispersion analysis, confirming that attenuation is governed by the local resonance of the cruciform elements. As damping increases, the transmission curve becomes smoother: peak attenuation decreases, but the effective attenuation range tends to broaden. The attenuation signature of locally resonant gaps is visually distinct from Bragg-type gaps, typically exhibiting a pronounced attenuation maximum at the resonance frequency and an asymmetric shape with respect to the gap's central frequency [170, 171]. Locally resonant gaps are often narrower than Bragg gaps, although specific mechanisms can significantly widen them.

One such mechanism is inertial amplification, which broadens the resonator anti-resonance, producing a wider stop band and a less asymmetric attenuation curve, often with two attenuation peaks within the band [172–174]. However, these architectures can be geometrically and mechanically complex, making parameter control—and practical integration into truss lattices—more challenging.

Another route relies on very compliant architectures, often based on curved beams, to realize resonators with an extremely low (or even negative) effective stiffness [162, 175–177]. These systems can achieve wide stop bands at very low frequencies with relatively small added mass, and can be tuned through pre-stress mechanisms to control the gap frequency. However, their extreme compliance may quickly lead to nonlinear behavior, which can trigger instabilities and ultimately make these solutions ineffective [176].

Another strategy is to open a locally resonant stop band just below the onset frequency of a Bragg band gap, so that the two attenuation regions effectively merge and form a wider "pseudo" band gap [178]. More generally, broader attenuation can be achieved by coupling local resonance with other filtering mechanisms. For instance, Sheng et al. [179] integrate an acoustic black hole mechanism [180] into the resonators to attract and trap waves through a smooth thickness taper near the ends of the resonant mass. Such hybrid designs can significantly widen the effective attenuation range, but they require careful parameter tuning to ensure that the coupled mechanisms operate synergistically.

Another interesting application of local resonances is their integration into sandwich structures with a lattice core [181, 182]. Unlike Bragg-type mechanisms—which often struggle to open stop bands for compressional waves that mainly travel through the stiff face sheets—embedded resonators can interact with compression through their subwavelength response. An example is shown in Fig. 1.11, adapted from Xiao et al. [159].

In this design, slender resonator beams are inserted within the core and attached on both sides of the lattice: one end is connected to a lattice joint, while the other carries a tip mass. Because this attachment has multiple natural frequencies, it can target different polarizations: its first resonance primarily couples with the waveguide's flexural motion, whereas a higher resonance couples with axial (compressional) motion. These resonance frequencies are tuned through the mass volume and the rectangular cross-section of the slender beams. At the first resonance, the dispersion branch associated with flexural waves is locally modified and splits, opening a polarization-selective band gap without significantly affecting other branches. A similar splitting occurs at the second resonance, this time on the compressional branch. The attenuation level, however, depends on the polarization: compressional wavelengths are typically much larger than flexural wavelengths (because of the higher

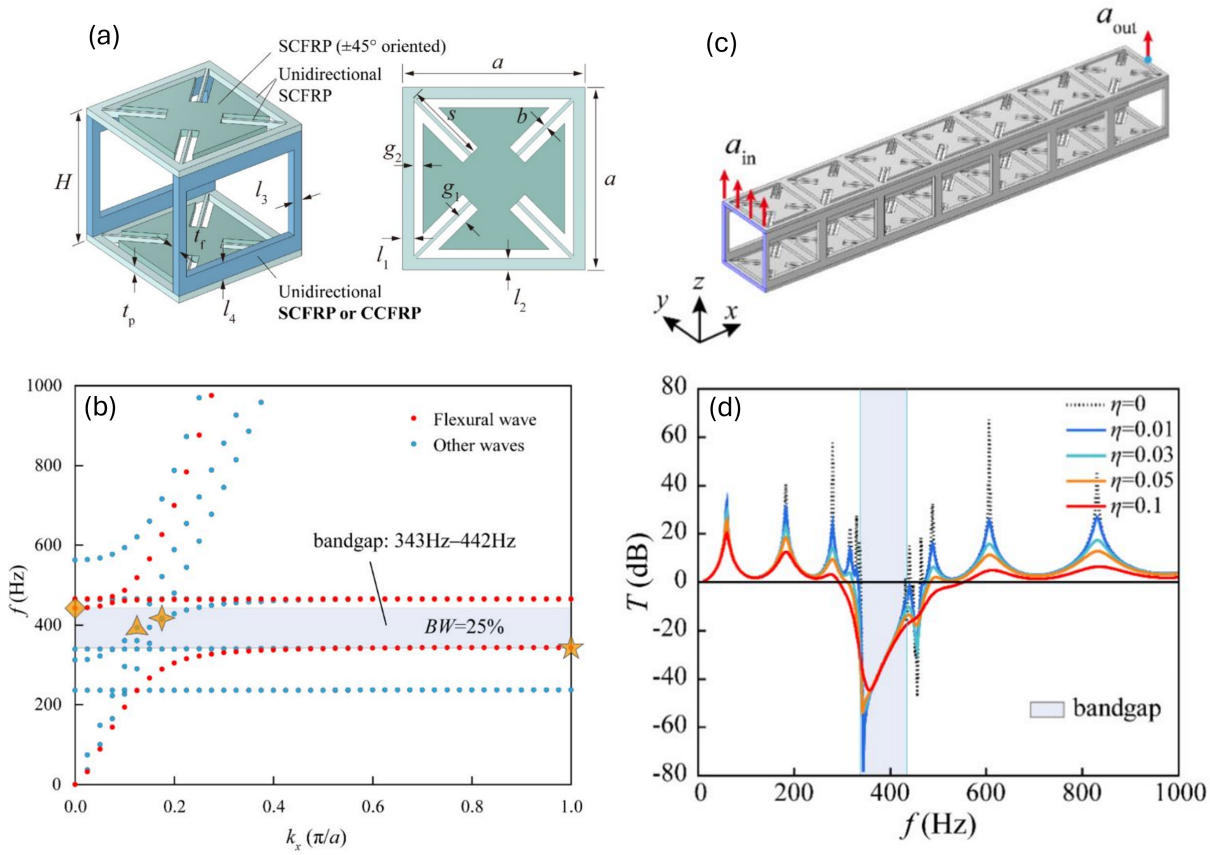

Figure 1.10: Extract from [169] :(a) Schematic of truss beam structures with cruciform resonators. (b) Dispersion relations (c) 7-cell configuration.(d) Transmission varying with the damping coefficient η

axial stiffness), so a given resonator generally interacts more strongly with flexural waves than with compressional waves, leading to better flexural attenuation than axial attenuation in practice. In summary, integrating local resonant mechanisms enables low-frequency attenuation bands without significantly compromising the waveguide's static stiffness. However, these attenuation bands are generally narrower than those produced by Bragg effects, and adding resonators can introduce a non-negligible mass penalty. In addition, implementation is not straightforward and requires tight control of the resonator integration and assembly. Finally, filtering effectiveness is strongly governed by resonator damping, which must be accurately identified and controlled to ensure reliable attenuation performance [183–185].

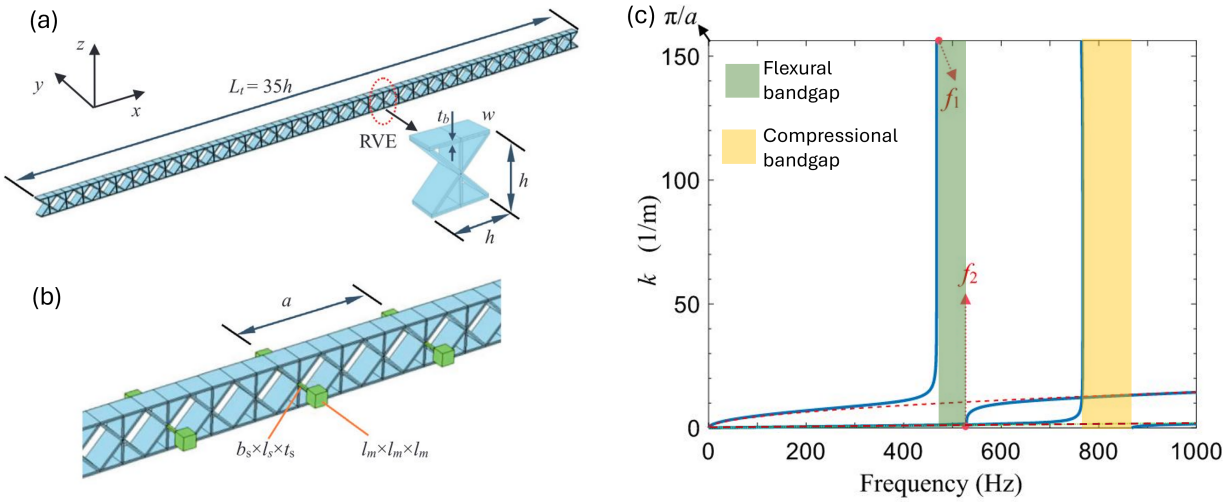

Figure 1.11: Extract from [159] : (a) Considered 1D periodic sandwich with a lattice core beam. (b) Construction of a beam-type metastructure by attaching periodic local resonators. The lattice constant of the metastructure is given by a = nh, where n is an integer dependent on design. (c) Comparison of dispersion relations of the host truss beam (red dashed lines) and those of the metastructure (blue solid lines)

1.3.4 Absolute bandgap in 1D elastic wave guide

In the present application, absolute filtering is required because the vibratory excitation is multi-directional and can activate several elastic-wave polarizations. In a 1D waveguide, this objective translates into the design of an absolute band gap, i.e., a frequency interval in which all wave polarizations are attenuated along the single propagation direction. In contrast, the term complete band gap is typically used for 2D and 3D periodic media, where the stop band simultaneously suppresses wave propagation for all polarizations and for all propagation directions within the medium [114, 149, 186]. Achieving complete band gaps in 2D and 3D periodic media is challenging and often results in highly intricate architectures, which can be difficult to manufacture and to integrate into real engineering systems. By contrast, one-dimensional periodic waveguides provide a simpler and more practical design space. If a 1D waveguide is engineered to block all wave polarizations within a given frequency band, then—because only one propagation direction exists by definition—no elastic wave can propagate along the guide. In this sense, an absolute band gap in a 1D waveguide can deliver a functional outcome comparable to a complete band gap in 2D or 3D media: wave transmission is suppressed over the targeted frequency range.

Absolute band gaps in bi-material 1D phononic crystals

Periodic beam waveguides with alternating materials—arranged through axial segmentation and/or radial layering—have been shown to exhibit absolute band gaps [187]. A representative implementation is presented in Fig. 1.12, adapted from Plisson et al. [188]. The key idea is that a circular beam is a continuous waveguide supporting three main wave types: one dispersive flexural wave, and two essentially non-dispersive waves associated with axial (compressional) and torsional motions. By

periodically alternating two beam segments made of materials with strongly contrasting stiffness (see Fig. 1.12f)), all three wave families become dispersive and Bragg-type stop bands can be created for each polarization.

By tuning the geometric parameters—segment lengths and cross-sectional dimensions—one can control the position and width of these polarization-specific stop bands and align them over a common frequency interval, thereby forming an absolute band gap. The absolute nature of the filtering is validated experimentally by measuring the transmission through a finite five-cell structure (see Fig. 1.12a)) under an oblique excitation designed to simultaneously trigger the different wave polarizations.

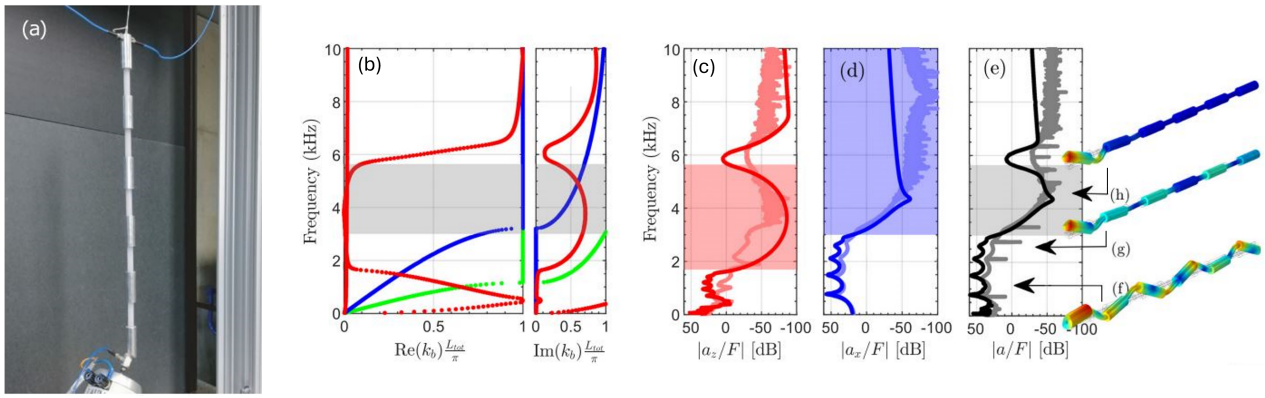

Figure 1.12: Extract from [188] : (a) Images of the manufactured crystal phononic pipe implemented in an experimental setup. The structure consists of five cells, introducing an alternation between an aluminum beam and a nylon beam. Numerical analysis and experimental characterisation of the optimal PC pipe: (b) real part and imaginary part of the complex dispersion relation obtained by the Floquet–Bloch method and considering the viscoelastic losses (blue) Longitudinal, (red) flexural, and (green) torsional; measured (light line) and simulated (dark line) acceleration transfer functions in the (c) flexural, (d) longitudinal, and (e) full loading cases; with the 3D views of the simulated total displacement in the full loading case at (f) 900 Hz where all wave types propagate, (g) 2500 Hz where only the flexural bandgap is opened, and (h) 4500 Hz within the absolute bandgap.

Extension to lattice structures

Absolute Bragg band gaps In the literature on 1D lattice waveguides, the notion of an absolute band gap is not stated explicitly, yet the phenomenon can be observed in many reported designs [128, 133, 161, 189, 190]. In practice, achieving an absolute band gap in a 1D lattice can be relatively straightforward: by controlling the angles between lattice members, one can promote strong coupling between wave polarizations. This typically generates multiple polarization-dependent Bragg stop bands, increasing the probability that polarized stop bands overlap over a common frequency interval.

A representative example is shown in Fig. 1.13, adapted from Zhao et al. [133]. In that work, the isotactic configuration (Fig. 1.13b)), where chiral units repeat with the same handedness along the lattice, produces Bragg-type stop bands that mainly affect waves polarized transversely to the propagation direction, while leaving waves polarized along the propagation axis (pseudo-compression and shear) largely unaffected. By contrast, in the syndiotactic configuration (Fig. 1.13c)), where left-

and right-handed units alternate, the change in member orientation modifies the coupling conditions and enables interaction between axial (compressional) motion and torsional motion. As a result, Bragg stop bands open for all polarizations and overlap over three distinct frequency ranges, thereby producing absolute band gaps.

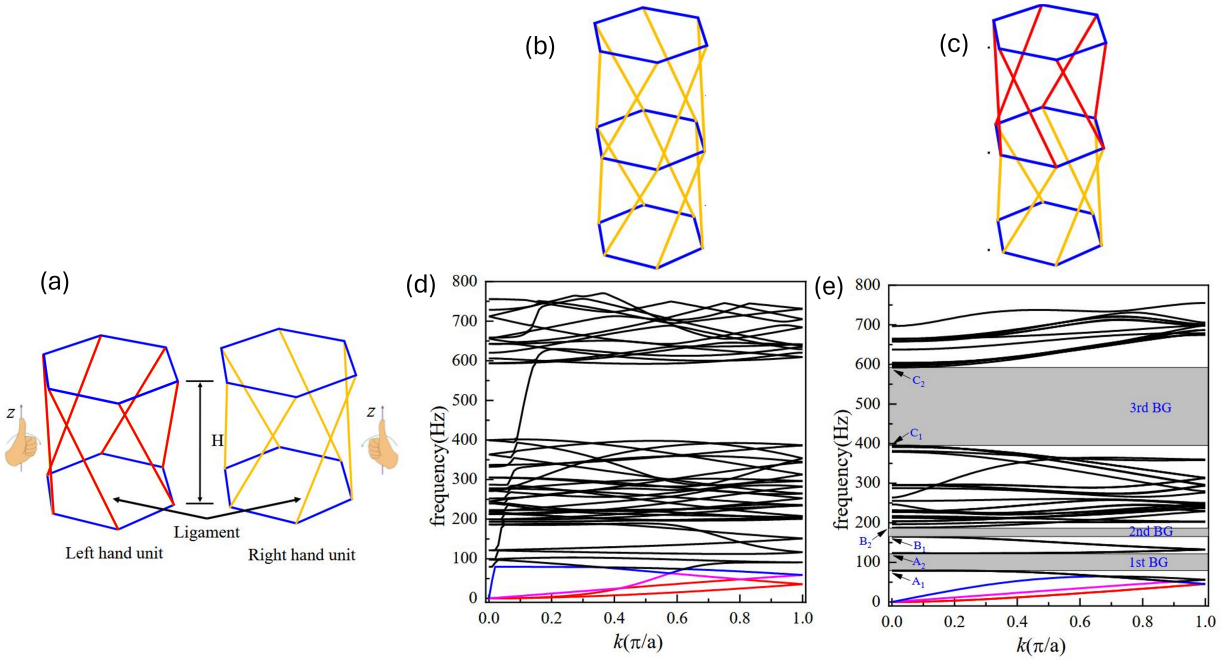

Figure 1.13: Extract from [133] : (a) Two chiral units. Unit-cells for b) isotactic and c) syndiotactic configuration. Band structures of 3D chiral mechanical metamaterial for (d) Isotactic configuration and (e) Syndiotactic configuration (Band gaps are highlighted in grey and the lowest four band branches are colored).

Locally resonant forbidden band For locally resonant lattice structures, Fujita et al. [191] provide a relevant example, with results reported in Fig. 1.14. The investigated structure is a lattice waveguide in which each unit cell embeds, at its center, an internal beam network acting as a set of four local resonators. The deformation patterns associated with these four resonances are designed to open locally resonant stop bands for the four propagating wave types supported by the meta-beam, namely the two flexural polarizations, axial motion, and torsion. With careful parameter optimization, these four polarization-selective gaps can be made to overlap over the same frequency range, thereby forming an absolute band gap.

This concept is particularly appealing because it adds absolute filtering functionality without significantly degrading the waveguide's static stiffness. However, in practice, optimizing the resonator geometry can be challenging: some geometric parameters simultaneously control both effective mass and stiffness, which strongly constrains the design space.

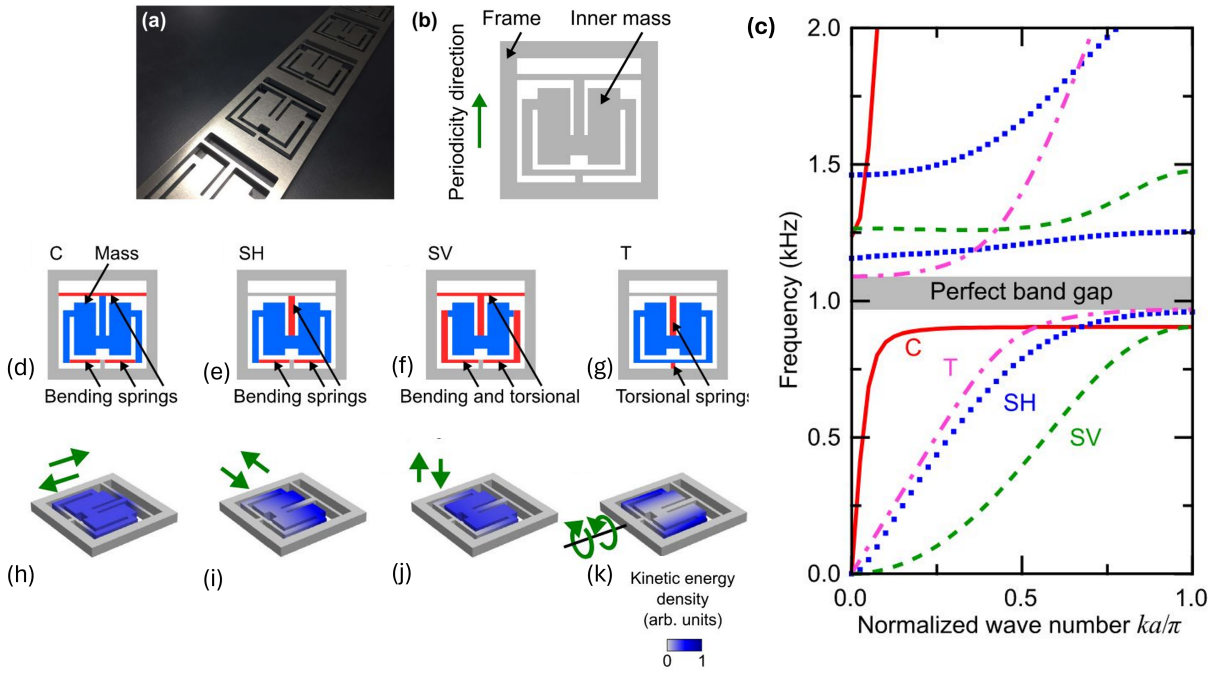

Figure 1.14: Extract from [191] : Metabeam design. (a) Photograph of the metamaterial beam. (b) Schematic of the top view of the unit cell. The gray region is aluminum, and the inner white areas are holes. The unit-cell geometry comprises a frame, an inner mass, and several ribs. (c) Acoustic dispersion relation for axial propagation in the metabeam; k and a are the wavevector and unit-cell length, respectively. The solid red, dotted blue, dashed green, and dashed-dotted pink curves correspond to compressional (C), shear-horizontal (SH), shear-vertical (SV), and torsional (T) modes, respectively. (d)–(e) Geometries used for the models. The blue regions and red ribs act as masses and springs, respectively, shown for the following modes: (d) compressional (C, motion along the axial direction), (e) shear-horizontal (SH, motion along the width direction), (f) shear-vertical (SV, out-of-plane flexural motion), and (g) torsional (T, rotation about the axis along the axial direction). (h)–(k): simulated kinetic- and strain-energy distributions for the lowest four eigenmodes, respectively. The green arrows show the displacements.

1.4 Outline of the thesis

This thesis focuses on mitigating vibration transmission in an aircraft, and more specifically along a rail that supports the passenger seats. This component constitutes a critical transmission path and can convey uncomfortable vibration levels to passengers, primarily generated by turbine imbalance, with engines typically located beneath the wings. Because vibration propagates through a complex assembly of interconnected subsystems before reaching the rail, the resulting excitation at rail level is multi-polarized.

The objective of this work is to redesign the rail so as to preserve its static load-bearing performance while integrating an absolute vibration-filtering function, i.e., one that is insensitive to the polarization of the incoming excitation. The proposed approach relies on lattice structures, selected for their high specific stiffness (stiffness-to-mass ratio), and used here as periodic waveguides engineered to generate frequency stop bands that prevent the propagation of elastic waves. Two complementary mechanisms are investigated: Bragg-type band gaps and band gaps induced by periodically embedded

local resonances. The overarching goal is to achieve effective low-frequency vibration attenuation while maintaining high specific stiffness.

The manuscript is organized into five chapters that progressively build the modeling and analysis framework by investigating, in each chapter, an innovative structural concept of increasing relevance for industrial implementation. At every step, the trade-off between vibration-filtering performance and static specific stiffness is analyzed. Each design iteration is then materialized through a prototype that is manufactured and experimentally characterized, enabling convergence toward an industrially applicable filter architecture. The final design is integrated into a laboratory-scale demonstrator that reproduces the intended use case. The overall structure of the thesis is summarized in Fig. 1.15 and the resume of each chapter is provided below.

- The current Chapter introduces the work by presenting the background, motivation, and scope of the thesis.

- Chapter 2 establishes the foundations for analyzing periodic lattice structures. It presents a clear methodology for analyzing and designing elastic waveguides using 3D-printed periodic truss architectures to control elastic-wave propagation. An algorithm is introduced to enable fast and efficient extraction of the full dispersion relation, based on applying Bloch boundary conditions to a beam spectral model. Using symmetry arguments, an identification procedure is then proposed to interpret the dispersion branches and clarify the underlying wave polarizations and coupling mechanisms. The approach is applied to a case study and used to design a structure exhibiting broadband absolute stop bands. Finally, the analytical predictions are validated through numerical simulations and experiments on an additively manufactured prototype

- Chapter 3 investigates a specific periodic sandwich architecture with a lattice core that can achieve absolute band gaps. The concept combines two periodic filtering skins, made of coupled plate and beam elements, connected by an architectured core in order to improve mechanical performance while preserving the filtering capabilities of the skins. To model this system, the semi-analytical framework from Chapter 2 is extended to plate elements and to the dynamic coupling between beam and plate components. Using dispersion relations as the central design observable, we quantify the trade-off between filtering performance and specific bending stiffness. The analytical predictions are then validated numerically and experimentally on an additively manufactured prototype.

- Chapter 4 proposes a design methodology for a one-directional periodic vibration filter based on embedded local resonances, with a particular emphasis on the trade-off between filtering performance and added mass. It starts from a simple 1D mass–spring waveguide supporting a single wave polarization. Within this reduced setting, we quantify how the added mass, the resonator frequency, and the resulting attenuation bandwidth are interrelated for undamped, damped, and nonlinear resonators. The analysis is then extended to the design of a multi-polarized lattice waveguide, modeled using the spectral element method and equipped with resonators primarily tuned to flexural motion. The two design routes are compared against

each other and validated experimentally using measurements on an additively manufactured prototype.

- Chapter 5 proposes a strategy to achieve a wide, tunable absolute bandgap by extending the methodology established in the previous chapters. Three main contributions are presented: (i) a multi-resonant unit cell that enables independent tuning of resonators coupled to each of the four propagating wave modes in the waveguide; (ii) an analysis of finite, damped filters showing why attenuation may remain polarization-dependent in the undamped case even when an absolute bandgap is predicted from dispersion; and (iii) an experimental validation on an application-oriented demonstrator tested under tri-axial excitation, supported by a full 3D numerical model.

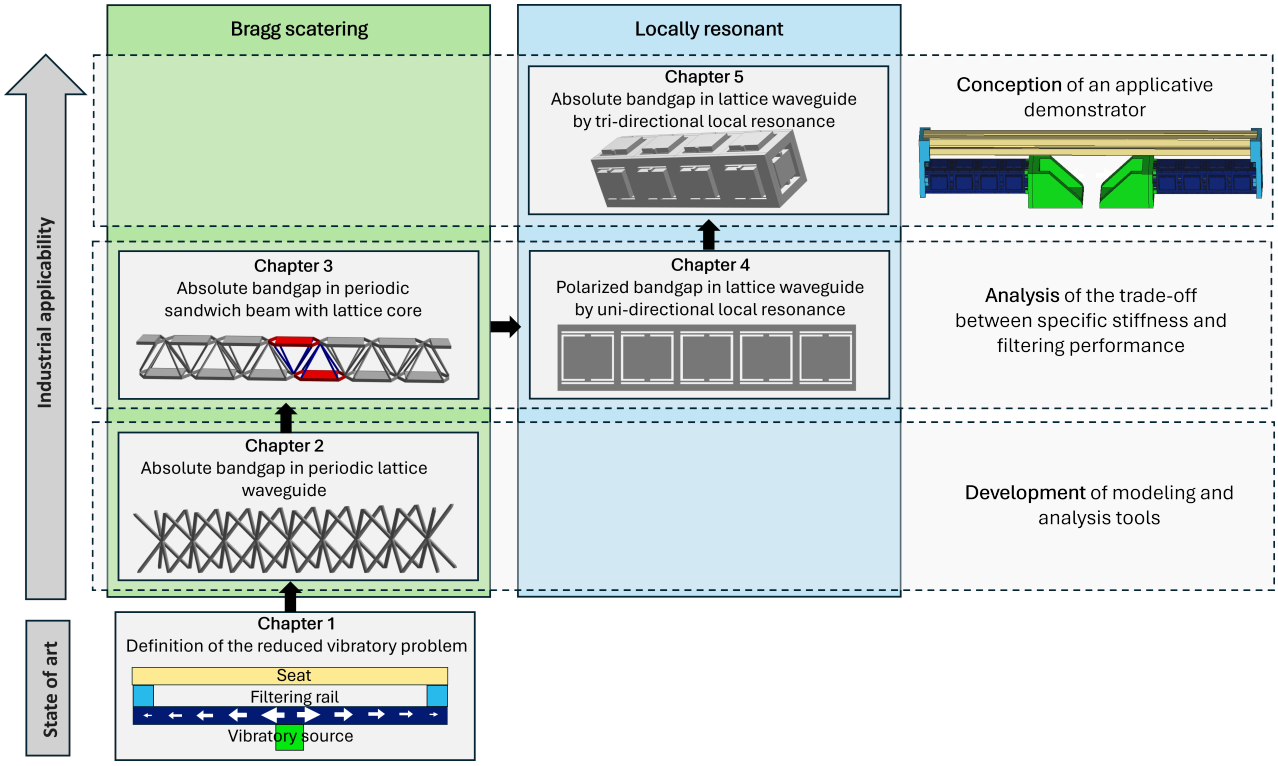

Figure 1.15: Structure of the thesis

CHAPTER 2

Dispersion analysis in a 3D lattice elastic waveguide for the design of an absolute filter

Contents

2.1 Introduction . . . 26
2.2 System under study . . . 27
2.2.1 Geometry of the investigated structure . . . 27
2.2.2 Example of configurations . . . 28
2.3 Spectral Element Method (SEM) in a three-dimensional assembly of beams . . . 29
2.3.1 Spectral stiffness matrices . . . 29
2.3.2 Application of Periodicity Conditions . . . 32
2.3.3 Dispersion of the reference structure . . . 33
2.4 Mode decomposition and dispersion analysis . . . 34
2.5 Parametric study of the unit cell geometry . . . 36
2.5.1 Mechanisms governing the band gap characteristics . . . 38
2.6 Experimental demonstration . . . 42
2.6.1 Material characterization . . . 42
2.6.2 Experimental setup . . . 42
2.6.3 Experimental results . . . 42
2.7 Conclusions . . . 46

2.1 Introduction

This chapter investigates the dispersion of elastic waves in periodic three-dimensional beam lattices, with the objective of understanding and engineering low-frequency vibration band gaps opened by Bragg-type interference mechanisms. While the general principles of wave propagation in periodic media and beam-based lattice structures have been reviewed in the previous chapter, the present contribution focuses on methodological developments and design-oriented insights specific to this class of architectures.

A major difficulty in analysing wave propagation in three-dimensional beam lattices lies in the strong coupling between wave polarizations and the resulting complexity of the dispersion diagrams. Standard numerical approaches can accurately predict dispersion relations, but they often provide limited physical insight and become impractical when extensive parametric studies or inverse design strategies are required. Addressing these limitations requires both an efficient computational framework and a clear interpretation methodology.

To this end, this chapter develops a spectral-element-based modelling approach for periodic beam lattices, enabling fast and accurate computation of dispersion relations under Bloch–Floquet conditions. Beyond numerical efficiency, a central contribution of this work is the introduction of a symmetry- and polarization-based classification of dispersion branches, inspired by lamb wave classification [192, 193]. This decomposition allows dense dispersion diagrams to be factorized into a small number of physically meaningful families, each directly associated with a fundamental deformation mechanism of the lattice.

Based on this framework, the chapter makes the following main contributions:

- the development of a computationally efficient spectral element model for the dispersion analysis of three-dimensional periodic beam lattices;
- the introduction of a symmetry- and polarization-based classification of dispersion branches, enabling a clear physical interpretation of dispersion diagrams;
- the identification of the geometrical mechanisms governing Bragg-type band-gap formation, leading to the design and experimental validation of lattice structures exhibiting low-frequency absolute band gaps.

The results presented in this chapter have led to a peer-reviewed scientific publication [194].

The chapter is organized as follows. Section 2.2 introduces the class of beam lattices under investigation and the associated geometric parametrization. Section 2.3 presents the spectral element formulation and its extension to periodic structures. In Section 2.4, the dispersion problem is reformulated using symmetry-based condensation, leading to a simplified and physically interpretable description. Section 2.5 explores the influence of unit-cell geometry on dispersion and band-gap formation through a large-scale parametric study. Finally, Section 2.6 presents an experimental validation of the proposed concepts.

2.2 System under study

In this section, we introduce a general default configuration from which one can explore a wide variety of structures upon parametric sweep.

2.2.1 Geometry of the investigated structure

The propagation of elastic waves in a one-dimensional structure composed of a three-dimensional network of beams is investigated (see figure 2.1a). We focus on a periodic network defined by a unit cell repeated along the x axis. Let us construct the unit cell by considering 4 beams connected together at points A, B, C, D and O (see figure 2.1c) and applying mirror symmetries with respect to the $(\mathbf{x}, \mathbf{y})$, $(\mathbf{x}, \mathbf{z})$ and $(\mathbf{y}, \mathbf{z})$ planes. The resulting structure is determined by 15 spatial coordinates and 3 geometric parameters a_x (lattice parameter), a_y and a_z. In addition, we apply the following structural constraints :

- $x_A = x_B = x_C = 0$
- $y_A = 0$
- $y_D = -a_y/2$
- $z_D = -a_z/2$
- $x_O = -a_x/2$
- $y_O = -a_y/2$
- $z_O = -a_z/2$

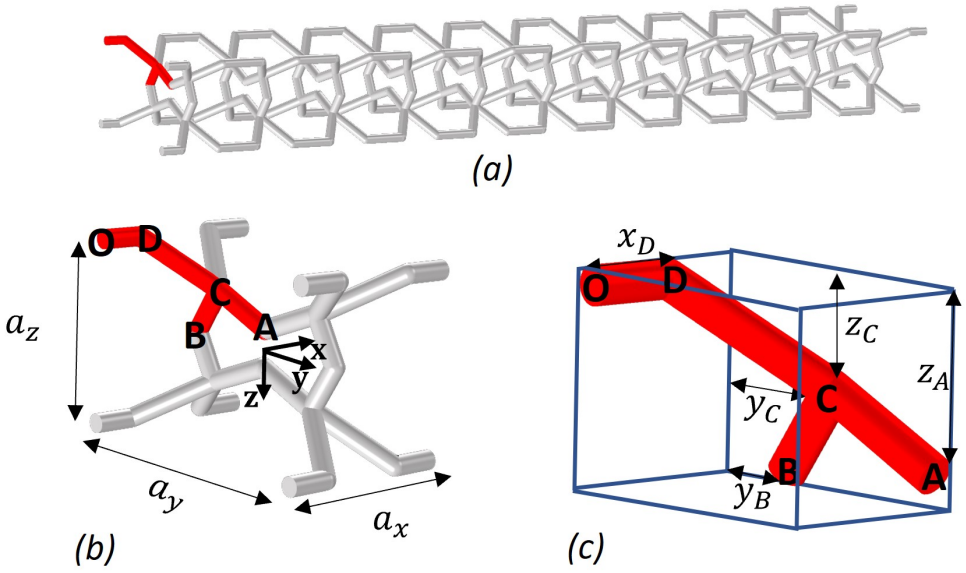

Figure 2.1: Investigated structure displayed at three different scales. (a) Mesoscopic scale, consisting of 11 unit cells, (b) a single unit cell, and (c) the elementary beam pattern from which the unit cell can be constructed by applying mirror symmetry operations with respect to all three planes: $(\mathbf{x}, \mathbf{y})$, $(\mathbf{x}, \mathbf{z})$ and $(\mathbf{y}, \mathbf{z})$.

Thus, the geometry has 8 independent parameters, 5 of which set the shape of the elementary beam pattern (x_D, y_C, z_C, z_A, y_B) while the remaining 3 define the aspect ratio of the unit cell (a_x, a_y, a_z). For a given unit cell, a_x must be determined in order to completely define the network with the following 7 non-dimensional parameters: $\hat{z}_A = 2z_A/a_z$, $\hat{y}_B = 2y_B/a_y$, $\hat{z}_C = 2z_C/a_z$, $\hat{y}_C = 2y_C/a_y$,

$\hat{x}_D = 2x_D/a_x$, $\hat{a}_{\mathrm{zy}} = a_z/a_y$, and $\hat{a}_{\mathrm{yx}} = a_y/a_x$. We explore the parameter space by varying the structural parameter vector $\mathbf{p_S} = [\hat{z}_A, \hat{y}_B, \hat{z}_C, \hat{y}_C, \hat{x}_D]$ and the lattice shape parameters $\hat{a}_{\mathrm{zy}}$ and $\hat{a}_{\mathrm{yx}}$.

2.2.2 Example of configurations

The default structure displayed on figure 2.1 corresponds to the following values for the parameters vectors: $\mathbf{p}_S = \left[0.8, 0.3, 0.5, 0.5, 0.5\right]$. When all structural parameters cancel, *i.e.* $\mathbf{p}_{S0} = \left[0, 0, 0, 0, 0\right]$, the unit-cell simplifies into a single rectangle connected at its edges by straight horizontal bars (see figure 2.2a). This configuration, denoted S_0, constitutes our reference structure. In contrast, when $\mathbf{p}_S = \left[1, 1, 1, 1, 1\right]$, the rectangles degenerate into crosses connected in the same fashion (see figure 2.2g).

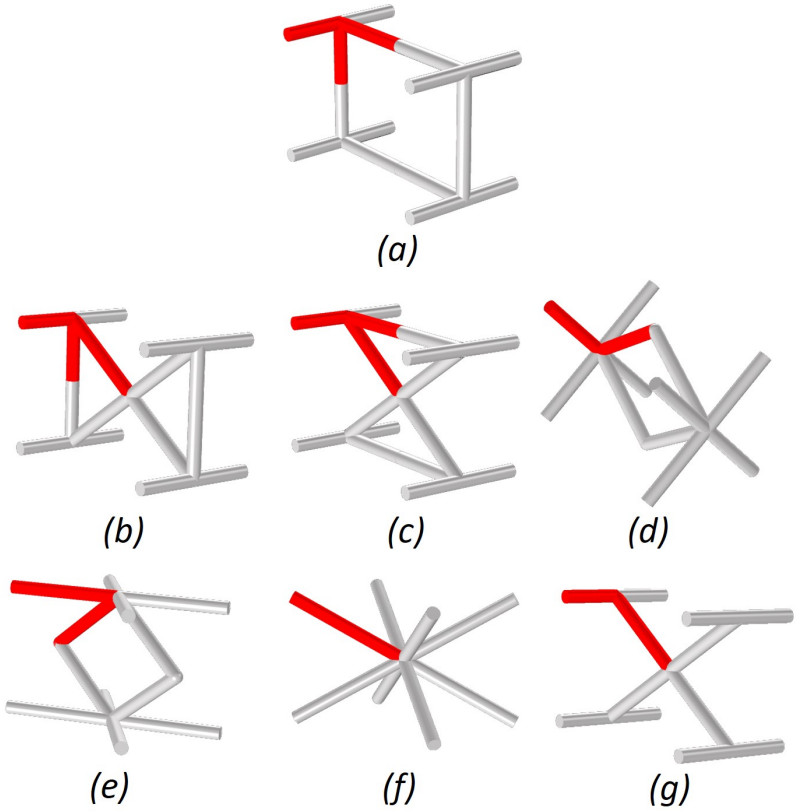

Figure 2.2: Seven different unit cells derived from the default structure for different values of the parameters vector $\mathbf{p}_S = \left[\hat{z}_A, \hat{y}_B, \hat{z}_C, \hat{y}_C, \hat{x}D\right]$. The $\mathbf{p}_{S0} = \left[0, 0, 0, 0, 0\right]$ unit cell (a) is considered as our reference. (b) $\mathbf{p}_S = \left[1, 0, 0, 0, 0\right]$, (c) $\mathbf{p}_S = \left[0, 1, 0, 0, 0\right]$, (d) $\mathbf{p}_S = \left[0, 0, 1, 0, 0\right]$, (e) $\mathbf{p}_S = \left[0, 0, 0, 1, 0\right]$, (f) $\mathbf{p}_S = \left[1, 1, 1, 1, 0\right]$ and (g) $\mathbf{p}_S = \left[1, 1, 1, 1, 1\right]$

Some other simple examples, and the associated parameter vectors $\mathbf{p}_S$, are gathered in figure 2.2. Playing with the coordinates of the $\mathbf{p}_S$ vector, one can explore a wide variety of structural configurations. Note that, in some cases, the amount of connecting nodes becomes smaller than 5. For instance, the structure in figure 2.2f only features 2 nodes. This is the consequence of a merging of points A, B and C on one hand and between points O and D on the other hand.

In addition to the coordinates of the connecting points, the beam radii (the radius of the circular

cross-section) should also be specified. This information is crucial since it governs the total mass of the structure. However, in this contribution, we are specifically interested in the effect of the $\mathbf{p}_S$-vector on the dispersion of elastic waves. We will thus consider only iso-density structures by systematically setting the beam radii (identical for all beams) in a way that the total mass of a single unit cell is equal to that of the reference $\mathbf{p}_{S0}$-configuration, when it is populated with 1.5 mm radii beams, corresponding to the structure used in the experiment (see section 3.4). Table 2.1 summarizes the parameters for the main structures examined here.

Configuration	$\mathbf{p}_S = \left[\hat{z}_A, \hat{y}_B, \hat{z}_C, \hat{y}_C, \hat{x}_D\right]$	$\hat{a}_{\mathrm{zy}}$	$\hat{a}_{\mathrm{yx}}$
S_0 (fig. 2.2a)	$[0, 0, 0, 0, 0]$	1.5	1
Default structure (fig. 2.1b)	$[0.8, 0.3, 0.5, 0.5, 0.5]$	1.5	1
Crosses (fig. 2.2g)	$[1, 1, 1, 1, 1]$	1.5	1
S_1^* (fig. 2.7)	$[0.3, 0.9, 0.1, 0.9, 0.1]$	0.9	1.4
S_1 (fig. 2.8)	$[0, 1, 0, 1, 0]$	1.5	1
S_2^* (fig. 2.7)	$[0.9, 0.3, 0.9, 0.1, 0.1]$	0.8	1.2
S_2 (fig. 2.9)	$[1, 0, 1, 0, 0]$	1.5	1
S_3^* (fig. 2.7)	$[0.9, 0.6, 0.9, 0.9, 0.1]$	0.9	0.9
S_3 (fig. 2.2f)	$[1, 1, 1, 1, 0]$	1.5	1

Table 2.1: Summary of the relevant configurations and the associated structural and lattice parameters.

2.3 Spectral Element Method (SEM) in a three-dimensional assembly of beams

In this section, we examine the dynamics of these structures, using an approach based on the SEM [152, 195]. Let us consider the single beam element of length L, sketched on Fig 2.3. It is connected to the rest of the structure at its two ends, here noted P and Q. We define the local coordinate system $\mathbf{e}_1$, $\mathbf{e}_2$, $\mathbf{e}_3$ so that $\mathbf{e}_1$ is colinear to the neutral axis of the beam **PQ**.

2.3.1 Spectral stiffness matrices

Practically, this method consists in reducing each constitutive beam to two connecting points.

The dynamic motion of the beam, at a distance s, from point P, is described by six degrees of freedom: three translations $U_1(s)$, $U_2(s)$, and $U_3(s)$, as well as the three rotations $\Theta_1(s)$, $\Theta_2(s)$, and $\Theta_3(s)$, as illustrated on figure 2.3.

These degrees of freedom are linked by 6 equations of motion, as described by the rod [196], and Timoshenko's [197] theories, expressed in the frequency domain for harmonic motion and considering isotropic material:

$$\rho\omega^2 U_1 + E\frac{\partial^2 U_1}{\partial s^2} = 0 \tag{2.1}$$

$$\rho\omega^2 \Theta_1 + G\frac{\partial^2 \Theta_1}{\partial s^2} = 0 \tag{2.2}$$

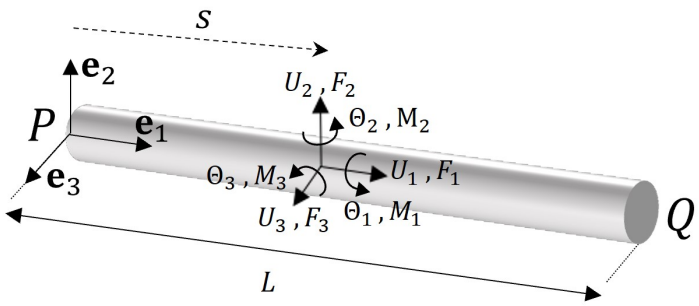

Figure 2.3: Schematic representation of a single beam element of length L, connecting two arbitrary points P and Q. The beam's deformation at any position s, can be described with 3 translational (U_1, U_2, U_3) and 3 rotational (θ_1, θ_2, θ_3) degrees of freedom. These are associated with three components for the internal force (F_1, F_2, F_3) and moment (M_1, M_2, M_3).

$$\begin{aligned} \kappa GA\left(\frac{\partial^2 U_2}{\partial s^2} - \frac{\partial \Theta_3}{\partial s}\right) + \rho A\omega^2 U_2 = 0 \\ EI_3\frac{\partial^2 \Theta_3}{\partial s^2} + \kappa GA\left(\frac{\partial U_2}{\partial s} - \Theta_3\right) + \rho I_3\omega^2\Theta_3 = 0 \end{aligned} \tag{2.3}$$

$$\begin{aligned} \kappa GA\left(\frac{\partial^2 U_3}{\partial s^2} - \frac{\partial \Theta_2}{\partial s}\right) + \rho A\omega^2 U_3 = 0 \\ EI_2\frac{\partial^2 \Theta_2}{\partial s^2} + \kappa GA\left(\frac{\partial U_3}{\partial s} - \Theta_2\right) + \rho I_2\omega^2\Theta_2 = 0 \end{aligned} \tag{2.4}$$

with A, the cross-sectional area, I_2 and I_3 the moments of inertia with respect to the $\mathbf{e}_2$ and $\mathbf{e}_3$ axes, κ the shear correction factor, E the material Young's modulus, G its shear modulus, ρ the mass density and ω the angular frequency. Note that, here, eqs. (2.3) and (2.4) are equivalent because of the cylindrical cross section of the considered beam.

The solution ansatz for equations (2.1- 2.4) are given by:

$$U_1 = A_1\,\mathrm{e}^{\mathrm{i}k_u s} + A_2\,\mathrm{e}^{-\mathrm{i}k_u s} \tag{2.5}$$

$$\Theta_1 = B_1\,\mathrm{e}^{\mathrm{i}k_\Theta s} + B_2\,\mathrm{e}^{-\mathrm{i}k_\Theta s} \tag{2.6}$$

$$\begin{aligned} U_2 = C_1\,\mathrm{e}^{\mathrm{i}k_{2t} s} + C_2\,\mathrm{e}^{-\mathrm{i}k_{2t} s} + C_3\,\mathrm{e}^{\mathrm{i}k_{2e} s} + C_4\,\mathrm{e}^{-\mathrm{i}k_{2e} s} \\ \Theta_3 = \beta_{2t}C_1\,\mathrm{e}^{\mathrm{i}k_{2t} s} - \beta_{2t}C_2\,\mathrm{e}^{-\mathrm{i}k_{2t} s} + \beta_{2e}C_3\,\mathrm{e}^{\mathrm{i}k_{2e} s} - \beta_{2e}C_4\,\mathrm{e}^{-\mathrm{i}k_{2e} s} \end{aligned} \tag{2.7}$$

$$\begin{aligned} U_3 = D_1\,\mathrm{e}^{\mathrm{i}k_{3t} s} + D_2\,\mathrm{e}^{-\mathrm{i}k_{3t} s} + D_3\,\mathrm{e}^{\mathrm{i}k_{3e} s} + D_4\,\mathrm{e}^{-\mathrm{i}k_{3e} s} \\ \Theta_2 = \beta_{3t}D_1\,\mathrm{e}^{\mathrm{i}k_{3t} s} - \beta_{3t}D_2\,\mathrm{e}^{-\mathrm{i}k_{3t} s} + \beta_{3e}D_3\,\mathrm{e}^{\mathrm{i}k_{3e} s} - \beta_{3e}D_4\,\mathrm{e}^{-\mathrm{i}k_{3e} s} \end{aligned} \tag{2.8}$$

where k_u,k_Θ and k_{nl} are wavenumbers relative to the different degrees of freedom wich expressions are provided in the section A of the appendix and $\beta_{\mathrm{nl}} = \mathrm{i}(\frac{k_G^4}{k_{\mathrm{nl}}} - k_{\mathrm{nl}})$ for $n = \left[2,3\right]$, $l = \left[t,e\right]$ and $k_G = \sqrt{\omega}(\rho A/\kappa GA)^{1/4}$.

The spectral components of the compression, transverse shear force, torsion and bending moment

are defined by [196, 197] :

$$F_1 = EA\frac{\partial U_1}{\partial s} \tag{2.9}$$

$$M_1 = GI_1\frac{\partial \Theta_1}{\partial s} \tag{2.10}$$

$$\begin{aligned} F_2 &= \kappa AG\left[\frac{\partial U_2}{\partial s} - \Theta_3\right] \\ M_3 &= EI_3\frac{\partial \Theta_3}{\partial s} \end{aligned} \tag{2.11}$$

$$\begin{aligned} F_3 &= \kappa AG\left[\frac{\partial U_3}{\partial s} - \Theta_2\right] \\ M_2 &= EI_2\frac{\partial \Theta_2}{\partial s} \end{aligned} \tag{2.12}$$

By substituting the solutions of Eqs. (2.5-2.8) into Eqs. (2.9-2.12), and setting the following boundary conditions:

$$\begin{aligned} U_j^P &= U_j(0),\ \Theta_j^P = \Theta_j(0) \\ U_j^Q &= U_j(L),\ \Theta_j^Q = \Theta_j(L) \\ F_j^P &= -F_j(0),\ M_j^P = -M_j(0) \\ F_j^Q &= F_j(L),\ M_j^Q = M_j(L) \\ j &= \left[1, 2, 3\right] \end{aligned} \tag{2.13}$$

we obtain the following matrix relationship:

$$\begin{aligned} \mathbf{\Phi} &= \mathbf{D}^{-1}\mathbf{d}_L \\ \mathbf{F}\mathbf{\Phi} &= \mathbf{f}_L \\ \mathbf{S}_L\mathbf{d}_L &= \mathbf{f}_L \end{aligned} \tag{2.14}$$

where $\mathbf{\Phi} = {}^t[A_1\ A_2\ B_1\ B_2\ C_1\ C_2\ C_3\ C_4\ D_1\ D_2\ D_3\ D_4]$ is the vector of waves coefficients,
$\mathbf{d}_L = {}^t\left[U_1^P U_2^P U_3^P \Theta_1^P \Theta_2^P \Theta_3^P U_1^Q U_2^Q U_3^Q \Theta_1^Q \Theta_2^Q \Theta_3^Q\right]$ is the vector consisting of the nodal displacements and rotations,
$\mathbf{f}_L = {}^t\left[F_1^P F_2^P F_3^P M_1^P M_2^P M_3^P F_1^Q F_2^Q F_3^Q M_1^Q M_2^Q M_3^Q\right]$ is the vector consisting of the nodal forces and moments and $\mathbf{S}_L = \mathbf{F}\mathbf{D}^{-1}$ the stiffness matrix. This matrix reduces the equations of the dynamics of a beam to the expression of the degrees of freedom at both ends: the continuous problem is therefore reduced to a discrete study at two points; this is the essence of the SEM. We will then see how to assemble different trunks of beams and apply periodicity conditions to them. The matrices **F** and **D** are 12x12 matrices given in the section A of the appendix.

These quantities can be transformed into the global coordinate system (**x**,**y**,**z**), thanks to a rotation

matrix $\mathbf{T}$:

$$\mathbf{d}_L = \mathbf{T}\mathbf{d}_G,\ \mathbf{f}_L = \mathbf{T}\mathbf{f}_G,\ \mathbf{T} = \begin{bmatrix} \mathbf{T}_c & \mathbf{0} & \mathbf{0} & \mathbf{0} \\ \mathbf{0} & \mathbf{T}_c & \mathbf{0} & \mathbf{0} \\ \mathbf{0} & \mathbf{0} & \mathbf{T}_c & \mathbf{0} \\ \mathbf{0} & \mathbf{0} & \mathbf{0} & \mathbf{T}_c \end{bmatrix} \tag{2.15}$$
$$\mathbf{S}_G\mathbf{d}_G = \left[{}^t\mathbf{T}\mathbf{S}_L\mathbf{T}\right]\mathbf{d}_G = \mathbf{f}_G$$

with $\mathbf{d}_G$, $\mathbf{f}_G$ and $\mathbf{S}_G$ the nodal motions, forces and the stiffness matrix in the global coordinate system. Here, $\mathbf{T}_c$ is a conventional 3x3 rotation matrix (see section B of the appendix for details). The assembly of the different stiffness matrices is carried out by applying motion continuity conditions and equilibrium conditions at the connection nodes.

2.3.2 Application of Periodicity Conditions

Bloch conditions [100, 198] are imposed on the degrees of freedom (DOFs) located at the boundaries of a unit cell. To formalize this, the global DOF vectors is defined as follows:

$$\mathbf{d}_G = \begin{bmatrix} \mathbf{d}_{\text{input}} \\ \mathbf{d}_{\text{interior}} \\ \mathbf{d}_{\text{output}} \end{bmatrix} \tag{2.16}$$

where $\mathbf{d}_{\text{input}}$ and $\mathbf{d}_{\text{output}}$ are vectors of the same size n_{io}, corresponding to the DOFs of the four boundary nodes at the left and right ends of the unit cell. Meanwhile, $\mathbf{d}_{\text{interior}}$ is vectors of size n_{int}, corresponding to the DOFs of the remaining internal nodes. Here n_{io} is equal to 24 for all the structures studied because the symmetry of point O in figure 2.1b always implies 4 points of connection between the unit cells, each of which has 6 degrees of freedom.

The DOFs on the left and right sides of the unit cell are related through the periodicity condition:

$$\begin{bmatrix} \mathbf{d}_{\text{input}} \\ \mathbf{d}_{\text{interior}} \\ \mathbf{d}_{\text{output}} \end{bmatrix} = \begin{bmatrix} \mathbf{d}_{\text{input}} \\ \mathbf{d}_{\text{interior}} \\ \lambda\mathbf{d}_{\text{input}} \end{bmatrix} \tag{2.17}$$

where $\lambda = \mathrm{e}^{\mathrm{i}ka_x}$, with k being the Bloch wavenumber [99].

The periodic boundary conditions are applied on $\mathbf{S}_G$ by a left and right multiplication of the following matrices:

$$\mathbf{T}_p^{\text{in}} = \begin{bmatrix} \mathbf{I}_{\text{io}} & \mathbf{0} \\ \mathbf{0} & \mathbf{I}_{\text{int}} \\ \lambda\mathbf{I}_{\text{io}} & \mathbf{0} \end{bmatrix}, \mathbf{T}_p^{\text{out}} = \begin{bmatrix} \mathbf{I}_{\text{io}} & \mathbf{0} \\ \mathbf{0} & \mathbf{I}_{\text{int}} \\ \lambda^{-1}\mathbf{I}_{\text{io}} & \mathbf{0} \end{bmatrix} \tag{2.18}$$

where $\mathbf{I}_{\text{io}}$ and $\mathbf{I}_{\text{int}}$ are square identity matrices of dimensions n_{io} and n_{int}, respectively.

To incorporate these conditions, the original system matrix $\mathbf{S}_G$ is reduced to $\mathbf{S}_p$ using the following transformation:

$$\mathbf{S}_p(\omega,\lambda) = {}^t\mathbf{T}_p^{\text{out}}\mathbf{S}_G\mathbf{T}_p^{\text{in}} \tag{2.19}$$

These conditions lead to solving an eigenvalue problem $\omega(\lambda)$ satisfying $\det(\mathbf{S}_p(\omega,\lambda)) = 0$. In the case of a non-dissipative material (with E purely real), the search for solutions is performed by restricting to real values of the wavenumber k in the first Brillouin zone $0 \leq k \leq \pi/a_x$ in order to identify propagative waves.

In this case, the eigenvalue problem is naturally solved in the form $\omega(\lambda)$, by scanning the wavenumber to extract the associated frequencies.

On the other hand, for a dissipative material (with E complex), the wavenumber is expressed as $k = k_r \pm \mathrm{i}\, k_i$, with k_r restricted to the first Brillouin zone and k_i unbounded. In this case, the distinction between propagative and evanescent waves is made by evaluating the ratio:

$$Z = \frac{|k_i|}{\sqrt{k_r^2 + k_i^2}}. \tag{2.20}$$

A high ratio indicates that the wave is evanescent, whereas a low ratio suggests that the wave is propagative. In this configuration, the complex nature of the wavenumber leads to solving the problem in the form $\lambda(\omega)$, which amounts to searching a complex wavenumber associated to a given frequency.

2.3.3 Dispersion of the reference structure

We start by solving the eigenvalue problem for the reference structure S_0 (see figure 2.2a) with $E = 3.3\,\text{GPa}$, $\rho = 1100\,\text{kg/m}^3$, $\nu = 0.3$, $a_x = 3\,\text{cm}$ and the beam radius $R = 1.5\,\text{mm}$. In this analysis, only the propagative solutions, *ie* those corresponding to purely real wavenumbers k confined to the first Brillouin zone, are solved. The associated dispersion graphs are displayed on figure 2.4. Here, we adopt the reduced reciprocal coordinates $K = ka_x/\pi$ and $\Omega = fa_x/c_t$, where f is the frequency and $c_t = \sqrt{\frac{E}{2\rho(1+\nu)}}$ corresponds to the speed of the torsional wave in a solid beam.

This dispersion diagram features a wide variety of branches. It is noticeable that some of these branches only exist above a certain frequency. This cut-off is a signature of the wave guiding process occurring in the **y** and **z** directions as a consequence of the stress-free condition at the edges. In comparison, we provide the dispersion diagram obtained with a FEM simulation using the Comsol® Solid module and report a convincing agreement with our model (see dashed lines on figure 2.4).
Up to $\Omega = 0.06$, the SEM and FEM simulations match. Beyond this frequency, however, a noticeable deviation emerges. Specifically, for $\Omega > 0.06$, modes appear in which the displacement field is no longer homogeneous in the transverse section of the beams. This phenomenon is particularly evident in Fig. 2.4b, which shows the deformed shape computed by Comsol® Solid (using a full three-dimensional elasticity model) at $K = 0$ for $\Omega = 0.079$, whereas Fig. 2.4c, corresponding to a lower-frequency branch ($\Omega = 0.018$), does not exhibit such inhomogeneity. These transverse deformations cannot be captured by classical beam theory, thereby underscoring the limitations of the SEM in this frequency regime. Overall, the SEM model consistently outperforms the FEM, delivering a solution in 12 seconds (using Matlab® code solving 48 DOFs), compared to 3 minutes for the FEM

(using the Comsol® Solid module using the automated mesh called "normal", resulting in 125,181 DOFs solved), showcasing its efficiency for quick and prompt analysis at sufficient low frequency.

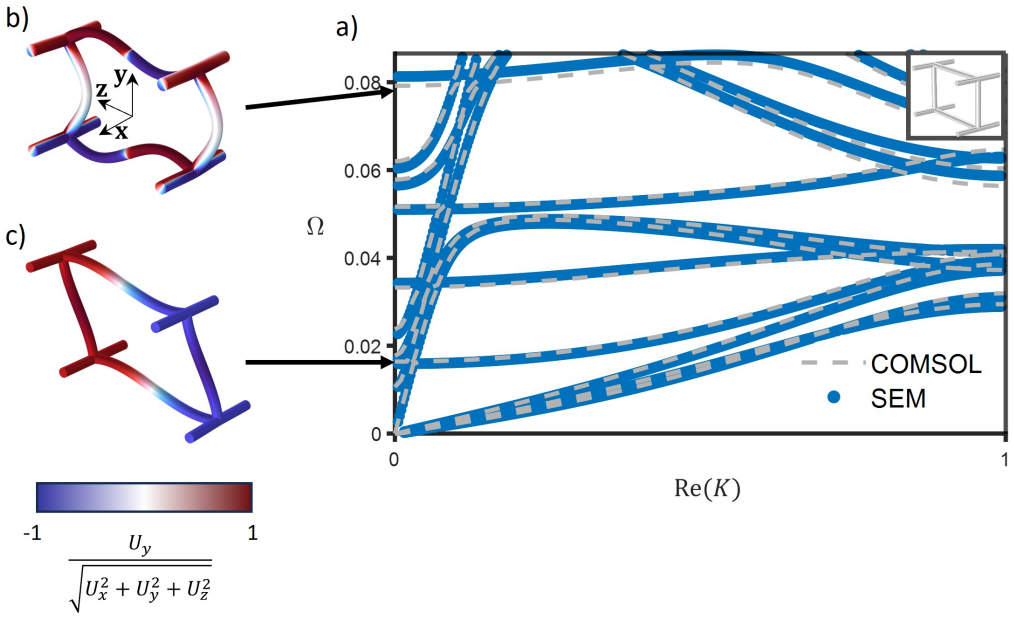

Figure 2.4: a) Dispersion graph obtained for the reference structure S_0 (sketched in the inset) with the SEM Matlab® code (blue symbols) and with Comsol® Solid Module (dashed line in gray). Here we adopt the reduced coordinates $K = ka_x/\pi$ and $\Omega = fa_x/c_t$. b) and c) show the deformed shapes of the unit cell computed with Comsol® Solid Module for $K = 0$ at $\Omega = 0.079$ and $\Omega = 0.018$, respectively. The normalized U_y-component is represented by a color gradient ranging from blue (negative) to red (positive).

2.4 Mode decomposition and dispersion analysis

Given the amount of branches, the dispersion diagram is challenging to interpret. Here we introduce a classification procedure, adapted from the Lamb modes [192, 193], allowing to sort the vibrational modes thanks to symmetry considerations. More specifically, we consider U_x, the displacement field in the propagation direction, and examine its symmetries with respect to the $(\mathbf{x}, \mathbf{z})$ and $(\mathbf{x}, \mathbf{y})$ planes, as highlighted in figure 2.5a. The modes are labeled using a double-letter convention: the first letter indicates whether the quantity is symmetric (S) or antisymmetric (A) with respect to the $(\mathbf{x}, \mathbf{z})$ plane, and the second letter indicates whether it is symmetric or antisymmetric with respect to the $(\mathbf{x}, \mathbf{y})$ plane. As an illustration, we report the deformation pattern corresponding to the 12 first modes on figure 2.5b, together with their corresponding symmetry label. With these convention, the original dispersion can be divided into four distinct diagrams, each featuring the branches corresponding to the four different classes of symmetries (SS, SA, AS, and AA). This decomposition is exact and corresponds to a factorisation of the dispersion relation. The section C of the appendix explains in detail how the matrix $\mathbf{S}_p$ is condensed by applying symmetry conditions to the degrees of freedom of each nodes with respect to the $(\mathbf{x}, \mathbf{y})$ and $(\mathbf{x}, \mathbf{z})$ planes. This process yields four matrices: $\mathbf{S}_p^{\mathrm{SS}}$, $\mathbf{S}_p^{\mathrm{SA}}$, $\mathbf{S}_p^{\mathrm{AS}}$ and $\mathbf{S}_p^{\mathrm{AA}}$.

Figure 2.5e shows the inverse of the determinant of $\mathbf{S}_p$ at an angular frequency Ω_t (indicated by a dotted line in figure 2.5c and d), as a function of the real and imaginary parts of K. The 24 visible solutions show that the resulting polynomial is of order 24. By way of comparison, Figure 2.5f shows the inverse of the determinant of the four condensed matrices, each with six solutions corresponding to those of $\mathbf{S}_p$. This factorisation reduces the original problem into four simpler sub-problems, each corresponding to a polynomial of order 6.

In the quasi-static limit $\Omega \to 0$, each quadrant of the dispersion diagram features exactly one propagative branch - these are labeled ss_0, sa_0, as_0, and aa_0. Upon inspection of the deformation patterns displayed in figure 2.5d, it becomes apparent that these four modes are analogous to the fundamental deformation modes of a simple plain beam, as described in section 2.3.1. They essentially represent a compressional (ss_0), two flexural (sa_0 and as_0), and a torsional (aa_0) mode. In other words, at sufficiently low frequencies, the structure exhibit a behaviour analogous to that of an effective homogeneous beam. As frequency increases, additional branches emerge, typical of a waveguide configuration. The index number refers to the order of the branch cut-off frequencies in each symmetry class.

In addition, the polarization of each mode is characterized by a scalar coefficient Φ, which is obtained by post-processing the eigenvectors of the generalized eigenvalue problem. The discrete eigenvectors are first mapped back to the continuous deformation fields of the full structure using the beam shape functions provided by the spectral formulation. The maximum absolute displacement amplitudes along the three spatial directions are then extracted, yielding the vector $\mathbf{S} = [S_x\ S_y\ S_z]$. The polarization coefficient is defined as

$$\Phi = \frac{\mathbf{S} \cdot [1\ 0\ 0]}{\|\mathbf{S}\|}, \tag{2.21}$$

so that $\Phi = 1$ corresponds to purely longitudinal waves (U_x), whereas $\Phi \to 0$ indicates predominantly transverse deformation (U_y,U_z). This scalar quantity is represented using a colour scale ranging from green (Transverse) to black (Longitudinal). Our analysis reveals that within a single subquadrant, distinct branches may exhibit different polarizations. For instance, the motion of the fundamental ss_0 mode is essentially longitudinal, in agreement with its *compressional* nature.

Similarly, sa_1, and as_1, which can be interpreted as shear deformations, are polarized longitudinally. The pseudo-flexural (sa_0 and as_0), together with the pseudo-torsional (aa_0, aa_1) and the breathing expansion (ss_1) modes involve deformations within the transverse plane. Note that for square cross-section lattices, *i.e.* $\hat{a}_{\mathrm{zy}} = 1$, the SA and AS should be perfectly equivalent. Here $\hat{a}_{\mathrm{zy}} = 1.5$ which explains for notable differences. This asymmetry impacts the shear modes (sa_1 and as_1) rather than the flexural ones (sa_0 and as_0).

In this section, starting from the reference structure S_0, characterized by its state vector $\mathbf{p}_{\mathrm{S0}} = \big[0, 0, 0, 0, 0\big]$, we have introduced a method to analyze the wave dispersion. We will now leverage this method to explore the parameter space – specifically, to assess the impact of geometrical modifications

at the scale of the unit cell on the dispersion behaviour.

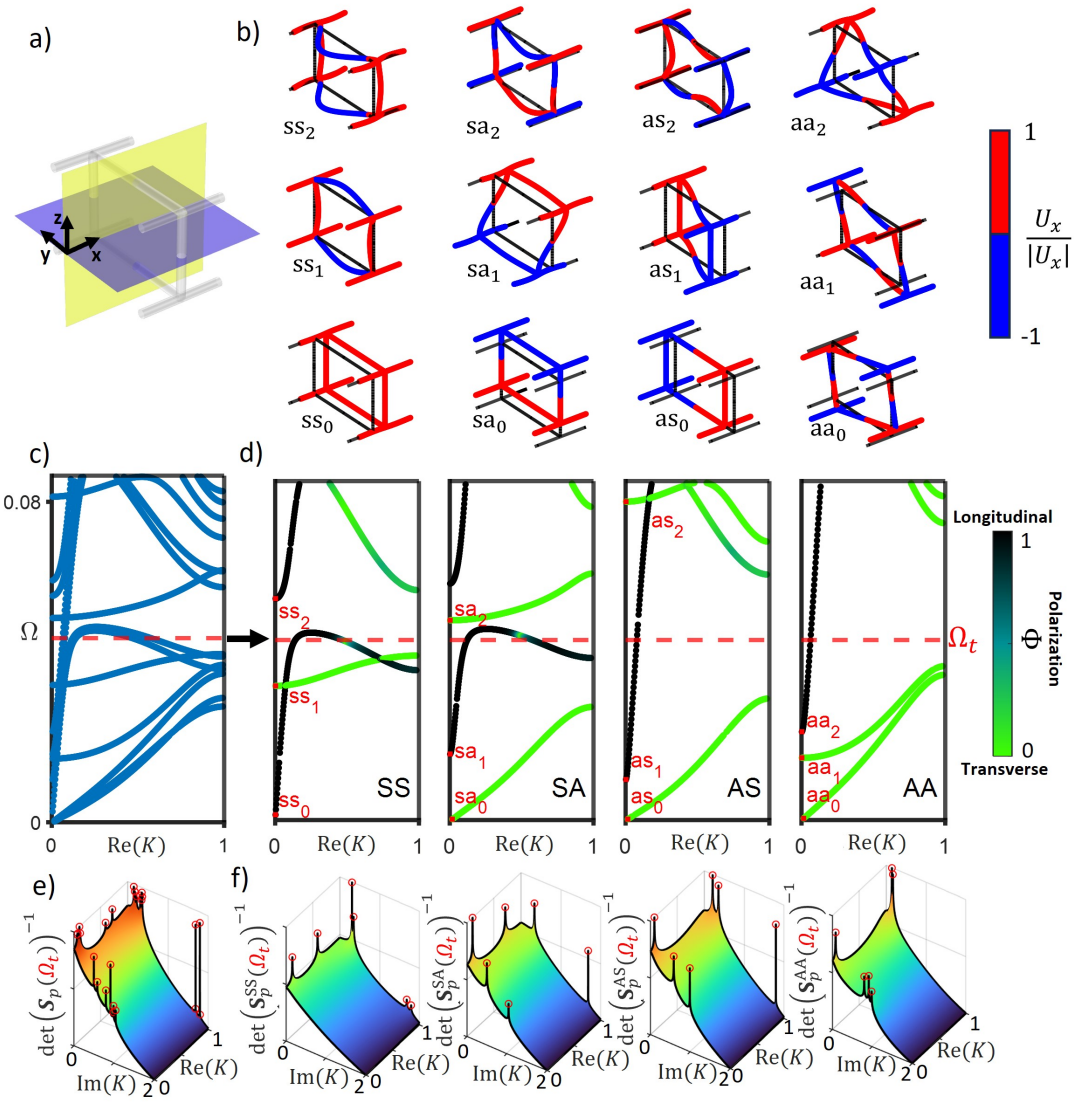

Figure 2.5: (a) Sketch of the reference unit cell displaying, in blue and yellow, the two planes considered to examine the eigenmodes symmetries. (b) Representation of deformed unit cells using the total displacement $\left(U_x^2 + U_y^2 + U_z^2\right)^{1/2}$ for the first twelve eigenmodes of the structure. The color is indicative of the sign of the longitudinal displacement U_x. (c) Dispersion diagram for the reference structure and (d) the same data sorted in four different diagrams according to the symmetries of U_x. The colormap indicates the dominant polarization of the total displacement; green (respectively black) for a transverse (respectively longitudinal) polarization. The red symbols refer to the solutions sketched in (b). (e) Inverse of the determinant of $\mathbf{S}_p$ at Ω_t versus $\mathrm{Re}(K)$ and $\mathrm{Im}(K)$, (f) Inverse of the determinant of condensed matrices $\mathbf{S}_p^{\mathrm{SS}}, \mathbf{S}_p^{\mathrm{SA}}, \mathbf{S}_p^{\mathrm{AS}}, \mathbf{S}_p^{\mathrm{AA}}$ at the same Ω_t.

2.5 Parametric study of the unit cell geometry

As illustrated in Figure 2.4, the reference structure S_0 does not exhibit an absolute bandgap (i.e., a frequency band with no propagative solutions for the four branch families SS, SA, AS, and AA) in the frequency range of interest, although it does produce an SS-polarized bandgap between $\Omega = 0.048$ and

$\Omega = 0.056$. In order to identify suitable designs for wave attenuation, we investigate how to reshape S_0 to generate the widest absolute bandgap. Our analysis covers the seven geometric parameters of the section 2.2, to reveal trends in optimal designs and clarify the impact of each parameter.

In order to explore the geometric space, we generate a diverse set of structures by using the Latin Hypercube Sampling (LHS) method [199] via Matlab's *lhsdesign* function. LHS divides the range of each parameter into intervals of equal probability and selects one sample from each interval, ensuring balanced coverage of our 7-dimensional space. This approach minimizes the risk of missing critical configurations. Although we considered alternative strategies, such as purely random sampling or a full parameter sweep, these would require many more samples to achieve the same level of coverage. After generating the dispersion diagrams for a total of 16.000 structures, 2.757 configurations turn out to exhibit at least one absolute vibrational band gap. Among these, the gap efficiencies are assessed by computing the reduced bandgap width $\Delta\Omega/\Omega_0$, with $\Delta\Omega$ the bandgap width and Ω_0 the gap central angular frequency. On figure 2.6, we report $\Delta\Omega/\Omega_0$ as a function of the seven parameters of the system. These plots reveal the contrasted impacts of the parameters on the band gap widths. For instance, among the unit-cell shape parameters (see figs 2.6 (a) and (b)), it appears that the transverse aspect ratio $\hat{a}_{\mathrm{zy}}$ matters, with broader band gaps for $\hat{a}_{\mathrm{zy}} = 1$ (that is $a_z = a_y$ - *ie* a structure of square cross section), when the longitudinal aspect ratio $\hat{a}_{\mathrm{yx}}$ does not. In addition, most structural parameters, especially $\hat{y}_C$ and $\hat{z}_C$, have a notable effect on the band gap width, making them prime candidates for optimizing the vibration mitigation performances. Among these structures, each is characterized by a seven-dimensional vector $\mathbf{v}_i = \left[\hat{a}_{\mathrm{zy}}, \hat{a}_{\mathrm{yx}}, \hat{x}_D, \hat{y}_C, \hat{z}_C, \hat{y}_B - \hat{y}_C, \hat{z}_B - \hat{z}_C\right]$, which represents its geometric features. We then use the *K-means* algorithm [200] via Matlab's `kmeans` function to cluster these vectors. In our approach, the vector $\mathbf{v}_i$ of each structure is compared with the vectors of all other structures using the cosine distance. For a set of vectors $\mathcal{V} = \{\mathbf{v}_1, \mathbf{v}_2, \ldots, \mathbf{v}_N\}$, the cosine distance between any two vectors $\mathbf{v}_i$ and $\mathbf{v}_j$ is given by:

$$d_{ij} = \frac{\mathbf{v}_i \cdot \mathbf{v}_j}{\|\mathbf{v}_i\| \, \|\mathbf{v}_j\|} \tag{2.22}$$

This metric quantifies the similarity between the geometric features of different structures. Through iterative updates, the *K-means* algorithm segments the data into three clusters, thereby grouping structures with similar shapes. These clusters are then visualized using distinct colors: blue, red, and magenta. Within each subpopulation, the structure with the largest band gap is marked with diamond symbols. The corresponding unit-cells, respectively labeled S_1^*, S_2^* and S_3^*, are reported in Figure 2.7.

Interestingly, these designs correspond to degenerate configurations. For instance, they involve a near merging of points O and D meaning that $\hat{x}_D \simeq 0$, in agreement with the conclusions from figure 2.6(c). Qualitatively, merging these two points supposes a lowering of the compressional rigidity and, thus amounts to lowering the slope of the pseudo-compressional ss_0 branch. As a matter of fact, slowing down the fundamental modes is crucial to produce low-frequency band gaps. In addition, the optimal design from cluster 1 comes with $\hat{z}_C \simeq 0$, $\hat{y}_C \simeq \hat{y}_B$, meaning that points A and B also merge and $\hat{z}_C \simeq 0$, $\hat{z}_C \simeq \hat{z}_A$ meaning that A and B migrate to the center of the unit-cell with point

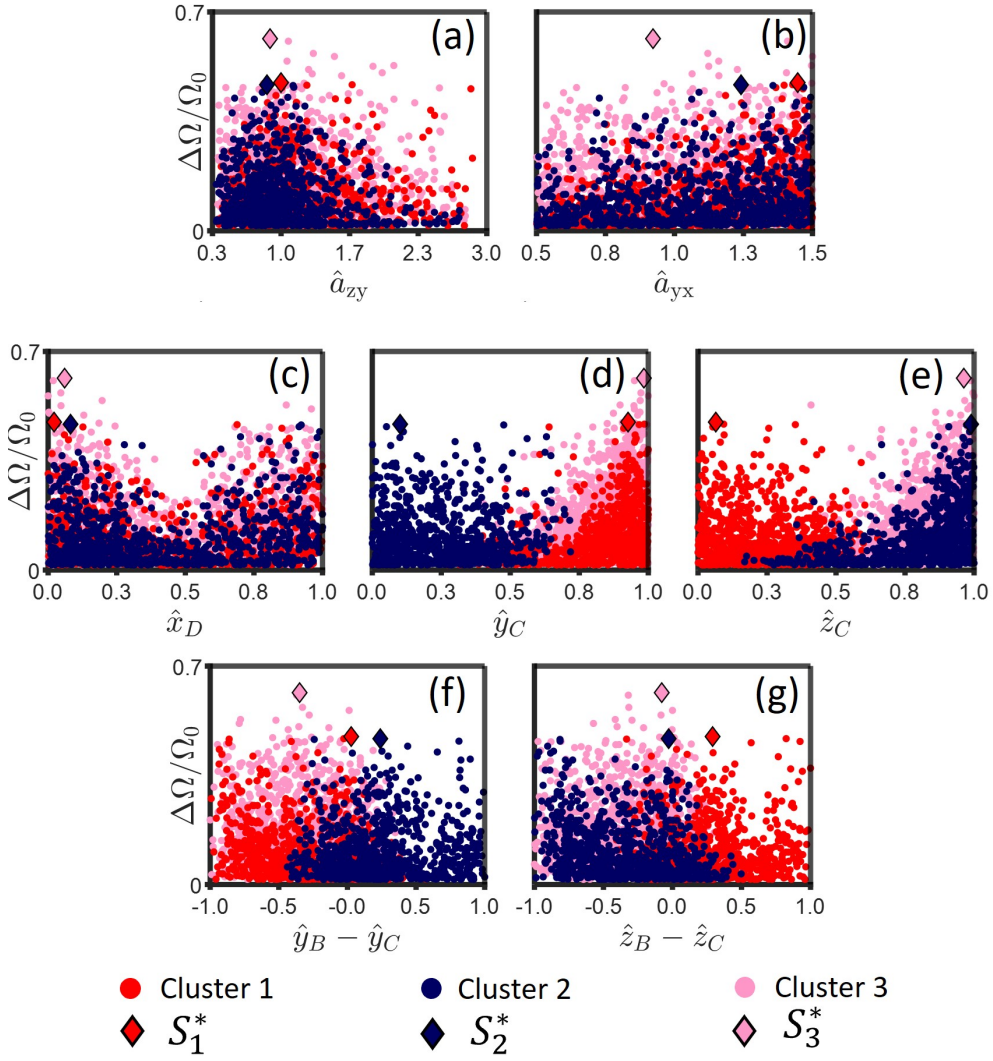

Figure 2.6: Reduced bandgap width $\Delta\Omega/\Omega_0$ of the absolute bandgaps exhibited from 2.757 structures selected from a starting pool of 16.000. The results are displayed as a function of all seven tuning parameters of the investigated system; with (a-b) the parameters governing the unit cell's aspect ratio and (c-g) the parameters setting the elementary beam pattern structure. Three clusters of structures showing strong geometrical similarities are identified and highlighted in blue, cyan and red. Among each cluster, the structures S_1^*, S_2^* and S_3^*, associated with the broadest total bandgaps are depicted with dark-edged diamond symbols.

C lying above them, at the center of the top edge of the unit-cell.

While all three designs yield absolute band gaps, as indicated by the grey areas in figure 2.7, it is worth pointing out the very different nature of the three band structures. For instance, the dispersion diagram for S_1^* features 3 branches below the band gap for the AS quadrant, while only two branches show up for S_2^* and S_3^*. In addition, S_3^* features a single AA mode below its band gap, while S_1^* and S_2^* have two. This indicates that theses band gaps have different physical origins.

2.5.1 Mechanisms governing the band gap characteristics

To elucidate the link between the geometry of the unit-cell and the characteristics of the band gap, we examine the transitions between the structures of interest.

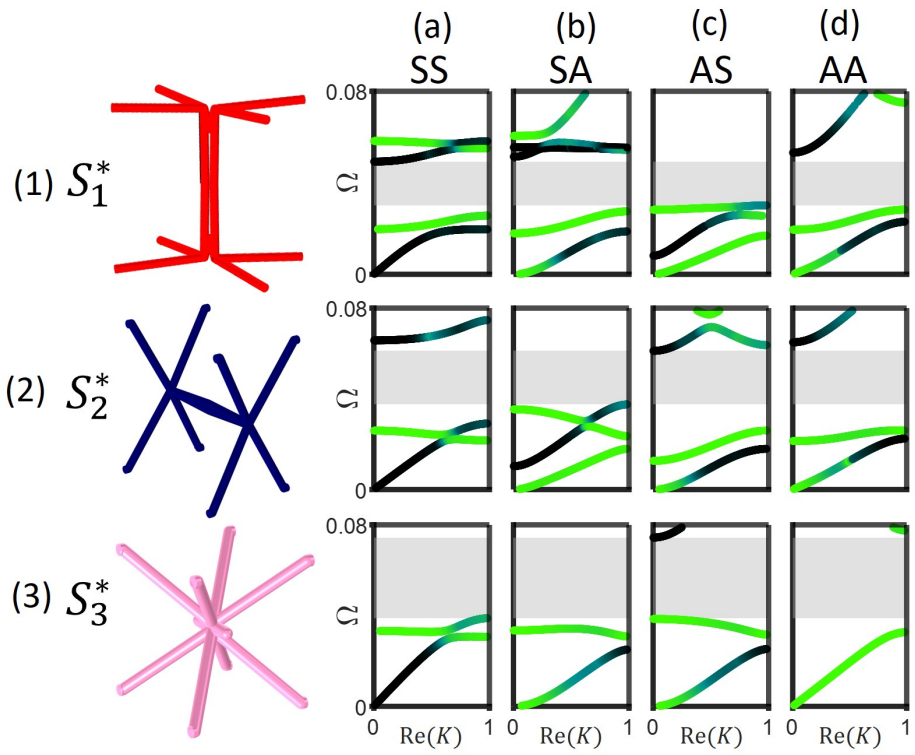

Figure 2.7: Unit cells of the three optimal structures S_1^* (top), S_2^* (middle) and S_3^* (bottom) along with their respective dispersion diagrams. The absolute band gaps are indicated by the grey-shaded area.

To simplify the analysis, we set $\hat{a}_{zy} = 1.5$ and $\hat{a}_{xy} = 1$, so that the unit cell has the same aspect ratio than for structure S_0. As a consequence, here we investigate structures S_1 and S_3 respectively inspired from S_1^* and S_3^*. Consider, for instance, the continuous transformation from S_0 (characterized by its vector $\mathbf{p}_{S0} = [0, 0, 0, 0, 0]$) to S_1 (characterized by its vector $\mathbf{p}_{S1} = [0, 1, 0, 1, 0]$). It involves sweeping through the parameters $\hat{y}_B$ and $\hat{y}_C$. Qualitatively, this amounts to narrowing the central rectangle of the unit cell (as illustrated in Figure 2.8) until it shrinks into a single vertical bar. The dispersion graphs show how this transformation reduces the slope of the ss_0 branch. As a matter of fact, slowing down the fundamental modes is key to opening a low-frequency band gap. Since the ss_0 mode is the fastest among these, it is particularly crucial to focus on. The transition from S_0 to S_1 amounts to decreasing the structure's compressive stiffness.

However, this alone is not enough to produce an absolute band gap; an increase in the cutoff frequency of higher-order modes is also necessary. This happens here because the structure's cross-sectional area, which governs the cut-off, is shrinked. In the dispersion diagram, one can observe the as_2 and aa_2 branches shifting towards higher frequencies, enabling the emergence of the band gap. The band gap width evolution with $\hat{y}_B$ and $\hat{y}_C$ is depicted in Figure 2.8 (column 4), with the absolute band gap, represented in pink, emerging and getting wider as $\hat{y}_B$ and $\hat{y}_C$ approach 1.

A similar analysis can be applied to the continuous transformation from S_1 (characterized by its vector $\mathbf{p}_{S1} = [0, 1, 0, 1, 0]$) to S_3 (characterized by its vector $\mathbf{p}_{S3} = [1, 1, 1, 1, 0]$), which involves simultaneously sweeping through $\hat{z}_A$ and $\hat{z}_C$. This qualitatively corresponds to compressing the central vertical bar of the unit cell until it reduces to a single point. Similarly, Figure 2.9 shows that this

local reduction in transverse extension induces a shift in the cutoff frequencies towards higher values, thereby evacuating the sa_1 and aa_1 branches beyond the band gap. It's also noteworthy that symmetric modes remain unaffected by this transformation. From the computational point of view, two nodes become merged when the distance separating them becomes smaller than a certain threshold equal to 0.01 mm. This fusion is equivalent to a condensation of the matrix $\mathbf{S}_p$, reducing the characteristic polynomial order from 24 in S_0, to 12 in S_1 and 6 in S_3.

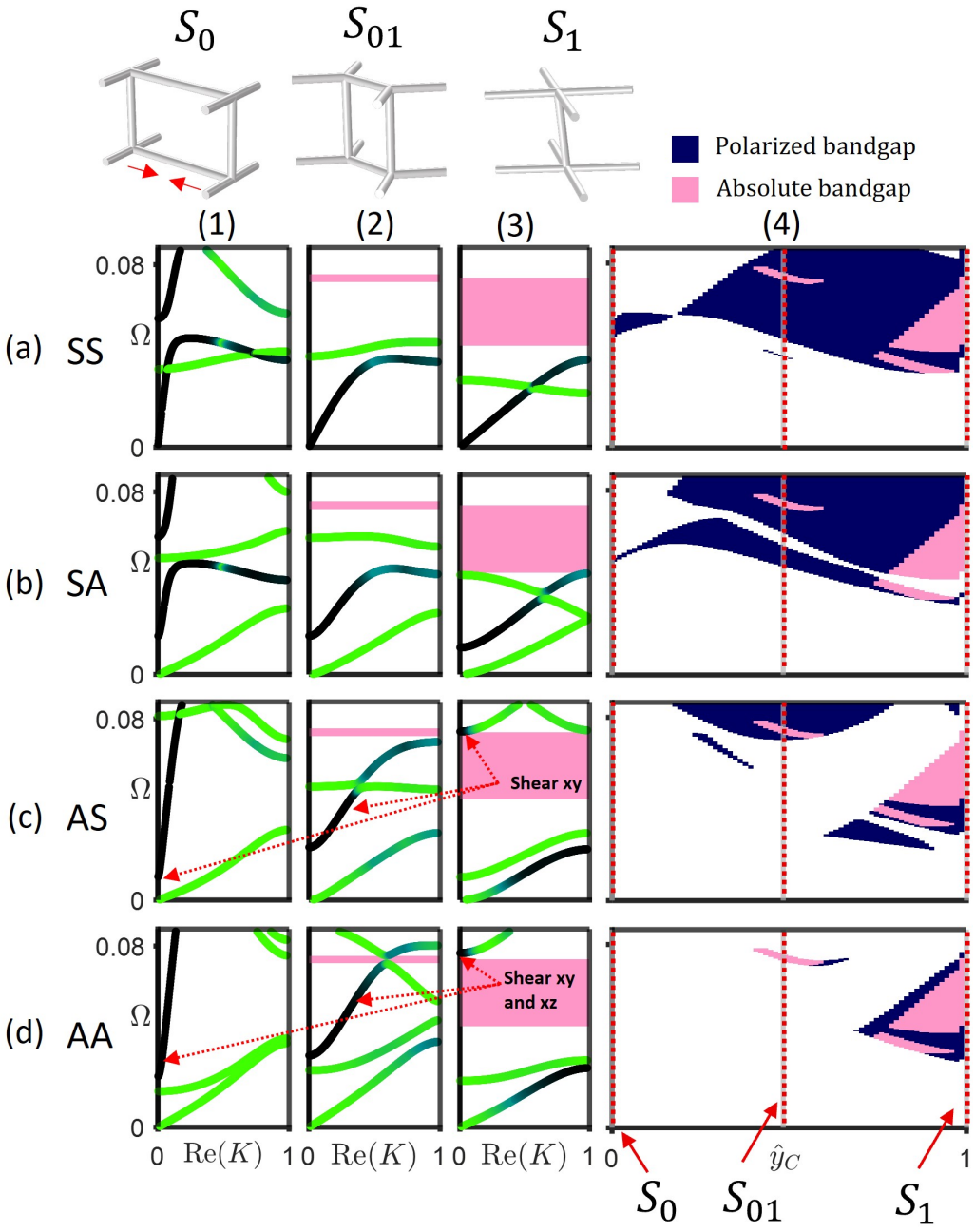

Figure 2.8: Evolution of the dispersion diagrams as structure S_0 (a) is continuously transformed into structure S_1 (c) by sweeping parameters $\hat{y}_B$ and $\hat{y}_C$, simultaneously (*i.e.* setting $\hat{y}_B = \hat{y}_C$) from 0 to 1. Right column: reduced bandgap width plotted as a function of $\hat{y}_C$. The coloured region indicates the bandgap extension as well as its nature (blue for a partial bandgap, pink for an absolute bandgap).

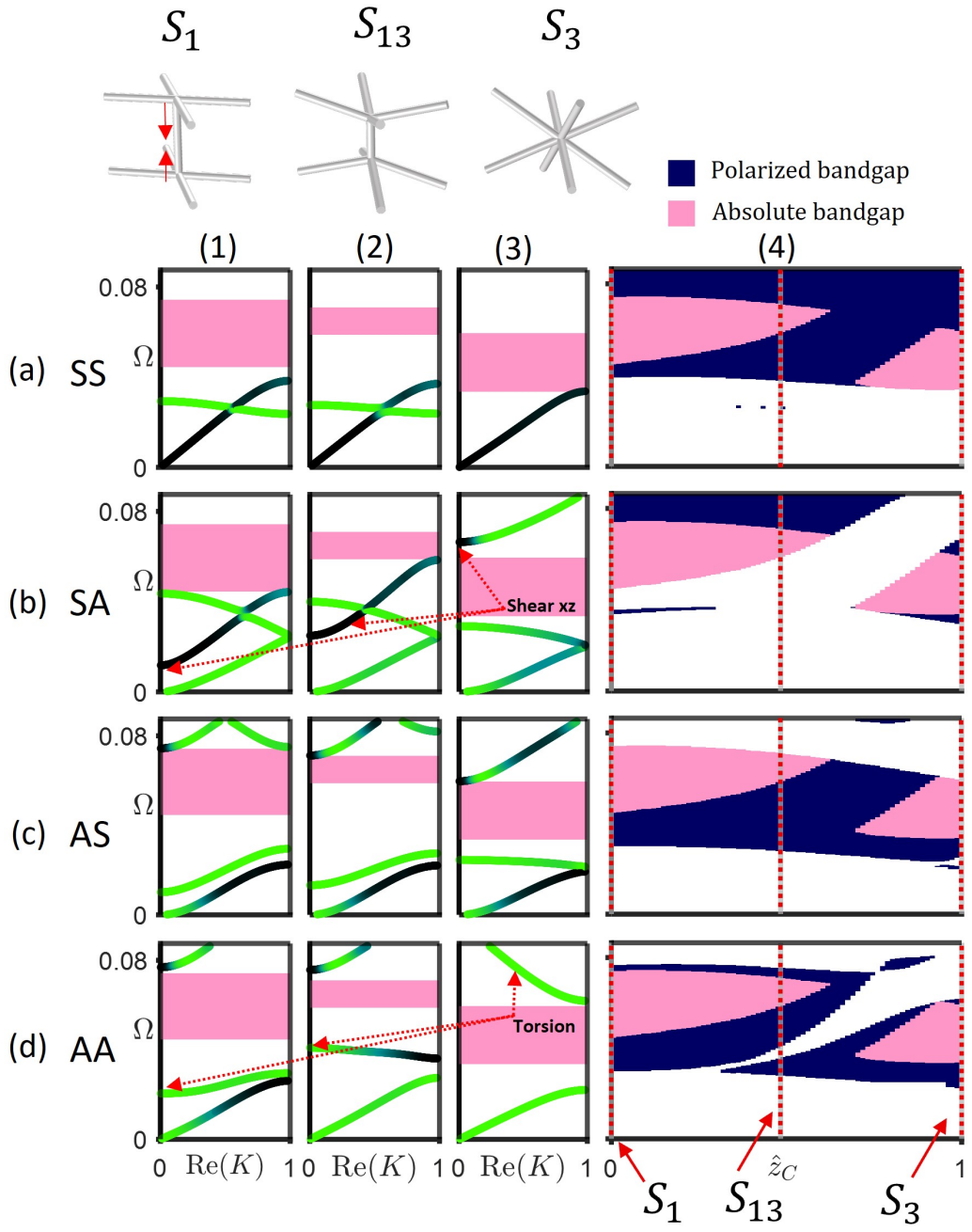

Figure 2.9: Evolution of the dispersion diagrams as structure S_1 (a) is continuously transformed into structure S_3 (c) by varying parameters $\hat{z}_A$ and $\hat{z}_C$, simultaneously (*i.e.* setting $\hat{z}_A = \hat{z}_C$) from 0 to 1. Right column: reduced bandgap width plotted as a function of $\hat{z}_C$. The coloured region indicates the bandgap extension as well as its nature (blue for a partial bandgap, pink for an absolute bandgap).

2.6 Experimental demonstration

The parametric analysis enabled to identify several lattice structures exhibiting low frequency absolute bandgaps, the most promising one being S_3. The scope of this section is to provide an experimental validation for its vibration filtering performances. To this end, a finite-size realization is manufactured from polylactic acid (PLA) using fused filament fabrication (FFF), a technique well suited to the production of complex periodic geometries while providing a simple and cost-effective prototyping process.

2.6.1 Material characterization

First, the mechanical parameters of PLA are extracted from a 250 mm long, 8 mm thick and 16 mm wide clamped sample beam, as pictured on figure 2.10(a). The response to a hammer impact, performed at a distance of 75 mm from the clamp, is measured using a laser vibrometer. From this, the input mobility defined as the ratio between the velocity of the response and the impact force is estimated and plotted in Figure 2.10(b).

The complex Young modulus $E = E'(1 + i\eta)$ with E' the elastic constant and η loss factor of the PLA are identified by fitting the mobility obtained by SEM where a Zener model describes the material with the experimental mobility. The identified parameters are shown in Figure 2.10(c) and are used in the SEM simulations presented in section 2.6.3, both for dispersion graphs and frequency responses shown in Figure 2.12.

2.6.2 Experimental setup

The demonstrator, shown in figure 2.11(a), consists of a 9-cell lattice material beam made from PLA, as characterised above. In order to quantify the manufacturing accuracy, the dimensions a_x, a_y, and a_z of each unit cell, as well as the radius R of each beam, is measured. The obtained values deviate from the exact dimensions by a tolerance of ± 0.3 mm for a_x, ± 0.2 mm for a_y, ± 0.5 mm for a_z, and ± 0.1 mm for R. The sample is mounted on a vibrating table by a holding base clamped in a vise. At the base of the structure, the excitation consists of an acceleration-controlled sine sweep (magnitude 3 g) from 100 Hz to 3000 Hz, either along the **x**, **y** or **z** directions, according to the mounting configurations respectively shown in figures 2.11(b),(c) and (d), respectively. The velocity in a given direction is measured thanks to a laser vibrometer pointing at a cubic target positioned at the top of the demonstrator excited in the same given direction. All the results shown below are obtained after averaging over 3 acquisitions.

2.6.3 Experimental results

As discussed in section 2.6.1, the Young's modulus of PLA and so wavenumber solutions from SEM are complex-valued. In the dispersion graphs in figure 2.12(A.1,B.1,C.1,D.1), the size of each dot of each dispersion branch represents the value of $1 - Z$ (Z defined in equation 2.20). A large/small dot corresponds to a strongly/weakly attenuated wave associated to an almost real/imaginary wavenumber

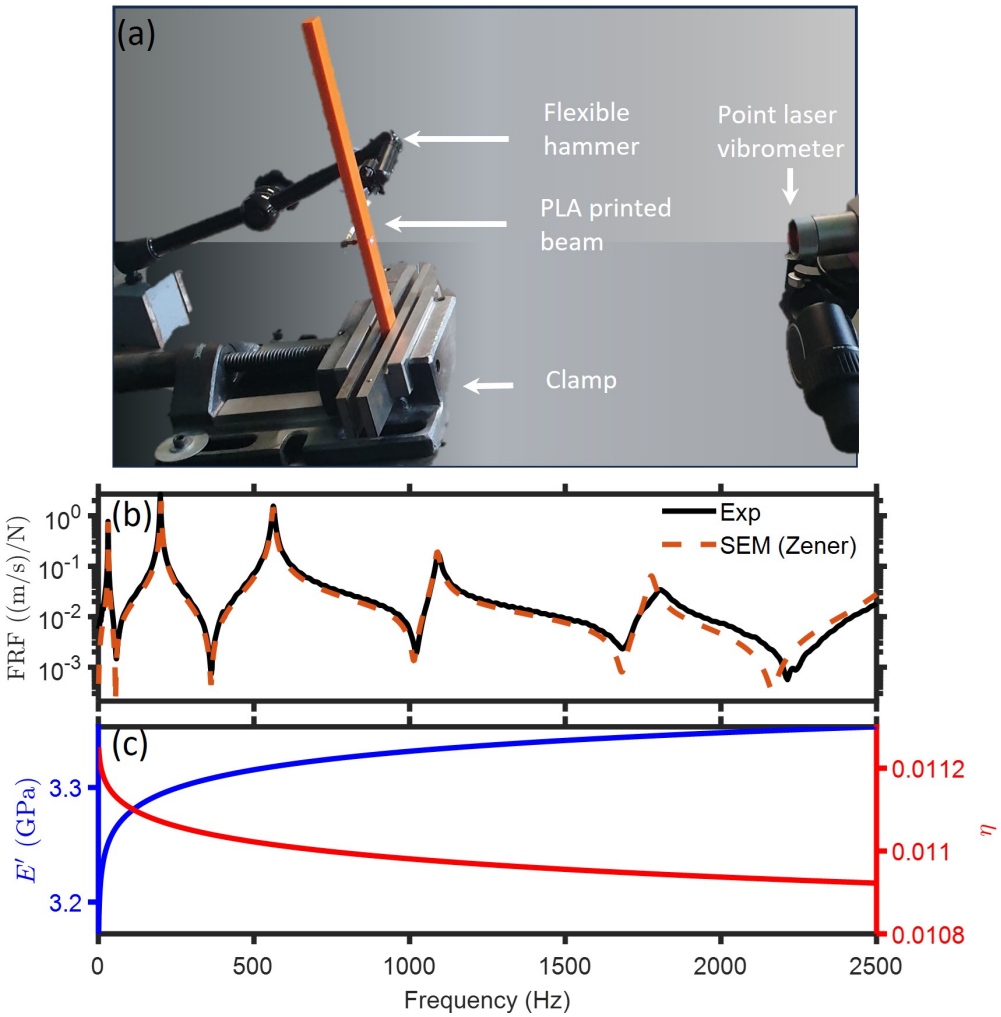

Figure 2.10: Characterization of the constitutive material (PLA): (a) photograph of the experimental setup. (b) Experimental frequency response function (black) and SEM prediction using a Zener model (red). (c) Frequency dependence of the real part of the Young modulus E' (blue) and of the loss factor η (red).

k, respectively. In this situation, band gaps are defined as frequency ranges where $Z > 0.95$ for all dispersion branches in a given dispersion graph (see grey areas in figure 2.12). To evaluate Z, it is necessary to compute the imaginary part of the wave-number as well. We report its evolution in section 5 of the *Supplementary materials* and show that, in accordance with previous works [201], the damping of the solid matrix tends to widen the bandgap.

Alongside the dispersion diagrams, the response of the demonstrator is plotted in figure 2.12(B.2,C.2,D.2) as the ratio γ_{Ti}/γ_{Bi} where γ_{Ti} and γ_{Bi} are the accelerations along the i direction (**x**, **y** or **z**), measured at the target and imposed at the base, respectively. SEM simulations are done following the three experimental configurations and show that, in each of them, the ratios γ_{Ti}/γ_{Bj} when $i \neq j$ are of negligible magnitude. Hence, figure 2.12(B,C,D) only plot γ_{Ti}/γ_{Bi} ratios.

The excitation is such that the holding base follows a uniform translation motion. As a consequence, the points belonging to a given cross-section of the structure always remain in phase and the AA

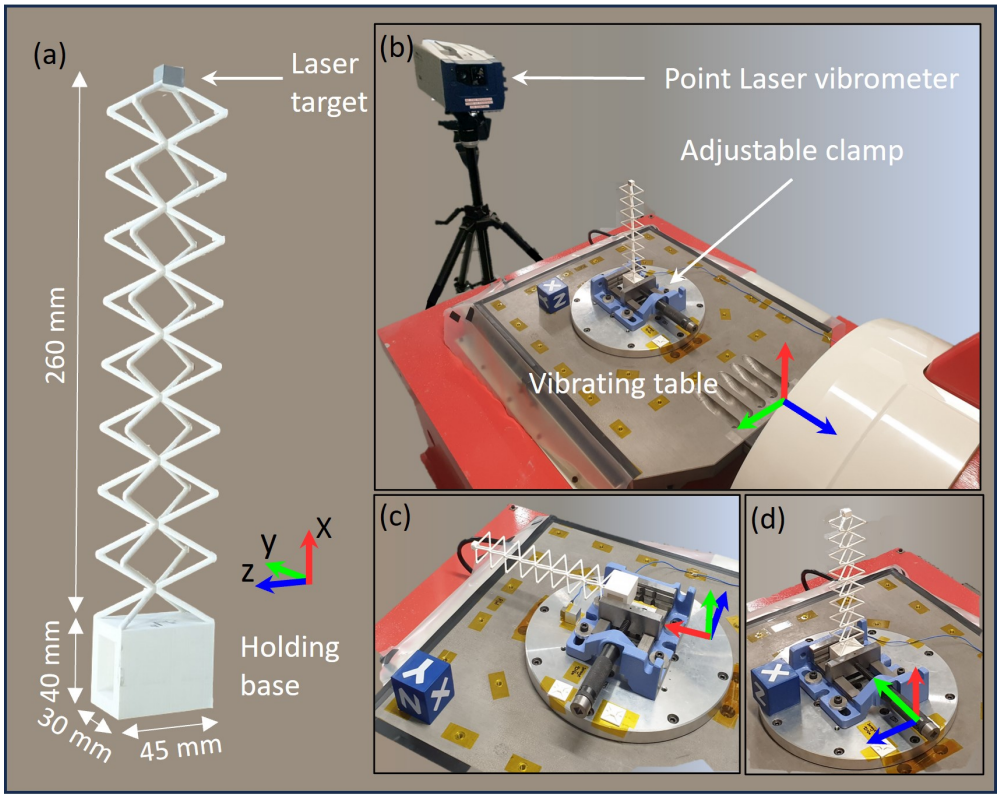

Figure 2.11: Experimental setup: (a) Finite-size 3D-printed structure S_3. (b) Experimental configuration with the lattice structure mounted in a configuration corresponding to an excitation along the **z** direction. (c-d) Same experimental setup but with the excitation along **x** and **y**.

modes, that are essentially associated with shear-like and torsional-like motions, are not excited here and are thus not considered in this experimental study.

In the case of **x**-axis excitation, longitudinal motions are mainly excited, corresponding to the SS wave shown in figure 2.12(B.1). An SS wave band gap is found in the range 1250-2870 Hz, leading to an attenuation of about 30 dB in the acceleration response at the top of the demonstrator. Below this band gap, the response exhibits an expected modal behavior. All over the frequency range of interest, numerical and experimental results are in good agreement, even some discrepancies appear mainly due to geometrical uncertainties of the 3D printed demonstrator.

In the case of **z**- and **y**-axes excitations, the transverse motions corresponding to the SA and AS modes respectively are mainly excited. The dispersion graphs associated with these waves are plotted in figure 2.12(C.1, D.1) and show more branches than for SS waves. For example, the graph in figure 2.12(C.1) for SA waves shows a weakly attenuated wave giving rise to a 1070-2290 Hz band gap, as well as a strongly attenuated wave almost over the entire frequency band represented here. The same comments apply to the figure 2.12(D.1) corresponding to AS waves. In both the SA wave or AS wave band gaps, an attenuation of about 30 dB is again measured. Outside these band gaps, the acceleration response also shows a modal behavior in which resonances above the band gap are significantly more damped than at below, due to the dissipation of the demonstrator material.

Finally, from the SEM calculations an absolute band gap in the range 1250-2100 Hz is found as the intersection of SS, SA and AS waves partial band gaps. As previously, a huge filtering effect is confirmed by the experimental result as shown as in figure 2.12 (A.2) where the ratio $\gamma_T/\gamma_B = \sqrt{\gamma_{\mathrm{Tx}}^2 + \gamma_{\mathrm{Ty}}^2 + \gamma_{\mathrm{Tz}}^2}/\sqrt{\gamma_{\mathrm{Bx}}^2 + \gamma_{\mathrm{By}}^2 + \gamma_{\mathrm{Bz}}^2}$ exhibits a 30dB attenuation.

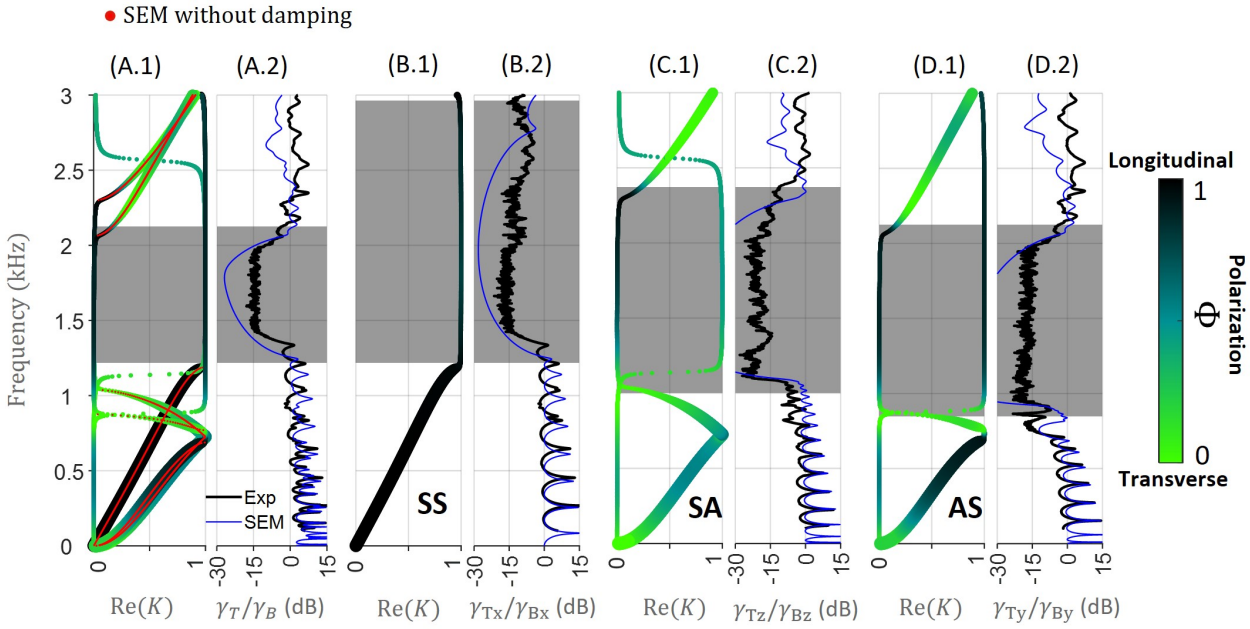

Figure 2.12: Experimental demonstration of the filtering effect: (A.1) Theoretical dispersion diagram of the unit cell S_3 with a complex Young's modulus $E = 3.2(1+\mathrm{i}0.011)$ GPa (coloured points between green and black) and a real Young's modulus $E = 3.2$ GPa (red points) . The sizes of the points corresponding to the case where E is complex are determined by the value $1 - Z = 1 - |k_i|/\sqrt{k_r^2 + k_i^2}$. The shaded areas highlight the theoretical expectations for the bandgap extension where $Z > 0.95$ for all points in the area. (A.2) Theoretical (blue) and experimental (black) transmissions of the γ_T /γ_B ratio whose components are shown in (B.2), (C.2) and (D.2) when the finite-size structure is excited in the **x**, **z** and **y** directions respectively. (B.1), (C.1) and (D.1) are the theoretical scatter plots classified into the SS, SA and AS mode families respectively.

The results in Figure 2.12(A.2) show a reduction of nearly 20 dB in the bandgap region (grey), indicating that the structure acts as an effective vibration filter in this frequency range. Figures 2.12(B.2,C.2 and D.2), show the existence of wider partial band gaps, leading to efficient filtering effect over wider frequency ranges but only for specific vibration. By correlating the dispersion graphs of the different families of modes presented in figures 2.12 B.1, C.1 and D.1 with the frequency response 2.12 B.2, C.2 and D.2, the polarised bands of the compression and bending modes can be highlighted. These bands are superimposed in the region between 1250 and 2100 Hz, creating an absolute filter. Further validation is provided by directly comparing our measurements (black lines) with SEM predictions (red lines) for the ratios γ_T/γ_B, $\gamma_{\mathrm{Tx}}/\gamma_{\mathrm{Bx}}$, $\gamma_{\mathrm{Ty}}/\gamma_{\mathrm{By}}$ and $\gamma_{\mathrm{Tz}}/\gamma_{\mathrm{Bz}}$. The comparison is qualitatively convincing, although a noticeable drift, probably resulting from inaccuracies linked to the printing process, can be observed. These simulations enable the absolute and polarised bandgap to be captured convincingly.

2.7 Conclusions

In this chapter, we investigated the propagation of elastic waves in slender periodic beam lattices and developed a fast and accurate spectral element framework incorporating Bloch–Floquet periodicity. This approach enables the efficient computation and systematic analysis of dispersion relations in complex three-dimensional lattice structures, making it possible to explore large design spaces, as illustrated here through the examination of more than 16,000 configurations.

Beyond numerical efficiency, a symmetry-based classification of vibrational modes was introduced, inspired by guided-wave theory. This decomposition provides a clear physical interpretation of dense dispersion diagrams and allows the key geometrical mechanisms governing Bragg-type band-gap formation to be identified. In particular, the analysis reveals that the opening of low-frequency absolute band gaps relies on two essential ingredients: (i) a strong reduction of the effective stiffness associated with the three fundamental wave polarizations—longitudinal, flexural, and torsional—in order to lower the band-gap onset frequency; and (ii) the maintenance of sufficiently high cut-off frequencies for higher-order modes, which otherwise close the band gap.

These conditions are exemplified by structure S_3, whose geometry promotes strong Bragg interferences through a reduced connection area and a spring-like deformation mechanism. While such architectures are highly effective from a wave-filtering standpoint, they are inherently characterized by low static stiffness. As a result, despite exhibiting wide low-frequency absolute band gaps, these lattice designs remain poorly suited for load-bearing applications.

This observation highlights a fundamental limitation of Bragg-based absolute filters when considered in isolation: the very mechanisms that enable broadband multi-polarization filtering also lead to a severe loss of mechanical rigidity. This trade-off constitutes a critical obstacle for industrial deployment, particularly in applications where structural components must simultaneously ensure vibration mitigation and load-carrying capability.

In the context of this thesis, this limitation is especially relevant to the targeted aeronautical application, namely the design of a passenger-cabin floor rail. Such a component must not only attenuate structure-borne vibrations but also sustain the static loads associated with seats and occupants.

Motivated by these considerations, the next chapter addresses this trade-off explicitly by extending the present dispersion-based analysis toward architectured sandwich configurations. By combining periodic filtering skins with mechanically efficient cores, the objective is to reconcile low-frequency absolute wave attenuation with sufficiently high structural stiffness, thereby bridging the gap between fundamental wave-control concepts and realistic industrial requirements.

CHAPTER 3

Analysis of the trade-off between bending stiffness and absolute bandgap width based on the dispersion relations of a periodic lattice sandwich beam

Contents

3.1 Introduction . . . 48
3.2 Semi-analytical model . . . 49
3.2.1 Spectral model of a free-edge plate element . . . 49
3.2.2 Plate–beam coupling formulation . . . 53
3.2.3 Extension to XBS structure . . . 56
3.2.4 Periodic condition . . . 56
3.2.5 Numerical validation . . . 57
3.2.6 Classification of modes . . . 58
3.3 Trade-off analysis . . . 60
3.4 Experimental validation . . . 63
3.5 Conclusion . . . 64

3.1 Introduction

In Chapter 2, we investigated the propagation of elastic waves in slender periodic beam lattices and showed that low-frequency absolute band gaps can be achieved through Bragg-type interferences, provided that the effective stiffness associated with the three fundamental wave polarizations (longitudinal, flexural, and torsional) is strongly reduced while maintaining sufficiently high cut-off frequencies for higher-order modes. While this strategy yields highly efficient absolute filters from a wave-control standpoint, the geometrical mechanisms that widen the absolute band gap also lead to inherently low static stiffness, which limits the relevance of standalone lattices for load-bearing components. This trade-off constitutes a central obstacle for industrial deployment, especially for the targeted aeronautical application considered in this thesis (passenger-cabin floor rail), where vibration mitigation must be reconciled with structural stiffness and load-carrying capability.

Motivated by these considerations, the present chapter addresses this trade-off explicitly by extending the dispersion-based approach of Chapter 2 to architectured sandwich configurations. Sandwich concepts are mechanically attractive because skins primarily sustain axial loads and dominate bending stiffness, while a lightweight core provides shear rigidity. In the context of wave control, architectured sandwich beams and plates have been widely investigated to enhance flexural attenuation; however, *absolute* filtering is generally not achieved, because sufficiently stiff skins still support the propagation of in-plane (compressional) waves [145, 150, 202, 203]. The objective here is therefore twofold: (i) to propose a sandwich architecture in which the stiffness of all wave modes is controlled so as to open an absolute band gap, and (ii) to quantify, in a design-oriented manner, the compromise between *absolute filtering performance* and *specific bending stiffness*.

To this end, we introduce a lattice-based geometry in which each skin is itself a periodic coupled plate–beam structure composed of an alternation of plain plates and X-shaped beam connectors, referred to as *X-Beam Plates* (XBPs), Fig. 3.1(a). The intended physical mechanism is a Bragg-type band-gap formation driven by a strong stiffness contrast between the constitutive elements, while preserving a compact unit-cell size. Yet, introducing X-shaped connectors into a single skin also reduces its bending efficiency. To mitigate this effect, two XBPs are assembled in a staggered configuration to form an *X-Beam Sandwich* (XBS), Fig. 3.1(b). The skins are connected by a lattice core made of four beams forming a pyramid, which links the plate corners of one skin to the central node of the opposite X-shaped beam network. This core provides a geometric tuning parameter (the pyramid height) to recover bending stiffness, while maintaining the stiffness contrasts required for Bragg interferences and multi-polarization filtering.

From a modelling standpoint, the proposed sandwich architecture requires a formulation that captures wave propagation in periodic *coupled plate–beam* systems with sufficient fidelity, while remaining efficient enough to support parametric sweeps and dispersion-driven design—in line with the methodological philosophy of Chapter 2. Accordingly, the second objective of this chapter is to develop a semi-analytical model to compute dispersion relations under Bloch–Floquet periodicity. Beam substructures follow the spectral-element lattice assembly introduced in the first chapter. Plate substructures follow the generalized dynamic-stiffness formulation of [204], building on Gorman's

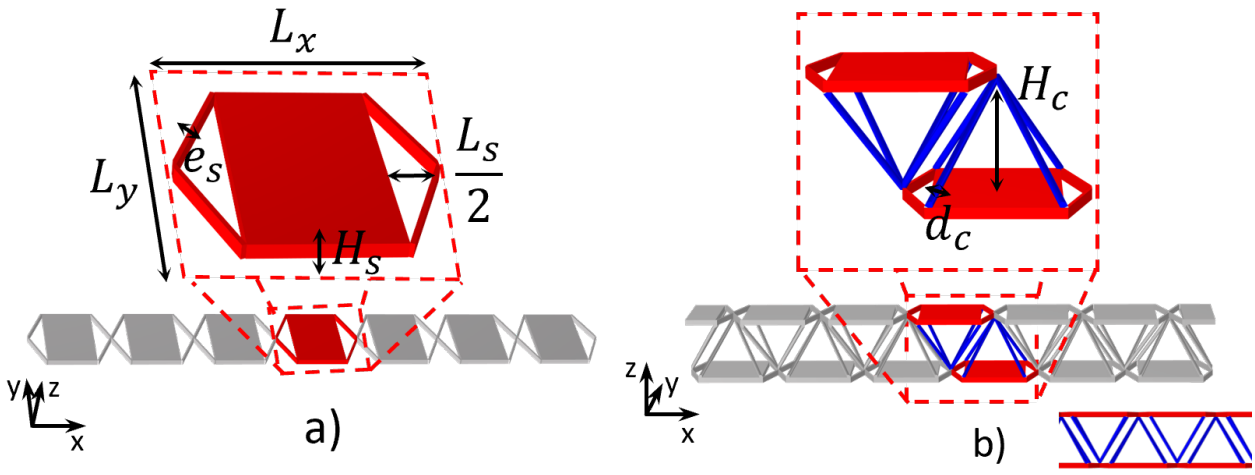

Figure 3.1: (a) Unit cell of the X-Beam Plate (XBP). (b) Unit cell of the X-Beam Sandwich (XBS), consisting of two XBP layers (red) connected by a lattice core (blue).

superposition method for completely free-edge plates [205–207]. Plate–beam junctions are enforced through continuity and equilibrium conditions, extending coupling ideas previously formulated for plate–spring connections [208]. Bloch–Floquet periodic boundary conditions are applied at the unit-cell boundaries [100, 198]. Together, these ingredients yield a unified engineering model to analyze and design periodic coupled plate–beam structures. In the present chapter, this tool is used to express the stiffness–filtering trade-off directly from dispersion relations and to identify configurations that best reconcile low-frequency absolute attenuation with mechanically meaningful bending stiffness. The chapter is organized as follows. Section 3.2 introduces the semi-analytical formulation and the coupled plate–beam assembly under Bloch–Floquet periodicity. Section 3.3 then leverages dispersion results to quantify the compromise between absolute band-gap performance and specific bending stiffness, and to identify a set of promising designs. Finally, the selected configuration is manufactured and experimentally validated in Section 3.4.

3.2 Semi-analytical model

The dispersion properties of the periodic structure are investigated using a semi-analytical spectral formulation that couples thin plate and beam elements. This approach enables an efficient computation of dispersion relations in periodic plate–beam assemblies. The complete derivation of the model is provided in section E of appendix.

3.2.1 Spectral model of a free-edge plate element

As shown in Fig. E.1, we consider a thin rectangular plate of dimensions $a \times b$ and thickness h, made of an isotropic material with Young's modulus E, density ρ, and Poisson's ratio ν. The formulation is divided into two independent contributions: (i) out-of-plane bending motion and (ii) in-plane motion. The objective is to derive a dynamic stiffness matrix relating generalized displacements and forces defined at the four free edges of the plate, enabling a posteriori application of boundary conditions

and coupling with other spectral elements.

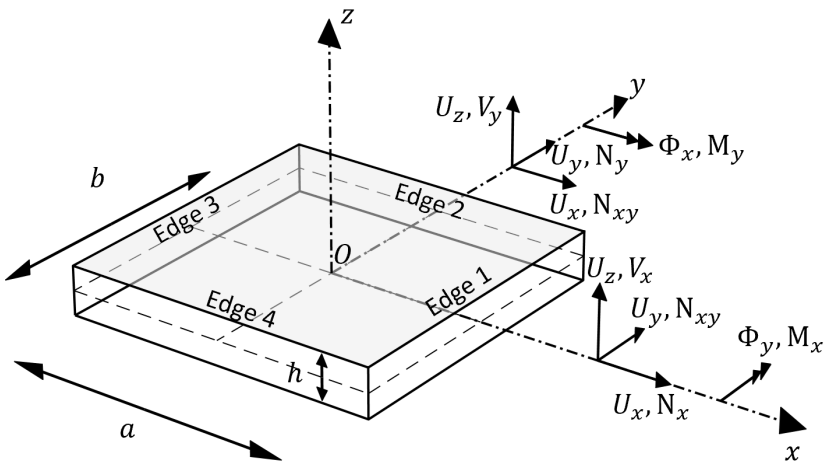

Figure 3.2: Coordinate system and notation for translations, rotations, forces, and moments of a thin plate.

Out-of-plane motion

Within the Kirchhoff–Love thin-plate approximation and assuming time-harmonic motion $u_z(x, y, t) = U_z(x, y)\mathrm{e}^{\mathrm{i}\omega t}$, the transverse displacement amplitude $U_z(x, y)$ satisfies the biharmonic equation

$$\frac{\partial^4 U_z}{\partial x^4} + 2\frac{\partial^4 U_z}{\partial x^2 \partial y^2} + \frac{\partial^4 U_z}{\partial y^4} - k^4 U_z = 0, \qquad k^4 = \frac{\rho h\, \omega^2}{D}, \qquad D = \frac{E h^3}{12(1-\nu^2)}. \tag{3.1}$$

Rotations, shear forces, and bending moments per unit length are defined as

$$\Phi_x = \frac{\partial U_z}{\partial y}, \qquad \Phi_y = -\frac{\partial U_z}{\partial x}, \tag{3.2}$$

$$\begin{aligned} V_x &= -D\left(\frac{\partial^3 U_z}{\partial x^3} + (2-\nu)\frac{\partial^3 U_z}{\partial x\, \partial y^2}\right), & V_y &= -D\left(\frac{\partial^3 U_z}{\partial y^3} + (2-\nu)\frac{\partial^3 U_z}{\partial x^2\, \partial y}\right), \\ M_x &= -D\left(\frac{\partial^2 U_z}{\partial x^2} + \nu\frac{\partial^2 U_z}{\partial y^2}\right), & M_y &= -D\left(\frac{\partial^2 U_z}{\partial y^2} + \nu\frac{\partial^2 U_z}{\partial x^2}\right). \end{aligned} \tag{3.3}$$

The free-edge plate problem is solved using the generalized superposition method [204–206]. In this framework, the transverse displacement is decomposed as

$$U_z(x, y) = U_{z_1}(x, y) + U_{z_2}(x, y), \tag{3.4}$$

where the two contributions enforce sliding and shear-free boundary conditions on complementary pairs of opposite edges. Their superposition therefore ensures that all free boundary conditions are simultaneously satisfied on the four edges of the plate.

The two auxiliary displacement fields are expressed using Lévy-type expansions consistent with

the boundary conditions imposed on each auxiliary subproblem.

$$
\begin{aligned}
U_{z_1}(x,y) &= \sum_{m=0}^{M_t} X_m(x)\,\cos\!\Big(\frac{m\pi y}{b}+\frac{m\pi}{2}\Big),\\
U_{z_2}(x,y) &= \sum_{m=0}^{M_t} Y_m(y)\,\cos\!\Big(\frac{m\pi x}{a}+\frac{m\pi}{2}\Big).
\end{aligned}
\tag{3.5}
$$

Substitution of each auxiliary expansion into (E.2) and exploitation of the orthogonality of the associated Lévy functions lead to two independent families of uncoupled fourth-order ordinary differential equations. Their solutions are linear combinations of exponential functions governed by the roots of the governing differential equation. For the amplitudes $X_m(x)$, these read

$$
\beta_{1m} = \sqrt{k^2 + \Big(\frac{m\pi}{b}\Big)^2}, \qquad \gamma_{1m} = \sqrt{\Big(\frac{m\pi}{b}\Big)^2 - k^2},
\tag{3.6}
$$

while the amplitudes $Y_m(y)$ involve

$$
\beta_{2m} = \sqrt{k^2 + \Big(\frac{m\pi}{a}\Big)^2}, \qquad \gamma_{2m} = \sqrt{\Big(\frac{m\pi}{a}\Big)^2 - k^2},
\tag{3.7}
$$

with

$$
k^4 = \frac{\rho h\,\omega^2}{D}.
\tag{3.8}
$$

Dynamic stiffness formulation

The dynamic stiffness formulation is constructed from the out-of-plane displacement and force fields evaluated along the four free edges of the plate, located at $x = \pm a/2$ and $y = \pm b/2$. Each edge carries the transverse displacement U_z and the rotation normal to the edge, together with the conjugate shear force and bending moment.

Along each plate edge, these fields depend on a single curvilinear coordinate s. On the vertical edges ($x = \pm a/2$), $s = y$ and the kinematic variables are $U_z(s) = U_z(\pm a/2, s)$ and $\Phi_y(s) = \Phi_y(\pm a/2, s)$, while on the horizontal edges ($y = \pm b/2$), $s = x$ and the variables are $U_z(s) = U_z(s, \pm b/2)$ and $\Phi_x(s) = \Phi_x(s, \pm b/2)$. The associated shear forces and bending moments are defined accordingly. Collecting this quantities leads to the edge-wise displacement and force vectors

$$
\begin{aligned}
\mathbf{q}^{\text{out}}(s) &= \begin{bmatrix} U_z^1(s) & \Phi_y^1(s) & U_z^2(s) & \Phi_x^2(s) & U_z^3(s) & \Phi_y^3(s) & U_z^4(s) & \Phi_x^4(s) \end{bmatrix}^{\mathsf{T}},\\
\mathbf{Q}^{\text{out}}(s) &= \begin{bmatrix} V_x^1(s) & M_x^1(s) & V_y^2(s) & M_y^2(s) & V_x^3(s) & M_x^3(s) & V_y^4(s) & M_y^4(s) \end{bmatrix}^{\mathsf{T}}.
\end{aligned}
\tag{3.9}
$$

For a Lévy truncation order $m = 0, \ldots, M_t$, the wave coefficients are assembled in the vector $\mathbf{C}^{\text{out}} \in \mathbb{C}^{8(M_t+1)}$. The associated continuous edge displacement and force fields read

$$
\mathbf{q}^{\text{out}}(s) = \mathbf{D}^{\text{out}}(s)\,\mathbf{C}^{\text{out}}, \qquad \mathbf{Q}^{\text{out}}(s) = \mathbf{F}^{\text{out}}(s)\,\mathbf{C}^{\text{out}},
\tag{3.10}
$$

with $\mathbf{D}^{\text{out}}(s) \in \mathbb{C}^{8\times 8(M_t+1)}$ and $\mathbf{F}^{\text{out}}(s) \in \mathbb{C}^{8\times 8(M_t+1)}$.

To eliminate the spatial dependence s along the edges, the continuous edge fields $\mathbf{q}^{\text{out}}(s)$ and $\mathbf{Q}^{\text{out}}(s)$ are projected onto orthogonal trigonometric bases using the Kevorkian–Pascal projection [209],

$$\hat{\mathbf{q}}_n^{\text{out}} = \frac{2}{L}\int_{\text{edge}} \mathbf{H}_n(s)\,\mathbf{q}^{\text{out}}(s)\,\mathrm{d}s, \qquad \hat{\mathbf{Q}}_n^{\text{out}} = \frac{2}{L}\int_{\text{edge}} \mathbf{H}_n(s)\,\mathbf{Q}^{\text{out}}(s)\,\mathrm{d}s, \tag{3.11}$$

where L is the edge length and $\mathbf{H}_n(s)$ denotes cosine basis functions consistent with the parity of the Lévy expansions. In order to obtain a square dynamic stiffness matrix, the projection index is chosen as $n = 0, \ldots, M_t$, consistently with the Lévy truncation order. Combining the projected displacement and force relations yields the out-of-plane dynamic stiffness relation

$$\hat{\mathbf{Q}}^{\text{out}} = \mathbf{K}^{\text{out}}\hat{\mathbf{q}}^{\text{out}}, \qquad \mathbf{K}^{\text{out}} \in \mathbb{C}^{8(M_t+1)\times 8(M_t+1)}. \tag{3.12}$$

In-plane motion

The in-plane dynamics of the plate are governed by the displacements (u_x, u_y), which are coupled through Poisson effects ν. Under the same harmonic assumption $u_{x,y}(x, y, t) = U_{x,y}(x, y)\, e^{\mathrm{i}\omega t}$, the governing equations can be written as a system of two coupled second-order partial differential equations

$$\begin{cases} \dfrac{\partial^2 U_x}{\partial x^2} + a_1\dfrac{\partial^2 U_x}{\partial y^2} + a_2\dfrac{\partial^2 U_y}{\partial x\partial y} + \dfrac{\rho h}{B}\,\omega^2 U_x = 0, \\ \dfrac{\partial^2 U_y}{\partial y^2} + a_1\dfrac{\partial^2 U_y}{\partial x^2} + a_2\dfrac{\partial^2 U_x}{\partial x\partial y} + \dfrac{\rho h}{B}\,\omega^2 U_y = 0, \end{cases} \tag{3.13}$$

with $B = Eh/(1-\nu^2)$, $a_1 = (1-\nu)/2$, and $a_2 = (1+\nu)/2$.

As in the out-of-plane case, the free-edge problem is solved using a generalized superposition strategy. The in-plane displacement field is decomposed into two auxiliary contributions associated with separated-variable expansions along x and y,

$$U_x = U_{x_1} + U_{x_2}, \qquad U_y = U_{y_1} + U_{y_2}, \tag{3.14}$$

each satisfying the governing equations and enforcing sliding boundary conditions on one pair of opposite edges.

Lévy-type trigonometric expansions are introduced in the transverse direction. For each truncation index $m \geq 1$, substitution into the in-plane governing equations leads to a coupled system which can be reduced to a single fourth-order ordinary differential equation. The special case $m = 0$ is treated separately. In this case, the coupling terms vanish and the problem reduces to two uncoupled second-order equations describing pure in-plane longitudinal motion, yielding only two exponential solutions.

The associated in-plane stress resultants are defined as

$$N_x = B\left(\frac{\partial U_x}{\partial x} + \nu\frac{\partial U_y}{\partial y}\right), \quad N_y = B\left(\nu\frac{\partial U_x}{\partial x} + \frac{\partial U_y}{\partial y}\right), \quad N_{xy} = Ba_1\left(\frac{\partial U_x}{\partial y} + \frac{\partial U_y}{\partial x}\right). \tag{3.15}$$

The continuous in-plane displacement and force fields are evaluated along the four plate edges and grouped into the edge-wise vectors $\mathbf{q}^{\text{in}}(s)$ and $\mathbf{Q}^{\text{in}}(s)$. These fields are parameterized by a finite set of internal modal coefficients collected in $\mathbf{C}^{\text{in}}$, whose dimension depends on the Lévy truncation order M_i. Projection onto orthogonal trigonometric bases using the Kevorkian–Pascal procedure removes the explicit spatial dependence along the edges.

After projection, the generalized in-plane displacement and force vectors $\hat{\mathbf{q}}^{\text{in}}$ and $\hat{\mathbf{Q}}^{\text{in}}$ contain $8M_i + 4$ projected edge variables. The additional four variables correspond to the $m = 0$ contribution, while each higher-order Lévy term $m \geq 1$ contributes eight in-plane edge variables. The projected relations are finally combined to define the in-plane dynamic stiffness relation

$$\hat{\mathbf{Q}}^{\text{in}} = \mathbf{K}^{\text{in}} \hat{\mathbf{q}}^{\text{in}}, \qquad \mathbf{K}^{\text{in}} \in \mathbb{C}^{(8M_i+4)\times(8M_i+4)}. \tag{3.16}$$

Assembly of the plate dynamic stiffness.

The complete dynamic stiffness of the plate element is obtained by assembling the out-of-plane and in-plane contributions derived above. Owing to the Kirchhoff–Love thin plate assumption and the membrane formulation adopted, bending and in-plane motions are decoupled at the plate level. The generalized displacement and force vectors are therefore partitioned into out-of-plane and in-plane components, and the plate dynamic stiffness matrix takes the block-diagonal form

$$\mathbf{K}^{\text{P}} = \begin{bmatrix} \mathbf{K}^{\text{out}} & \mathbf{0} \\ \mathbf{0} & \mathbf{K}^{\text{in}} \end{bmatrix}, \tag{3.17}$$

3.2.2 Plate–beam coupling formulation

The plate–beam coupling methodology builds upon a dynamic formulation inspired by the work of Li et al. [208], which addresses plate–spring coupling. In this study, the coupling is implemented in the context of the X-beam plate (XBP) configuration, depicted in Fig. F.1a). The structure is shown in an exploded view to facilitate the identification of plate edges and corner connection nodes, as well as the associated force and moment components exchanged between beam node 1 and plate edges 1 and 2. While a complete and detailed implementation for the XBP configuration is provided in the section F of the appendix. the present section outlines the general principles underlying the coupling strategy.

From the previous sections, the plate element is described in the frequency domain by the dynamic stiffness relation

$$\hat{\mathbf{Q}}^{P} = \mathbf{K}^{P}\, \hat{\mathbf{q}}^{P}. \tag{3.18}$$

For the purpose of coupling with beam elements, the generalized plate variables are further partitioned edge-wise as

$$\hat{\mathbf{q}}^{P} = \begin{bmatrix} \hat{\mathbf{q}}_1^{P} & \hat{\mathbf{q}}_2^{P} & \hat{\mathbf{q}}_3^{P} & \hat{\mathbf{q}}_4^{P} \end{bmatrix}^{T}, \qquad \hat{\mathbf{Q}}^{P} = \begin{bmatrix} \hat{\mathbf{Q}}_1^{P} & \hat{\mathbf{Q}}_2^{P} & \hat{\mathbf{Q}}_3^{P} & \hat{\mathbf{Q}}_4^{P} \end{bmatrix}^{T}. \tag{3.19}$$

Each block $\hat{\mathbf{q}}_j^{P}$ and $\hat{\mathbf{Q}}_j^{P}$ corresponds to plate edge j and contains both in-plane and out-of-plane

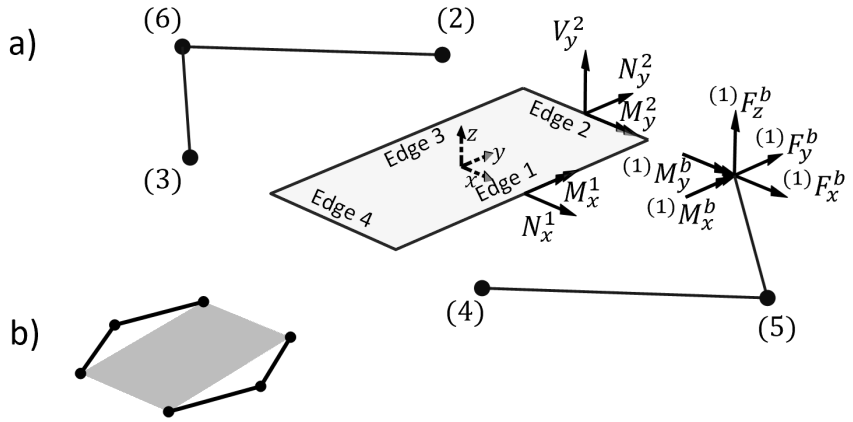

Figure 3.3: (a) Coordinate system and notation of displacements and forces involved in the coupling between plate edges and beam nodes. (b) Diagram of the complete plate–beam assembly.

generalized variables. Its size is $L_e^P = (2M_i + 1) + 2(M_t + 1)$, where the first term arises from the in-plane formulation and the second from the transverse bending formulation. The generalized displacement and force vectors associated with each edge are given by

$$\begin{aligned}
\hat{\mathbf{q}}_1^P &= \begin{bmatrix} \mathbf{U}_x^1 & \mathbf{U}_y^1 & \mathbf{U}_z^1 & \mathbf{\Phi}_y^1 \end{bmatrix}^T, \quad \hat{\mathbf{Q}}_1^P = \begin{bmatrix} \mathbf{N}_x^1 & \mathbf{N}_{xy}^1 & \mathbf{V}_x^1 & \mathbf{M}_x^1 \end{bmatrix}^T, \\
\hat{\mathbf{q}}_2^P &= \begin{bmatrix} \mathbf{U}_x^2 & \mathbf{U}_y^2 & \mathbf{U}_z^2 & \mathbf{\Phi}_x^2 \end{bmatrix}^T, \quad \hat{\mathbf{Q}}_2^P = \begin{bmatrix} \mathbf{N}_{xy}^2 & \mathbf{N}_y^2 & \mathbf{V}_y^2 & \mathbf{M}_y^2 \end{bmatrix}^T, \\
\hat{\mathbf{q}}_3^P &= \begin{bmatrix} \mathbf{U}_x^3 & \mathbf{U}_y^3 & \mathbf{U}_z^3 & \mathbf{\Phi}_y^3 \end{bmatrix}^T, \quad \hat{\mathbf{Q}}_3^P = \begin{bmatrix} \mathbf{N}_x^3 & \mathbf{N}_{xy}^3 & \mathbf{V}_x^3 & \mathbf{M}_x^3 \end{bmatrix}^T, \\
\hat{\mathbf{q}}_4^P &= \begin{bmatrix} \mathbf{U}_x^4 & \mathbf{U}_y^4 & \mathbf{U}_z^4 & \mathbf{\Phi}_x^4 \end{bmatrix}^T, \quad \hat{\mathbf{Q}}_4^P = \begin{bmatrix} \mathbf{N}_{xy}^4 & \mathbf{N}_y^4 & \mathbf{V}_y^4 & \mathbf{M}_y^4 \end{bmatrix}^T.
\end{aligned} \tag{3.20}$$

Beam model and partition of degrees of freedom

The beam substructure is modeled using the spectral element formulation introduced in a previous studies [194]. Each beam is reduced to its end nodes and described in the frequency domain by exact wave solutions of the rod and Timoshenko beam equations. The resulting dynamic stiffness matrix $\mathbf{K}^b$ relates nodal displacements and rotations $\mathbf{d}^b$ to the corresponding forces and moments $\mathbf{F}^b$.

To distinguish beam nodes directly connected to the plate from the remaining beam nodes, the beam degrees of freedom are partitioned as

$$\mathbf{d}^b = \begin{bmatrix} \mathbf{d}_c^b \\ \mathbf{d}_f^b \end{bmatrix}, \qquad \mathbf{F}^b = \begin{bmatrix} \mathbf{F}_c^b \\ \mathbf{F}_f^b \end{bmatrix}, \qquad \mathbf{K}^b = \begin{bmatrix} \mathbf{K}_{cc}^b & \mathbf{K}_{cf}^b \\ \mathbf{K}_{fc}^b & \mathbf{K}_{ff}^b \end{bmatrix}. \tag{3.21}$$

The subscript c refers to the four beam nodes connected to the plate corners, while the subscript f refers to the two remaining beam nodes. At each coupling node, five beam degrees of freedom are retained (three translations and rotations about the x and y axes), while the rotation about the z axis is

neglected in the coupling formulation. This leads to

$$ {}^{(j)}\mathbf{d}_c^b = \left[{}^{(j)}U_x^b,\ {}^{(j)}U_y^b,\ {}^{(j)}U_z^b,\ {}^{(j)}\Theta_x^b,\ {}^{(j)}\Theta_y^b \right]^T, \tag{3.22} $$

$$ {}^{(j)}\mathbf{F}_c^b = \left[{}^{(j)}F_x^b,\ {}^{(j)}F_y^b,\ {}^{(j)}F_z^b,\ {}^{(j)}M_x^b,\ {}^{(j)}M_y^b \right]^T, \tag{3.23} $$

with $j \in \{1, 2, 3, 4\}$. For the free beam nodes ($j \in \{5, 6\}$), all six degrees of freedom are retained.

Kinematic continuity at plate–beam junctions

Kinematic continuity at the plate corners imposes equality between the beam nodal displacements and rotations and the plate kinematic fields evaluated at the same locations. These constraints relate the beam degrees of freedom $\mathbf{d}_c^b$ to the generalized plate edge variables $\hat{\mathbf{q}}^P$ and can be written in compact matrix form as

$$ \mathbf{d}_c^b = \mathbf{T}_d\, \hat{\mathbf{q}}^P. \tag{3.24} $$

The transfer matrix $\mathbf{T}_d \in \mathbb{C}^{20\times 4L_e^P}$ results from the evaluation of the in-plane and out-of-plane plate kinematic fields at the coordinates (x_c, y_c) of each beam–plate connection node, using the trigonometric bases introduced in the previous edge motion formulations.

Projection of beam forces

Beam nodal forces and moments are applied at the plate corners as discrete point loads. Their coupling with the plate formulation relies on the Kevorkian–Pascal projection, here applied to concentrated efforts rather than to continuous edge fields. At a given corner, this projection is performed independently on the two incident plate edges, yielding $2L_e^P$ generalized force coefficients. By assembling the contributions of the four plate corners, the projected beam forces are collected into a global generalized force vector,

$$ \hat{\mathbf{Q}}^b = \mathbf{T}_F\, \mathbf{F}_c^b. \tag{3.25} $$

The projection matrix $\mathbf{T}_F \in \mathbb{C}^{8L_e^P\times 20}$ gathers the evaluations of the plate trigonometric bases at all corner locations, consistently mapping discrete beam efforts onto the generalized force space of the plate edges.

Equilibrium

The equilibrium of generalized forces at the plate edges is enforced by requiring that the sum of the internal plate forces and the projected beam forces vanishes,

$$ \hat{\mathbf{Q}}^P + \mathbf{T}_e\, \hat{\mathbf{Q}}^b = \mathbf{0}, \tag{3.26} $$

where $\mathbf{T}_e \in \mathbb{C}^{4L_e^P\times 8L_e^P}$ is a Boolean assembly matrix that distributes the projected beam contributions to the corresponding plate edges. Combining plate dynamics, beam dynamics, kinematic continuity,

and force equilibrium yields the global system

$$\underbrace{\left(\underbrace{\begin{bmatrix} \mathbf{K}^P & \mathbf{0} \\ \mathbf{0} & \mathbf{0} \end{bmatrix}}_{\text{augmented plate matrix}} + \underbrace{\begin{bmatrix} \mathbf{T}_e & \mathbf{0} \\ \mathbf{0} & \mathbf{I} \end{bmatrix} \begin{bmatrix} \mathbf{T}_F & \mathbf{0} \\ \mathbf{0} & \mathbf{I} \end{bmatrix} \begin{bmatrix} \mathbf{K}^b_{ff} & \mathbf{K}^b_{fc} \\ \mathbf{K}^b_{cf} & \mathbf{K}^b_{cc} \end{bmatrix} \begin{bmatrix} \mathbf{T}_d & \mathbf{0} \\ \mathbf{0} & \mathbf{I} \end{bmatrix}}_{\text{contribution of the beams}} \right)}_{\mathbf{K}^{Pb}} \begin{bmatrix} \hat{\mathbf{q}}^P \\ \mathbf{d}^b_f \end{bmatrix} = \mathbf{0}. \tag{3.27}$$

The matrix $\mathbf{K}^{Pb} \in \mathbb{C}^{(4L_e^P+12)\times(4L_e^P+12)}$ denotes the global dynamic stiffness matrix of the plate–beam assembly.

3.2.3 Extension to XBS structure

The plate–beam coupling formulation introduced above is extended to the X-Beam Sandwich (XBS) architecture shown in Fig. 3.1(b).

From a modelling standpoint, the XBS structure is described by two plate–beam subsystems. Each subsystem consists of an X-Beam Plate (XBP) to which four beams are connected at the plate corners and joined at a common node, thereby forming a pyramidal configuration. These beams are coupled to the plate using the plate–beam formulation presented in the previous section, leading to two dynamic stiffness matrices, denoted $\mathbf{K}^{(1)}$ and $\mathbf{K}^{(2)}$. The two subsystems differ only in the orientation of the pyramid, which is directed along the $-z$ axis for the upper skin and along the $+z$ axis for the lower skin.

The resulting global dynamic stiffness matrix of the XBS unit-cell ($\mathbf{K}^{1+2}$) is obtained by assembling the two subsystems through classical beam–beam nodal connections between the apex of the pyramidal beams of one subsystem and the central node of the X-shaped beam structure of the opposite subsystem.

3.2.4 Periodic condition

The unit cell is governed by the assembled plate–beam system

$$\mathbf{K}^{Pb} \begin{bmatrix} \hat{\mathbf{q}}^P \\ \mathbf{d}^b_f \end{bmatrix} = \mathbf{0}, \tag{3.28}$$

where $\hat{\mathbf{q}}^P$ collects the projected degrees of freedom of the four plate edges, and $\mathbf{d}^b_f$ denotes the beam nodal degrees of freedom that are not connected to any plate.

In the present formulation, the periodic condition is applied exclusively to these free beam nodes. For both the XBP and XBS configurations, they correspond to the junction nodes of the X-shaped beams. Specifically, two such nodes are involved in the XBP unit cell, whereas four nodes are concerned in the XBS case, corresponding pairwise to the upper and lower skins.

The unknowns are partitioned into internal and left and right boundary degrees of freedom, with

$\mathbf{u}_i = \hat{\mathbf{q}}^P$, $\mathbf{u}_\ell = \mathbf{d}^b_{f,\ell}$ and $\mathbf{u}_r = \mathbf{d}^b_{f,r}$, leading to the block decomposition

$$\mathbf{K}^{Pb} = \begin{bmatrix} \mathbf{D}^{(0)}_{\ell\ell} & \mathbf{D}^{(0)}_{\ell i} & \mathbf{D}^{(0)}_{\ell r} \\ \mathbf{D}^{(0)}_{i\ell} & \mathbf{D}^{(0)}_{ii} & \mathbf{D}^{(0)}_{ir} \\ \mathbf{D}^{(0)}_{r\ell} & \mathbf{D}^{(0)}_{ri} & \mathbf{D}^{(0)}_{rr} \end{bmatrix}. \tag{3.29}$$

Condensation of the internal degrees of freedom $\mathbf{u}_i$ yields the reduced boundary system

$$\begin{bmatrix} \mathbf{D}_{\ell\ell} & \mathbf{D}_{\ell r} \\ \mathbf{D}_{r\ell} & \mathbf{D}_{rr} \end{bmatrix} \begin{bmatrix} \mathbf{u}_\ell \\ \mathbf{u}_r \end{bmatrix} = \begin{bmatrix} \mathbf{F}_\ell \\ \mathbf{F}_r \end{bmatrix}, \tag{3.30}$$

Floquet–Bloch periodicity is introduced through the Floquet multiplier $\lambda = e^{\mathrm{i}kL_x}$, where k denotes the Floquet wavenumber and L_x is the periodicity length along the x direction, corresponding to the size of the unit cell. Continuity of displacements and forces between adjacent unit cells is therefore expressed as

$$\mathbf{u}_r = \lambda\, \mathbf{u}_\ell, \qquad \mathbf{F}_r = -\lambda\, \mathbf{F}_\ell. \tag{3.31}$$

Applying (3.31) to the condensed system (3.30) leads to the displacement-based formulation

$$\lambda \begin{bmatrix} \mathbf{I} & \mathbf{0} \\ -\mathbf{D}_{\ell\ell} & -\mathbf{D}_{\ell r} \end{bmatrix} \begin{bmatrix} \mathbf{u}_\ell \\ \mathbf{u}_r \end{bmatrix} = \begin{bmatrix} \mathbf{0} & \mathbf{I} \\ \mathbf{D}_{r\ell} & \mathbf{D}_{rr} \end{bmatrix} \begin{bmatrix} \mathbf{u}_\ell \\ \mathbf{u}_r \end{bmatrix}. \tag{3.32}$$

Introducing $\mathbf{L} = \begin{bmatrix} \mathbf{I} & \mathbf{0} \\ -\mathbf{D}_{\ell\ell} & -\mathbf{D}_{\ell r} \end{bmatrix}$, $\mathbf{N} = \begin{bmatrix} \mathbf{0} & \mathbf{I} \\ \mathbf{D}_{r\ell} & \mathbf{D}_{rr} \end{bmatrix}$, $\mathbf{w} = \begin{bmatrix} \mathbf{u}_\ell \\ \mathbf{u}_r \end{bmatrix}$, the dispersion problem finally reads

$$\lambda\, \mathbf{L}\, \mathbf{w} = \mathbf{N}\, \mathbf{w}. \tag{3.33}$$

For a fixed angular frequency ω, (3.33) constitutes a generalized eigenvalue problem in λ, whose solutions are obtained using a standard eigensolver (e.g. `eig`$(\mathbf{L}, \mathbf{N})$ in MATLAB).

3.2.5 Numerical validation

This section assesses the accuracy of the proposed semi-analytical formulation by comparison with a three-dimensional Finite Element Method (FEM) reference computed using COMSOL MULTIPHYSICS.

The material and geometric parameters used in both simulations are $E = 4$ GPa, $\rho = 1100\ \mathrm{kg\,m^{-3}}$, $\nu = 0.3$, $L_s = 20$ mm, $e_s = 0.5$ mm, $H_s = 3$ mm, and $L_x = 50$ mm.

For meshing efficiency, Floquet–Bloch periodicity is imposed in the 3D FEM model directly on the plate cross-section (Fig. 3.4a). Using the same periodicity length L_x makes this configuration equivalent to the semi-analytical model, in which periodicity is applied at the junctions of the cross-shaped beams.

The dispersion curves obtained from the 3D FEM model are shown in Fig. 3.4c (Black lines), with the corresponding results predicted by the present semi-analytical formulation (Blue dots).

The comparison between FEM and SEM model shows that, over the frequency range of interest,

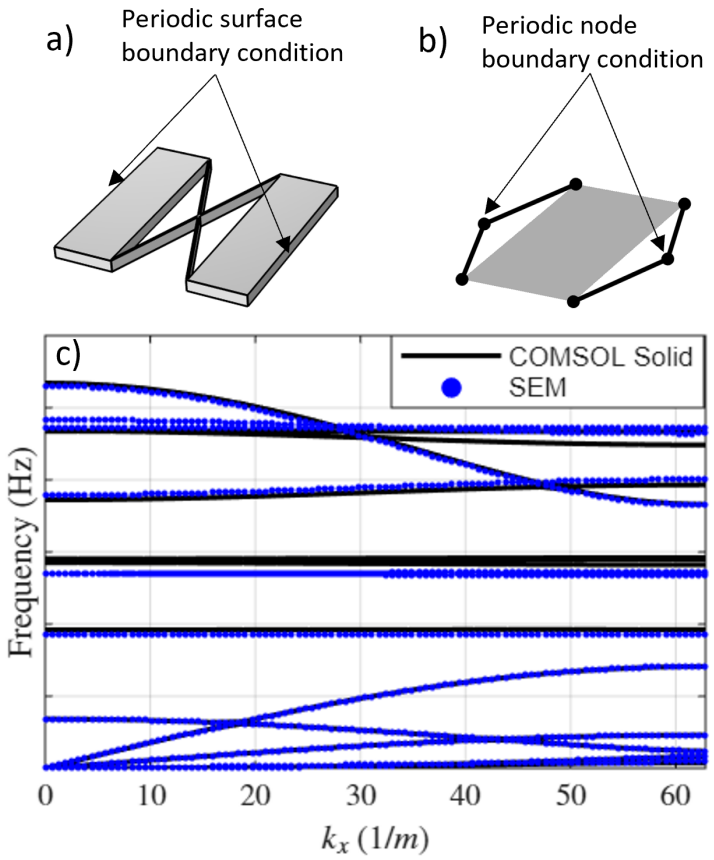

Figure 3.4: (a) Three-dimensional FEM unit cell with Floquet–Bloch periodicity imposed on the plate cross-section. (b) Equivalent unit cell reduced to plate and beam elements in the semi-analytical model. (c) Dispersion curves computed using the 3D FEM model in COMSOL (Black lines) and predicted by the proposed semi-analytical formulation (Blue dots).

the semi-analytical model captures the main trends of the wave propagation behaviour observed in the full 3D FEM reference. The remaining discrepancies can be attributed to the modelling assumptions adopted in the reduced formulation: (i) the rotation Φ_z is neglected at plate–beam junctions, and (ii) plate and beam elements are reduced along their neutral plane or axis by assuming a uniform deformation field over the cross-section. As the frequency increases, the modal deformation patterns become more complex, which naturally amplifies the deviations between the reduced and full-order models.

3.2.6 Classification of modes

The classification of the dispersion branches follows an approach similar to that introduced in Article 1 and is based on the symmetry properties of the structures considered. As shown in Fig. 3.1, both the X-Beam Plate (XBP) and the X-Beam Sandwich (XBS) unit cells exhibit symmetry with respect to the xOz plane ($y = 0$). This symmetry is exploited by modelling only the half-domain $y \geq 0$ and imposing appropriate boundary conditions on the nodes and edges lying on $y = 0$. For the symmetric problem (Fig. 3.5b), rotations about the x and z axes and the translation along y are constrained, whereas for the antisymmetric problem (Fig. 3.5c), the rotation about the y axis and the translations

along x and z are constrained. The symmetric and antisymmetric mode families obtained from the two reduced problems (Figs. 3.5e and f) together reproduce the full dispersion relation (Fig. 3.5d).

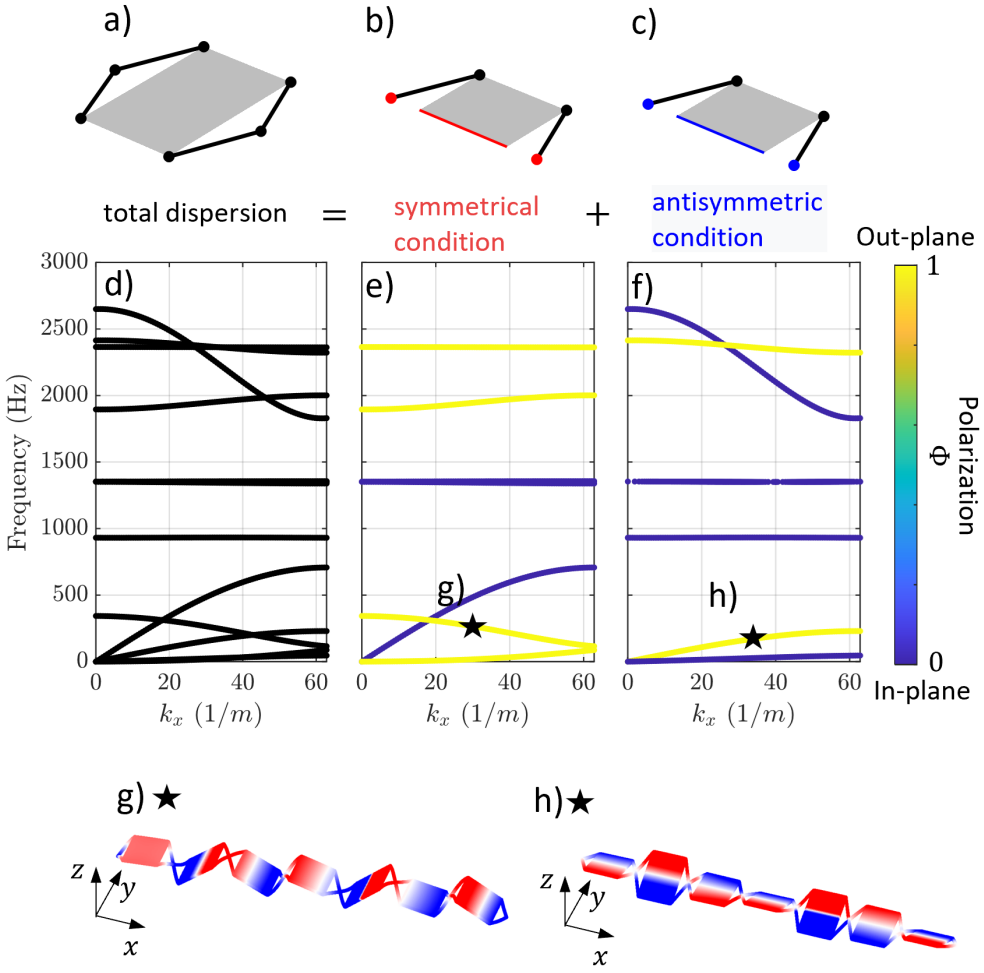

Figure 3.5: (a) Complete XBS unit cell. (b) Half XBS model with symmetric boundary conditions imposed on the $y = 0$ plane (red-highlighted elements). (c) Half XBS model with antisymmetric boundary conditions imposed on the $y = 0$ plane (blue-highlighted elements). (d) Dispersion relation computed on the complete unit cell. (e) Dispersion branches obtained from the symmetric half-model. (f) Dispersion branches obtained from the antisymmetric half-model. In (e) and (f), the color of each branch indicates the mode polarization, ranging from predominantly in-plane deformation (blue) to predominantly out-of-plane deformation (yellow). (g) shows the propagation of a symmetric out-of-plane–polarized mode and (h) shows an antisymmetric out-of-plane–polarized mode.

The polarization of each mode is characterized by a scalar coefficient Φ, which is obtained by post-processing the eigenvectors of the generalized eigenvalue problem. The discrete eigenvectors are first mapped back to the continuous deformation fields of the full structure using the plate and beam shape functions provided by the spectral formulation. The maximum absolute displacement amplitudes along the three spatial directions are then extracted, yielding the vector $\mathbf{S} = [S_x \; S_y \; S_z]$. The polarization coefficient is defined as

$$\Phi = \frac{\mathbf{S} \cdot [0\ 0\ 1]}{\|\mathbf{S}\|}, \tag{3.34}$$

so that $\Phi = 0$ corresponds to purely in-plane deformation (U_x, U_y), whereas $\Phi \to 1$ indicates predominantly out-of-plane deformation (U_z). This scalar quantity is represented using a colour scale ranging from blue (in-plane) to yellow (out-of-plane) in Figs. 3.5e and f.

This classification allows dispersion branches to be identified directly, thereby avoiding the manual, mode-by-mode inspection commonly encountered in the literature.

3.3 Trade-off analysis

The following analysis uses the proposed semi-analytical model together with the symmetry-based mode classification to investigate the trade-off between filtering performance and specific bending stiffness of the X-Beam Plate (XBP) and X-Beam Sandwich (XBS) structures. This analysis is carried out only from the dispersion diagram, without relying on any additional indicators.

For figure compactness, symmetric and antisymmetric dispersion branches are displayed together on the same plots. Among the symmetric modes, we identify longitudinal waves (black line in Fig. 3.6) and z-bending waves (green line), corresponding respectively to in-plane and out-of-plane motion relative to the horizontal XY-plane of the structure. For the antisymmetric modes, we distinguish y-bending waves (blue line in Fig. 3.6) and torsional waves (red line), also corresponding respectively to in-plane and out-of-plane motions. Along each dispersion branch, the motion associated with the corresponding Bloch wave may evolve from in-plane to out-of-plane without changing its symmetry class. This evolution is represented through colormaps transitioning from black to green and from blue to red, in accordance with the definitions above.

The analysis of the trade-off between static stiffness and dynamic filtering performance relies on two metrics. First, the specific stiffness in z-bending $\tilde{D}_z$ of the lattice beam sandwich structure is obtained by identifying the dispersion branch corresponding to flexural motion in the low-frequency regime, using Euler beam theory, which yields $\omega^2 = D_z k^4$ with $D_z = (EI)/(\rho A)$. The different geometric configurations studied hereafter are compared via a specific stiffness ratio defined as

$$C_{\mathrm{RIG}} = D_z / D_{\mathrm{ref}}, \tag{3.35}$$

where D_{ref} is the specific stiffness of a reference bulk beam shown in Fig. 3.6. Second, the filtering performance is quantified through the absolute band gap ratio defined as

$$C_{\mathrm{ABG}} = \frac{1}{\Omega_5} \sum_{j=1}^{N_{\mathrm{BG}}} \Delta\Omega_j, \tag{3.36}$$

where $\Delta\Omega_j$ is the width of the jth band gap within the range from 0 Hz to the frequency of the fifth dispersion branch, denoted Ω_5. The choice to restrict the analysis to the first five branches is motivated by: (i) the possibility of including multiple band gaps within the analysis window (typically, three are observed); and (ii) the focus on low-frequency performance, by defining the maximum frequency relatively to the number of propagating modes, which depends on the structure's geometry, and thus on its stiffness and mass properties, which vary significantly across the parametric variations considered

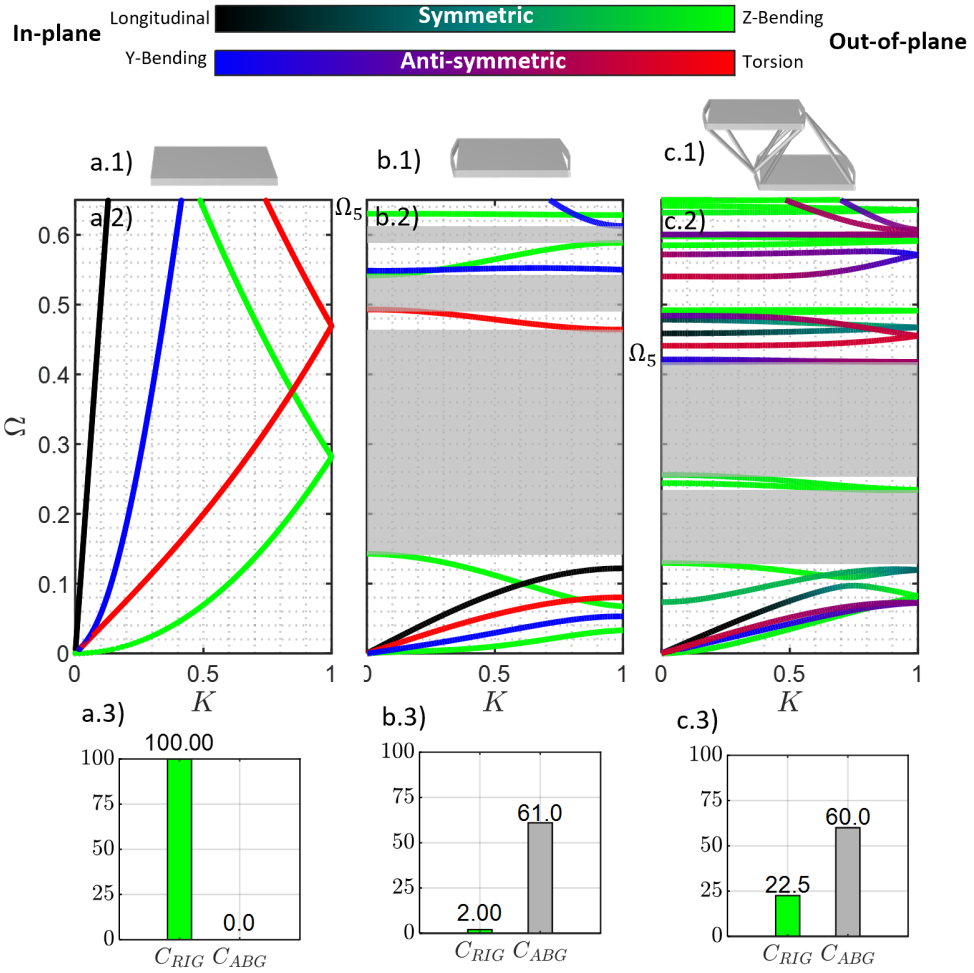

Figure 3.6: (a), (b), and (c) show dispersion diagrams computed using the semi-analytical plate+beam model for three unit cells: (a) homogeneous plate, (b) X-beam Plate (XBP), and (c) X-beam Sandwich (XBS). Dispersion branches are color-coded using two gradients to distinguish four wave polarizations: z-bending/compression (green → black) and y-bending/torsion (red → blue). The bar charts display, in green, the value of C_{RIG} (bending stiffness-to-mass ratio) and, in grey, the value of C_{ABG} (absolute band gap percentage below Ω_5) for each unit cell.

in the optimization presented below.

To assess the performance, we start from the least filtering and most rigid possible configuration, that is a solid homogeneous beam (Fig. 3.6). This non-filtering configuration is used as a reference with a specific z-bending stiffness $\tilde{D}_z = 2.2\ \mathrm{m}^4 \cdot \mathrm{s}^{-2}$. Its corresponding C_{RIG} and C_{ABG} values are 100% and 0%, respectively.

Introducing an X-like arrangement of beams at the unit plate's edge generates large absolute forbidden bands ($C_{\mathrm{ABG}} = 61\%$), but at the cost of a drastic reduction in structural rigidity ($C_{\mathrm{RIG}} = 2\%$). Mechanical performance can be improved by using this filter structure as the two skins of a sandwich structure with a beam lattice core. In this configuration, the specific stiffness increases significantly ($C_{\mathrm{RIG}} = 22.5\%$), while the filtering performance is essentially preserved, with the band gap ratio remaining of the same order ($C_{\mathrm{ABG}} = 60\%$).

To carry on our parametric study shown in figure 3.7, we set the thickness of all beams and plates

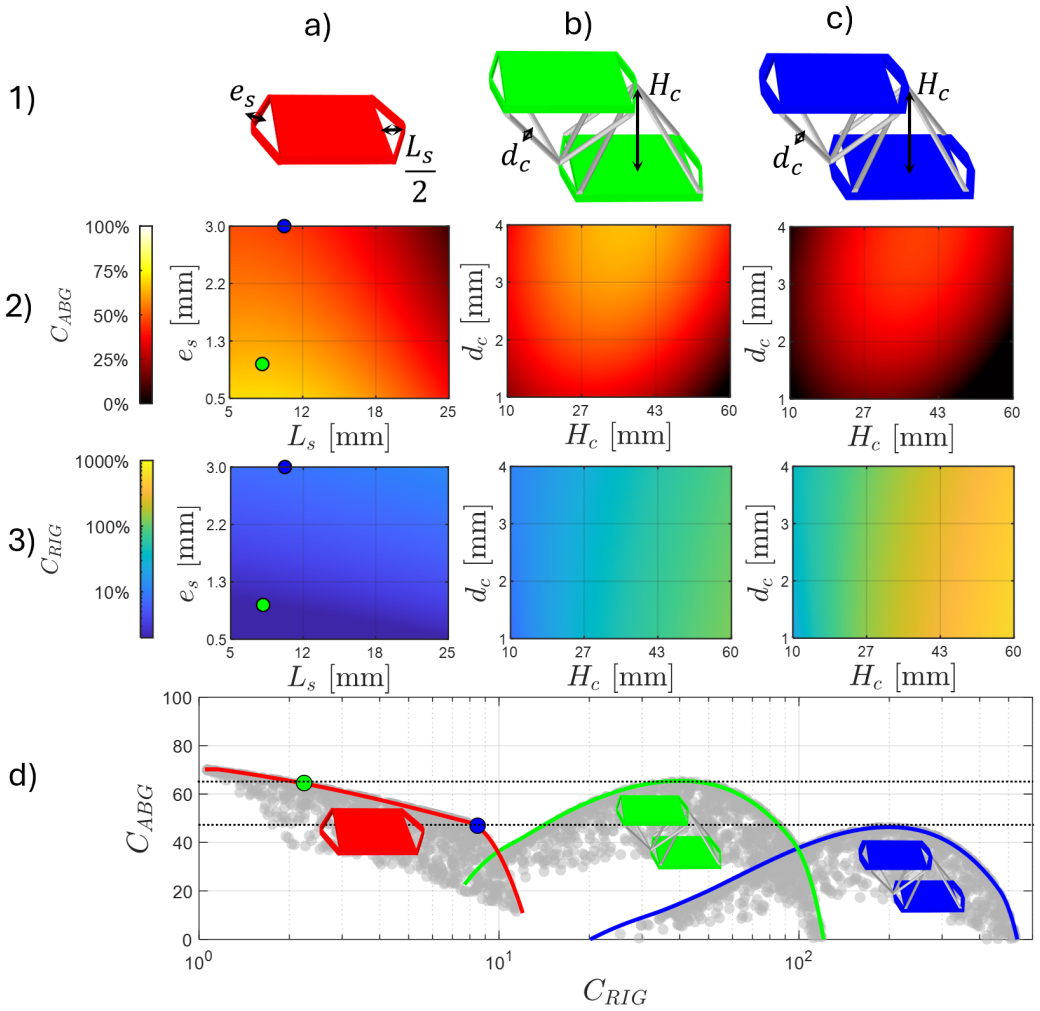

Figure 3.7: Column (a): (a.1) schematic of the X-Beam Plate (XBP); (a.2) absolute band gap ratio C_{ABG} and (a.3) specific flexural stiffness C_{RIG}, as functions of beam width e_s and span L_s. Columns (b) and (c): performance maps for X-Beam Sandwich (XBS) structures using skins corresponding to the two selected points in (a), showing variation of C_{ABG} and C_{RIG} with core diameter d_c and height H_c. (d): Pareto fronts comparing all configurations studied.

constitutive of the skins to $H_s = 3$ mm. Hence, the geometry of the XBP skin is defined by the beam width e_s and the span of the cross L_s. The lattice core consists of struts with circular cross-section, characterized by their diameter d_c and height H_c.

The first analysis focuses on the skin-only configuration (XBP), varying L_s and e_s jointly. Smaller values of both parameters produce wider band gaps C_{ABG}, reaching up to 70%. However, this occurs at the expense of mechanical performance: the specific bending stiffness C_{RIG} can drop as low as 1% that of the reference.

Each geometry tested yields a pair $(C_{\mathrm{ABG}}, C_{\mathrm{RIG}})$, and the corresponding Pareto front illustrates the trade-off between filtering and stiffness. In the low-stiffness regime, increasing C_{RIG} from 1% to 10% causes only a moderate reduction in C_{ABG} from 70% to 50%. Beyond this, further stiffness improvements lead to sharp losses in filtering performance.

To mitigate this limitation, a second study focuses on sandwich configurations (XBS). Two skins are selected: a filtering-oriented one and a stiffness-oriented one. For each skin, we assess the influence of d_c and H_c through a parametric sweep. This design strategy enables configurations that maintain large band-gap coverage while enhancing the specific stiffness by a factor of ~ 20 compared to that of the skin alone. For each case, the resulting $(C_{\mathrm{ABG}}, C_{\mathrm{RIG}})$ pairs trace out a distinct Pareto front, confirming the existence of optimal trade-offs.

3.4 Experimental validation

The demonstrator consists of five XBS unit cells connected in series and manufactured by polymer fused filament fabrication (FFF). The printed material exhibits a complex Young's modulus that was characterized in Ref. [194].

The structure is clamped at its base using a vise mounted on a unidirectional shaker controlled in acceleration. The input signal is a sine sweep of constant amplitude A_i, applied along a given direction $i \in \{x, y, z\}$. A PCB HT356B21 triaxial ICP accelerometer measures the three output components at the top of the structure. Its mass is 4.0 g, i.e., 2.37% of the measured specimen mass $m_{\mathrm{tot}} = 168.95$ g. This single sensor therefore provides the three simultaneous components while limiting the added mass; its residual loading is nevertheless retained among the experimental uncertainties. The total output acceleration is computed as $A_T = \sqrt{A_{Tx}^2 + A_{Ty}^2 + A_{Tz}^2}$. For each excitation direction, the frequency response function (FRF) is reported in decibels as $20 \log_{10}\left(\frac{A_T}{A_i}\right)$, so that values below 0 dB indicate effective attenuation.

Figure 3.8(d) reports the dispersion relation obtained with the semi-analytical model; the grey regions indicate the predicted absolute band gaps. Figures 3.8(a)–3.8(c) show the three experimental configurations (excitation along x, y, and z, respectively). The measured FRFs are plotted in black, together with the corresponding COMSOL predictions in blue.

In Ref. [194], it was shown that, in the present frequency range, the associated damping has a negligible influence on the width of Bragg band gaps. Therefore, to improve readability, damping is not included in the dispersion curves reported here. In finite structures, however, damping governs the amplitude levels, i.e., the height of amplification peaks and the depth of attenuation valleys. For this reason, it is included in the COMSOL simulations to recover the same order of magnitude of amplification as in the experiments.

The experimental FRFs exhibit attenuation bands reaching about 20 dB for the three excitation directions, confirming the filtering capability of the structure for different polarizations. While the width of the attenuation bands depends on the excitation direction (reflecting partial band gaps), two frequency intervals are common to all three configurations, namely 825–1450 Hz and 1550–1830 Hz. These ranges match the absolute band gaps predicted by the dispersion analysis and are highlighted in grey in Fig. 3.8. The comparison between experiments (black) and simulations (blue) shows a qualitative agreement: the attenuation regions are well reproduced, although noticeable frequency shifts remain. This mismatch is likely due to geometric uncertainties introduced by the 3D-printing process.

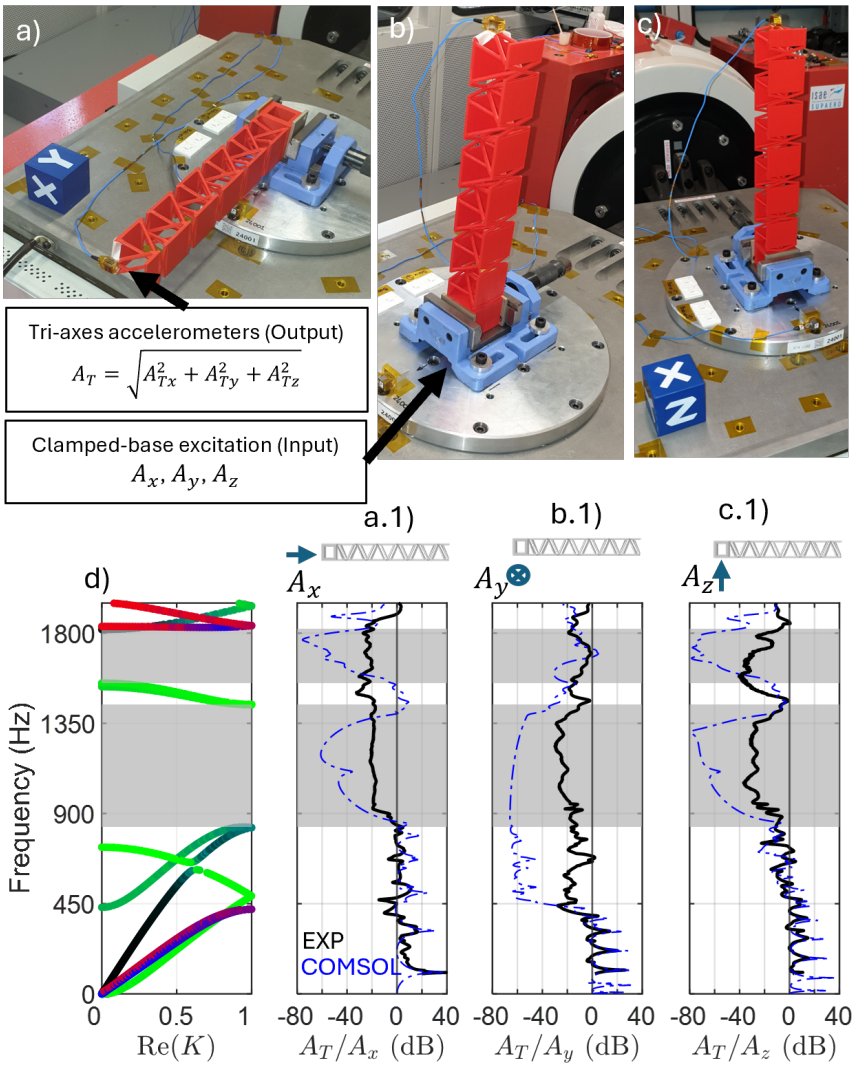

Figure 3.8: (a–c) Photographs of the experimental setup under x-, y-, and z-axis excitation, respectively. Subfigures (a.1), (b.1), and (c.1) show the corresponding measured FRFs (black) and COMSOL simulations (blue). (d) Dispersion relation predicted by the semi-analytical model; grey bands indicate the predicted absolute band gaps.

3.5 Conclusion

This chapter addressed the stiffness limitation inherent to Bragg-based absolute filters identified in the previous developments. We showed that embedding *two periodic filters as sandwich skins* provides an effective way to recover mechanical efficiency while preserving multi-polarization wave attenuation. In the proposed X-Beam Sandwich (XBS) concept, the X-Beam Plate (XBP) skins supply the stiffness contrasts and periodicity required to open *absolute* band gaps, whereas the architectured core restores bending efficiency and offers an additional geometric tuning lever. As a result, the XBS architecture achieves absolute filtering with a significantly improved *specific bending stiffness* compared with standalone lattice filters.

To support a dispersion-driven design methodology, we developed a semi-analytical model for periodic coupled plate–beam assemblies under Bloch–Floquet conditions. The formulation provides

fast access to dispersion relations and enables systematic exploration of the geometric design space. Relying on dispersion data only, the compromise between mechanical performance and filtering capability was quantified through two scalar metrics: the normalized specific bending stiffness ratio C_{RIG} and the absolute band-gap coverage ratio C_{ABG}. The resulting Pareto fronts make the stiffness–filtering trade-off explicit and identify configurations that best reconcile low-frequency absolute attenuation with mechanically meaningful bending stiffness.

Although the present study emphasized the flexural component of static stiffness, the proposed framework is not restricted to bending. By adapting the reference-mode identification and the associated dispersion-based indicators, the same approach can be extended to other stiffness components and wave polarizations, such as axial and torsional behaviours, thereby providing a generic basis for multi-objective design of periodic architectured structures.

Beyond the specific XBS results, this chapter also underlines a fundamental bound of Bragg-type filtering: the lowest attainable opening frequency of a Bragg band gap remains intrinsically linked to a wavelength-scale mechanism, and therefore to the unit-cell length. In practice, the corresponding wavelengths are tightly connected to the effective stiffness of the waveguide; consequently, pushing the attenuation band further down in frequency tends to require either a loss of stiffness (hence of specific stiffness) or an increase in characteristic length scales, which conflicts with compact, load-bearing industrial requirements. This motivates the shift performed in the next chapter towards *subwavelength* mechanisms. By relying on local resonances rather than on Bragg interferences, locally resonant architectures can open very-low-frequency stop bands while preserving the high specific stiffness demanded by the targeted industrial application.

CHAPTER 4

From Bragg lattices to locally resonant vibration filters

Contents

4.1 Introduction . . . 68
4.2 Undamped periodic resonator chain . . . 69
4.2.1 Unit-cell model and equations of motion . . . 69
4.2.2 Non-dimensional parameters . . . 70
4.2.3 Floquet–Bloch analysis and dispersion relation . . . 70
4.2.4 Mass–bandwidth trade-off . . . 72
4.3 Damped periodic resonator chain . . . 74
4.3.1 Damped unit cell and complex dispersion . . . 75
4.3.2 Attenuation band of a finite chain . . . 75
4.3.3 Influence of damping and number of cells . . . 77
4.3.4 Mass–attenuation trade-off . . . 77
4.4 Nonlinear resonator chains . . . 78
4.4.1 Nonlinear unit cell . . . 79
4.4.2 Nonlinear dispersion . . . 83
4.4.3 Attenuation performance . . . 85
4.5 Design guidelines . . . 87
4.6 Structural modeling of the resonant filter . . . 88
4.6.1 Waveguide definition . . . 89
4.6.2 Dispersion analysis . . . 89
4.6.3 Resonator design . . . 90
4.6.4 Mass–bandwidth trade-off . . . 92
4.6.5 Mass–attenuation trade-off . . . 93
4.7 Experimental validation of the resonant waveguide filter . . . 97

4.7.1 Prototype design and experimental setup 97
4.7.2 Linear regime 98
4.7.3 Nonlinear regime 99
4.8 Conclusion 102

4.1 Introduction

The previous chapter focused on periodic waveguides relying on Bragg scattering to inhibit wave propagation. In such systems, stop bands arise from destructive interference, and their onset frequency depends on the lattice parameter and the waveguide stiffness. While this mechanism is efficient at mid and high frequencies, it becomes less effective for low-frequency vibration isolation.

Indeed, shifting Bragg bandgaps towards lower frequencies requires either increasing the unit-cell size or significantly reducing the stiffness of the waveguide [57, 80]. Both strategies are detrimental in practical applications: the former limits compactness, while the latter leads to a severe reduction of the specific stiffness, thereby compromising the load-bearing function of the structure. As a result, Bragg-based lattice filters are poorly suited to applications where vibration attenuation is required at low frequencies without sacrificing static rigidity [133, 144, 190].

To overcome this limitation, the present chapter investigates the case of locally resonant systems. By embedding local resonators into an otherwise stiff waveguide, attenuation bands can be opened at frequencies dictated primarily by the internal resonance of the added subsystems, rather than by the periodicity of the host structure. This decoupling between filtering frequency and lattice parameter enables the design of subwavelength attenuation bands, while preserving the global stiffness and load-carrying capability of the waveguide [158, 169].

The objective of this chapter is to establish a clear and systematic design method for such resonant filters, starting from an idealised one-dimensional resonator chain and progressively increasing the level of physical realism. A simple lumped mass–spring model is first introduced to identify the fundamental mechanisms governing dispersion, bandgap formation, and the trade-off between added mass and attenuation bandwidth. Viscous dissipation is then incorporated to assess the robustness of the filtering performance for finite chains, and the analysis is further extended to account for weak geometric nonlinearities, which may become relevant at moderate vibration levels. It is important to note, that this lumped description implicitly assumes that wave propagation is governed by a single scalar degree of freedom. As such, it can only represent one propagation channel and one dispersion branch, which is sufficient to explain the physical origin of locally resonant bandgaps but not to describe the full wave dynamics of a real structure.

In practical waveguides, several wave polarisations coexist and may interact with the resonators in fundamentally different ways [159, 185]. Moreover, the attenuation of finite, dissipative structures is governed by the complex dispersion relation, and in particular by the imaginary part of the wavenumber, which cannot be uniquely inferred from a single-branch lumped model [183, 184]. These aspects motivate the introduction of a structural beam-lattice model in the second part of the chapter.

The validity and limitations of the simplified description are examined by comparing dispersion

properties, attenuation bands, and optimal trade-offs in both models. Finally, the proposed resonant filtering concept is validated experimentally on a 3D-printed demonstrator, under both linear and nonlinear excitation conditions.

4.2 Undamped periodic resonator chain

This section presents a simplified periodic resonator-chain model that will serve as a reference throughout the chapter. We first consider the undamped case to emphasize the mechanisms behind locally resonant bandgaps, then introduce dissipation and nonlinear effects in later sections.

4.2.1 Unit-cell model and equations of motion

To clarify how local resonances can induce wave filtering, and to identify the parameters that govern this mechanism, we adopt the simplest possible model.

To capture the underlying physics, a minimum of two ingredients are required: (i) a single-mode transmission line to capture wave propagation (e.g., a beam supporting a single polarization or a one-dimensional mass–spring chain); and (ii) periodically distributed resonant attachments to account for local resonance (e.g., cantilever beams in structural systems or Helmholtz resonators in acoustics), which can be idealized as local mass–spring oscillators.

Here, we use a mass–spring model because it efficiently represents both ingredients while keeping the model analytically tractable. Its main limitation is that it neglects the multi-polarized nature of real waveguides.

The periodic resonator chain is described at the scale of a single unit cell, whose mechanical analogue is shown in Fig. 4.1. The waveguide is modelled by a lumped mass m_1 connected to adjacent cells by linear springs of stiffness k_1, while a local resonator of mass m_2 is attached to the waveguide mass through a spring of stiffness k_2. In the literature, periodic mass–spring chains are most often studied by writing the governing equations for the k-th unit cell and its coupling with the $(k-1)$-th and $(k+1)$-th cells, which naturally leads to an analytical introduction of the Floquet–Bloch periodicity condition [170, 210]. Here, we instead describe the unit cell using a 3-DOF matrix formulation (see Fig. 4.1): one internal DOF, x_2, associated with the local resonator, and two boundary DOFs, x_0 (left) and x_1 (right), which lead—in the frequency domain—to the following dynamic equilibrium:

$$\mathbf{D}(\omega)\,\mathbf{u} = \mathbf{0}, \qquad \mathbf{D}(\omega) = \mathbf{K} - \omega^2\mathbf{M}, \tag{4.1}$$

with the stiffness matrix, mass matrix and the generalized displacement vector :

$$\mathbf{K} = \begin{bmatrix} k_1 & -k_1 & 0 \\ -k_1 & k_1+k_2 & -k_2 \\ 0 & -k_2 & k_2 \end{bmatrix}, \qquad \mathbf{M} = \begin{bmatrix} 0 & 0 & 0 \\ 0 & m_1 & 0 \\ 0 & 0 & m_2 \end{bmatrix}, \qquad \mathbf{u} = \begin{bmatrix} x_0 \\ x_1 \\ x_2 \end{bmatrix}. \tag{4.2}$$

This choice enables a direct enforcement on boundary DOFs of the periodic Floquet–Bloch condition via the transfer-matrix approach presented and used in the previous chapters.

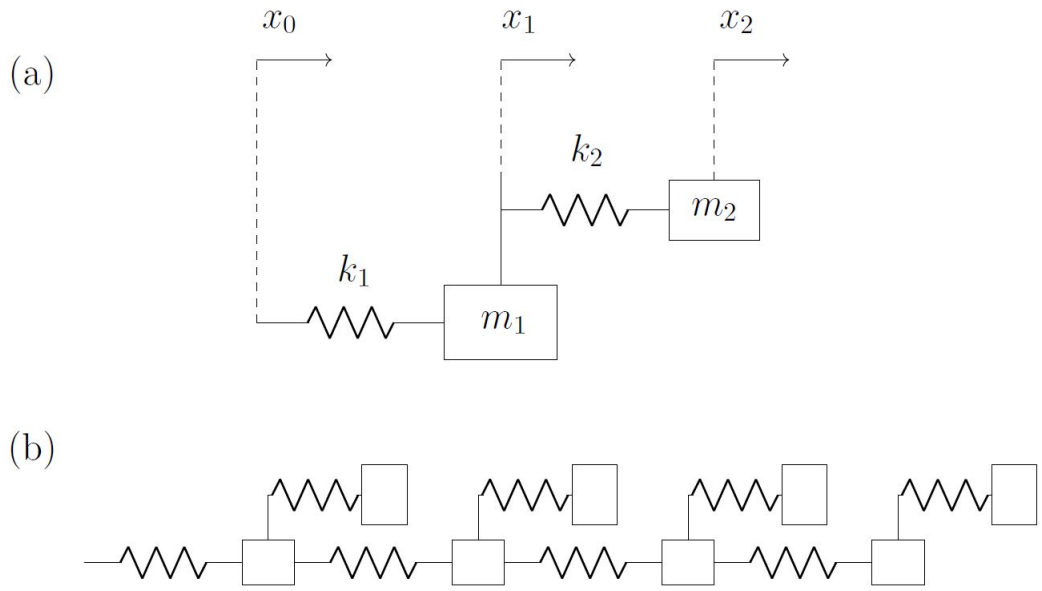

Figure 4.1: (a) Lumped resonator unit cell. (b) Finite periodic resonator chain.

4.2.2 Non-dimensional parameters

In order to identify the governing parameters of the dispersion properties, the problem is recast in non-dimensional form. Two characteristic angular frequencies are first introduced: one associated with the waveguide (ω_1) and the other with the resonators (ω_2):

$$\omega_1 = \sqrt{\frac{k_1}{m_1}}, \qquad \omega_2 = \sqrt{\frac{k_2}{m_2}}, \tag{4.3}$$

Based on these definitions, the following non-dimensional parameters are introduced:

$$\mu_2 = \frac{m_2}{m_1 + m_2}, \qquad \kappa_1 = \frac{k_1}{k_1 + k_2}, \qquad \Omega = \frac{\omega}{\omega_2}, \qquad \alpha = \frac{\omega_2}{\omega_1}. \tag{4.4}$$

The parameters μ_2 and κ_1 are bounded ratios in $[0, 1]$ and represent, respectively, the mass fraction added by the resonators and the fraction of stiffness carried by the waveguide. The parameter α positions the resonant bandgap relative to the waveguide characteristic frequency ω_1, whereas Ω denotes the studied frequency normalized by the resonator natural frequency ω_2.

4.2.3 Floquet–Bloch analysis and dispersion relation

To obtain the dispersion relation, the internal degree of freedom associated with the local resonator is condensed out of the dynamic equilibrium 4.1. In the frequency domain, this leads to the following

reduced (2×2) system written in terms of the boundary displacements x_0 and x_1:

$$\underbrace{\begin{bmatrix} k_1 & -k_1 \\ -k_1 & k_1 + k_2 - \dfrac{k_2^2}{k_2 - m_2\omega^2} - m_1\omega^2 \end{bmatrix}}_{\mathbf{D}_c(\omega)} \begin{bmatrix} x_0 \\ x_1 \end{bmatrix} = \begin{bmatrix} F_0 \\ F_1 \end{bmatrix}. \tag{4.5}$$

For a wave propagating along the chain with wavenumber q and lattice parameter a, the boundary degrees of freedom satisfy the Floquet–Bloch relations

$$x_0 = \lambda\, x_1, \qquad F_0 = -\lambda\, F_1, \qquad \lambda = \mathrm{e}^{\mathrm{i}qa}. \tag{4.6}$$

Substituting these relations into (4.5) and rearranging the resulting equations leads to the following eigenvalue problem :

$$\lambda\, \mathbf{L} \begin{bmatrix} x_0 \\ x_1 \end{bmatrix} = \mathbf{N}(\omega) \begin{bmatrix} x_0 \\ x_1 \end{bmatrix}, \tag{4.7}$$

with

$$\mathbf{L} = \begin{bmatrix} 1 & 0 \\ -k_1 & k_1 \end{bmatrix}, \qquad \mathbf{N}(\omega) = \begin{bmatrix} 0 & 1 \\ -k_1 & k_1 + k_2 - m_1\omega^2 - \dfrac{k_2^2}{k_2 - m_2\omega^2} \end{bmatrix}. \tag{4.8}$$

Solving 4.7 leads to a quadratic characteristic equation in λ,

$$A(\Omega)\, \lambda^2 + B(\Omega)\, \lambda + A(\Omega) = 0, \tag{4.9}$$

whose palindromic structure reflects the reciprocal nature of wave propagation. Using the non-dimensional parameters introduced in 4.2.2, the coefficients read

$$A(\Omega) = \kappa_1\, (1 - \Omega^2), \tag{4.10}$$

$$B(\Omega) = -2\kappa_1 + \Big(2\kappa_1 + \frac{1 - \kappa_1}{\mu_2}\Big)\Omega^2 - \frac{(1 - \kappa_1)(1 - \mu_2)}{\mu_2}\, \Omega^4. \tag{4.11}$$

The solutions of (4.9) are

$$\lambda_{1,2}(\Omega) = \frac{-B(\Omega) \pm \sqrt{\delta(\Omega)}}{2A(\Omega)}, \tag{4.12}$$

where

$$\delta(\Omega) = B(\Omega)^2 - 4A(\Omega)^2. \tag{4.13}$$

The resulting dispersion relation is illustrated in Fig. 4.2 for a representative set of parameters ($\mu_2 = 0.5$ and $\alpha = 0.6$). Figure 4.2(a) shows the imaginary part of the Floquet multiplier λ as a function of the reduced frequency Ω. Within pass bands, $\mathrm{Im}(\lambda) \neq 0$ and $|\lambda| = 1$, whereas inside bandgaps λ becomes real. This transition is directly reflected in the reduced wavenumber qa, whose real and imaginary parts are shown in Figs. 4.2(b) and (c), respectively.

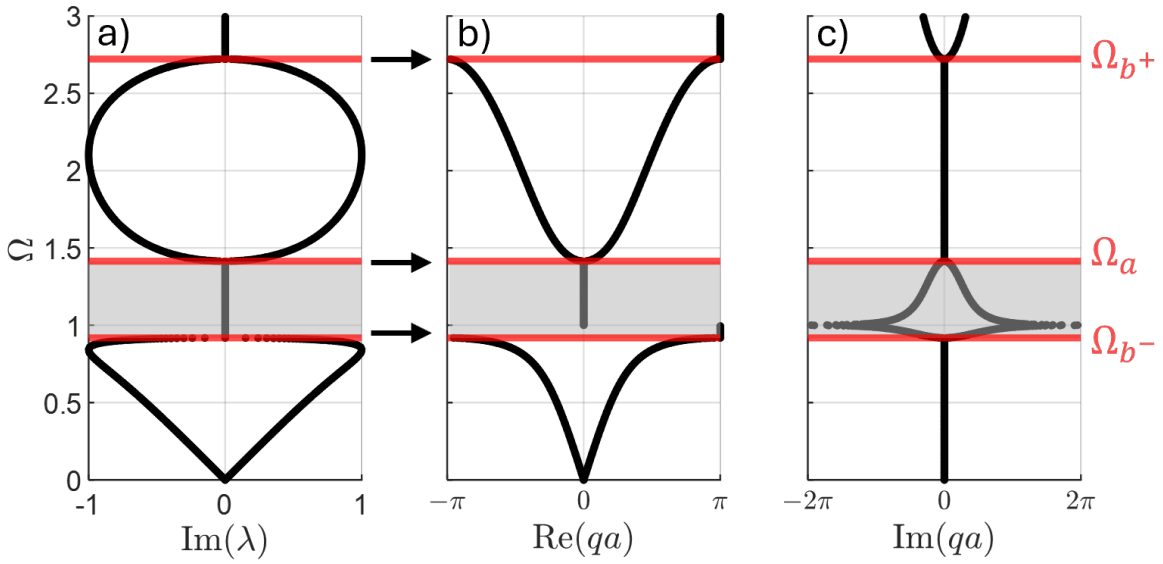

Figure 4.2: Dispersion diagram of the undamped periodic resonator chain ($\mu_2 = 0.5$ and $\alpha = 0.6$). (a) Imaginary part of the Floquet multiplier λ. (b) Real part of the reduced wavenumber qa. (c) Imaginary part of qa. The shaded region indicates the resonant bandgap

As shown in Fig. 4.2, the locally resonant bandgap is characterised by a non-zero imaginary part of the reduced wavenumber (Fig. 4.2(c)), indicating exponential spatial attenuation of waves along the chain. The band edges Ω_{b^-}, Ω_a and Ω_{b^+} correspond to the frequencies at which $\mathrm{Im}(\lambda) = 0$, i.e. $qa = 0$ or $qa = \pi$, and mark the transition between propagative and evanescent regimes. Solving $\mathrm{Im}(\lambda) = 0$ yields the analytical formulation of the three critical reduced frequencies

$$\Omega_a^2 = \frac{1}{1-\mu_2}, \tag{4.14}$$

$$\Omega_{b\pm}^2 = \frac{4\zeta\,\mu_2 + 1}{2(1-\mu_2)} \pm \frac{\mu_2}{2(1-\mu_2)}\sqrt{\left(4\zeta - \frac{1}{\mu_2}\right)^2 + 16\zeta}, \qquad \zeta = \frac{1-\mu_2}{\mu_2\alpha^2}. \tag{4.15}$$

In the usual ordering $\Omega_{b^-} < \Omega_a < \Omega_{b^+}$, the bandgaps and pass bands are :

$$\text{bandgaps:} \quad \Omega \in]\,\Omega_{b^-},\, \Omega_a\,[\, \cup\,]\,\Omega_{b^+},\, +\infty\,[, \tag{4.16}$$

$$\text{pass bands:} \quad \Omega \in [0,\, \Omega_{b^-}]\, \cup\, [\Omega_a,\, \Omega_{b^+}]. \tag{4.17}$$

4.2.4 Mass–bandwidth trade-off

The introduction of a local resonator inevitably induces two antagonistic effects. On the one hand, increasing the resonator mass enhances the dynamic contrast between the waveguide and the resonant subsystem, which tends to enlarge the locally resonant bandgap. On the other hand, this improvement is achieved at the cost of an increased added mass, which is detrimental from a structural and practical standpoint.

To capture this compromise we introduce the following trade-off function:

$$\Phi(\mu_2, \alpha) = (1 - \mu_2)\, \beta(\mu_2, \alpha), \tag{4.18}$$

where

$$\beta = \frac{2\left(\Omega_a - \Omega_{b^-}\right)}{\Omega_a + \Omega_{b^-}} \tag{4.19}$$

denotes the relative bandgap width. The trade-off function Φ can be interpreted as an attenuation efficiency per unit added mass: it rewards large bandgaps while penalizing solutions that require excessive added mass, and it also discards lightweight configurations that yield only marginal attenuation.

Figure 4.3 illustrates the resulting trade-off by varying μ_2 from 0 to 1 and α from 0 to 2. As shown in Fig. 4.3(a), the relative bandgap width β increases with μ_2 for any fixed value of α.

Figure 4.3(b) reveals a markedly different behaviour for the trade-off function Φ. When $\mu_2 \to 0$, the resonator becomes dynamically ineffective, the bandgap collapses, and $\Phi \to 0$. Conversely, when $\mu_2 \to 1$, the configuration becomes nearly trivial: the waveguide mass is negligible compared to the resonator mass, so the modest additional gain in bandgap width is outweighed by the mass penalty, and Φ again vanishes. The trade-off function Φ exhibits a well-defined maximum at an intermediate value of μ_2 for each α, indicating that neither extreme parameter value yields an efficient filtering solution.

In the low-frequency regime $\alpha \ll 1$, the trade-off between bandgap width (β) and added mass (μ_2) progressively collapses onto a well-defined Pareto front (dark-blue curve), and the optimal black points converge towards a unique value as $\alpha \to 0$. In this limit, setting $\alpha = 0$ in (4.15) and substituting into (4.18) yields the Pareto-front function:

$$\beta(\mu_2, 0) = \frac{2\left(1 - \sqrt{1 - \mu_2}\right)}{1 + \sqrt{1 - \mu_2}}, \qquad \Phi(\mu_2, 0) = (1 - \mu_2)\beta(\mu_2, 0)\,. \tag{4.20}$$

The optimal point is obtained by enforcing $\mathrm{d}\Phi/\mathrm{d}\mu_2 = 0$, which gives

$$\frac{\mathrm{d}\Phi(\mu_2, 0)}{\mathrm{d}\mu_2} = 0 \quad \Longleftrightarrow \quad \mu_2^2 + \mu_2 - 1 = 0, \tag{4.21}$$

whose unique root in $(0, 1)$ is

$$\mu_2^\star = \frac{\sqrt{5} - 1}{2} \approx 0.618. \qquad \beta^\star = \beta(\mu_2^\star, 0) \approx 0.472. \tag{4.22}$$

As $\alpha \to 0$, the emergence of a single optimum indicates that, when aiming to open the widest possible low-frequency bandgap with the smallest added mass, the optimal solution corresponds to a resonator mass fraction of $\mu_2 \approx 0.61$. This configuration yields a relative bandwidth of about 47%. Although such a mass contribution is unrealistically large in practice, it provides an order-of-magnitude estimate of the upper limit of the mass–filtering compromise.

In the same limit $\alpha \to 0$, the dark-blue Pareto front $\beta(\mu_2, 0)$ in Fig. 4.18(a), whose analytical expression is given in Eq. (4.20), also provides useful guidance for sizing lighter filters. For example, this curve indicates that achieving a low-frequency bandgap with a relative width of 10% requires $\mu_2 \approx 0.18$. These values therefore serve as robust reference points for low-frequency filter design, against which more realistic configurations are compared in the remainder of the chapter.

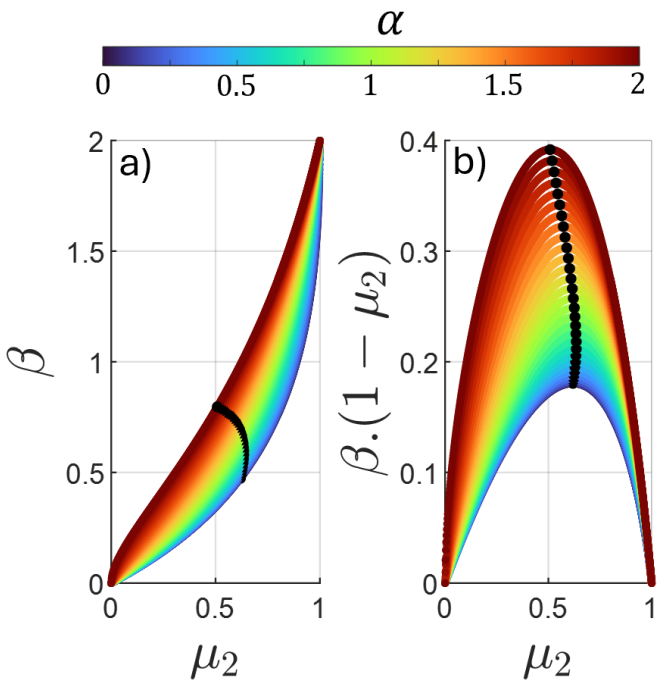

Figure 4.3: Mass–bandgap trade-off for the undamped resonator chain. (a) Relative bandgap width β as a function of the resonator mass fraction μ_2 for different α. Each curve corresponds to a distinct value of α and is distinguished by a colour gradient. (b) Trade-off function $\Phi = (1 - \mu_2)\beta$ for the same set of parameters. For each value of α, the black dot marks the optimal operating point, defined as the maximum of Φ; the corresponding optimal mass fractions are also indicated in (a).

4.3 Damped periodic resonator chain

The previous section established the dispersion properties and optimal design rules of an ideal, undamped periodic resonator chain. In practical applications, however, both the waveguide and the local resonators exhibit intrinsic dissipation. Moreover, real filters are necessarily finite and consist of a limited number of unit cells. As a consequence, the strict notion of a bandgap derived from infinite periodic media must be revisited.

This section extends the analysis to finite resonator chains with viscous losses. The objectives are threefold. First, we examine how damping modifies the complex dispersion relation of the infinite chain. Second, we introduce a practical definition of an attenuation band based on the frequency response of a finite structure. Finally, we analyse how damping and chain length affect the mass–bandwidth trade-off identified in the undamped case.

4.3.1 Damped unit cell and complex dispersion

Viscous dissipation is introduced by adding dashpots in parallel with the linear springs k_1 and k_2 of the undamped unit cell. The resulting mechanical analogue is shown in Fig. 4.4. The damping coefficients c_1 and c_2 are defined from the corresponding loss factors ξ_1 and ξ_2 as

$$c_1 = 2\,\xi_1\,\sqrt{k_1 m_1}, \qquad c_2 = 2\,\xi_2\,\sqrt{k_2 m_2}. \tag{4.23}$$

In the frequency domain, the dynamic stiffness matrix of the unit cell becomes

$$\mathbf{D}(\omega) = \mathbf{K} + \mathrm{i}\,\omega\,\mathbf{C} - \omega^2\,\mathbf{M}, \tag{4.24}$$

where $\mathbf{C}$ is the viscous damping matrix.

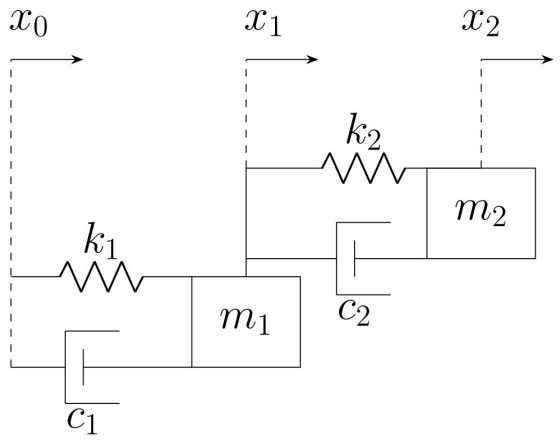

Figure 4.4: Damped unit cell of the periodic resonator chain. Viscous dampers c_1 and c_2 are added in parallel with k_1 and k_2 to the undamped unit cell of Fig. 4.1a).

Applying Floquet–Bloch conditions and condensing the resonator degree of freedom as in the undamped case again leads to a quadratic characteristic equation in the Floquet multiplier λ. However, due to dissipation, the coefficients of this equation are now complex. As a result, the reduced wavenumber qa becomes complex for all frequencies, and neither purely propagative nor purely evanescent waves exist anymore.

The effect of viscous losses on the dispersion relation is illustrated in Fig. 4.5. Figures 4.5(a) and (b) show the real and imaginary parts of the reduced wavenumber qa for increasing values of the loss factor $\xi = \xi_1 = \xi_2$. For comparison, the undamped bandgap identified in Section 4.2 is recalled as a grey region. As soon as $\xi > 0$, the real part of qa no longer reaches exactly 0 or π, and the imaginary part never vanishes. This confirms that the classical bandgap concept associated with infinite, lossless periodic systems no longer strictly applies.

4.3.2 Attenuation band of a finite chain

In the presence of damping, the filtering performance must be assessed at the scale of a finite structure. We therefore consider a chain composed of N_c identical unit cells and define the frequency response

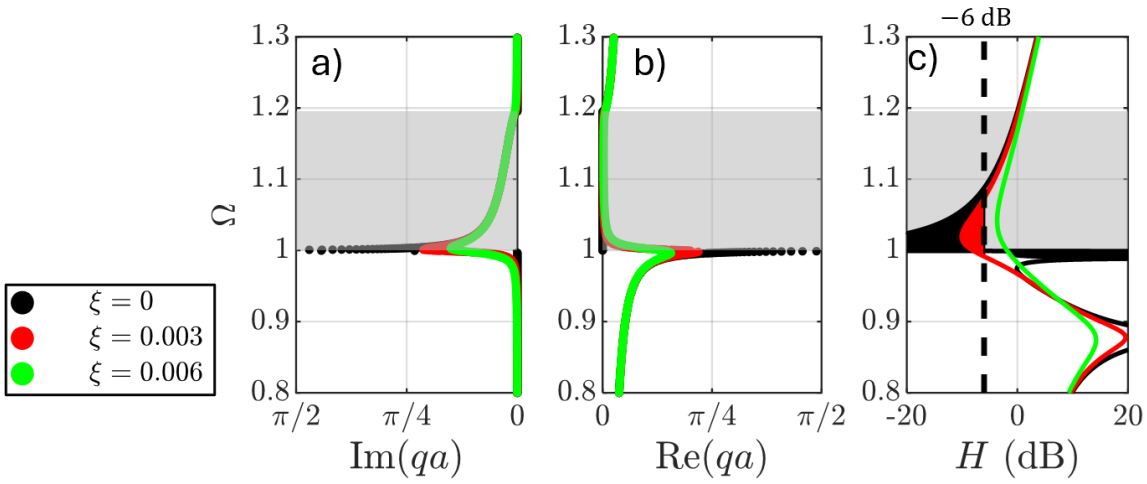

Figure 4.5: Effect of viscous dissipation on the dispersion and finite-chain response of the resonator chain. (a) Real part Re(qa) and (b) imaginary part Im(qa) of the propagation constant for different loss factors. (c) Frequency response function H in dB for a finite chain of $N_c = 10$ cells. The grey region recalls the undamped bandgap, while the filled areas below $H_{\text{lim}} = -6$ dB define the attenuation bands.

function

$$H(\Omega) = 20\text{Log}\left|\frac{U_{N_c}}{U_1}\right|, \tag{4.25}$$

where U_1 and U_{N_c} denote the displacement amplitudes at the input and output of the chain, respectively.

Figure 4.5(c) shows typical frequency responses for a chain of $N_c = 10$ cells and increasing loss factors. Although no strict bandgap exists, a frequency interval over which the response is significantly attenuated can still be identified. To quantify this behaviour, we introduce the concept of an *attenuation band*, defined as the frequency range for which

$$H(\Omega) \leq -6\text{dB}, \tag{4.26}$$

The corresponding attenuation band is highlighted by shaded areas in Fig. 4.5(c).

As the loss factor increases, two effects are observed. First, the maximum attenuation decreases, reflecting the reduced contrast between propagative and evanescent behaviour. Second, the attenuation band becomes progressively narrower and may eventually vanish when dissipation dominates the resonant mechanism. As shown in Fig. 4.5(c), for the highest loss level (green curve), no frequency interval satisfies the −6 dB criterion, so that no effective attenuation band can be identified.

As shown by the black and red curves in Fig. 4.5(c), the attenuation band is defined as the frequency interval where $H(\Omega) \leq -6$ dB. Denoting its bounds by Ω_- and Ω_+, the corresponding relative attenuation bandwidth is defined as

$$\beta_{6\text{dB}} = \frac{2(\Omega_+ - \Omega_-)}{\Omega_+ + \Omega_-}. \tag{4.27}$$

This definition provides a dimensionless measure of the filtering bandwidth, which can be directly compared to the relative bandgap width β introduced in the undamped, infinite-chain case.

4.3.3 Influence of damping and number of cells

The relative attenuation bandwidth $\beta_{6\text{dB}}$ is now analysed as a function of the loss factors and the number of cells N_c. Figure 4.6 summarises the results for fixed α and resonator mass fraction μ_2.

Figure 4.6(a) shows the influence of the waveguide loss factor ξ_1 for several values of N_c. The attenuation bandwidth is not affected by ξ_1, while increasing the number of cells systematically improves the filtering performance.

In contrast, Fig. 4.6(b) reveals a strong sensitivity to the resonator loss factor ξ_2. At first, introducing resonator damping slightly broadens the attenuation band. However, beyond a critical value of ξ_2, the attenuation band collapses, regardless of the chain length. This behaviour highlights the central role of resonator dissipation in limiting the effectiveness of locally resonant filters, and therefore the need to control it.

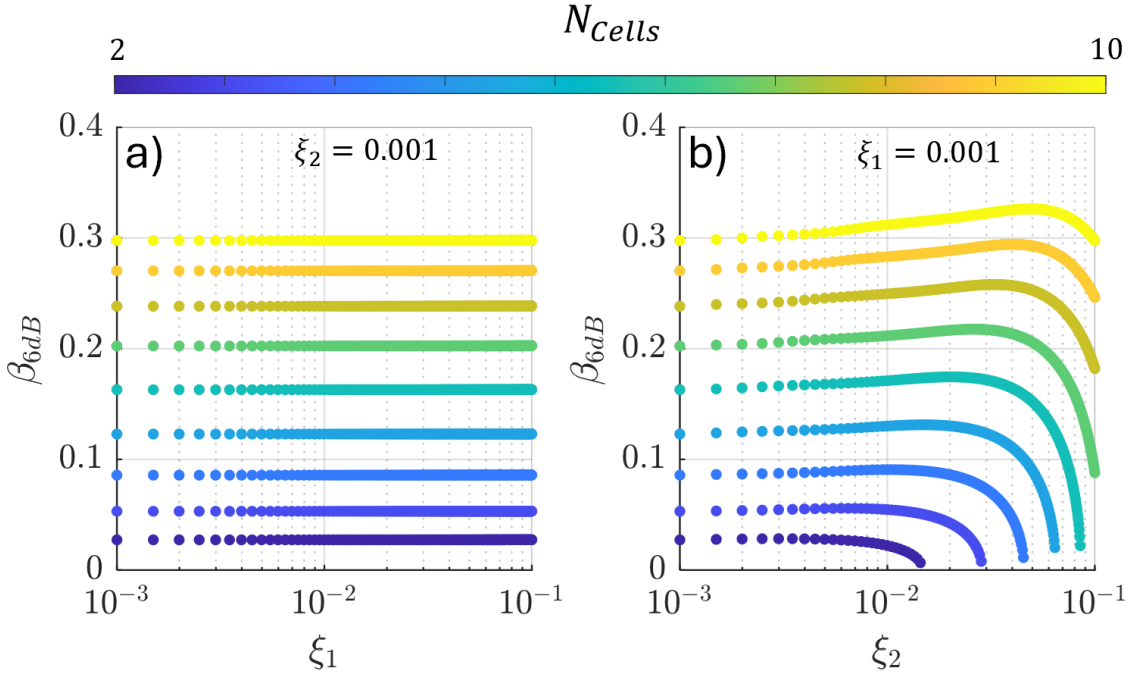

Figure 4.6: Relative attenuation bandwidth $\beta_{6\text{dB}}$ as a function of damping and number of cells. (a) Influence of the waveguide loss factor ξ_1 for $\xi_2 = 10^{-3}$. (b) Influence of the resonator loss factor ξ_2 for $\xi_1 = 10^{-3}$. Curves are colour-coded by the number of cells N_c.

4.3.4 Mass–attenuation trade-off

We now revisit the mass–bandwidth trade-off introduced in Section 4.2.4, accounting for viscous dissipation and finite chain length. Figure 4.7 shows the evolution of the attenuation bandwidth $\beta_{6\text{dB}}$ and of the trade-off function $\Phi = (1 - \mu_2)\beta_{6\text{dB}}$ for a chain of $N_c = 5$ cells and a uniform loss factor $\xi = 0.01$. As shown in Figs. 4.7(a) and (b), when damping is introduced the optimal mass–bandwidth compromise shifts towards larger resonator mass fractions as the targeted attenuation band is pushed to lower frequencies ($\alpha \to 0$). This contrasts with the undamped case (see Fig. 4.3), for which a unique Pareto front is recovered in the limit $\alpha \to 0$.

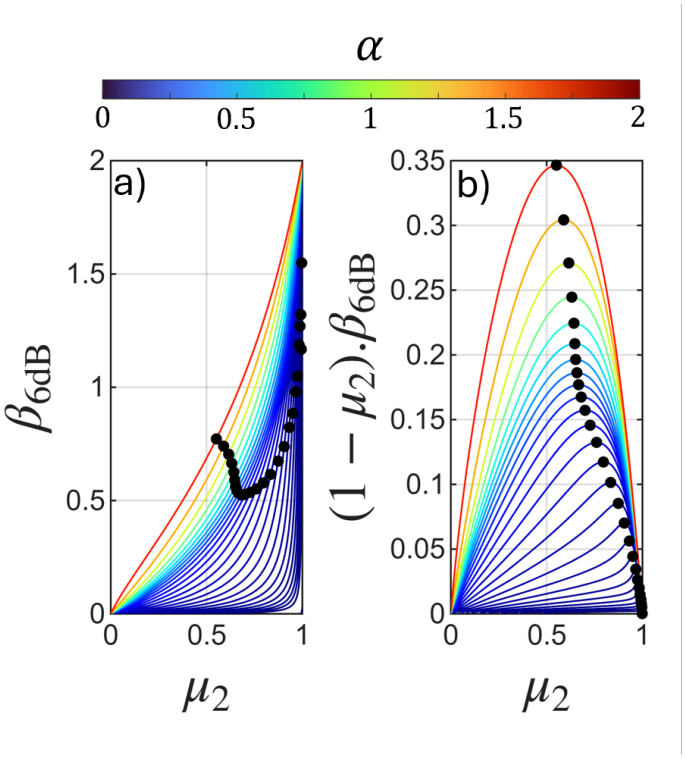

Figure 4.7: Mass–attenuation trade-off for a finite resonator chain with damping ($\xi_1 = \xi_2 = 0.01$, $N_c = 5$). (a) Relative attenuation bandwidth β_{6dB} as a function of the resonator mass fraction μ_2 for different value of α, distinguished by a colour gradient. (b) Trade-off function $\Phi = (1 - \mu_2)\beta_{6dB}$ for the same set of parameters. For each value of α, the black dot marks the optimal operating point, defined as the maximum of Φ.

Physically, this behaviour reflects the fact that, at very low frequencies, the resonator stiffness must be strongly reduced. When damping is present, this leads to a loss-dominated response in which the resonator can no longer efficiently store and return energy, so that increasing the resonator mass becomes the primary means of recovering a measurable attenuation effect.

As a consequence, the unique optimum obtained in the undamped case for low-frequency limit should be regarded as an ideal upper bound rather than a universal design rule. In practical configurations, viscous losses and finite chain length progressively shift the optimum towards heavier resonators and longer filters, especially when targeting deep-subwavelength attenuation.

In the following section, the analysis is extended to account for weak geometric nonlinearities, which introduce amplitude-dependent dispersion properties and further modify the attenuation performance of resonant filters.

4.4 Nonlinear resonator chains

The analyses presented so far were restricted to linear resonator chains, for which dispersion relations and attenuation properties follow directly from linear eigenvalue problems. In many practical applications, however, the vibration levels required to activate low-frequency resonant mechanisms are sufficiently high for geometric or material nonlinearities to become active within the resonators. Under such conditions, the filtering performance becomes amplitude dependent and cannot be fully

captured by a linear model.

This section extends the previous analyses by introducing a weak cubic nonlinearity in the local resonators. The objective is twofold. First, we investigate how nonlinearities modify wave propagation in an infinite periodic chain through an amplitude-dependent dispersion relation. Second, we analyse how these nonlinear dispersion properties translate into the frequency response of finite resonator chains, with direct implications for vibration attenuation.

4.4.1 Nonlinear unit cell

As illustrated in Fig. 4.8, nonlinearity is introduced at the level of the local resonator by adding an additional cubic stiffness term to the linear restoring force of the spring connecting masses 1 and 2 :

$$f_{\mathrm{nl}} = k_3(x_2 - x_1)^3, \tag{4.28}$$

where k_3 is the cubic stiffness coefficient. Positive values of k_3 correspond to a hardening behaviour, whereas negative values yield a softening response. The nonlinearity strength is quantified through the non-dimensional parameter

$$\kappa_3 = \frac{k_3}{k_2}, \tag{4.29}$$

defined relative to the linear resonator stiffness. Viscous damping is retained in both the waveguide and the resonator, consistently with the linear damped model introduced in Section 4.2. By action–reaction, the corresponding nonlinear force vector in physical coordinates is

$$\boldsymbol{f}_{nl}^{\mathrm{phys}}(t) = \begin{bmatrix} 0 \\ f_{nl}(t) \\ -f_{nl}(t) \end{bmatrix}. \tag{4.30}$$

The local equations of motion read

$$\boldsymbol{M}\,\ddot{\boldsymbol{u}}(t) + \boldsymbol{C}\,\dot{\boldsymbol{u}}(t) + \boldsymbol{K}\,\boldsymbol{u}(t) + \boldsymbol{f}_{nl}^{\mathrm{phys}}(t) = \boldsymbol{0}. \tag{4.31}$$

with $\boldsymbol{u}(t) = \begin{bmatrix} x_0(t) & x_1(t) & x_2(t) \end{bmatrix}^T$

Harmonic Balance Method (HBM) to obtain the non linear dispersion relation

In contrast to linear periodic systems, nonlinear periodic structures do not admit uniquely defined free traveling-wave solutions. This is because the oscillation frequency depends on the vibration amplitude, meaning that a dispersion relation cannot be defined independently of the input level.

To enforce periodicity, we introduce the reduced vector:

$$\boldsymbol{y}(t) = \begin{bmatrix} x_1(t) \\ x_2(t) \end{bmatrix} = \begin{bmatrix} y_1(t) \\ y_2(t) \end{bmatrix}. \tag{4.32}$$

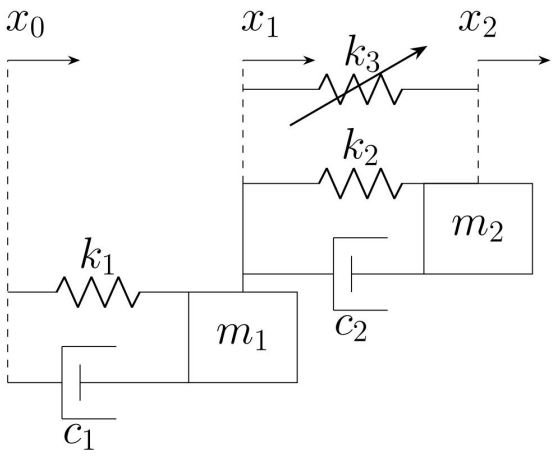

Figure 4.8: Nonlinear extension of the damped unit cell shown in Fig. 4.4, obtained by adding a cubic stiffness k_3 to the local resonator.

We impose the periodic Floquet-Bloch condition here using the following transfer matrix:

$$\boldsymbol{u}(t) = \boldsymbol{T}(\lambda)\,\boldsymbol{y}(t), \quad \boldsymbol{T}(\lambda) = \begin{bmatrix} \lambda^{-1} & 0 \\ 1 & 0 \\ 0 & 1 \end{bmatrix}, \quad \boldsymbol{T}^{+}(\lambda) = \begin{bmatrix} \lambda & 0 \\ 1 & 0 \\ 0 & 1 \end{bmatrix}. \tag{4.33}$$

Substituting $\boldsymbol{u} = \boldsymbol{T}(\lambda)\boldsymbol{y}$ into Eq. (4.31), and premultiplying by $\boldsymbol{T}^{+}(\lambda)^{\mathsf{T}}$ yields the reduced equations:

$$\boldsymbol{M}_r(\lambda)\,\ddot{\boldsymbol{y}}(t) + \boldsymbol{C}_r(\lambda)\,\dot{\boldsymbol{y}}(t) + \boldsymbol{K}_r(\lambda)\,\boldsymbol{y}(t) + \boldsymbol{f}_{nl}^{r}(t) = \boldsymbol{0}, \tag{4.34}$$

with reduced matrices:

$$\boldsymbol{M}_r(\lambda) = \boldsymbol{T}^{+}(\lambda)^{\mathsf{T}}\boldsymbol{M}\boldsymbol{T}(\lambda), \quad \boldsymbol{C}_r(\lambda) = \boldsymbol{T}^{+}(\lambda)^{\mathsf{T}}\boldsymbol{C}\boldsymbol{T}(\lambda), \quad \boldsymbol{K}_r(\lambda) = \boldsymbol{T}^{+}(\lambda)^{\mathsf{T}}\boldsymbol{K}\boldsymbol{T}(\lambda). \tag{4.35}$$

$$\boldsymbol{f}_{nl}^{r}(t) = \boldsymbol{T}(\lambda)^{\mathsf{T}}\boldsymbol{f}_{nl}^{\mathrm{phys}}(t). \tag{4.36}$$

In this work, we apply the Harmonic Balance Method (HBM) [211, 212] to obtain a $2\pi/\Omega$-periodic steady-state response at the angular frequency Ω. For each reduced degree of freedom $y_k(t)$, we employ a truncated complex Fourier series representation with N_h harmonics:

$$y_k(t) = \sum_{n=1}^{N_h} U_{k,n}\, e^{in\Omega t} + \sum_{n=1}^{N_h} \overline{U_{k,n}}\, e^{-in\Omega t}, \tag{4.37}$$

so that $y_k(t)$ is real-valued. The complex coefficients are collected as:

$$\boldsymbol{U}_1 = \begin{bmatrix} U_{1,1} & \cdots & U_{1,N_h} \end{bmatrix}^{\mathsf{T}}, \quad \boldsymbol{U}_2 = \begin{bmatrix} U_{2,1} & \cdots & U_{2,N_h} \end{bmatrix}^{\mathsf{T}}. \tag{4.38}$$

We discretize one period using N_t equally spaced points:

$$\theta_j = \frac{2\pi j}{N_t}, \quad j = 0, \dots, N_t - 1, \quad t_j = \frac{\theta_j}{\Omega}. \tag{4.39}$$

Define the synthesis matrix $\boldsymbol{E} \in \mathbb{C}^{N_t \times N_h}$ with entries:

$$E_{j,n} = e^{in\theta_j}, \quad n = 1, \dots, N_h. \tag{4.40}$$

The complex partial sums are:

$$\boldsymbol{s}_1 = \boldsymbol{E}\boldsymbol{U}_1, \quad \boldsymbol{s}_2 = \boldsymbol{E}\boldsymbol{U}_2, \tag{4.41}$$

and the real time signals are recovered by:

$$\boldsymbol{y}_1 = 2\,\mathrm{Re}(\boldsymbol{s}_1), \quad \boldsymbol{y}_2 = 2\,\mathrm{Re}(\boldsymbol{s}_2), \tag{4.42}$$

Derivatives are computed analytically on the Fourier basis:

$$\frac{d}{dt}\left(e^{in\Omega t}\right) = in\Omega e^{in\Omega t}, \quad \frac{d^2}{dt^2}\left(e^{in\Omega t}\right) = -(n\Omega)^2 e^{in\Omega t}. \tag{4.43}$$

Hence, at collocation points:

$$\dot{\boldsymbol{s}}_k = \boldsymbol{E}\big(i\Omega\, \boldsymbol{n}\boldsymbol{U}_k\big), \quad \ddot{\boldsymbol{s}}_k = \boldsymbol{E}\big(-\Omega^2\, \boldsymbol{n}^2\boldsymbol{U}_k\big), \qquad \boldsymbol{n} = [1, \dots, N_h]^\mathsf{T}. \tag{4.44}$$

Real derivatives are then obtained as:

$$\dot{\boldsymbol{y}}_k = 2\,\mathrm{Re}(\dot{\boldsymbol{s}}_k), \quad \ddot{\boldsymbol{y}}_k = 2\,\mathrm{Re}(\ddot{\boldsymbol{s}}_k). \tag{4.45}$$

Let $\boldsymbol{Y} \in \mathbb{R}^{N_t \times 2}$ stack the reduced displacements over time:

$$\boldsymbol{Y} = \begin{bmatrix} \boldsymbol{y}_1 & \boldsymbol{y}_2 \end{bmatrix}, \quad \dot{\boldsymbol{Y}} = \begin{bmatrix} \dot{\boldsymbol{y}}_1 & \dot{\boldsymbol{y}}_2 \end{bmatrix}, \quad \ddot{\boldsymbol{Y}} = \begin{bmatrix} \ddot{\boldsymbol{y}}_1 & \ddot{\boldsymbol{y}}_2 \end{bmatrix}. \tag{4.46}$$

At each collocation time t_j, the reduced equation (4.34) should hold, so we define a discrete-time residual matrix:

$$\boldsymbol{R}(t_j) = \boldsymbol{M}_r(\lambda)\, \ddot{\boldsymbol{y}}(t_j) + \boldsymbol{C}_r(\lambda)\, \dot{\boldsymbol{y}}(t_j) + \boldsymbol{K}_r(\lambda)\, \boldsymbol{y}(t_j) + \boldsymbol{f}_{nl}^r(t_j), \tag{4.47}$$

or, in matrix form over all times:

$$\boldsymbol{R} = \ddot{\boldsymbol{Y}}\, \boldsymbol{M}_r(\lambda)^\mathsf{T} + \dot{\boldsymbol{Y}}\, \boldsymbol{C}_r(\lambda)^\mathsf{T} + \boldsymbol{Y}\, \boldsymbol{K}_r(\lambda)^\mathsf{T} + \boldsymbol{F}_{nl}^r, \tag{4.48}$$

Harmonic balance requires that the Fourier coefficients of the residual vanish. Using the discrete

orthogonality of $\boldsymbol{E}$ on the grid, the Fourier coefficients of each residual component are obtained by:

$$\boldsymbol{\mathcal{R}}_k = \frac{1}{N_t} \boldsymbol{E}^{\mathsf{H}} \boldsymbol{R}_{(:,k)}, \quad k = 1, 2, \tag{4.49}$$

where $(\cdot)^{\mathsf{H}}$ is the conjugate transpose and $\boldsymbol{R}_{(:,k)}$ is the k-th column of $\boldsymbol{R}$.

The core HBM conditions are therefore:

$$\boldsymbol{\mathcal{R}}_1 = \mathbf{0} \in \mathbb{C}^{N_h}, \quad \boldsymbol{\mathcal{R}}_2 = \mathbf{0} \in \mathbb{C}^{N_h}. \tag{4.50}$$

The nonlinear dispersion relation is not uniquely parameterized unless the wave amplitude is fixed. We enforce a prescribed amplitude $A^\star$ on the *first harmonic* of the interface motion by defining :

$$\widehat{A} = \lambda^{-1} U_{1,1}. \tag{4.51}$$

and applying the following constraints :

$$g_1(\boldsymbol{U}_1, \lambda) = |\widehat{A}|^2 - (A^\star)^2 = 0, \quad g_2(\boldsymbol{U}_1, \lambda) = \mathrm{Im}(\widehat{A}) = 0. \tag{4.52}$$

The first constraint sets the amplitude, while the second fixes the arbitrary phase. The complex residual vector is collected as:

$$\boldsymbol{F}_c(\boldsymbol{U}_1, \boldsymbol{U}_2, \lambda, \Omega) = \begin{bmatrix} \boldsymbol{\mathcal{R}}_1 \\ \boldsymbol{\mathcal{R}}_2 \\ g_1 + i g_2 \end{bmatrix} \in \mathbb{C}^{(2N_h+1)}. \tag{4.53}$$

Then, the complete residual is solved numerically :

$$\boldsymbol{R}_{\text{phys}}(\boldsymbol{X}) = \begin{bmatrix} \mathrm{Re}(\boldsymbol{F}_c) \\ \mathrm{Im}(\boldsymbol{F}_c) \end{bmatrix} \in \mathbb{R}^{(4N_h+2)}. \tag{4.54}$$

where $\boldsymbol{X}$ is the unknown vector, with the exception of Ω, which is imposed:

$$\boldsymbol{X} = \begin{bmatrix} \mathrm{Re}(\boldsymbol{U}_1) \\ \mathrm{Im}(\boldsymbol{U}_1) \\ \mathrm{Re}(\boldsymbol{U}_2) \\ \mathrm{Im}(\boldsymbol{U}_2) \\ \mathrm{Re}(\lambda) \\ \mathrm{Im}(\lambda) \\ \Omega \end{bmatrix} \in \mathbb{R}^{(4N_h+3)}. \tag{4.55}$$

The solution set of (4.54) may experience bifurcations, causing a simple parameter continuation in Ω to fail. To address this, we employ Pseudo-ArcLength (PAL) continuation [213], which introduces an additional constraint to guide the progression along the solution curve.

Given a previous converged solution $\boldsymbol{X}_{\text{prev}}$ and a unit tangent direction $\boldsymbol{d}$, the PAL constraint is:

$$R_{\text{arc}}(\boldsymbol{X}) = (\boldsymbol{X} - \boldsymbol{X}_{\text{prev}})^{\mathsf{T}}\boldsymbol{d} - ds = 0, \tag{4.56}$$

where ds is the continuation step length.

The augmented residual becomes:

$$\boldsymbol{R}(\boldsymbol{X}) = \begin{bmatrix} \boldsymbol{R}_{\text{phys}}(\boldsymbol{X}) \\ R_{\text{arc}}(\boldsymbol{X}) \end{bmatrix} \in \mathbb{R}^{(4N_h+3)}. \tag{4.57}$$

At step k, a predictor is built as:

$$\boldsymbol{X}_{\text{pred}} = \boldsymbol{X}_{\text{prev}} + ds\,\boldsymbol{d}. \tag{4.58}$$

A Newton corrector then solves $\boldsymbol{R}(\boldsymbol{X}) = \boldsymbol{0}$ starting from $\boldsymbol{X}_{\text{pred}}$. After convergence, the tangent is updated from the secant direction:

$$\tilde{\boldsymbol{d}} = \boldsymbol{W}(\boldsymbol{X}_k - \boldsymbol{X}_{k-1}), \quad \boldsymbol{d} = \frac{\tilde{\boldsymbol{d}}}{\|\tilde{\boldsymbol{d}}\|}, \tag{4.59}$$

where $\boldsymbol{W}$ is a diagonal weight matrix that balances the influence of amplitudes, Bloch phase, and frequency. The stability of these multiple solutions is assessed by comparing the results of the PAL continuation with those obtained from a straightforward forward and backward frequency sweep [214].

4.4.2 Nonlinear dispersion

The nonlinear dispersion characteristics of the infinite periodic resonator chain are now examined using the numerical model introduced in the previous subsections. Figure 4.9 presents the complex dispersion relation obtained under Floquet–Bloch conditions, for both softening and hardening nonlinearities and for increasing prescribed vibration amplitudes $A^\star$.

The results are displayed in terms of the complex wavenumber q. Figure 4.9(a) shows the imaginary part $\text{Im}(qa)$ as a function of the non-dimensional angular frequency Ω, which directly quantifies spatial attenuation. Figure 4.9(b) reports the corresponding real part $\text{Re}(qa)$, associated with phase propagation. In both cases, the frequency interval $\Omega \in [0.98,\ 1.03]$ is highlighted by a red dashed rectangle and displayed in enlarged views in Figs. 4.9(a.1) and (b.1), respectively.

In the linear reference case (green curves), the transition between propagative and attenuated regimes is unique. In the presence of cubic nonlinearity, this transition exhibits a systematic amplitude-dependent shift.

For hardening nonlinearities ($\kappa_3 > 0$, orange and brown curves), increasing the prescribed vibration amplitude $A^\star$ shifts the beginning of the attenuation band towards higher frequencies.

This behaviour reflects an effective stiffening of the local resonator, which raises its resonance frequency and, in turn, the lower edge of the attenuation band. Conversely, for softening nonlinearities

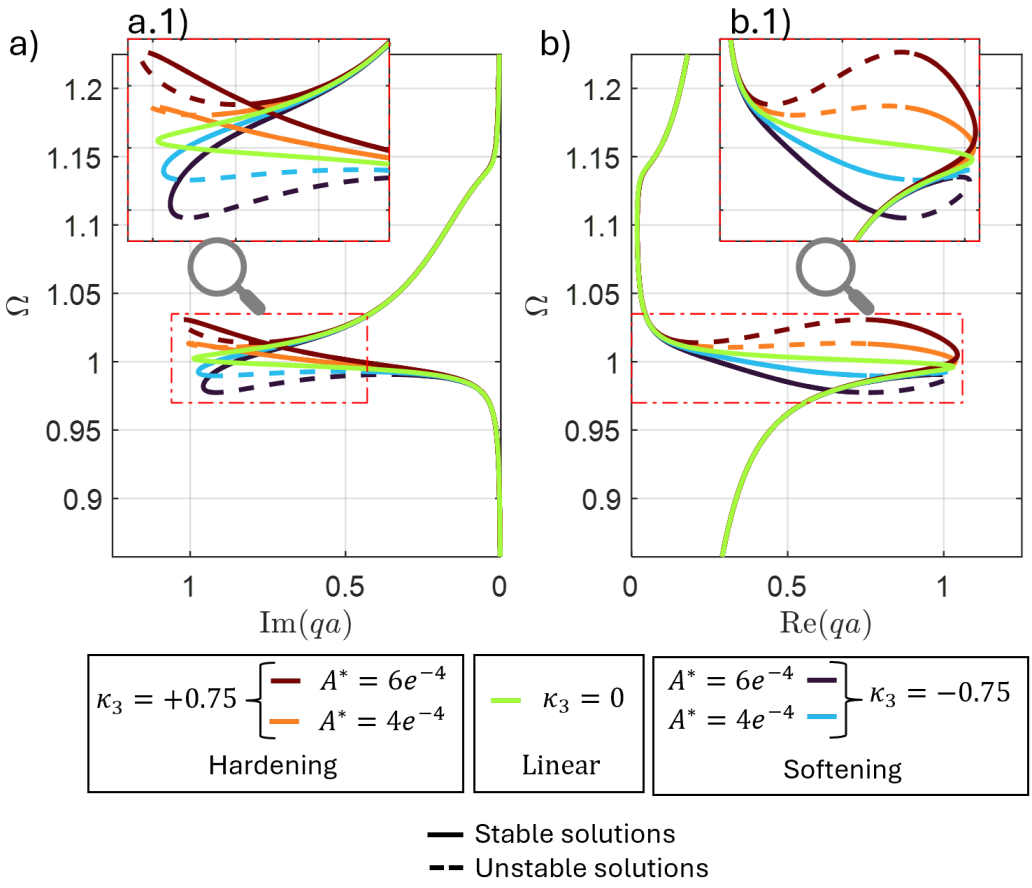

Figure 4.9: Complex nonlinear dispersion relation of the damped periodic resonator chain under Floquet–Bloch conditions computed for $N_h = 1$. (a) Imaginary part and (b) real part of the complex wavenumber qa as functions of the reduced frequency Ω. Enlarged views around the onset of the attenuation band ($\Omega \in [0.98, 1.03]$) are shown in (a.1) and (b.1). The linear dispersion is reported in green. Nonlinear branches are shown for softening ($\kappa_3 < 0$, blue) and hardening ($\kappa_3 > 0$, orange-to-brown) nonlinearities; lighter to darker shades correspond to increasing prescribed vibration amplitudes $A^\star$. Solid lines denote stable solutions, while dashed lines indicate unstable branches. Results are obtained for $\alpha = 0.25$, $\mu_2 = 0.25$ and $\xi = 0.01$.

($\kappa_3 < 0$, dark and light blue curves), the same increase in amplitude results in a downward shift of the lower edge of the attenuation band, consistent with a reduction of the effective resonator stiffness.

The enlarged views shown in Figs. 4.9(a.1) and (b.1) further reveal the emergence of multiple solution branches in a narrow frequency range around $\Omega \simeq 1$. For a given frequency, several admissible solutions of the complex wavenumber coexist, among which stable (solid lines) and unstable (dashed lines) branches can be identified. This multivalued structure is a characteristic feature of nonlinear periodic systems and reflects the fact that the dispersion relation is no longer unique, but depends on the vibration amplitude and on the continuation path.

The coexistence of stable and unstable branches implies that wave propagation in the nonlinear regime may become history-dependent and potentially hysteretic. As a result, the notion of an attenuation band must be interpreted with care: unlike the linear case, the boundary between propagative and attenuated behaviour is neither unique nor purely frequency-based, but becomes

intrinsically amplitude dependent. Similar phenomena, including amplitude-dependent bandgap shifts, branch multiplicity and instability regions, have been reported in previous studies on nonlinear periodic and locally resonant media [215–217].

4.4.3 Attenuation performance

The nonlinear response of a finite resonator chain is now investigated in order to assess how the amplitude-dependent dispersion properties identified above manifest themselves at the structural scale. In contrast with the dispersion analysis, the finite chain is excited through a physical boundary condition rather than through an imposed travelling wave.

Specifically, a harmonic displacement is imposed at the left boundary of the chain,

$$x_1(t) = U_{\text{in}}\, \mathrm{e}^{\mathrm{i}\omega t},$$

where the excitation amplitude U_{in} directly controls the vibration level of the nonlinear system. For a chain composed of N_c unit cells, the steady-state response is computed at each excitation frequency ω using the same Harmonic Balance and pseudo–arc-length continuation method as for the nonlinear dispersion analysis. The frequency response function is defined as

$$H(\Omega) = 20\mathrm{Log}\left|\frac{U_{N_c}(\Omega)}{U_{\text{in}}}\right|, \tag{4.60}$$

where U_{N_c} denotes the complex displacement amplitude of the last waveguide mass at the right end of the chain. Several features observed in the nonlinear dispersion analysis are directly reflected in the frequency response of the finite chain. In particular, the overall shift of the attenuation band with increasing excitation amplitude is fully consistent with the amplitude-dependent behaviour of the complex wavenumber.

For a hardening nonlinearity ($\kappa_3 > 0$), increasing the excitation amplitude shifts the onset of attenuation towards higher frequencies, as clearly visible in the zoomed view shown in Fig. 4.10(a.1). More importantly, the enlarged view in Fig. 4.10(a.2) reveals a pronounced degradation of the filtering performance. The minimum value of H within the attenuation band increases with amplitude, and a local resonance peak emerges inside the nominal stop band. This behaviour indicates that nonlinear interactions enable energy transmission through the chain even in frequency ranges that are strongly attenuated in the linear regime.

In contrast, for a softening nonlinearity ($\kappa_3 < 0$), the onset of attenuation is shifted towards lower frequencies as the excitation amplitude increases, again in agreement with the nonlinear dispersion results. However, the depth of the attenuation band is largely preserved, and no significant resonance peak develops within the band. As a result, the filtering performance remains robust with respect to excitation level, while benefiting from a downward shift of the effective stop-band frequency.

These results highlight a strong correspondence between the nonlinear dispersion properties of the infinite periodic medium and the frequency response of the associated finite structure. They also demonstrate that the sign of the nonlinear stiffness plays a critical role, not only in tuning the position

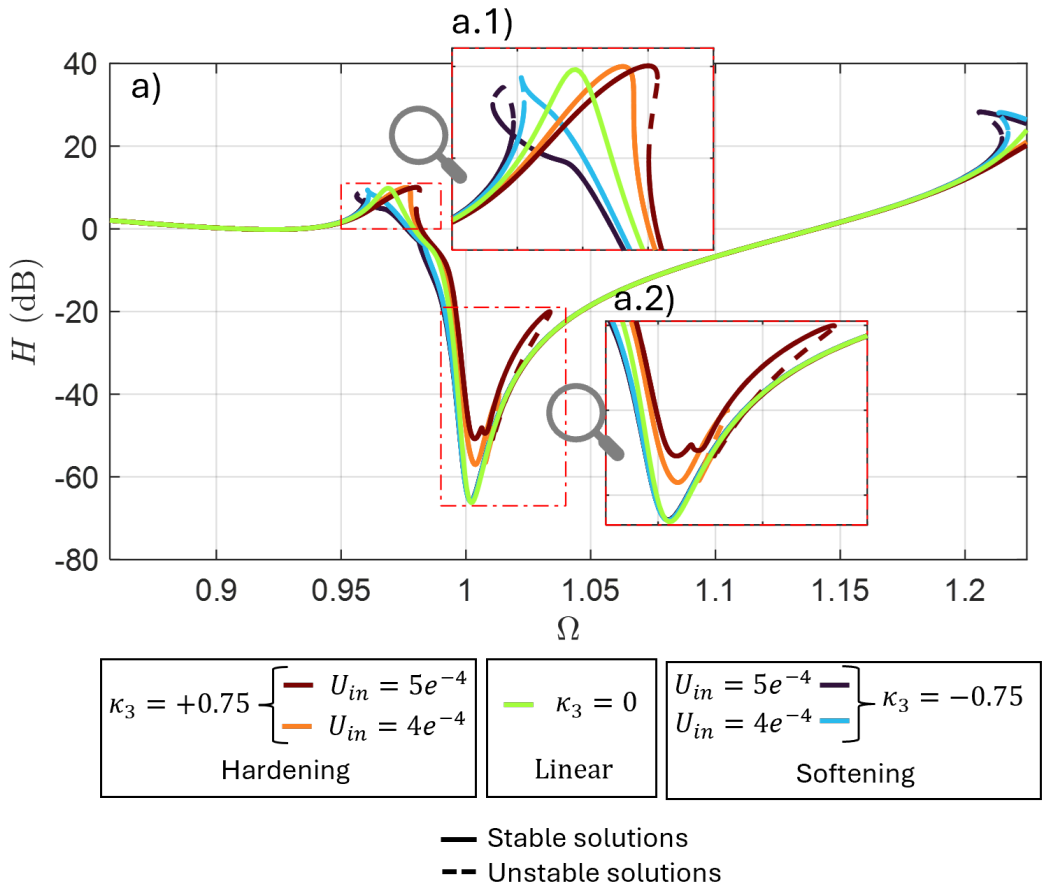

Figure 4.10: Nonlinear frequency response of a finite resonator chain composed of $N_c = 8$ unit cells computed for $N_h = 1$. Transfer function magnitude H as a function of the reduced frequency Ω. Enlarged views highlight the onset of attenuation ($\Omega \in [0.95,\ 0.98]$) and the attenuation region ($\Omega \in [0.98,\ 1.04]$). The linear response is shown in green. For hardening nonlinearities ($\kappa_3 = +0.75$), orange and brown curves correspond to excitation amplitudes $U_{\text{in}} = 4\times10^{-3}$ and 5×10^{-3}, respectively. For softening nonlinearities ($\kappa_3 = -0.75$), light and dark blue curves correspond to the same amplitudes. Solid lines denote stable solutions, while dashed lines indicate unstable branches. Results are obtained for $\alpha = 0.25$, $\mu_2 = 0.25$ and $\xi = 0.01$.

of the attenuation band, but also in governing the robustness of vibration isolation under increasing excitation amplitudes.

4.5 Design guidelines

The analyses presented above show that the filtering performance of a periodic resonator chain is governed by a limited number of key parameters. In the undamped case, the band structure is primarily controlled by the resonator mass fraction μ_2 and the frequency of the resonance α. In the low-frequency limit ($\alpha \to 0$), the trade-off between added mass and relative bandgap width admits a unique optimum, corresponding to a balanced design rather than an extreme configuration.

In the absence of dissipation, the filtering performance of the periodic system can be characterized by a bandgap, i.e., a frequency interval in which propagating Bloch waves are not supported by the corresponding infinite periodic medium. When viscous dissipation is introduced, however, the distinction between propagating and non-propagating waves becomes less sharp, and the filtering performance of a finite chain is more appropriately described in terms of an attenuation band. Unlike the bandgap, which is an intrinsic property of the infinite periodic system, the attenuation band depends on the finite number of cells, the damping level, and the selected attenuation threshold. Here, it is quantified through the relative $-6\,\mathrm{dB}$ bandwidth, denoted by $\beta_{6\mathrm{dB}}$. Waveguide losses are found to have only a limited influence on $\beta_{6\mathrm{dB}}$, whereas resonator losses significantly reduce the attenuation bandwidth and therefore degrade the filtering performance, particularly for short chains.

As $\alpha \to 0$, the optimal mass–bandwidth compromise progressively shifts towards heavier resonators, so that the undamped optimum should be regarded as an upper bound attainable only under low-loss conditions and for sufficiently large numbers of cells. Increasing N_c, however, also penalises mass, length and static stiffness. These observations motivate the design workflow summarised in Fig. 4.11. Starting from structural requirements, the waveguide properties and the number of cells are fixed. The target attenuation frequency then sets α, while resonator losses are largely imposed by material and geometric constraints. On this basis, the resonator parameters (k_2, m_2) are selected so as to maximise the objective $\Phi = (1 - \mu_2)\beta_{6\mathrm{dB}}$. If no satisfactory solution is obtained, the design loop is iterated by adjusting the waveguide, reducing resonator losses, or relaxing the target frequency.

Beyond linear and dissipative effects, geometric nonlinearities may further affect the robustness of the attenuation mechanism by introducing amplitude-dependent shifts or a degradation of attenuation depth. Moreover, the lumped-mass model remains an idealised description of the physical system. For these reasons, the remainder of this chapter revisits the resonant filter concept using a more detailed structural model, in order to assess how the design guidelines derived here translate into realistic periodic implementations.

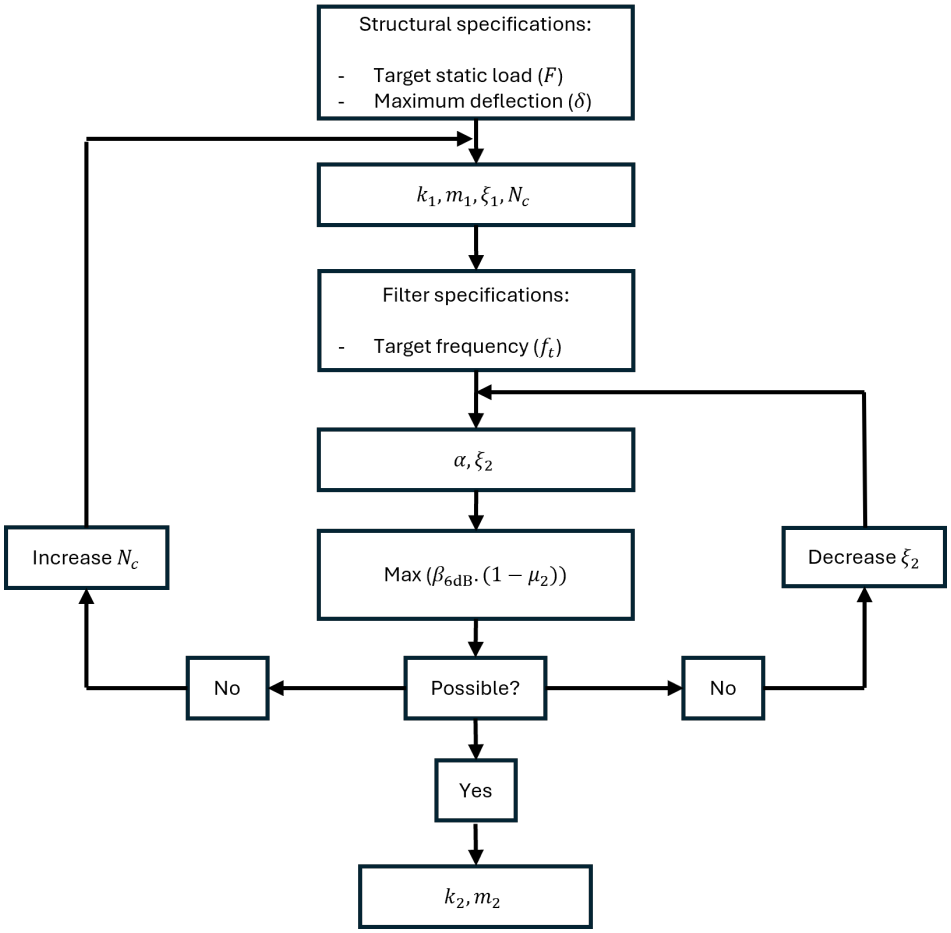

Figure 4.11: Schematic design workflow for the optimisation of a periodic resonant vibration filter based on a resonator chain.

4.6 Structural modeling of the resonant filter

The analyses developed so far were based on an idealised lumped-parameter representation of periodic resonator chains. This study made it possible to isolate the physical origin of locally resonant attenuation bands, derive closed-form mass–bandwidth trade-offs, and study the influence of damping and weak nonlinearities in a controlled setting. However, extending these results to real structures requires a structural model that accounts for the continuous nature of the waveguide. Beyond increased geometric realism, the structural beam-lattice model provides qualitative insights that are inaccessible to lumped descriptions. In particular, it allows the dispersion relation to be analysed for all wave polarisations supported by the waveguide and reveals the existence of multiple complex branches, whose imaginary parts govern the effective attenuation of finite, dissipative structures.

In this section, the resonant filtering concept is therefore revisited using a beam-lattice assemblies as a way to realize the transmission line and the resonators. The objectives are threefold: (i) to introduce a periodic structural waveguide and analyse its dispersion properties; (ii) to integrate a structural resonator and relate its parameters to the non-dimensional quantities (μ_2, α) introduced in the lumped model; (iii) to assess the mass–bandwidth trade-off of the damped and undamped resonant waveguide and compare it with the simplified mass-spring model.

4.6.1 Waveguide definition

The host structure for the resonant filter is a periodic beam-lattice waveguide. Its structural unit cell, hereafter referred to as the *frame*, is shown in Fig. 4.12(a). It consists of three Euler–Bernoulli beams connected at four nodes, forming an open rectangular lattice.

The two vertical beams (green in Fig. 4.12) are aligned with the x-direction and form the primary load-bearing path of the waveguide. The transverse beam (blue) is aligned with the y-direction and provides the mechanical coupling between the two vertical beams.

The unit cell is symmetric with respect to the mid-plane xOz and is defined by the dimensions L_x and L_y.

As detailed in Fig. 4.12(b), the longitudinal beams have rectangular cross-sections $a_{f1} \times b_{f1}$, while the transverse beam has cross-section $a_{f2} \times b_{f2}$. The periodic waveguide is obtained by repeating this frame with pitch L_x along the x-direction and by connecting the right nodes $(2, 4)$ of each cell to the left nodes $(1, 3)$ of the next one. An example composed of five unit cells is shown in Fig. 4.12(c).

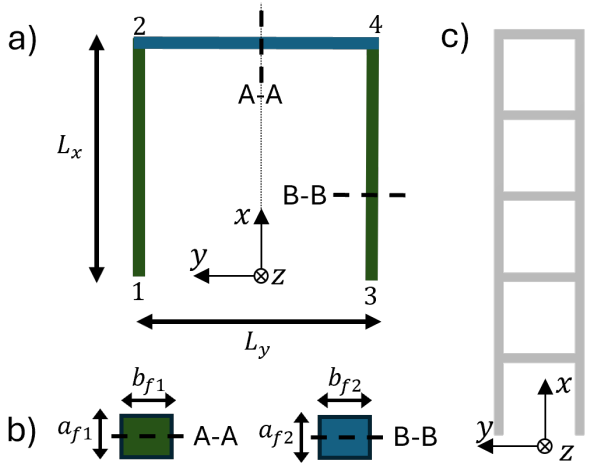

Figure 4.12: Beam-lattice waveguide. (a) Unit cell (frame) and node numbering. (b) Cross-sections of the longitudinal (green) and transverse (blue) beams. (c) Periodic waveguide composed of five unit cells.

4.6.2 Dispersion analysis

The dynamic behaviour of the frame is analysed using the beam spectral-element formulation (see chapter 1) combined with Floquet–Bloch theory. Assuming time-harmonic motion at angular frequency $\omega = 2\pi f$, the unit-cell dynamic equilibrium can be written in the frequency domain as

$$\mathbf{S}_g(\omega)\,\mathbf{d} = \mathbf{F}, \tag{4.61}$$

where $\mathbf{S}_g(\omega)$ is the 24×24 dynamic stiffness matrix of the frame, and $\mathbf{d}$ and $\mathbf{F}$ collect the nodal displacements and forces, respectively.

Periodic boundary conditions between the left (nodes 1 and 3) and right (nodes 2 and 4) interfaces of the cell lead to the Floquet–Bloch relation $\lambda = \mathrm{e}^{\mathrm{i}kL_x}$, from which the complex wavenumber k is

obtained. Solving the resulting eigenproblem over a frequency grid yields the dispersion relation of the infinite waveguide.

Owing to the symmetry of the frame with respect to the planes xOz and xOy, the dispersion problem can be decomposed into four independent symmetry families, denoted SS, SA, AS and AA (see chapter 1). This classification follows the same convention as in the first chapter: the first letter refers to symmetry or antisymmetry with respect to xOz, and the second to xOy. Applying the corresponding kinematic constraints reduces the full problem to four decoupled eigenproblems, each associated with a distinct family of propagating modes.

The resulting dispersion diagrams are shown in Fig. 4.13. Figure 4.13(a) presents the full dispersion of the frame, while Figs. 4.13(b)–(e) show the condensed problem for the SS, SA, AS and AA families. Each branch is colour-coded according to the dominant polarization of the associated eigenvector (green: x, red: y, blue: z), and representative mode shapes are displayed for selected points.

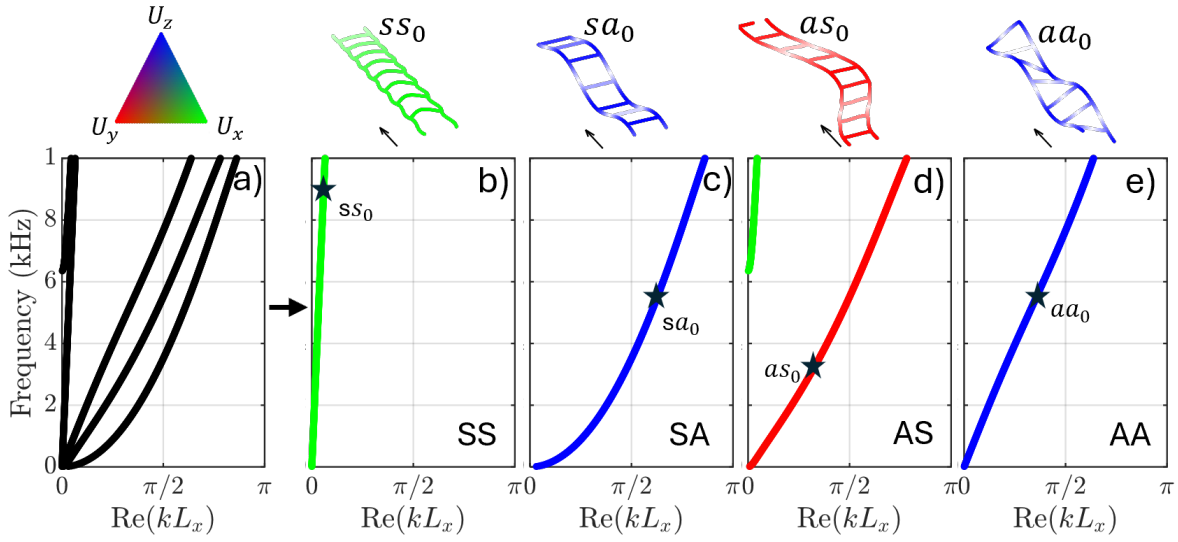

Figure 4.13: Dispersion of the beam-lattice waveguide. (a) Full dispersion diagram of the frame. (b)–(e) Dispersion diagrams for the SS, SA, AS and AA symmetry families. Colours indicate the dominant polarization of the mode (green: x, red: y, blue: z). Representative mode shapes are shown above each sub-figure and correspond to the black star markers positioned on the dispersion branches.

In the following, attention is restricted to the AS family, which includes bending modes polarised along the y-direction. A reference frequency for this family is defined as the first bending eigenfrequency f_{AS} of an isolated frame subjected to AS symmetry conditions. The corresponding angular frequency $\omega_{\mathrm{AS}} = 2\pi f_{\mathrm{AS}}$ plays a role analogous to $\omega_1 = \sqrt{k_1/m_1}$ in the lumped model.

4.6.3 Resonator design

A local resonator is now integrated into the frame to form a resonant unit cell, illustrated in Fig. 4.14(a). The resonator is composed of seven beam elements with three different cross-sections, shown in Fig. 4.14(b).

Four slender beams (red), aligned with the x-direction and symmetrically placed, act as compliant stiffness elements. Their geometry is chosen such that bending along y is dominant. The central beam

(black) of length L_m acts as the resonant mass, while two short junction beams (violet) ensure the mechanical connection. When isolated, the first mode of this resonator corresponds to an almost rigid translation of the mass along the y-direction, ensuring efficient coupling with the AS bending motion of the waveguide.

The resonant mass is defined as

$$m_r = \rho \left(a_m b_m L_m + 2 a_j b_j L_j\right), \tag{4.62}$$

while the mass of the bare frame is denoted m_c. The non-dimensional resonator mass fraction is then

$$\mu_2 = \frac{m_r}{m_c + m_r}. \tag{4.63}$$

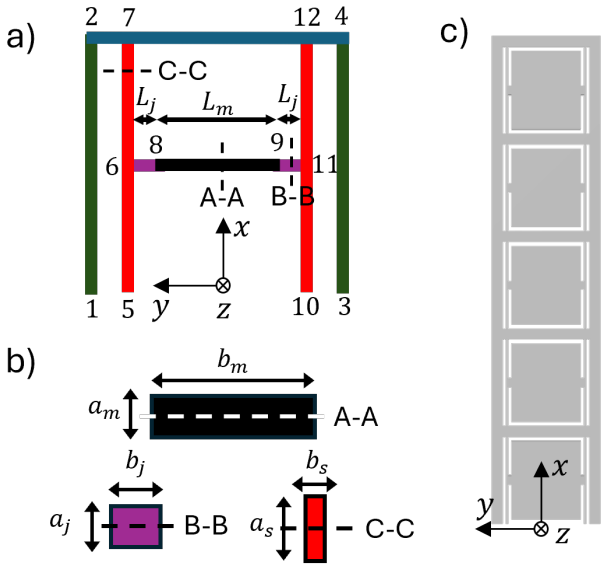

Figure 4.14: Resonant waveguide. (a) Resonant unit cell and node numbering. (b) Cross-sections of the resonator beams (red/black/violet). (c) Periodic waveguide composed of five resonant unit cells.

To establish a direct correspondence with the lumped mass–spring model, we introduce

$$\alpha = \frac{f_r}{f_{\mathrm{AS}}}, \tag{4.64}$$

where f_r denotes the resonance frequency of the integrated resonator and f_{AS} is the reference AS bending frequency of the bare waveguide (presented above). The reduced frequency is then defined as

$$\Omega = \frac{f}{f_r}, \tag{4.65}$$

consistently with the non-dimensional formulation used for the lumped model.

4.6.4 Mass–bandwidth trade-off

We first analyse the filtering performance of the resonant waveguide in the absence of damping. All geometric and material parameters of the frame are kept fixed, and for each pair (μ_2, α) the resonator geometry is tuned so as to satisfy the target mass fraction and the frequency of the bandgap, as described in the previous subsection.

Figure 4.15 presents representative AS dispersion diagrams for a fixed mass fraction $\mu_2 = 0.25$ and three values of α. These examples illustrate three typical scenarios for the closure of the locally resonant bandgap.

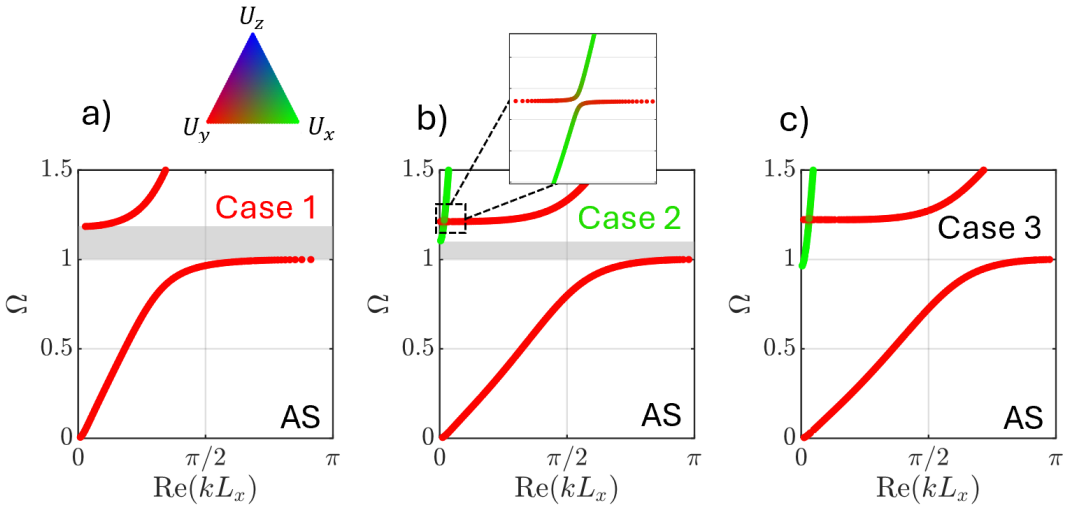

Figure 4.15: Dispersion of the resonant unit cell (AS family) for $\mu_2 = 0.25$ and (a) $\alpha = 0.5$, (b) $\alpha = 1.1$, (c) $\alpha = 1.7$. Colours indicate the dominant polarization of the propagating mode (green: x, red: y). Grey rectangles highlight the AS-polarized bandgap.

In the first case, the bandgap opens and closes between two branches of identical bending polarization along y. This situation corresponds to a purely locally resonant mechanism and is directly comparable to the lumped mass–spring model. In the second case, although a bandgap still exists, its upper edge is closed by a cut-off branch with a different dominant polarization. Finally, in the third case, a cut-off branch appears below the resonant frequency, which prevents the formation of an effective attenuation band.

A systematic sweep over the design space (μ_2, α) is then performed. For each configuration, the AS dispersion relation is computed and the effective relative bandgap width β is extracted. The results are summarised in Fig. 4.16.

Figure 4.16(a) shows that large effective bandgaps are obtained in a restricted region of the design space, located near the boundary between cases 1 and 2. In this region, the locally resonant mechanism remains dominant, while the proximity of an additional structural branch limits the attainable bandwidth. Moving further into cases 2 or 3 leads to a rapid degradation of the filtering performance, as the bandgap is partially or fully closed by cut-off modes that are not controlled by the resonator.

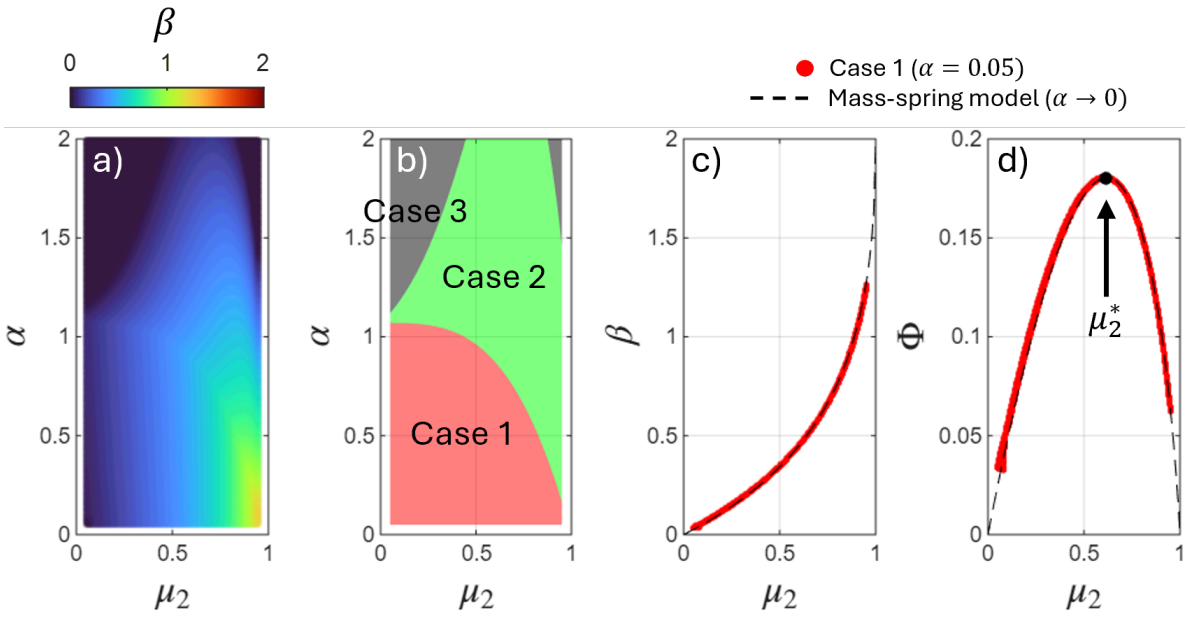

Figure 4.16: Mass–bandwidth trade-off for the undamped resonant waveguide. (a) Colormap of the effective relative bandgap width β as a function of μ_2 and α. (b) Classification of bandgap closure scenarios: case 1 (pure resonant bandgap), case 2 (closure by a cut-off branch), and case 3 (no effective bandgap). Evolution of (c) β and (d) Φ. Red markers indicate the results for case 1 ($\alpha = 0.05$), while the black dashed curve recalls the Pareto front of the lumped mass–spring model in the limit $\alpha \to 0$. .

For configurations belonging to case 1, the effective bandwidth β increases monotonically with the resonator mass fraction μ_2, as shown in Fig. 4.16(c). More importantly, when $\alpha \to 0$, the Pareto front obtained from the beam-lattice model closely follows that of the lumped mass–spring chain. For instance, at $\alpha = 0.05$, the maximum of the trade-off function $\Phi = (1-\mu_2)\,\beta$ is obtained for $\mu_2^\star \approx 0.61$, in excellent agreement with the analytical optimum $\mu_2^\star \approx 0.618$ predicted by the simplified model.

This result confirms that, in the undamped case and provided that the resonant bandgap is not contaminated by cut-off branches, the optimal compromise between added mass and attenuation bandwidth is primarily governed by the local resonant mechanism itself. The structural beam-lattice model therefore reproduces not only the qualitative trends, but also the quantitative optimal design identified using the idealised lumped-parameter model. At the same time, Fig. 4.16(b) show that this agreement is conditional. The structural model explicitly identifies regions of the parameters space where additional waveguide branches interfere with the resonant mechanism. In these regions, the lumped model fails to predict both the existence and the width of the attenuation band, highlighting the necessity of a full structural dispersion analysis.

In the following, material dissipation is introduced in the beam-lattice model to assess how viscous losses and finite chain length modify the mass–bandwidth trade-off and to what extent the undamped optimal design is relevant to predict realistic situations.

4.6.5 Mass–attenuation trade-off

We now investigate the influence of material dissipation and finite chain length on the filtering performance of the resonant waveguide. The geometric parameters of the frame and the resonator

are kept identical to those used in the undamped analysis, while dissipation is introduced through a complex Young's modulus

$$E = E_r\,(1 + 2\mathrm{i}\,\xi), \tag{4.66}$$

where ξ denotes a uniform loss factor (applied to all beam elements of the waveguide and the resonator).

As in the lumped mass–spring model, the filtering performance of a damped, finite structure is quantified through a Frequency Response Function (FRF) computed for a chain of N_c identical unit cells. The FRF relates the response at the free end of the chain to a prescribed excitation applied at the opposite end and provides a direct measure of the attenuation achieved by the resonant filter.

Finite-chain formulation and frequency response

The degrees of freedom of the unit cell are reordered as $[L, I, R]$, where L and R denote the left and right ports (each consisting of 4 nodes with 6 DOFs per node, i.e., 24 DOFs per port), and I collects the internal DOFs. With this ordering, the global dynamic stiffness matrix is expressed as

$$\mathbf{S}_g(\omega) = \begin{bmatrix} \mathbf{S}_{LL} & \mathbf{S}_{LI} & \mathbf{S}_{LR} \\ \mathbf{S}_{IL} & \mathbf{S}_{II} & \mathbf{S}_{IR} \\ \mathbf{S}_{RL} & \mathbf{S}_{RI} & \mathbf{S}_{RR} \end{bmatrix}. \tag{4.67}$$

A condensation of the internal DOFs I yields an equivalent two-port dynamic stiffness matrix

$$\bar{\mathbf{S}}_g(\omega) = \begin{bmatrix} \bar{\mathbf{S}}_{LL} & \bar{\mathbf{S}}_{LR} \\ \bar{\mathbf{S}}_{RL} & \bar{\mathbf{S}}_{RR} \end{bmatrix} = \begin{bmatrix} \mathbf{S}_{LL} & \mathbf{S}_{LR} \\ \mathbf{S}_{RL} & \mathbf{S}_{RR} \end{bmatrix} - \begin{bmatrix} \mathbf{S}_{LI} \\ \mathbf{S}_{RI} \end{bmatrix} \mathbf{S}_{II}^{-1} \begin{bmatrix} \mathbf{S}_{IL} & \mathbf{S}_{IR} \end{bmatrix}, \tag{4.68}$$

which depends only on the left and right port DOFs.

The transmission through a chain of N_c cells is then evaluated by an impedance/propagation recursion. Let $\mathbf{Z}_j$ denote the impedance seen from the left of the j-th cell and $\mathbf{R}_j$ the corresponding transmission matrix. For a given frequency, they satisfy the backward recurrence

$$\mathbf{R}_j = \left(\bar{\mathbf{S}}_{RR} + \mathbf{Z}_{j+1}\right)^{-1} \bar{\mathbf{S}}_{RL}, \qquad \mathbf{Z}_j = \bar{\mathbf{S}}_{LL} - \bar{\mathbf{S}}_{LR}\,\mathbf{R}_j, \tag{4.69}$$

with a free termination at the right end,

$$\mathbf{Z}_{N_c+1} = \mathbf{0}. \tag{4.70}$$

Once the impedance recursion is completed, the displacement at the left port of each cell is obtained from the forward propagation

$$\mathbf{u}^{(j+1)} = -\,\mathbf{R}_j\,\mathbf{u}^{(j)}, \qquad \mathbf{u}^{(1)} = \mathbf{u}_L, \qquad \mathbf{u}^{(Nc+1)} = \mathbf{u}_R \tag{4.71}$$

where $\mathbf{u}_L$ and $\mathbf{u}_R$ is respectively the displacement vector prescribed at the left end and right end of the chain. This impedance-based formulation is numerically stable and computationally efficient even for large N_c.

To focus on the bending-dominated behaviour of interest, a unit displacement is prescribed on the y-translation degrees of freedom of the four input nodes at the left end of the chain. The response is extracted on the corresponding y-translation degrees of freedom at the right end. The scalar FRF is defined as

$$H_y(\Omega) = 20\mathrm{Log}\frac{\|\mathbf{u}_{R,y}\|}{\|\mathbf{u}_{L,y}\|}, \tag{4.72}$$

where $\Omega = f/f_{\mathrm{AS}}$ is the reduced frequency. The attenuation bandwidth $\beta_{6\mathrm{dB}}$ is defined from the frequency interval over which $H_y(\Omega)$ falls below -6 dB.

Complex dispersion and finite-chain response

The relationship between complex dispersion properties and finite-chain attenuation is illustrated in Fig. 4.17 for a representative configuration with $\mu_2 = 0.5$ and $\alpha = 0.5$.

Figures 4.17(a) and (b) show the imaginary and real parts of the AS wavenumber kL_x in the undamped case $\xi = 0$. The grey rectangle highlights the bandgap predicted from purely real dispersion branches.

Compared with the previous mass–spring model, the complex dispersion behaviour is markedly different. Even in the lossless configuration, a complex branch with non-zero real and imaginary parts of kL_x traverses the nominal bandgap region. Although only weakly propagative, this branch affects the attenuation performance of the finite filter.

The corresponding FRF of a chain with $N_c = 5$ cells is reported in Fig. 4.17(c). The in-gap response differs from that of the mass–spring model, notably through the presence of multiple attenuation peaks rather than a single one located near the resonator resonance. This multi-peak pattern is characteristic of inertial amplification mechanisms [172–174]. The resonator deformation is primarily a translation of the internal mass along the y-axis (see Fig. 4.17, s.2); within the bandgap, this translation couples with a rotational motion about the z-axis (see Fig. 4.17, s.1). The resulting rotation increases the effective inertia and amplifies the translational deformation.

To highlight the influence of dissipation, Figs. 4.17(a.1), (b.1) and (c.1) provide zoomed views of the dispersion and FRF for increasing loss factors $\xi = 0$, 0.05 and 0.1. As damping increases, the imaginary part of the wavenumber inside the gap is progressively reduced, which directly translates into a decrease of the maximum attenuation. In contrast, the attenuation bandwidth $\beta_{6\mathrm{dB}}$ is noticeably less sensitive to damping than in the mass–spring case. .

These observations highlight the limitations of an overly simplified model that accounts for a single wave type only. By neglecting the coupling between the different polarizations and the resonator, such a reduced description may misrepresent the attenuation performance of the filter in a non-negligible way.

To delineate the range of validity of this simplification, Fig. 4.18 compares the evolution of the attenuation bandwidth $\beta_{6\mathrm{dB}}$ and of the trade-off function Φ for the beam-lattice model and for the lumped mass–spring chain, for different numbers of cells N_c. Results are reported for $\alpha = 0.1$ (so that only case 1 occurs), $\xi = 0.01$, and for resonator mass fractions in the range $\mu_2 \in [0.05, 0.95]$.

For both models, increasing N_c widens the attenuation band and shifts the optimal mass fraction

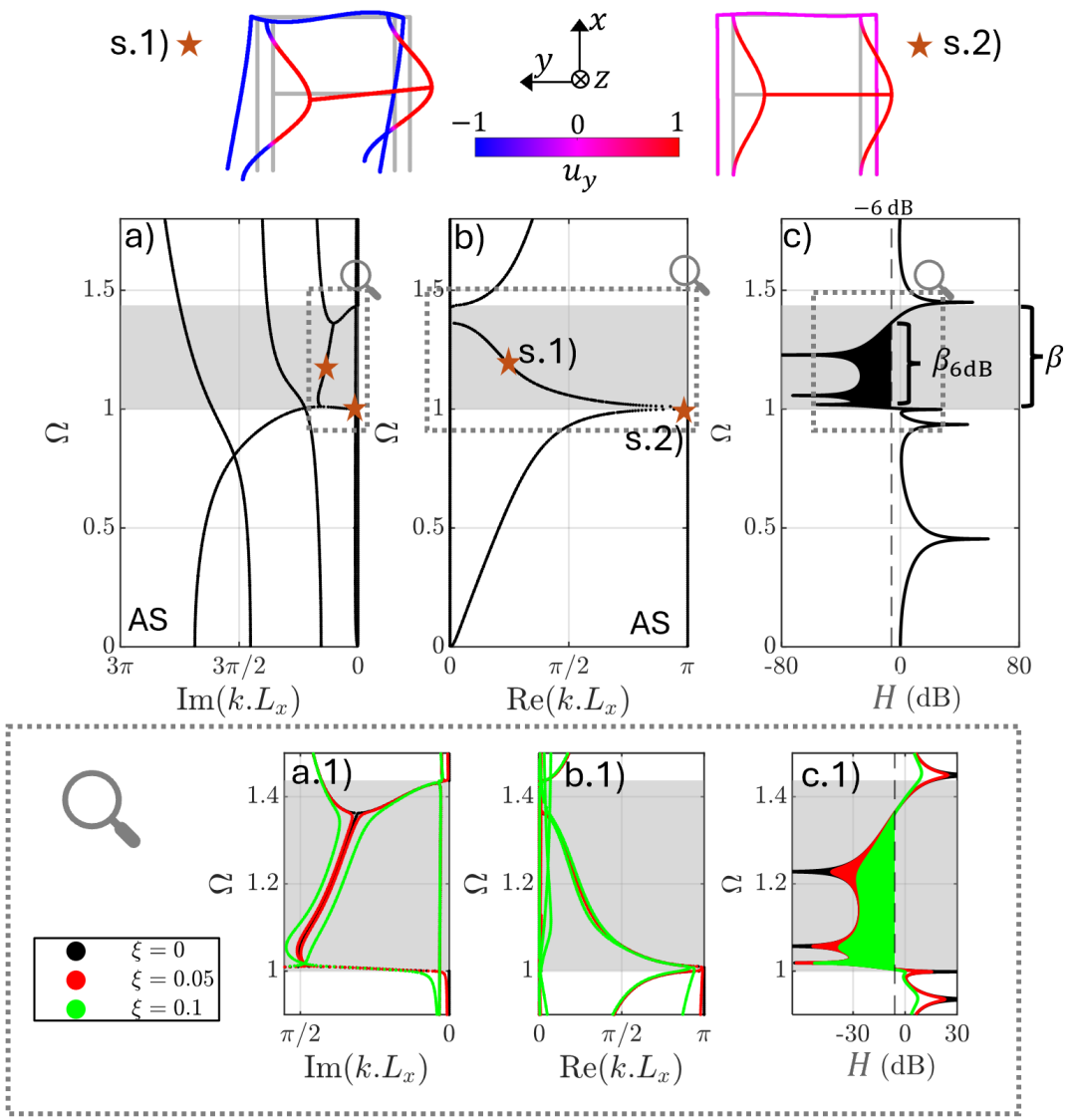

Figure 4.17: Complex dispersion and finite-chain response of the damped resonant waveguide for $\mu_2 = 0.5$ and $\alpha = 0.5$. The AS-family dispersion of the unit cell is shown through (a) the imaginary part $\mathrm{Im}(kL_x)$ and (b) the real part $\mathrm{Re}(kL_x)$ of the complex wavenumber in the undamped case ($\xi = 0$). (c) Corresponding frequency response function H_y (in dB) of a finite chain composed of $N_c = 5$ unit cells. s.1) and s.2) respectively show the mode shape associated with the complex solution within the bandgap and the edge mode at the resonance frequency. Sub-figures (a.1), (b.1) and (c.1) present zoomed views over $\Omega \in [0.9,\ 1.45]$ for increasing loss factors: $\xi = 0$ (black), $\xi = 0.05$ (red) and $\xi = 0.1$ (green)

towards lower values. For sufficiently long chains, the optimal mass fractions and bandwidths predicted by the beam-lattice model closely match those obtained with the lumped model. In contrast, for small N_c, the polarization-coupling effects captured by the beam model are no longer negligible compared with the weaker attenuation provided by a limited number of resonators. As a result, the optima predicted by the two models differ, with the beam-lattice model yielding a beneficial shift towards lower added mass for a comparable attenuation bandwidth.

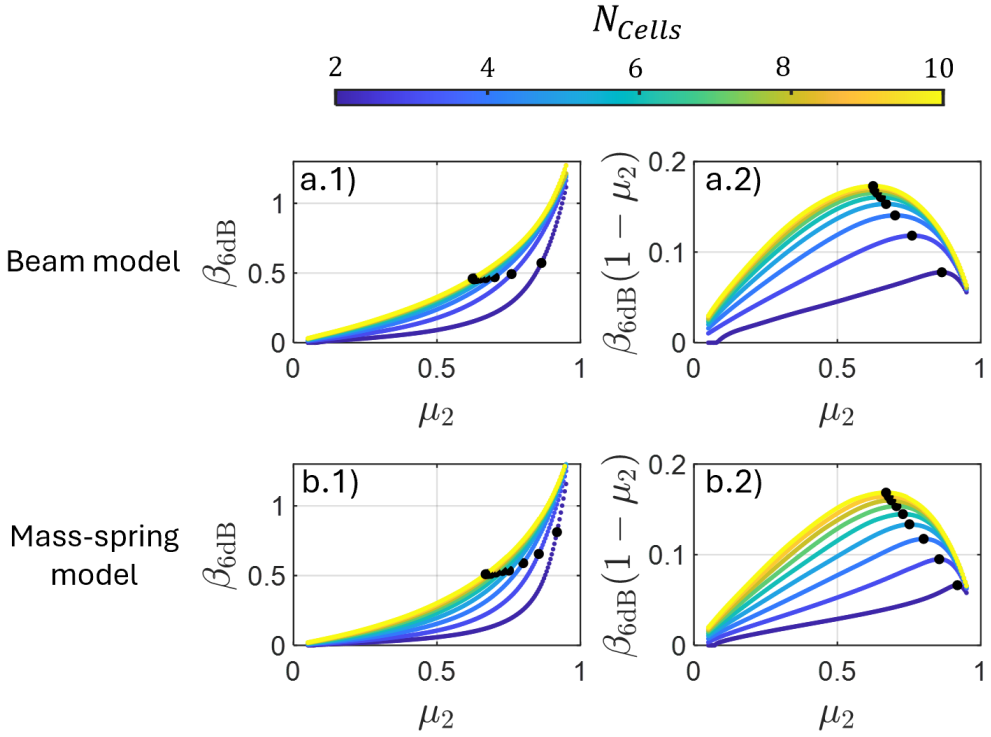

Figure 4.18: Comparison of the damped mass–bandwidth trade-off for $\alpha = 0.1$ and $\xi = 0.01$. (a.1) Evolution of the attenuation bandwidth $\beta_{6\text{dB}}$ with μ_2 for the beam-lattice model. (b.1) Corresponding evolution for the lumped mass–spring model. (a.2) Trade-off function $\Phi = (1-\mu_2)\beta_{6\text{dB}}$ for the beam-lattice model. (b.2) Corresponding trade-off for the lumped model. Curves correspond to increasing numbers of cells N_c (from blue to yellow); black dots indicate the optimal points corresponding to the maximum of each trade-off function Φ .

4.7 Experimental validation of the resonant waveguide filter

This section presents the experimental validation of the resonant waveguide filter designed and analysed in the previous sections. The objective is twofold. First, we confirm the ability of the beam-lattice model to predict the attenuation performance of a finite resonant filter in the linear regime. Second, we investigate the influence of geometric nonlinearities on the amplitude-dependent response of the structure and relate the experimental observations to the predictions formulated in section 4.4.

4.7.1 Prototype design and experimental setup

The resonant filter is manufactured by additive manufacturing in PLA. The mechanical properties of the material were independently characterised in [194] and are recalled here:

$$E = 3.4\ \text{GPa}, \qquad \rho = 1100\ \text{kg m}^{-3}, \qquad \nu = 0.33, \qquad \xi = 0.01.$$

The prototype consists of five identical locally resonant unit cells arranged in series.

The geometry of the structural frame (waveguide) is defined by

$$L_x = 50\ \text{mm}, \qquad L_y = 50\ \text{mm}, \qquad a_{f1} = a_{f2} = 5\ \text{mm}, \qquad b_{f1} = b_{f2} = 5\ \text{mm},$$

which yields a unit-cell mass without resonator of

$$m_f = 3.9 \text{ g}.$$

From the AS-family dispersion of the bare frame, the reference bending frequency is

$$f_{\text{AS}} = 654.78 \text{ Hz}.$$

The resonator geometry is chosen so as to target a low-frequency attenuation band. The stiffness beams have cross-section

$$a_s = 5 \text{ mm}, \qquad b_s = 1.3 \text{ mm},$$

the central mass beam has

$$a_m = 18.4 \text{ mm}, \qquad b_m = 36 \text{ mm}, \qquad L_m = 32 \text{ mm},$$

and the junction beams connecting the mass to the stiffness elements are defined by

$$L_j = 2.5 \text{ mm}, \qquad a_j = 5 \text{ mm}, \qquad b_j = 4 \text{ mm}.$$

The first resonance frequency of the resonator is then

$$f_r = 120 \text{ Hz},$$

with an effective resonant mass

$$m_r = 23.7 \text{ g}.$$

The corresponding non-dimensional parameters are

$$\mu_2 = \frac{m_r}{m_r + m_f} \approx 0.86, \qquad \alpha = \frac{f_r}{f_{\text{AS}}} \approx 0.18. \tag{4.73}$$

A photograph of the experimental setup is shown in Fig. 4.19(a). The prototype is clamped over a length of 40 mm using an adjustable vice mounted on an electrodynamic shaker. The structure is oriented such that the y-axis coincides with the excitation direction. A base acceleration A_b is imposed as a swept sine excitation between 80 and 350 Hz. The response at the free end of the filter is measured using a laser Doppler vibrometer, which provides the velocity V_y along the y-direction.

4.7.2 Linear regime

Figures 4.19(b) and (c) show the dispersion of the corresponding damped unit cell in the AS family, computed using the beam-lattice model. Figure 4.19(b) displays the imaginary part $\text{Im}(kL_x)$ of the eigenvalues, while Fig. 4.19(c) shows their real part $\text{Re}(kL_x)$. The colour scale from green to red indicates the dominant polarization of the mode shape, ranging from motion along x (green) to motion along y (red). In both plots, the grey rectangle highlights the bandgap predicted for the corresponding

unit cell in the undamped configuration.

The experimental frequency response function is defined as the ratio between the output velocity and the base acceleration,

$$H^{y}_{\mathrm{exp}}(f) = 20\log_{10}\left|\frac{\mathrm{i}\,\omega\, V_y(f)}{A_b(f)}\right|, \tag{4.74}$$

where both $A_b(f)$ and $V_y(f)$ are expressed in RMS amplitude.

For a low excitation level, corresponding to a base acceleration amplitude $A_b \approx 4.9\ \mathrm{m\,s^{-2}}$, the measured FRF is shown in black in Fig. 4.19(d). The blue curve shows the FRF predicted by the beam-lattice model using the same input and output degrees of freedom, while the yellow curve corresponds to the prediction of the lumped mass–spring model. The horizontal black line at $H_{\mathrm{lim}} = -6$ dB is used to define the effective attenuation bandwidth $\beta_{6\mathrm{dB}}$.

The experimental FRF exhibits a pronounced attenuation within the predicted bandgap, approximately spanning the frequency range [120, 316] Hz. The frequencies at which the response crosses the −6 dB threshold are $f_L \approx 120$ Hz and $f_H \approx 295$ Hz, yielding

$$\beta_{6\mathrm{dB}} = \frac{2(f_H - f_L)}{f_H + f_L} \approx 0.84. \tag{4.75}$$

This value is in excellent agreement with the beam-model predictions. Compared with the lumped mass–spring model, the beam-lattice formulation reproduces the experimentally observed attenuation level within the stop band more accurately, as it can capture additional evanescent contributions.

4.7.3 Nonlinear regime

We now investigate experimentally the influence of geometric nonlinearities on the dynamic response of the resonant waveguide filter. The nonlinear dispersion analysis presented in Section 4.4 indicated that amplitude-dependent effects may significantly alter both the width and the depth of the attenuation band. The experimental study therefore focuses on identifying the source of nonlinearity at the resonator level and on assessing its impact on the response of a finite resonator chain.

Figure 4.20 characterises the nonlinear behaviour of a single resonator. A finite-element model of a unit cell, shown in Fig. 4.20(a), is used to compute the static force–displacement relation by imposing a transverse displacement u_y at the centre of the resonator mass and extracting the corresponding reaction force F_y. The resulting curve, reported in Fig. 4.20(c), is well approximated by a cubic polynomial of the form $F_y = k_2 u_y + k_3 u_y^3$, revealing a hardening geometric nonlinearity. This behaviour originates from the flexural deformation of the slender stiffness beams connecting the resonator mass to the frame.

The dynamic consequences of this nonlinearity are illustrated in Fig. 4.20(d), which shows the experimentally measured FRF of a single resonator for increasing excitation levels. As the base acceleration increases, the resonance frequency shifts towards higher values and jump phenomena appear, consistently with a hardening nonlinear response.

The impact of this nonlinearity on the filtering performance of the complete five-cell resonant waveguide is shown in Fig. 4.21. As the excitation level increases, the onset frequency of the

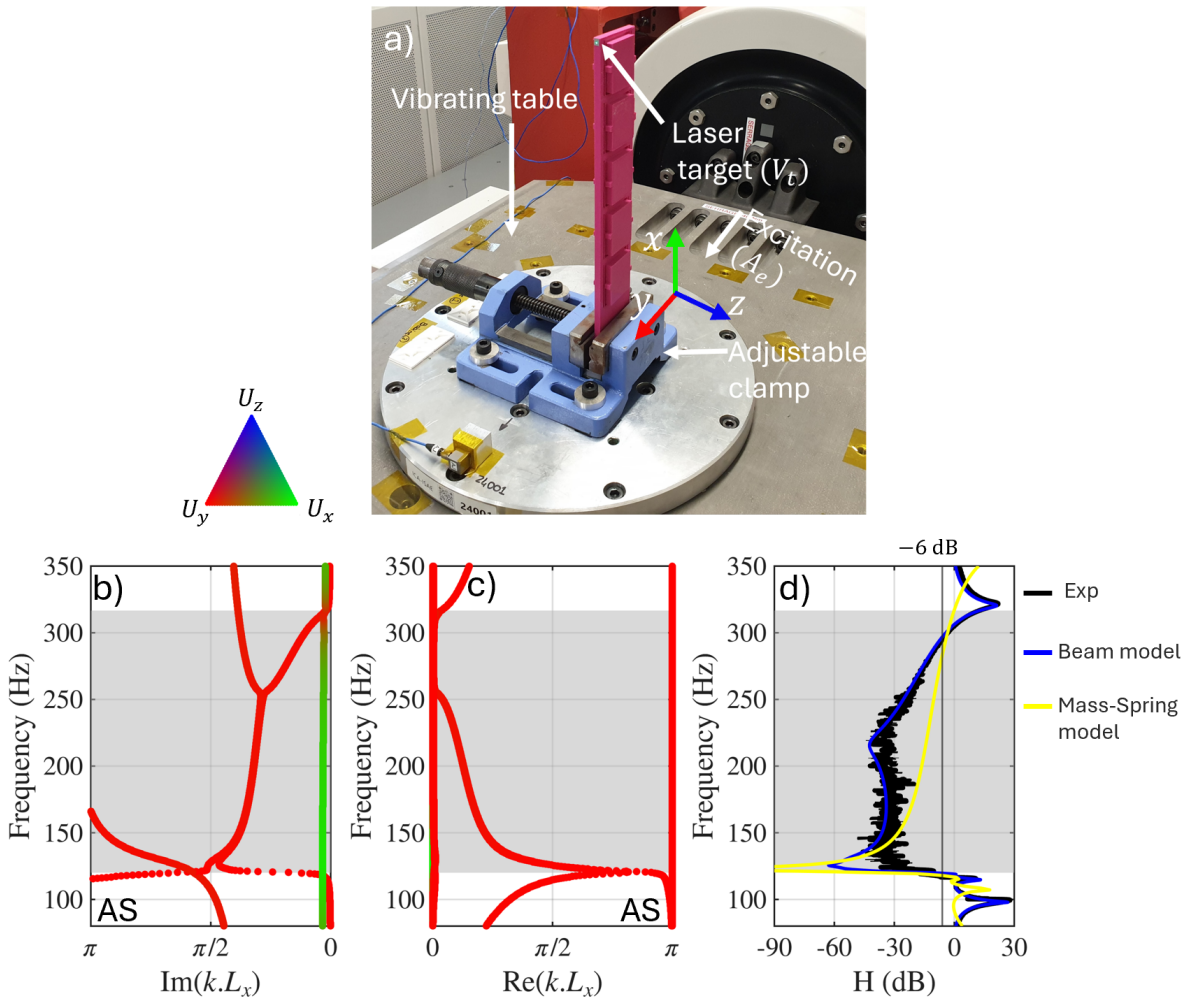

Figure 4.19: Experimental validation of the resonant waveguide filter. (a) Photograph of the experimental setup showing the five-cell resonant filter clamped at the base and excited by a shaker, with a laser vibrometer measuring the response at the free end. (b) Imaginary part $\mathrm{Im}(kL_x)$ and (c) real part $\mathrm{Re}(kL_x)$ of the AS eigenvalues of the damped unit cell, computed using the beam-lattice model; the colour scale from green to red indicates the dominant polarization from x- to y-motion. (d) Experimental FRF H^y_{exp} (black) compared to numerical FRFs from the beam-lattice model (blue) and the lumped mass–spring model (yellow). The grey rectangle indicates the undamped bandgap, and the horizontal line at -6 dB defines the attenuation bandwidth $\beta_{6\mathrm{dB}}$.

attenuation band progressively shifts towards higher values. Above a critical acceleration level (around $1.2\,g$), a pronounced resonance peak emerges inside the nominal attenuation band, leading to a strong reduction of the achievable attenuation.

These observations mirror the theoretical predictions of the nonlinear dispersion analysis, which revealed the coexistence of multiple branches and unstable solutions in the vicinity of the resonant frequency. They confirm experimentally that geometric nonlinearities, although weak at low amplitudes, can significantly affect the robustness of resonant filtering under realistic vibration levels.

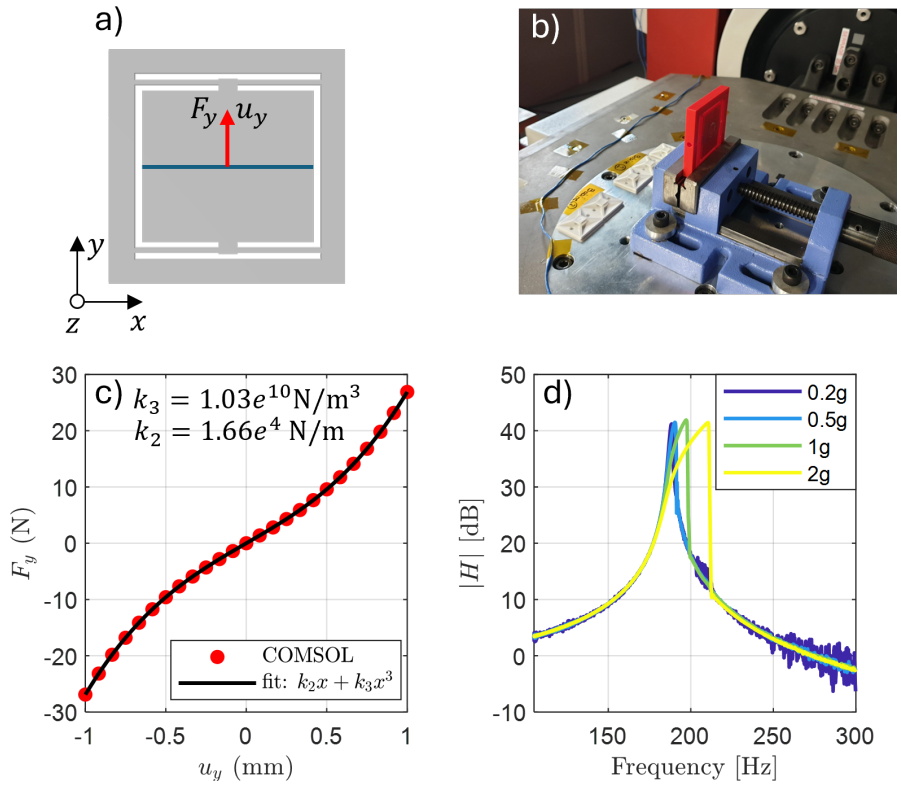

Figure 4.20: Characterisation of the geometric nonlinearity of a single resonator. (a) Finite-element model used to compute the static force–displacement relation. (b) Photograph of the experimental setup for dynamic testing of a single unit cell. (c) Static force–displacement relation obtained from finite-element simulations (red markers) and cubic polynomial fit (black line). (d) Measured frequency response function of the single resonator for increasing base excitation amplitudes.

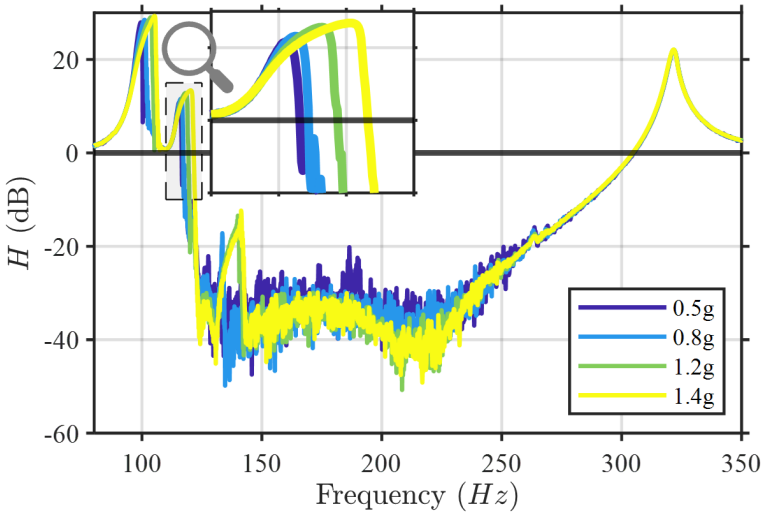

Figure 4.21: Measured frequency response function H of the five-cell resonant filter, obtained from the same experimental configuration as in Fig. 4.19(a), but for higher excitation levels. The curves correspond to base acceleration amplitudes of 0.5 g (dark blue), 0.8 g (light blue), 1.2 g (green), and 1.4 g (yellow). Zoomed views highlight the amplitude-dependent shift of the attenuation band around 130 Hz

4.8 Conclusion

This chapter investigated the design and performance limits of locally resonant vibration filters based on periodic resonator chains. Starting from an idealised lumped mass–spring description, closed-form relationships were derived to clarify how the resonance frequency and the resonator mass fraction govern the width and location of low-frequency attenuation bands. In the undamped limit, this analysis revealed the existence of an intrinsic optimal compromise between added mass and relative bandwidth, which emerges independently of the specific structural realisation and provides a useful reference for design.

The study was then extended to dissipative configurations, which necessitated a finite-chain analysis. In this context, the strict notion of a bandgap is replaced by that of an attenuation band, and the optimal mass–bandwidth trade-off progressively shifts towards heavier resonators as damping increases and/or the number of cells decreases. Geometric nonlinearities were further shown to introduce amplitude-dependent dispersion effects, leading to shifts of the attenuation band and, in some cases, to a degradation of the filtering performance at high excitation levels. These results highlight the importance of accounting for dissipation and nonlinear effects when translating idealised designs into practical structures.

To bridge the gap between lumped models and real implementations, the resonant filter was next analysed using a beam-lattice structural description. The comparison confirmed that, in the undamped case and away from cut-off branches, the simplified mass–spring model accurately predicts both the trends and the optimal design parameters of the structural waveguide. In contrast, for damped finite chains, evanescent and weakly propagative modes captured by the beam-lattice formulation play a significant role and must be included to correctly predict attenuation levels. An experimental validation on a five-cell additively manufactured prototype further confirmed these findings, and demonstrated both the relevance and the limitations of the resonant filtering concept under realistic conditions.

Overall, this chapter establishes a design methodology for polarization-selective resonant filters, clarifies the respective roles of mass ratio, resonance frequency, damping and nonlinearity, and identifies the key mechanisms that limit their performance in practice. A fundamental limitation nevertheless remains: the filters considered here are intrinsically selective with respect to the polarization of the propagating waves. In multi-axial structural environments, such polarization-selective attenuation may leave significant transmission paths open.

These observations naturally motivate the next step of this work, addressed in Chapter 5, which aims at extending the resonant-filtering strategy towards an *absolute* objective. By combining several oriented local resonators within a single lattice waveguide, the goal is to simultaneously inhibit wave propagation for all symmetry families, and to assess the feasibility, performance limits and design trade-offs of absolute resonant vibration filters in realistic structural configurations.

CHAPTER 5

Design of an absolute resonant vibration filter

Contents

5.1 Introduction . . . 103
5.2 Definition of the lattice waveguide . . . 104
5.2.1 Dispersion analysis . . . 105
5.2.2 Reference frequencies . . . 106
5.3 Definition of the local resonators . . . 106
5.4 Mass–bandwidth trade-off . . . 108
5.4.1 Illustrative scenarios for a fixed mass fraction . . . 109
5.4.2 Parametric sweep . . . 110
5.4.3 Influence of resonant mass distribution . . . 112
5.5 Performance limits of the damped absolute resonant filter . . . 114
5.6 Design guidelines . . . 115
5.7 Development of an applied demonstrator . . . 117
5.7.1 System-level demonstrator and interfaces . . . 119
5.7.2 Numerical model . . . 120
5.7.3 Performance indicators . . . 122
5.7.4 Role of the x-oriented resonator . . . 124
5.7.5 Experimental analysis . . . 125

5.1 Introduction

We saw in the previous chapter, that locally resonant metastructures provide a practical strategy to block elastic-wave propagation at subwavelength scales, enabling low-frequency stopbands without relying on Bragg scattering. In structural waveguides, vibrations may propagate through several polarizations (compression, bending, and torsion). As a result, to provide an effective filtering effect, a bandgap has to be effective for all polarization simultaneously.

Designing an *absolute* low-frequency filter, however, remains challenging. In practical architectures, the resonators that effectively couple to the different polarizations are generally not independently tunable [191, 218], which severely restricts the design space and limits the achievable performance. Moreover, absolute bandgaps predicted by dispersion analysis do not necessarily translate into uniform attenuation in a finite size filter: the strong stiffness contrasts between wave polarizations can lead to markedly uneven filtering levels [119, 219, 220].

This chapter proposes a strategy to achieve a wide, tunable, absolute bandgap by extending the methodology established in the previous chapter. Three main contributions are presented: (i) a multi-resonant unit cell enabling targeted tuning of resonators coupled to each of the four symmetry families; (ii) an analysis of finite, damped filters explaining why attenuation can remain polarization-dependent even when an absolute bandgap is predicted in the undamped case; (iii) an experimental validation on an applicative demonstrator under tri-axial excitation, supported by a 3D numerical model.

A cubic lattice waveguide is first defined and the implementation of the multiple resonators is described. The absolute mass–bandwidth trade-off is then examined in the undamped case, with emphasis on the distribution of resonant mass among the different polarizations. Performance limits in damped finite chains are then characterized and optimization guidelines are proposed. The approach is then validated on a laboratory-scale demonstrator representative of the application introduced in Chapter 1, in which cabin floor rails can form preferential vibration transmission paths and transmit vibration amplifications induced by the propulsion architecture to the passenger seats.

5.2 Definition of the lattice waveguide

To accommodate multiple local resonators within a single waveguide, a three-dimensional beam-lattice guide is introduced by extending the 2D structure of Chapter 4 in the z-direction. As shown in Fig. 5.1(a), the unit cell is obtained by stacking two identical frames separated by L_z and connecting their right-hand sides ($x = L_x$) with two vertical beams (yellow) of cross-section $a_{f2} \times b_{f2}$. The resulting assembly forms an open cubic lattice.

The waveguide is built by repeating this cell with period L_x along x and coupling neighbouring cells through node-to-node continuity (Fig. 5.1(b)). The unit-cell mass m_c is defined as the total mass of the eight beams forming the cube lattice. The dynamics are computed using beam spectral elements with six generalized DOFs per node in the global frame, following the same formulation as in Chapter 4.

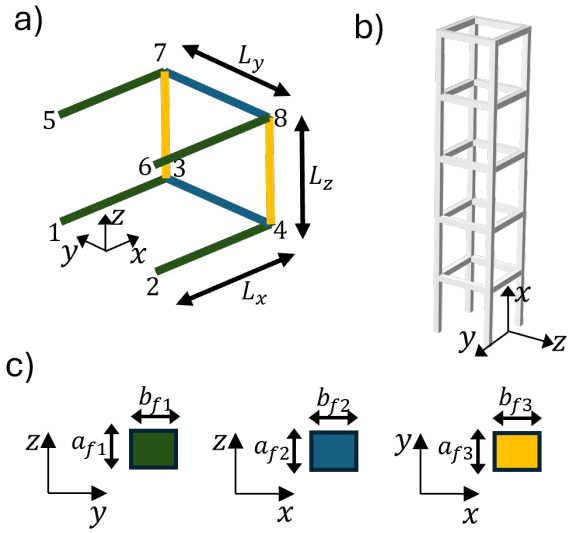

Figure 5.1: Cube-lattice waveguide. (a) Beam layout and node numbering of the unit cell. (b) Periodic lattice waveguide composed of five unit cells in series. (c) Cross-sections of the different beams

5.2.1 Dispersion analysis

The dynamic behaviour of the cube-lattice waveguide is analysed using the beam spectral-element formulation (see chapter 1) combined with Floquet–Bloch theory. Assuming time-harmonic motion at angular frequency $\omega = 2\pi f$, the unit-cell dynamic equilibrium can be written in the frequency domain as

$$\mathbf{S}_g(\omega)\,\mathbf{d} = \mathbf{F}, \tag{5.1}$$

where $\mathbf{S}_g(\omega)$ is the 48×48 dynamic stiffness matrix of the frame, and $\mathbf{d}$ and $\mathbf{F}$ collect the nodal displacements and forces, respectively.

Periodic boundary conditions between the left (nodes 1, 2, 5 and 6) and right (nodes 3, 4, 7 and 8) interfaces of the cell lead to the Floquet–Bloch relation $\lambda = \mathrm{e}^{\mathrm{i}kL_x}$, from which the complex wavenumber k is obtained. Solving the resulting eigenproblem over a frequency grid yields the dispersion relation of the infinite waveguide.

Owing to the symmetry of the cube lattice with respect to the planes xOz and xOy, the dispersion problem can be decomposed into four independent symmetry families, denoted SS, SA, AS and AA (see chapter 1). This classification follows the same convention as in the first chapter: the first letter refers to symmetry or antisymmetry with respect to xOz, and the second to xOy. Applying the corresponding kinematic constraints reduces the full problem to four decoupled eigenproblems, each associated with a distinct family of propagating modes. The resulting dispersion diagrams are shown in figures 5.2(a)–(d) corresponding respectively to the four condensed problem ; SS, SA, AS and AA. Each branch is colour-coded according to the dominant polarization of the associated eigenvector (green: x, red: y, blue: z), and representative mode shapes are displayed for selected points.

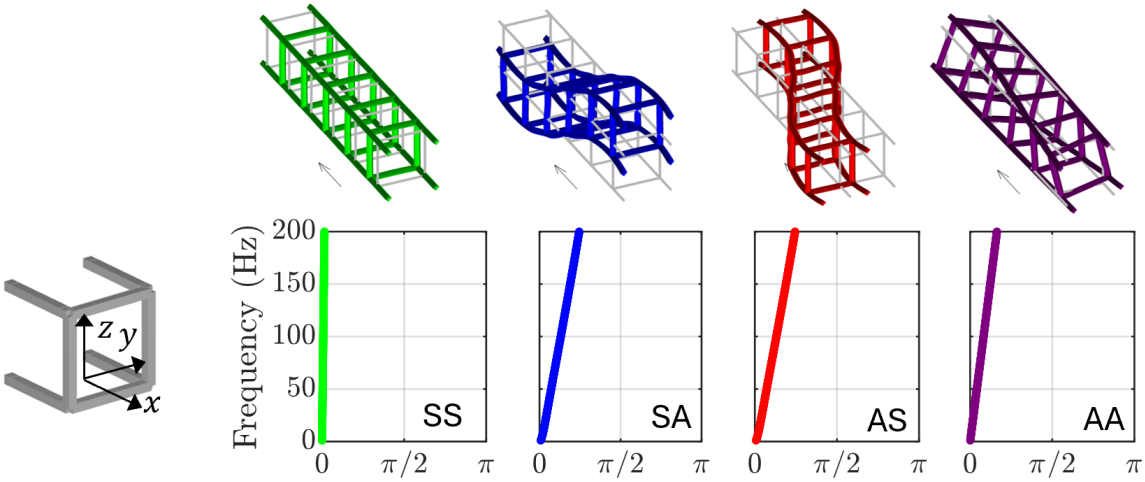

Figure 5.2: Dispersion of the beam-lattice waveguide. (a)–(d) Dispersion diagrams for the SS, SA, AS and AA symmetry families. Colours indicate the dominant polarization of the mode (green: x, red: y, blue: z). Representative mode shapes are shown above each sub-figure.

5.2.2 Reference frequencies

A reference frequency for the four families is defined as the first eigenfrequency of the isolated unit cell, subjected to the considered symmetry conditions with nodes 1, 2, 5, and 6 clamped. The corresponding four angular frequencies, ω_{SS}, ω_{SA}, ω_{AS}, and ω_{AA}, serve an analogous role to $\omega_1 = \sqrt{k_1/m_1}$ in the lumped model from Chapter 4 (4.2.2).

The global reference frequency of the cubic lattice is defined as the smallest of the four family-dependent reference values:

$$\omega_1 = \min\left(\omega_{SS}, \omega_{SA}, \omega_{AS}, \omega_{AA}\right), \tag{5.2}$$

so that ω_1 is governed by the most compliant (least stiff) symmetry family, serving as a conservative stiffness-based normalization. In practice, for the cube lattice geometry, the reference frequencies typically follow the hierarchy $\omega_{SS} \gg \omega_{AA} > \omega_{SA} \approx \omega_{AS}$, reflecting the significantly higher effective stiffness of compressional motion compared to bending-dominated responses.

5.3 Definition of the local resonators

As illustrated in Fig. 5.3(a), the absolute resonant filter consists of a cubic frame carrying five local resonators, with the same design as that presented in chapter 4 (4.6.1). Their orientation is chosen so that the first resonance is predominantly polarized along one of the Cartesian directions. Two resonators mounted on the faces lying in the xOz plane (blue) provide resonance along the z axis, two others attached to the faces lying in the xOy plane (red) are dedicated to the y axis, while the resonator positioned on the internal face (section) is oriented so as to deform mainly along the x axis.

The geometric parameters of the three resonator types are summarized in Fig. 5.3(b.1)–(b.3): panel (b.1) corresponds to the z-resonators, (b.2) to the y-resonators, and (b.3) to the x-resonator. For each type $i \in \{x, y, z\}$, the stiffness beams have a rectangular cross-section $a_s^i \times b_s^i$, which mainly

governs the resonant stiffness. The central mass beam is defined by $a_m^i \times b_m^i$ and length L_m^i, while the two junction beams are defined by $a_j^i \times b_j^i$ and length L_j^i. The corresponding effective mass is

$$m_i = \rho\left(L_m^i a_m^i b_m^i + 2L_j^i a_j^i b_j^i\right), \qquad i \in \{x, y, z\}, \tag{5.3}$$

where ρ denotes the material density.

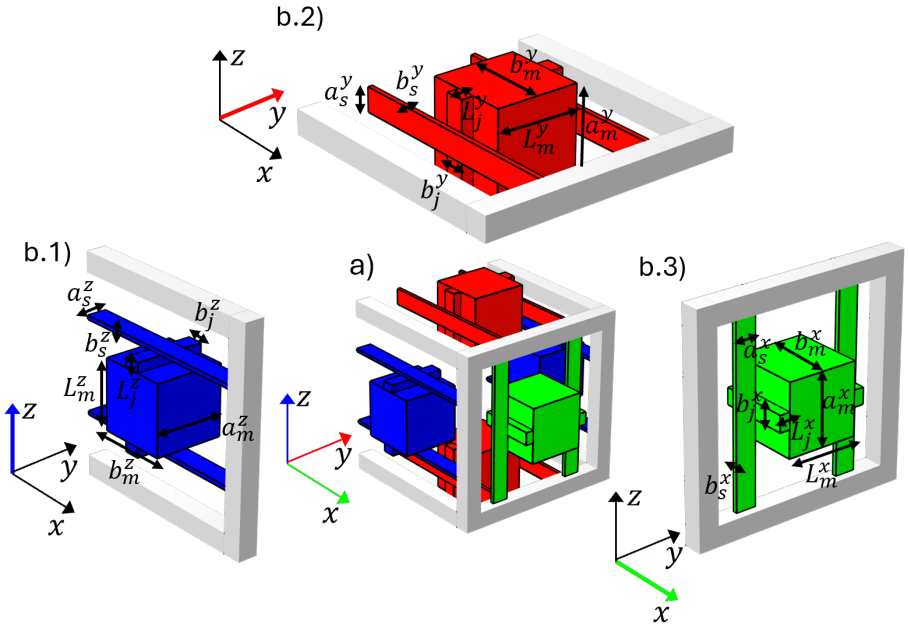

Figure 5.3: Multi-resonant cubic unit cell for the absolute filter. (a) Cube-lattice waveguide with attached local resonators. (b) Details of the resonator integration: (b.1) external face carrying the z-resonators, (b.2) external face carrying the y-resonators, and (b.3) internal face carrying the x-resonator.

The figure. 5.4 is organized into three rows, labeled (a)–(c), which illustrate the successive opening of bandgaps as the y-, z-, and x-oriented resonators are added to the cube lattice. All resonators share the same mass ($m_x = m_y = m_z$) and are tuned to the same natural frequency, $f_r = 103$ Hz.

Row (a) corresponds to the introduction of the two y-resonators. This addition opens a bandgap in the AS family (column 3), associated with an in-phase motion of the two resonators, and a bandgap in the AA family (column 4), associated with an out-of-phase motion. A similar mechanism occurs in row (b) when the two z-resonators are added: a SA bandgap (column 2) emerges in addition to the AS and AA gaps already present. Finally, row (c) shows that adding the last resonator oriented along the x-axis yields an absolute bandgap; its bandwidth is ultimately limited by the SS family (column 1), which remains the narrowest gap and therefore governs the achievable overlap across all four symmetry families.

In the following, this iso-mass configuration is first used to highlight the primary trends linking added resonant mass to achievable bandwidth. The analysis is then extended by examining the effect of redistributing the resonant mass among the different polarization directions.

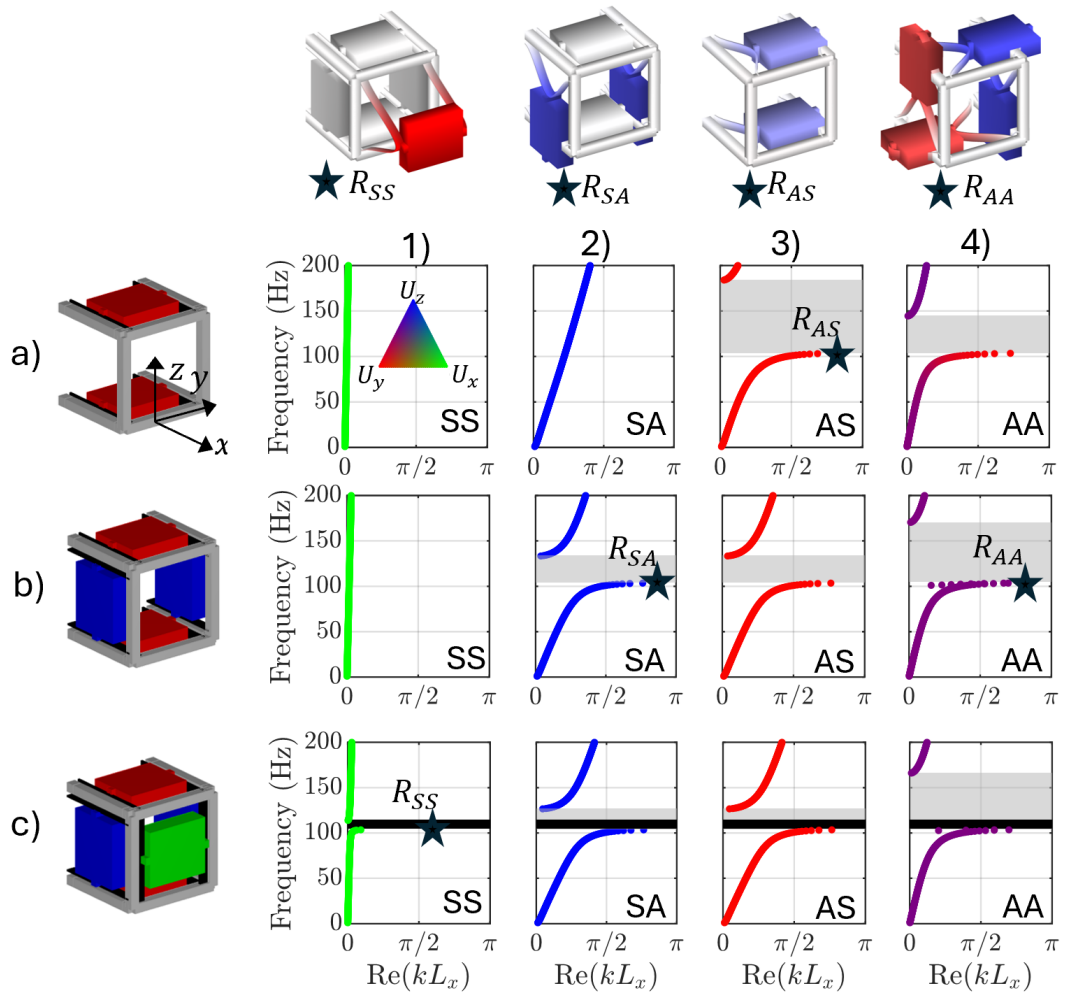

Figure 5.4: Successive addition of resonators to the cube lattice: (a) two y-oriented resonators, (b) two y-oriented plus two z-oriented resonators, and (c) two y-oriented plus two z-oriented plus one x-oriented resonator. Columns 1)–4) report the dispersion curves for the SS, SA, AS, and AA mode families, respectively. Branches are coloured according to the dominant modal polarization along the x- (green), y- (red), and z-axes (blue). Polarized bandgaps are highlighted by grey shaded regions, while the absolute bandgap is indicated by the black shaded region. The modal deformations associated with the starred black markers R_{SS}, R_{SA}, R_{AS}, and R_{AA} are shown above the corresponding panels.

5.4 Mass–bandwidth trade-off

The influence of the added resonant mass on the absolute bandgap of the cubic resonant lattice is analysed in the undamped case. Let $i \in \{x, y, z\}$ denote the resonator orientation. The beam-lattice parameters are fixed to

$$E = 4\ \mathrm{GPa}, \qquad \rho = 1100\ \mathrm{kg\,m^{-3}}, \qquad \nu = 0.33, \tag{5.4}$$

$$L_x = L_y = L_z = 50\ \mathrm{mm}, \qquad a_{f1} = a_{f2} = a_{f3} = 5\ \mathrm{mm}, \qquad b_{f1} = b_{f2} = b_{f3} = 5\ \mathrm{mm}. \tag{5.5}$$

The parameters of all resonators are identical :

$$a_s^i = 5 \text{ mm}, \qquad b_j^i = 4 \text{ mm}, \qquad L_j^i = 2 \text{ mm}, \qquad b_s^i = b_s, \qquad \forall i. \tag{5.6}$$

and each resonant mass is modeled as a cube of edge a_c,

$$a_m^i = a_c, \qquad b_m^i = a_c, \qquad L_m^i = a_c, \qquad \forall i. \tag{5.7}$$

The resonnance frequency is defined as f_2 and the total added resonant mass is :

$$m_r = m_x + 2m_y + 2m_z, \tag{5.8}$$

The resonant mass fraction is defined as in the chapter 4 (4.2.2) and reads

$$\mu_2 = \frac{m_r}{m_r + m_c}, \tag{5.9}$$

where m_c denotes the mass of the bare beam-lattice unit cell. The dimensionless resonance frequency is introduced as

$$\alpha = \frac{f_2}{f_1}, \tag{5.10}$$

where $f_1 = \omega_1/2\pi$ is the reference frequency of the bare beam lattice defined in section 5.2.2. To normalize the following plots, the frequency axis is defined by :

$$\Omega = \frac{f}{f_2}. \tag{5.11}$$

5.4.1 Illustrative scenarios for a fixed mass fraction

For a representative mass fraction $\mu_2 = 0.7$, Fig. 5.5 shows the dispersion diagrams of the four symmetry families (SS, SA, AS, AA) for three values of the dimensionless resonance frequency: $\alpha = 0.5$ (green box), $\alpha = 1.05$ (red box), and $\alpha = 1.5$ (black box). Each column corresponds to one family, and locally resonant bandgaps are indicated by grey rectangles. Where the four grey intervals overlap, their intersection defines an absolute bandgap, highlighted by a black outline.

For $\alpha = 0.5$ (green box, case 1), an absolute bandgap is obtained and its width is dictated by the SS waves: the compressional gap is the narrowest and therefore defines the overall frequency bounds. For $\alpha = 1.05$ (red box, case 2), an absolute bandgap still exists but is reduced, as the cut-off branches of the SA and AS families enter the same frequency range. Finally, for $\alpha = 1.5$ (black box, case 3), the SA and AS gaps disappear because the corresponding cut-off frequency is smaller than the resonance frequency, and no absolute bandgap remains.

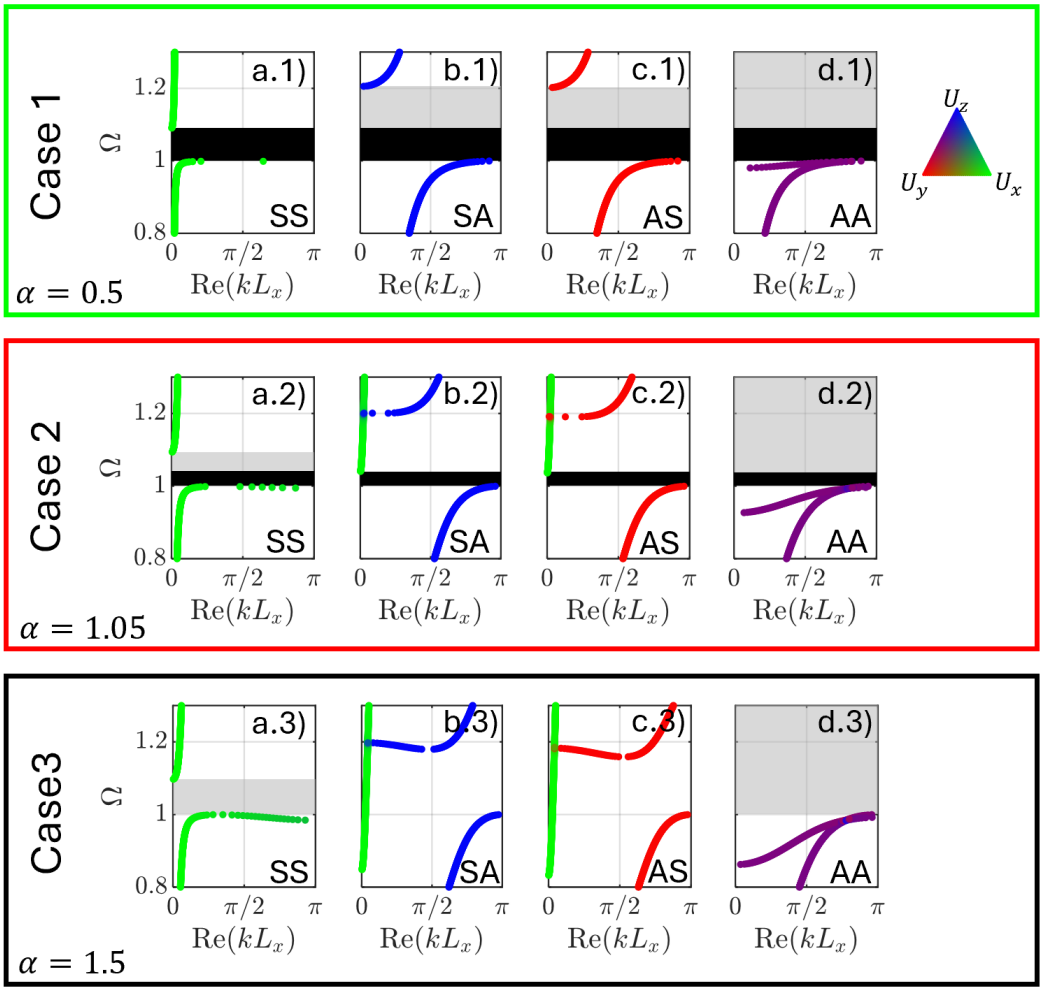

Figure 5.5: Dispersion diagrams of the four symmetry families for a cubic resonant lattice with resonant mass fraction equal to $\mu_2 = 0.7$. The three rows correspond to different frequency location of the resonance: $\alpha = 0.5$ (green box), $\alpha = 1.05$ (red box) and $\alpha = 1.5$ (black box). Columns (a)–(d): SS, SA, AS and AA families, respectively. For each family, the locally resonant bandgap is shaded in grey, and the overlap between the four families defines the absolute bandgap (black rectangle).

5.4.2 Parametric sweep

To generalize these observations, a parametric sweep is performed over

$$\mu_2 \in [0.05,\, 0.95], \qquad \alpha \in [0.05,\, 2].$$

For each symmetry family $J \in \{\text{SS}, \text{SA}, \text{AS}, \text{AA}\}$, we denote by f_L^J and f_H^J the lower and upper edges of its locally resonant bandgap. When the four polarized bandgaps overlap, the absolute bandgap is defined as

$$[f_L^{\max},\, f_H^{\min}], \qquad f_L^{\max} = \max_J f_L^J, \quad f_H^{\min} = \min_J f_H^J, \tag{5.12}$$

and its relative width by

$$\beta_{\text{abs}} = \frac{2(f_H^{\min} - f_L^{\max})}{f_H^{\min} + f_L^{\max}}. \tag{5.13}$$

Figure 5.6(a) reports the absolute bandgap relative width β_{abs} in the (μ_2, α)-plane, using a colormap from dark blue ($\beta_{\text{abs}} = 0$) to red ($\beta_{\text{abs}} = 0.1$). Figure 5.6(b) assigns each point to the closure scenario introduced above: case 1 (absolute bandgap limited by the SS family), case 2 (closure induced by the SA/AS cut-off branches), and case 3 (no absolute bandgap).

The region corresponding to case 1 closely matches the domain previously identified in Chapter 4 for the AS-polarized filter. Case 2 appears as a narrow transition layer surrounding this region, beyond which the system rapidly enters case 3, where no absolute bandgap is obtained.

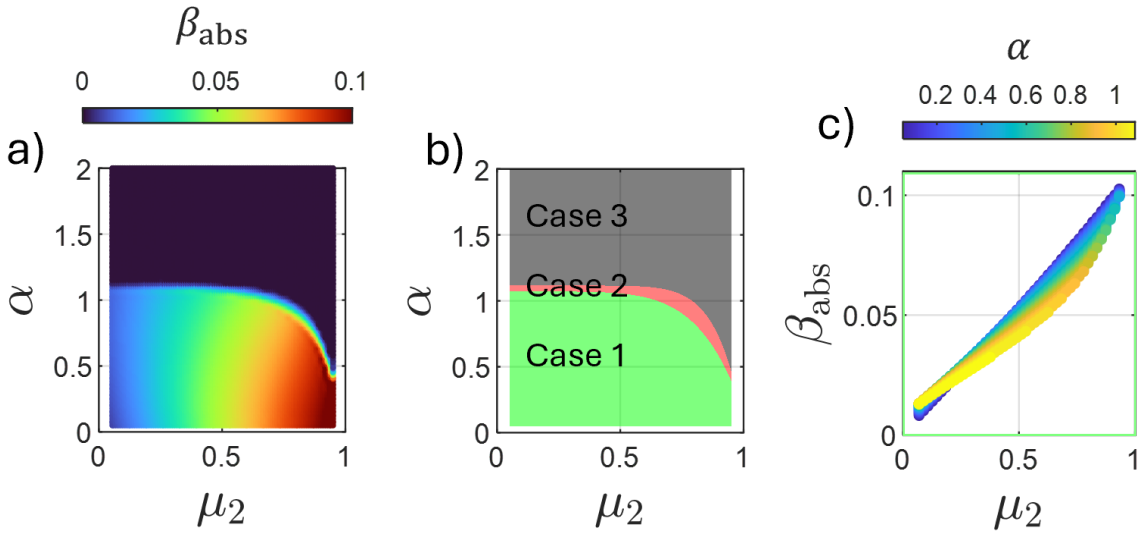

Figure 5.6: Mass–bandwidth trade-off for the undamped absolute resonant filter. (a) Absolute bandgap width β_{abs} in the (μ_2, α)-plane, shown using a colour map ranging from dark blue ($\beta_{\text{abs}} = 0$) to red ($\beta_{\text{abs}} = 0.1$). (b) Classification of the closure scenarios of Fig. 5.5: case 1 in green (absolute bandgap limited by SS), case 2 in red (closure driven by SA/AS cut-off branches), and case 3 in black (no absolute bandgap). (c) Relative width β_{abs} as a function of μ_2 restricted to case 1; the resonance placement α is encoded by the point colour using a colour map ranging from dark blue ($\alpha = 0.05$) to yellow ($\alpha \simeq 1.12$).

Overall, Fig. 5.6(a) indicates that the mass fraction μ_2 is the primary control parameter governing the effective width of the absolute bandgap β_{abs}. For a fixed dimensionless resonance frequency α within the case 1 domain, increasing μ_2 systematically widens the absolute bandgap, whereas leaving this domain results in a rapid collapse of β_{abs}. The dependence of β_{abs} on μ_2 in case 1 is examined in more detail in Fig. 5.6(c). For small values of α, the results approximately follow increasing linear trends with μ_2.

In the limit $\alpha \to 0$, the trade-off function between the added resonant mass and the absolute bandgap width is defined as

$$\Phi(\mu_2) = (1 - \mu_2)\beta_{\text{abs}}(\mu_2), \tag{5.14}$$

which becomes approximately quadratic in μ_2 and reaches an optimum close to

$$\mu_2^\star \approx 0.5, \qquad \beta_{\text{abs}}^\star \approx 0.053. \tag{5.15}$$

The corresponding optimal absolute bandgap therefore remains relatively narrow (about 5.3%), when compared with the bandwidth that can be achieved for the same amount of added resonant mass in the polarized configuration studied in Chapter 4.

This limitation originates from the way the total resonant mass m_r is distributed among the different symmetry families. The fraction of resonant mass effectively associated with each modal family can be expressed as

$$\gamma_{\text{SS}} = \frac{m_x}{m_r}, \quad \gamma_{\text{SA}} = \frac{2m_y}{m_r}, \quad \gamma_{\text{AS}} = \frac{2m_z}{m_r}, \quad \gamma_{\text{AA}} = \frac{2(m_y + m_z)}{m_r}. \tag{5.16}$$

In the case where all resonators are identical ($m_x = m_y = m_z$), this yields

$$\gamma_{\text{SS}} = \frac{1}{5}, \quad \gamma_{\text{SA}} = \gamma_{\text{AS}} = \frac{2}{5}, \quad \gamma_{\text{AA}} = \frac{4}{5}. \tag{5.17}$$

These results show that only one fifth of the resonant mass directly contributes to the compressional (SS) family, whereas the AA family mobilizes $4/5$ of the total mass and the SA and AS families $2/5$. As a result, the width of the absolute bandgap is mainly constrained by the relatively small mass fraction associated with the SS family, which therefore opens only a narrow polarization-controlled bandgap.

5.4.3 Influence of resonant mass distribution

To improve the absolute bandgap, the resonant mass is redistributed while keeping $\alpha = 0.05$ and $\mu_2 = 0.5$ fixed. The SS mass share γ_{SS} is increased from $1/5$ to $1/2$ by raising m_x and reducing m_y and m_z accordingly, so that the total resonant mass m_r (and therefore μ_2) remains unchanged.

Figure 5.7(b) tracks the upper edges of the polarized bandgaps as a function of γ_{SS}, using the reduced frequency $\Omega = f/f_2$. The grey region denotes the resulting absolute bandgap (common overlap). The violet, red and green curves correspond to the AA, SA/AS and SS families, respectively.

For $\gamma_{\text{SS}} = 1/5$, the compressional bandgap is the narrowest and therefore sets the absolute bandgap. As γ_{SS} increases, the compressional bandgap widens; however, this improvement comes at the expense of the bending bandgaps and the torsional bandgap, which shrink as m_y and m_z are reduced. For $\gamma_{\text{SS}} = 1/2$, the compressional and torsional bandgaps coincide, since $\gamma_{\text{SS}} = \gamma_{\text{AA}}$, while the bending bandgaps become significantly narrower. The best compromise is achieved for an intermediate distribution around $\gamma_{\text{SS}} = 1/3$: in this case, the compressional and bending bandgaps overlap, with $\gamma_{\text{SS}} = \gamma_{\text{SA}} = \gamma_{\text{AS}}$, leading to a maximal absolute bandgap.

This improvement is confirmed by Figs. 5.7(d,e), which compare $\beta_{\text{abs}}(\mu_2)$ and $\Phi(\mu_2)$ for $\gamma_{\text{SS}} = 1/5$ (black) and $\gamma_{\text{SS}} = 1/3$ (cyan). For a given value of μ_2, the $\gamma_{\text{SS}} = 1/3$ configuration systematically yields a larger absolute bandgap than $\gamma_{\text{SS}} = 1/5$. In both cases, the optimum of Φ remains close to

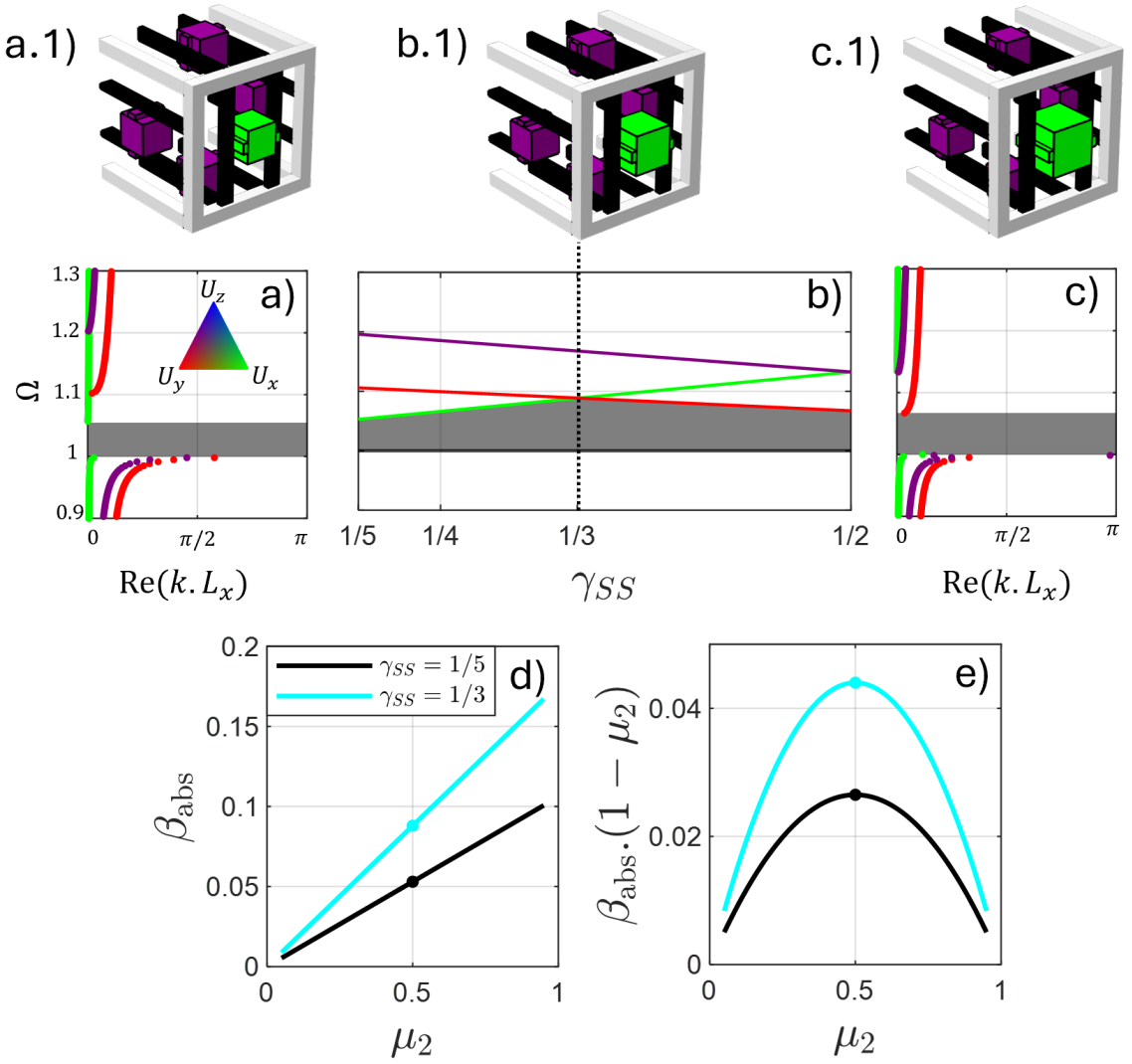

Figure 5.7: Influence of γ_{SS} (resonant mass share of the x-oriented resonator) on the undamped absolute bandgap. For $\mu_2 = 0.5$ and $\alpha = 0.05$: (a) dispersion diagram for $\gamma_{SS} = 1/3$; (b) upper bandgap edges versus γ_{SS} (AA: violet, SA/AS: red, SS: green), with the resulting absolute bandgap shaded in grey; (c) dispersion diagram for $\gamma_{SS} = 1/2$. For $\mu_2 \in [0.05, 0.95]$ and $\alpha = 0.05$: (d) absolute bandgap width β_{abs} versus μ_2 for $\gamma_{SS} = 1/5$ (black) and $\gamma_{SS} = 1/3$ (cyan); (e) trade-off function $\Phi = (1-\mu_2)\beta_{abs}$ versus μ_2 for the same cases, with the optimal points marked.

$\mu_2^\star \simeq 0.5$, but the associated maximum absolute bandgap increases from about 5.3% at $\gamma_{SS} = 1/5$ to about 8.8% at $\gamma_{SS} = 1/3$. Thus, increasing the SS mass share from $1/5$ to $1/3$ almost doubles the absolute bandgap width, without shifting the optimal total resonant mass fraction $\mu_2^\star$.

5.5 Performance limits of the damped absolute resonant filter

The above results were obtained in the idealized lossless setting. To assess how robust these trends remain under more realistic conditions, material damping is now introduced in the lattice through a complex Young's modulus $E = E_r(1 + 2\mathrm{i}\,\xi)$. The attenuation of a finite filter composed of N_c unit cells is quantified, as in the previous chapter, by the ratio between the displacement amplitudes at the right and left ports. Here, a unit oblique translation is imposed at the input port, with equal components along the three cartesian axes x, y and z, and the same translational degrees of freedom are monitored at the output port. The associated FRF is defined as

$$H_{x,y,z}(\Omega) = 20\log_{10}\left(\frac{\|\mathbf{u}_{\mathrm{out},x,y,z}\|}{\|\mathbf{u}_{\mathrm{in},x,y,z}\|}\right), \tag{5.18}$$

where $\mathbf{u}_{\mathrm{in},x,y,z}$ and $\mathbf{u}_{\mathrm{out},x,y,z}$ collect the translational DOFs of the four input and output nodes in the three directions. This scalar FRF characterizes the attenuation provided by the filter under a generic multi-axial excitation. The absolute attenuation band $\beta^{\mathrm{abs}}_{6\mathrm{dB}}$ is defined from the reduced frequencies Ω_L and Ω_H such that $Hx, y, z(\Omega) \leq -6$ dB for $\Omega \in [\Omega_L, \Omega_H]$.

Figure 5.8 illustrates this behaviour for a representative design with $\mu_2 = 0.5$, $\alpha = 0.1$, $\gamma_{\mathrm{SS}} = 1/3$, $\xi = 0.005$, and $N_c = 5$. Subfigures (a) and (b) display the imaginary and real parts of kL_x, respectively, obtained from the fully damped eigenvalue problem and including the four symmetry families SS, SA, AS, and AA. For each family, only the most propagative branch is retained. A colour code is used to indicate the corresponding polarization: green for compression, red for bending in the y direction, blue for bending in the z direction, and purple for torsion. The blue curve does not appear here because the y- and z-bending modes are degenerate, with the blue branch lying below the red one.

Subfigure (c) presents the FRFs of the finite chain composed of five unit cells. The black curve corresponds to the multiaxial excitation $H_{x,y,z}$, while the red and blue dotted curves, labelled $H_{y,z}$, correspond to excitations restricted to the y and z directions. The grey shaded region indicates the absolute bandgap predicted from the undamped dispersion relation.

This example shows that, for a finite damped chain, attenuation may remain polarization-dependent even when the resonant mass is distributed in an apparently balanced way. Although $\gamma_{\mathrm{SS}} = 1/3$ assigns comparable shares of resonant mass to compression (SS) and bending (SA/AS), Fig. 5.8(a) shows that the SA/AS solutions (red) exhibit a much larger imaginary part than the SS branch (green) within the absolute forbidden band (grey shaded region).

To explain this difference, two dimensionless resonance locations must be distinguished. The parameter $\alpha = 0.1$ is defined with respect to the reference bending frequency ($f_1 = f_{\mathrm{SA}} = f_{\mathrm{AS}}$). In contrast, compression must be referenced to f_{SS}, which yields

$$\alpha_{\mathrm{SS}} = \frac{f_r}{f_{\mathrm{SS}}} \simeq 0.02 \ll \alpha. \tag{5.19}$$

As shown in the previous chapter, pushing the resonance frequency deep into the subwavelength regime can severely penalize the attenuation performance of the short, damped filters.

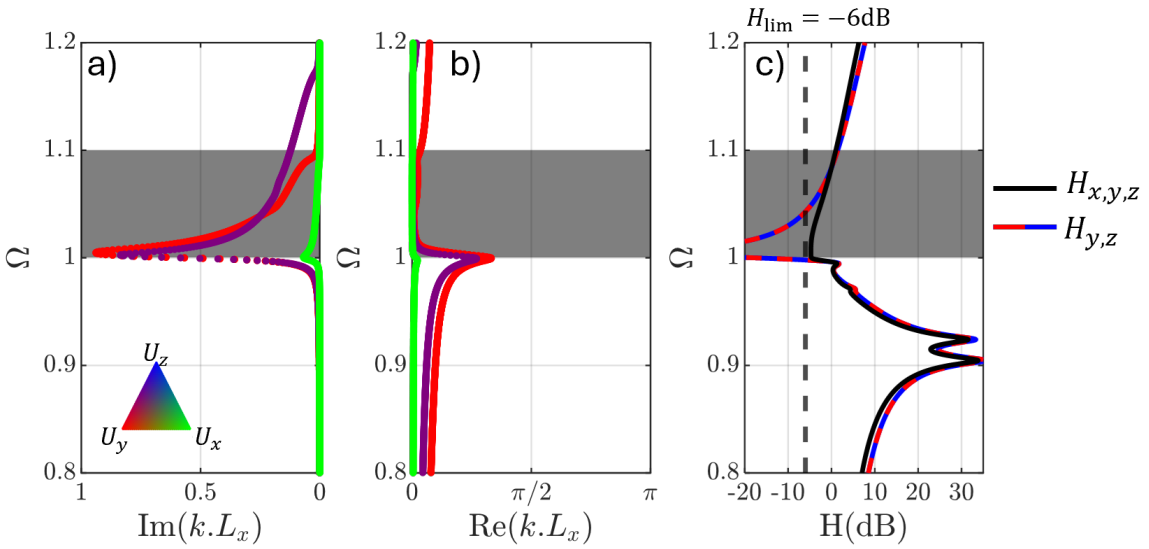

Figure 5.8: Damped dispersion diagram for $\mu_2 = 0.5$, $\alpha = 0.1$, $\gamma_{SS} = 1/3$ and $\xi = 0.005$. (a) Imaginary part $\text{Im}(kL_x)$ and (b) real part $\text{Re}(kL_x)$. Only the most propagative solutions are shown, corresponding to compression (green), bending in y and z (red), and torsion (violet). (c) FRFs of a finite chain of $N_c = 5$ unit cells: $H_{x,y,z}$ (black) for an oblique excitation with equal components along x, y and z, and $H_{y,z}$ (red and blue dashed curves) for an excitation restricted to the y and z directions. The black dashed line indicates the -6 dB level. In all panels, the grey band denotes the absolute bandgap predicted by the undamped dispersion relation.

This behaviour is clearly observed in Fig. 5.8(c). When only the y- and z-polarized responses are considered, $H_{y,z}$ (red and blue dotted lines) falls below -6 dB over a wide frequency range. By contrast, the full multiaxial response $H_{x,y,z}$ (black line) does not. The performance of the finite damped filter is therefore limited by the high compressive stiffness of the beam-lattice cube.

5.6 Design guidelines

Using the analysis tools and trends mentioned above, we will now illustrate, with a concrete example, how to design and optimise an absolute resonant filter. The different steps of the procedure are summarised in Figure 5.9.

1. Structural design of the beam-lattice waveguide. The first step focuses on the purely structural design of the beam-lattice waveguide. The material (here a 7075-T6 aluminium alloy), the number of unit cells N_c, and the beam cross-sections are selected to meet static requirements in terms of stiffness, mass, and mechanical strength. Panel (1) of Fig. 5.9 shows the result of a finite-element analysis performed on a five-cell assembly, clamped at one end and subjected to a 500 N load in the z direction at the free end. The colour map represents the von Mises stress field. Based on this analysis, the maximum stresses and strains are compared with allowable limits, and the design is iteratively refined until all criteria are satisfied.

2. Definition of dimensionless parameters. Once the geometry of the waveguide has been defined, its dimensionless parameters can be extracted. In particular, the reference frequency f_1 is defined as

the minimum of the first natural frequencies of the clamped–free problem associated with the different symmetry families f_{SS}, f_{SA}, f_{AS}, and f_{AA}. The dimensionless parameter α is then introduced as

$$\alpha = \frac{f_{\text{target}}}{f_1}, \tag{5.20}$$

where f_{target} denotes the desired filtering frequency.

3. Optimisation of the mass–bandwidth trade-off. The third step consists in optimising the trade-off between the added resonant mass and the −6 dB attenuation bandwidth. This bandwidth corresponds to the frequency range over which the vibratory quantity measured at the output of the filter is at least halved with respect to the quantity applied at its input. The trade-off is optimised by maximising the cost function

$$\Phi = \beta_{6\text{dB}}^{\text{abs}}(1 - \mu_2). \tag{5.21}$$

4. Evaluation of the resulting dynamic properties. The final step evaluates the dynamic behaviour of the optimised filter and identifies possible side effects outside the target band. Panel (4) compares the frequency response function of the bare waveguide (blue curve) with that of the optimised filter (black curve). The light grey rectangle indicates the theoretical stopband predicted by the dispersion analysis, while the dark grey rectangle highlights the effective −6 dB attenuation band of the finite structure. Within this band, the optimised filter provides a clear reduction of the transmitted response, as expected from the optimisation. Outside the band, however, the modified dynamics of the complete structure may introduce additional resonances at lower frequencies than those of the original waveguide. This final verification step is therefore essential to assess potential out-of-band vibration issues and to determine whether further adjustments to the structural design or frequency placement are required.

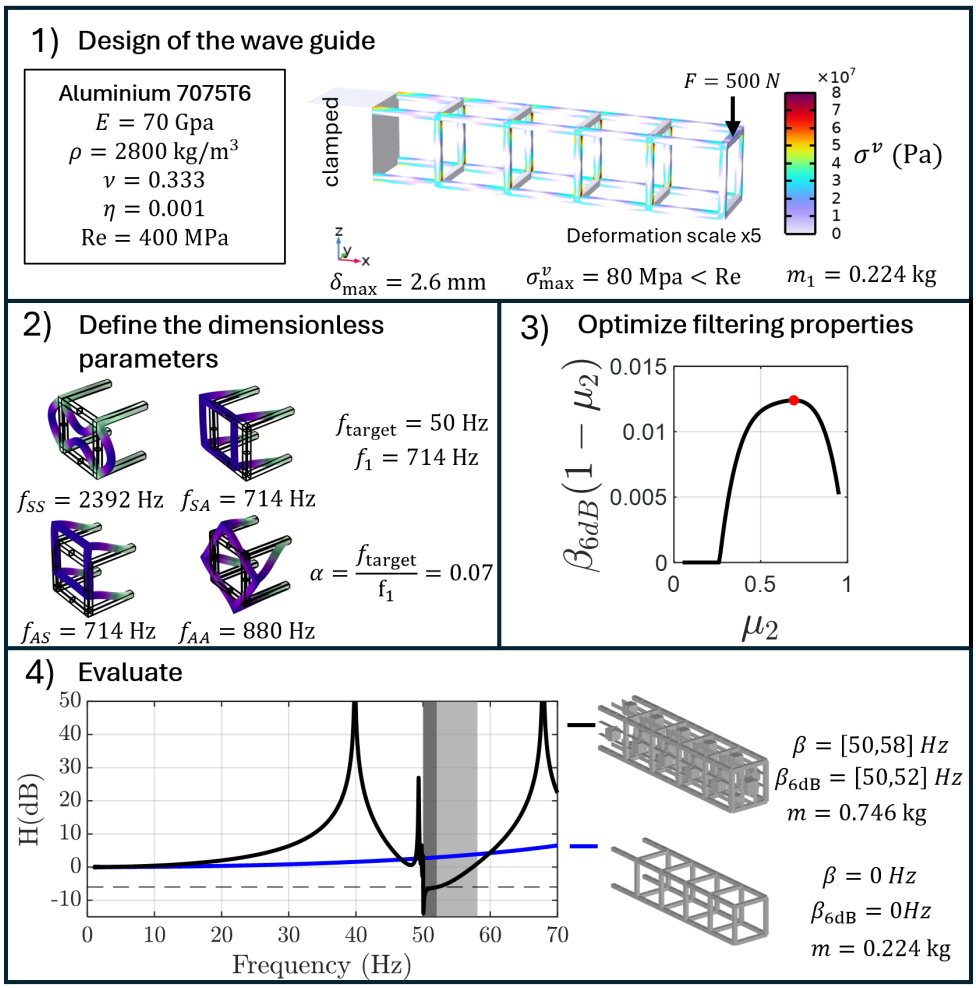

Figure 5.9: Four-step design for the absolute resonant filter. (1) Bare lattice waveguide is sized to meet static stiffness, mass, and strength constraints (FE stress check under representative loading). (2) Dimensionless parameters are defined from the bare-waveguide design and the target filtering frequency. (3) The absolute mass–attenuation bandwidth trade-off is optimised. (4) FRFs of the bare waveguide and the optimised filter are compared to confirm the attenuation band and identify potential side effects.

5.7 Development of an applied demonstrator

As shown in the previous sections, the geometry and mass distribution of a resonant cube lattice control the opening of an absolute bandgap and the performance of a finite, realistic vibration filter. We now investigate how these concepts translate to an actual structure, designed to mimic an industrial use case. The demonstrator is modelled numerically, manufactured by additive processes, and tested experimentally under multi-axial excitation.

The targeted application is the improvement of passenger vibration comfort in aircraft by reducing the transmission of engine-induced structural vibrations to the cabin floor. In current airframe architectures, the passenger seats are supported by longitudinal rails periodically connected to the primary structure. While these rails provide the required load-bearing capability, they also constitute a preferential waveguide for elastic vibrations to propagate into the cabin. The objective is therefore to endow the rail with an additional function, namely the filtering of elastic-wave propagation.

The demonstrator considered here simplifies this configuration by replacing the seat with a simple aluminum beam and the rail with the cubic lattice waveguide presented above. Multi-axial resonators are integrated into the waveguide to introduce the desired filtering function. The resulting prototype is approximately 1 meter long, which corresponds to the spacing between two consecutive rows of seats in an aircraft cabin.

With the aim of producing a low-cost prototype that can be manufactured quickly, additive manufacturing is adopted. To facilitate the fabrication of the absolute filter, the unit cell of the cubic lattice is designed as an assembly of five separate faces with embedded resonators. The faces are joined using a tongue-and-groove interface, which both simplifies alignment and locking during assembly, and enables repeatable interconnection of adjacent unit cells along the filter. Figure 5.10(a)–(c) show the CAD models of the faces: (a) face carrying the z-resonators, (b) face carrying the y-resonators, and (c) face carrying the x-resonator. Faces (a) and (b) are in double, so that five faces are assembled to form a single unit cell. Sub-figure (d) illustrate the assembled unit cell and e) present an example of a four-cell filter obtained by this assembly process.

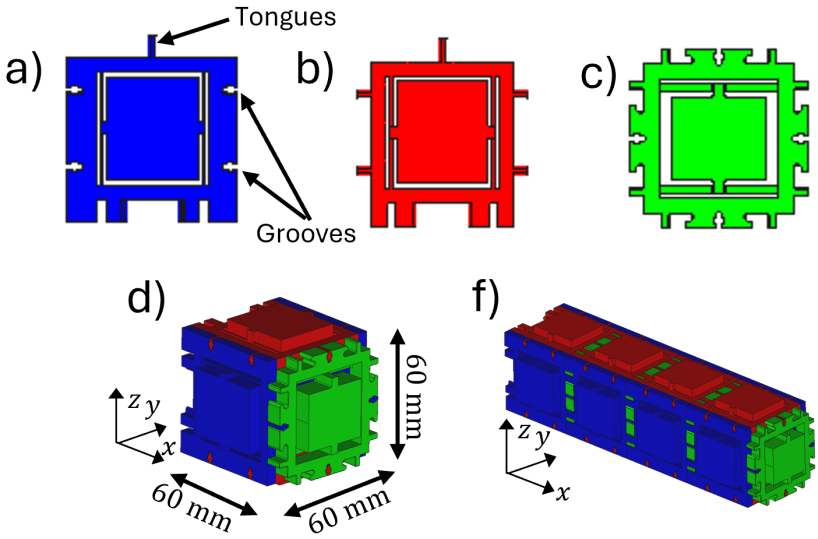

Figure 5.10: Design and assembly of the printed cube-lattice unit cell. (a) CAD view of the face carrying the z-resonators. (b) CAD view of the face carrying the y-resonators. (c) CAD view of the face carrying the x-resonator. (d) Assembled unit cell (e) Example of a four-cell filter obtained by assembling four unit cells in series.

Separate printing of the resonant faces ensures that each resonant element is produced in a single continuous piece, without requiring support structures for 3D printing. This ensures that the geometry of the stiffness and mass elements remain close to the target values. However, the mechanical joints between the faces reduce the overall stiffness of the structure compared to the designed structure. Nevertheless, our previous analyses showed that the parameters controlling the bandgap are essentially the resonance frequency of the local resonators (defining the opening frequency of the bandgap) and the mass ratio between the resonators and the waveguide (setting its width). The stiffness of the waveguide mainly affects the level of attenuation in the finished filter: the lower the specific stiffness, the greater the attenuation for a given fraction of resonant mass (see Figures 4.7). The flexibility of

the joints therefore penalises static rigidity more than filtering capacity.

5.7.1 System-level demonstrator and interfaces

In many aircraft cabin architectures, the cabin passenger is supported by longitudinal rails designed to carry the associated static loads (see figure 5.11a). These rails may also act as preferential transmission paths for unwanted structural vibrations, which can reach the passenger seats. The demonstrator presented here addresses this issue in a simplified setting, illustrating how a rail can be designed to simultaneously fulfil its load-bearing function and provide vibration filtering by limiting elastic-wave propagation toward the cabin floor.

The underlying concept is sketched in Fig. 5.11(b). The passenger seats (beige) are periodically connected, via interface parts (cyan), to a long rail (dark blue), which is itself periodically attached to the aircraft structure through additional interface parts (green). In this reduced problem, the aircraft structure is represented by a multi-axial vibration source. The black dashed box highlights the portion implemented in the manufactured demonstrator, which corresponds to a single rail–seat connection pair and one source–rail connection.

The laboratory-scale implementation is shown in Fig. 5.11(c). The seat element is represented by an 800 mm-long aluminium Norcan beam (profile N0115, 45×45 mm cross-section, beige), while the rail is realised using the previous design assemblies (dark blue), each composed of four unit cells (see Fig. 5.10(f)).

On the passenger seat side, each filter is connected to the aluminium beam through an interface part (detail in Fig. 5.11(b.2)). This part combines a tongue-and-groove joint with the lattice and a bolted connection to the Norcan beam. On the excitation side, both filters are attached to the support brackets through similar tongue-and-groove joints (green, Fig. 5.11(b.1)). The brackets are clamped to the vibrating support using two bolts passing through oblong holes, which allow alignment adjustments during assembly.

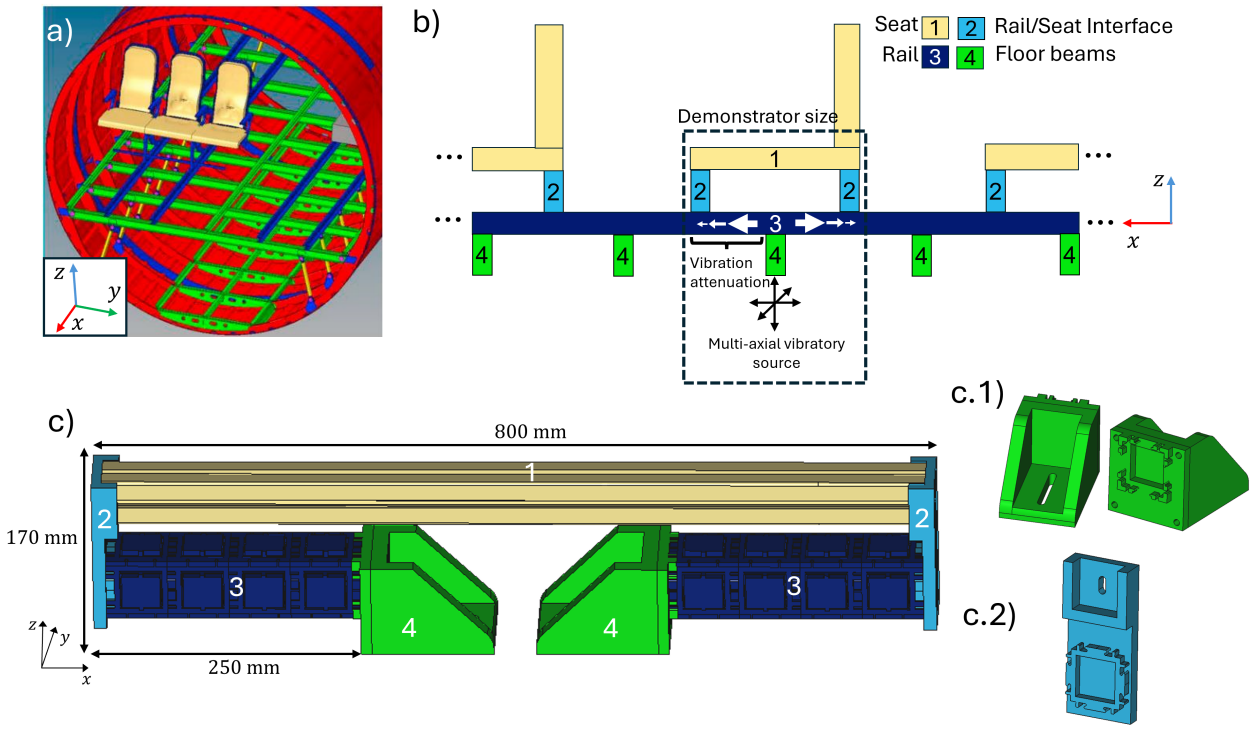

Figure 5.11: Applicative demonstrator inspired by the passenger-cabin floor assembly of an aircraft. a) CAD model plot of cabin passenger extraded from [21] (b) Schematic of the reduced problem: the seats (beige) is periodically connected, via interface parts (cyan), to a long rail (dark blue), which is itself periodically attached to the aircraft structure through additional interface parts (green). The aircraft structure is here reduced to a multi-axial vibration source. The black dashed box indicates the size of the manufactured demonstrator relative to this schematic. (c) CAD model of the demonstrator using the same colour code: Norcan aluminium beam (beige, representing one seat), two resonant lattice filters (dark blue, representing the rail), and interface parts connecting the filters to the beam (cyan, zoomed in c.2) and to the support brackets (green, zoomed in c.1).

5.7.2 Numerical model

To predict the demonstrator performance, a finite-element (FEM) model of the unit cell is first built in COMSOL. Figure 5.12(a) shows the FEM model of the beam-lattice cell. All interfaces are assumed perfectly bonded, with no slip or clearance.

The reference frequencies of the four symmetry families are obtained from eigenvalue analyses of the clamped unit cell ($x = 0$), with the corresponding symmetry conditions imposed. The resulting values are reported in Fig. 5.12(c). Following the reference-frequency definition introduced above, the smallest of the four values is selected, yielding $f_1 = f_{AS/SA} = 672$ Hz.

Figure 5.12(b) introduces the same cell equipped with resonators. In the first configuration, all resonators have equal masses ($\gamma_{SS} = 1/5$) and are designed to satisfy $\mu_2 = 0.5$ and $\alpha = 0.157$, leading to a target resonance $f_r = \alpha f_1 \simeq 105$ Hz.

The corresponding dispersion relation is shown in Fig. 5.12(d): coloured lines denote the beam model and black markers the FEM solutions. An absolute bandgap is obtained between 105 and 110.5 Hz (dark grey), i.e. a relative width $\beta \simeq 0.05$. A wider polarized gap associated with the SA/AS

families extends from 105 to 131 Hz (light grey).

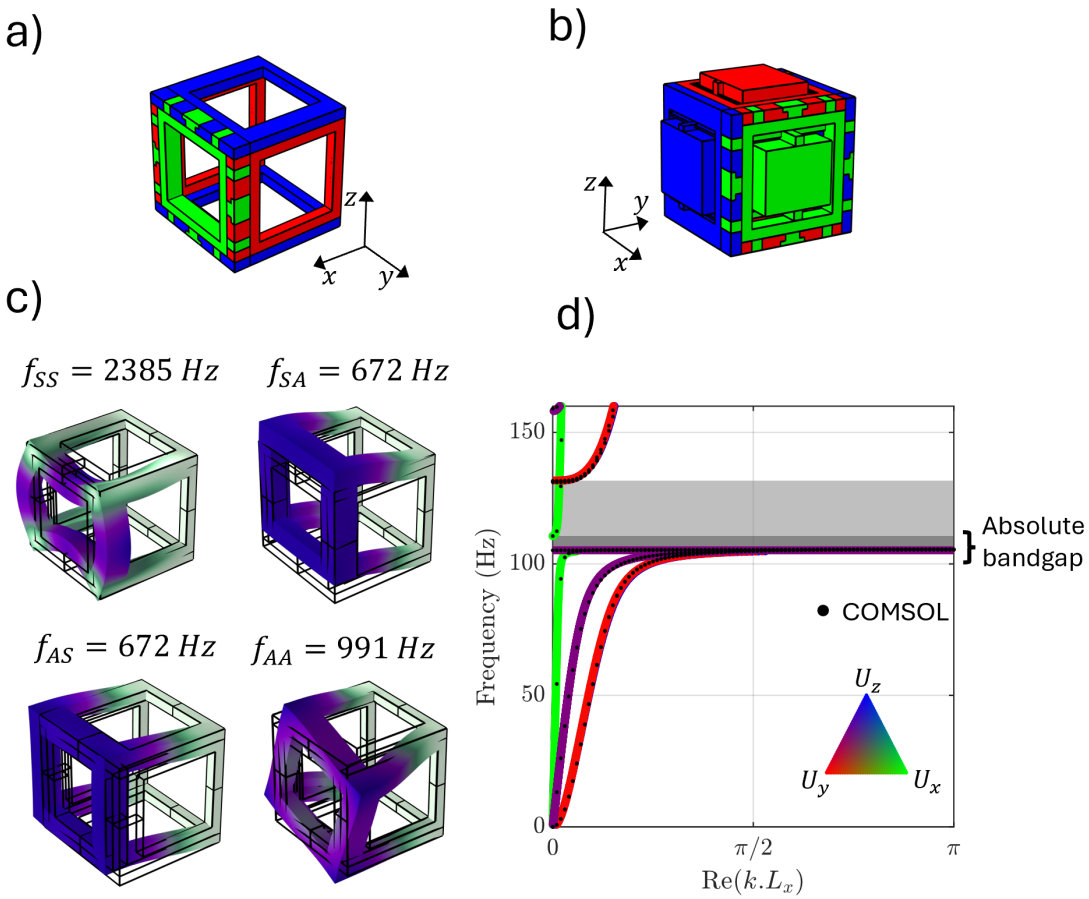

Figure 5.12: Numerical modelling of the printed unit cell. (a) COMSOL model of the bare cube-lattice cell, (b) COMSOL model of the unit cell with three identical resonators ($\gamma_{SS} = 1/5$, $\mu_2 = 0.5$, $\alpha = 0.157$). (c) Reference frequencies of the four symmetry families (SS, SA, AS, AA) for the bare waveguide cell. (d) Dispersion diagrams: coloured curves from the beam spectral-element model and black dots from the 3D COMSOL model. The dark grey rectangle indicates the absolute bandgap; the light grey rectangle shows the SA/AS-polarised bandgap.

5.7.3 Performance indicators

The full demonstrator shown in Fig. 5.11(b) is modelled using 3D finite elements, including the aluminium beam, the lattice filters, the interface parts, and the steel brackets. Perfect contact is assumed at all joints. Regarding the mechanical properties, we consider those of PLA, i.e, a standard additive manufacturing material :

$$E = 3.3 \times 10^9 \text{ Pa}, \quad \rho = 1100 \text{ kg/m}^3, \quad \nu = 0.3, \quad \xi = 0.015, \tag{5.22}$$

whereas the Norcan beam is described with aluminium properties

$$E = 70 \times 10^9 \text{ Pa}, \quad \rho = 2700 \text{ kg/m}^3, \quad \nu = 0.3, \quad \xi = 0.001. \tag{5.23}$$

Material damping is included for both materials through complex moduli.

To isolate the effect of the resonators, a reference model is defined with identical geometry and boundary conditions, except that the resonant elements inside the lattice filters are removed. The comparison between the “resonant” and “reference” configurations (see figure 5.13 a and b) therefore directly quantifies the resonator contribution.

The excitation is prescribed as three base accelerations $A_{x,0}$, $A_{y,0}$, and $A_{z,0}$ applied on the bracket support surfaces (highlighted in blue in Figs. 5.13(a,b)), with identical amplitudes

$$A_{x,0} = A_{y,0} = A_{z,0} = 1.96 \text{ m s}^{-2}. \tag{5.24}$$

The input level is characterised by the acceleration norm

$$A_0 = \sqrt{A_{x,0}^2 + A_{y,0}^2 + A_{z,0}^2}. \tag{5.25}$$

The response is evaluated at the centre of the upper surface of the Norcan beam, using the corresponding norm

$$A_1 = \sqrt{A_{x,1}^2 + A_{y,1}^2 + A_{z,1}^2}. \tag{5.26}$$

The global transmission from the base to the protected point is then defined (in dB) as

$$T_1 = 20 \log_{10}\left(\frac{A_1}{A_0}\right). \tag{5.27}$$

Figure 5.13(c) compares T_1 for the filtered configuration (solid black) and the reference configuration (black dashed). In addition, insertion-loss indicators are introduced for each component at the same point:

$$IL_x = 20 \log_{10}\left(\frac{A_{x,1}^{\text{ref}}}{A_{x,1}}\right), \quad IL_y = 20 \log_{10}\left(\frac{A_{y,1}^{\text{ref}}}{A_{y,1}}\right), \quad IL_z = 20 \log_{10}\left(\frac{A_{z,1}^{\text{ref}}}{A_{z,1}}\right), \tag{5.28}$$

where $(A_{x,1}^{\text{ref}}, A_{y,1}^{\text{ref}}, A_{z,1}^{\text{ref}})$ denotes the response in the reference configuration. Positive IL_i values correspond to attenuation of the i-th component, whereas negative values indicate amplification. The

insertion losses are plotted in Fig. 5.13(d) (IL_x in green, IL_y in red, IL_z in blue). In both plots, the dark and light grey rectangles recall the absolute and SA/AS-polarised bandgaps predicted by the dispersion analysis.

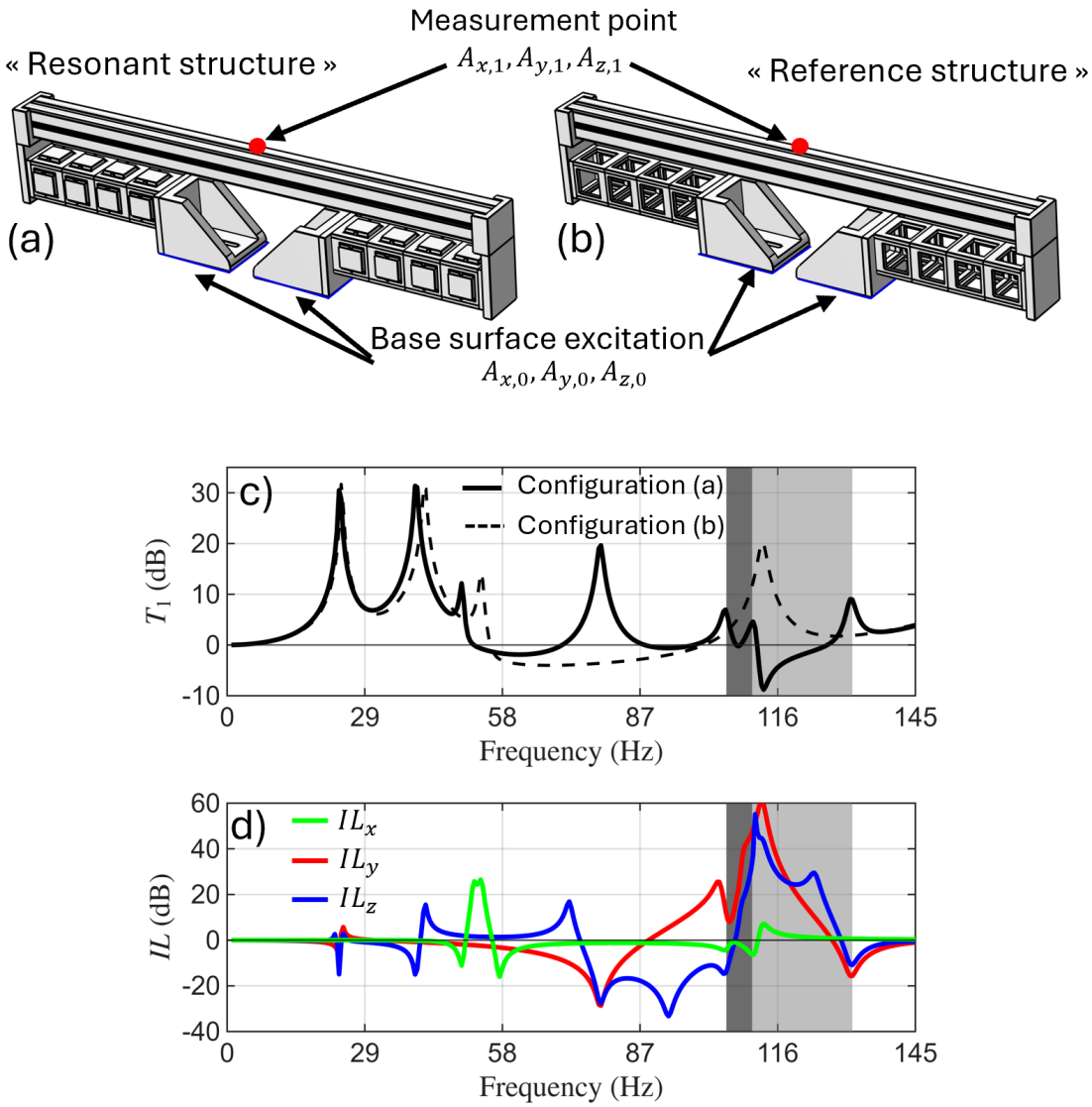

Figure 5.13: Numerical response of the full demonstrator. (a) Resonant structure: full FE model including the resonant elements. (b) Reference structure: same model without the resonant elements. The blue lines indicate the excitation areas and the red point indicate where the response is evaluated. (c) Global transmission T_1 (in dB) at the observation red point on the Norcan beam for the filtered (solid black) and reference (dashed black) configurations. (d) Insertion loss for each acceleration component: IL_x (green), IL_y (red) and IL_z (blue). Positive/negative values indicate that, at a given frequency, the response of the resonant configuration is attenuated/amplified relative to the reference configuration. Dark grey rectangle: predicted absolute bandgap; light grey rectangle: predicted SA/AS-polarised bandgap.

Adding resonators increases the total mass and shifts the resonance peaks toward lower frequencies. Over the grey frequency interval, the transmitted vibration is reduced, with a maximum attenuation of about 9 dB around 113 Hz. Inside the predicted absolute bandgap, however, the gain remains limited:

T_1 decreases by only ≈ 0.25 dB at 108 Hz.

The insertion losses help to identify the origin of this limited global improvement. The y- and z-components exhibit clear attenuation over the broader SA/AS band, whereas the x-component is only weakly reduced within the absolute bandgap. This indicates that the compressional contribution is filtered much less efficiently than the bending-dominated responses, in agreement with the trends discussed in Fig. 5.8. In the present design, the compressional bandgap is associated with a much lower effective resonant frequency :

$$\alpha_{\mathrm{SS}} = 0.044 \quad \text{vs.} \quad \alpha_{SA/AS} = \alpha = 0.157, \tag{5.29}$$

and it also receives a smaller share of the resonant mass ($\gamma_{\mathrm{SS}} = 1/5$). As a result, the compressional attenuation is both narrower and weaker, and the x-oriented resonator provides only a marginal contribution to the overall (absolute) performance.

5.7.4 Role of the x-oriented resonator

To further assess the role of compressional-wave attenuation in the overall response, Fig. 5.14 compares the demonstrator equipped with five resonators per unit cell to an otherwise identical configuration in which the x-oriented resonator is removed from every cell, while all remaining components and parameters are kept unchanged. The corresponding effect on the finite demonstrator is reported in Fig. 5.14(b). Within the absolute bandgap predicted for the five-resonator configuration (dark grey rectangle in Fig. 5.14a), the change in global transmission remains modest: at 110 Hz, the complete configuration reaches about -0.25 dB, whereas removing the x-resonator results in only $\approx +0.35$ dB. In contrast, over the wider SA/AS-polarised band, the configuration without the x-resonator exhibits slightly stronger and broader attenuation. This trend is consistent with the fact that removing the x-resonator increases the effective mass fraction associated with the y- and z-resonators,

$$\begin{aligned} \mu_2^{SA/AS} &= \frac{2m_r}{5m_r + m_c} \approx 0.20 \quad \text{(with } x\text{-resonator)}, \\ \mu_2^{SA/AS} &= \frac{2m_r}{4m_r + m_c} \approx 0.22 \quad \text{(without } x\text{-resonator)}. \end{aligned} \tag{5.30}$$

where m_c denotes the mass of the beam-lattice waveguide cell, unchanged between the two cases.

This comparison suggests that the x-oriented resonator brings limited benefit in the present design. It provides only a small gain in compressional attenuation, while adding mass and assembly complexity. Conversely, removing it yields a lighter and simpler filter with slightly improved performance in the bending-dominated band, at the expense of losing a strict absolute bandgap in the dispersion sense.

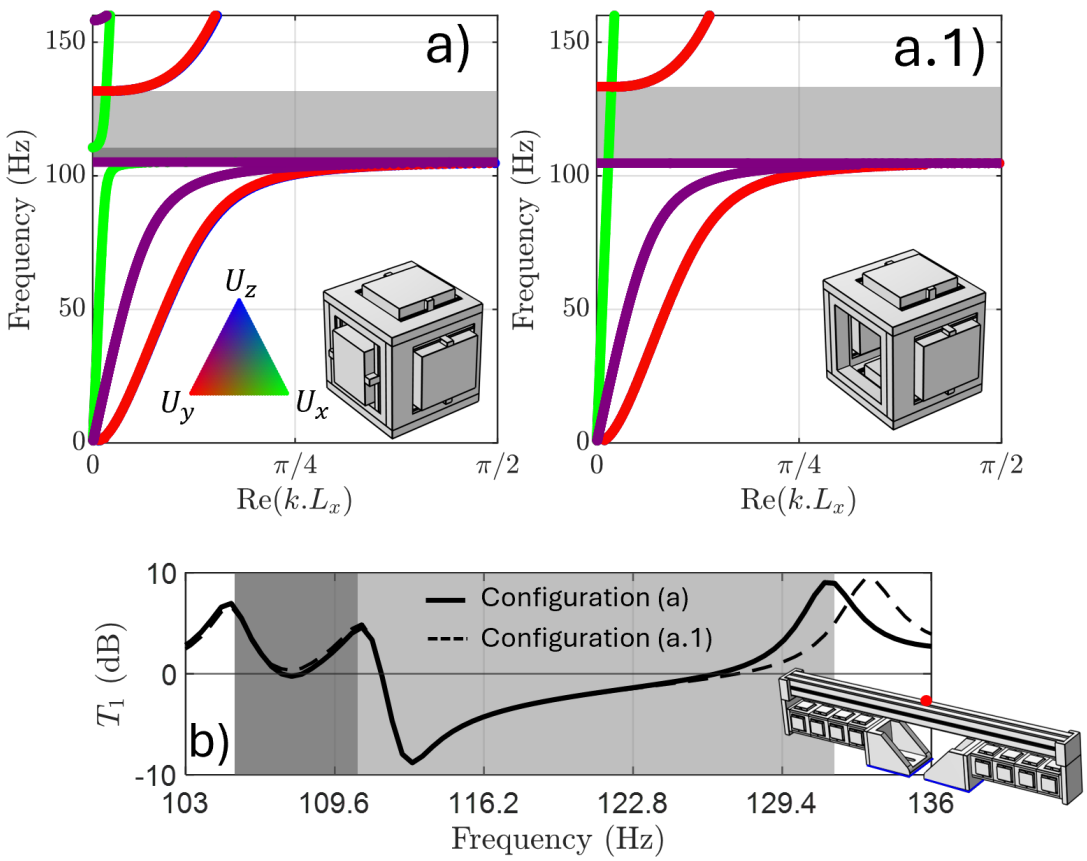

Figure 5.14: Influence of the x-oriented resonator on the demonstrator performance. (a) Dispersion diagrams of the periodic unit cell with all five resonators (a.1) Dispersion diagrams of the unit cell without the x-resonator (b) Global transmission T_1 at the observation point for the full demonstrator with (solid line) and without (dashed line) the x-resonator. Dark grey rectangle: absolute bandgap of the five-resonator case; light grey rectangle: SA/AS-polarised bandgap.

5.7.5 Experimental analysis

The demonstrator is mounted on a tri-axial shaker. Figure 5.15(a) shows the experimental set-up. The shaker is driven in three directions by six internal actuators arranged in pairs along the x, y, and z axes.

The demonstrator is bolted to the shaker providing an clamped condition at the base. A tri-axial reference accelerometer is fixed to the top face and measures the base acceleration components, denoted $(A_{x,0}, A_{y,0}, A_{z,0})$ in the demonstrator coordinate system.

Three additional tri-axial accelerometers are glued on the top part of the Norcan beam: one at mid-span and one close to each end. They are denoted sensors (1)–(3) and measure the transmitted acceleration components $(A_{x,i}, A_{y,i}, A_{z,i})$ with $i \in \{1, 2, 3\}$ (see figure 5.15a)

For each sensor i, the experimental transfer function is defined (in dB) as the ratio between the top and base acceleration norms,

$$T_i = 20 \log_{10} \left(\frac{\sqrt{A_{x,i}^2 + A_{y,i}^2 + A_{z,i}^2}}{\sqrt{A_{x,0}^2 + A_{y,0}^2 + A_{z,0}^2}} \right). \tag{5.31}$$

The experimental transfer functions are shown in black in Figs. 5.15(1)–(3) for sensors (1), (2), and (3), respectively. The corresponding numerical predictions are plotted in blue. In each sub-figure, the dark and light grey rectangles indicate the absolute and SA/AS-polarised bandgaps predicted by the dispersion analysis (see Fig. 5.12), respectively.

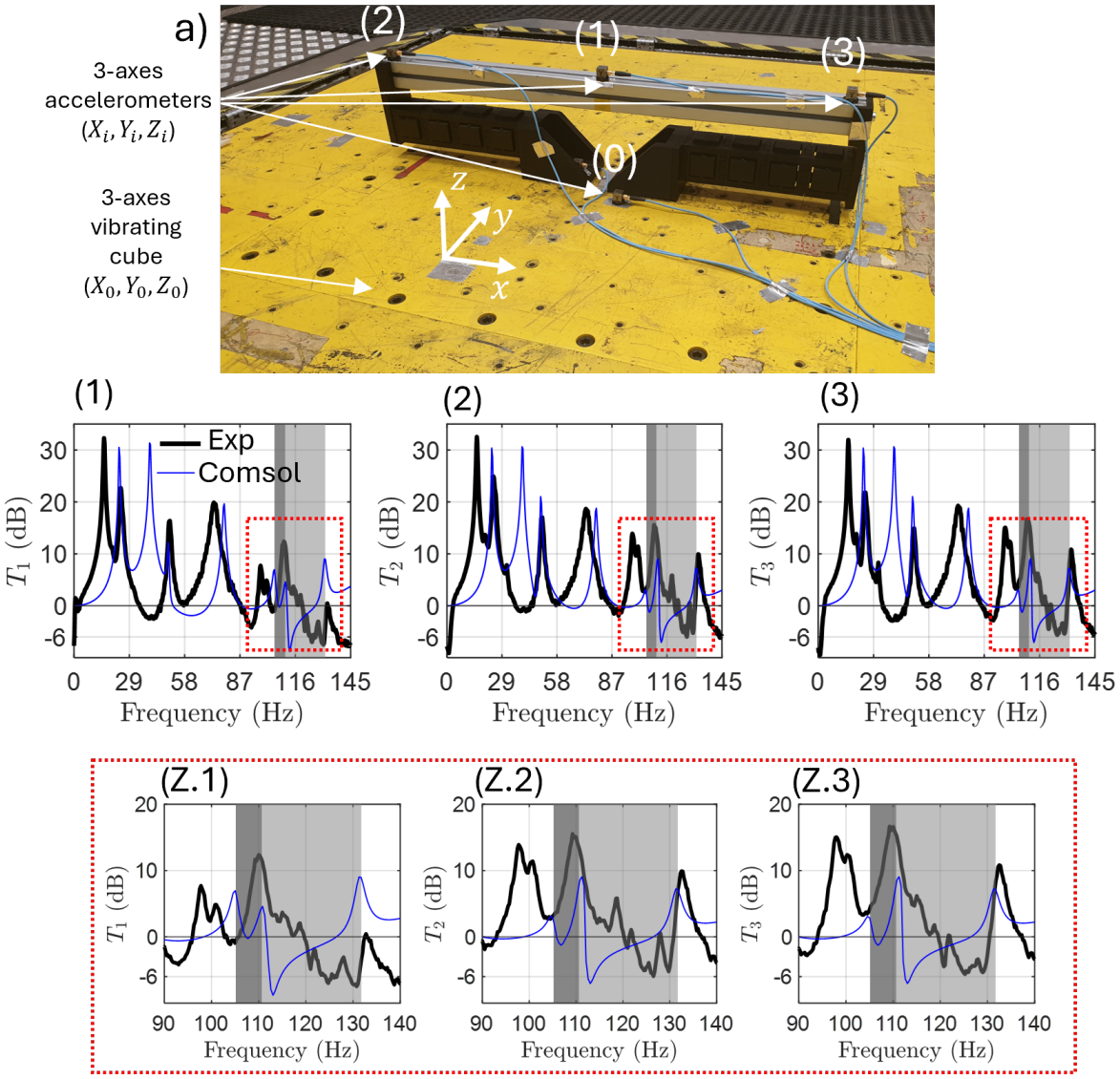

Figure 5.15: Experimental and numerical transfer functions of the demonstrator. (a) Photograph of the test set-up: the demonstrator is bolted to the top plate of a tri-axial shaker; the reference accelerometer on the shaker table and the three accelerometers mounted on the Norcan beam are indicated. (1)–(3) Transfer functions T_1 (mid-span), T_2 (right) and T_3 (left): experiments (black) and corresponding numerical predictions (blue). Dark grey bands denote the predicted absolute bandgap and light grey bands the SA/AS-polarised bandgap. Insets (Z.1)–(Z.3) provide zoomed views over $[90, 140]$ Hz.

The experimental transfer functions exhibit resonance peaks that do not align with the numerical predictions, suggesting that the assembled structure is more compliant than the idealised FEM model. This discrepancy is primarily attributed to clearance and micro-slip at the mechanical joints, effects that are not represented in the numerical model.

The zoomed views in Figs. 5.15(Z.1)–(Z.3) over $[90, 140]$ Hz reveal an attenuation trend in the

measurements, but it does not match the numerical curves closely enough to conclude on the existence of the absolute bandgap or to evaluate filtering performance. Even in the numerical model, the predicted attenuation remains modest; once manufacturing and assembly imperfections are introduced, this attenuation can easily be masked by parasite vibration mechanisms or by external disturbances affecting the measurement (e.g. background noise, imperfect shaker control, or unintended excitation paths).

Improving the comparison would require tighter control of the assembly clearances through more accurate fabrication tolerances. In addition, designing a configuration with stronger filtering performance would make the demonstrator more robust to experimental uncertainties.

Conclusion

This chapter extended the resonant-filter design methodology, previously devised for polarization-selective filtering, toward an *absolute* objective, *i.e.* the simultaneous opening of locally resonant bandgaps for the four symmetry families (SS, SA, AS and AA) of a cubic beam-lattice waveguide. A multi-resonant unit cell combining several oriented local resonators was introduced and analysed using the proposed semi-analytical framework.

In the undamped case, the parametric study identified the resonant mass fraction μ_2 as the dominant control parameter of the absolute bandgap width. For identical resonators, the absolute bandgap is primarily limited by the SS family, because only a small share of the total resonant mass effectively contributes to compression. Redistributing the resonant mass alleviates this limitation and widens the overlap between polarised gaps. The best compromise is obtained when the x-oriented resonator accounts for approximately one third of the total resonant mass: below this value, the SS gap remains limiting, whereas above it the bending-dominated (SA/AS) gaps become the bottleneck.

When material damping and a finite number of cells are considered, additional performance limits arise. Although an absolute bandgap may exist in the undamped dispersion relation, attenuation levels can remain polarization-dependent for short chains. This behaviour is mainly driven by the strong stiffness contrast between compressional and bending motions, which results in a much lower effective resonance placement for compression than for bending.

These concepts were implemented in a laboratory-scale demonstrator inspired by an aircraft passenger seat-rail application. Tri-axial shaker tests reveal clear resonance shifts and significant discrepancies with respect to the numerical model: the assembled structure is more compliant than the idealised representation, mainly due to manufacturing tolerances that introduce joint clearance and micro-slip at the interfaces. Consequently, the attenuation measured in the target band cannot be conclusively attributed to the predicted absolute bandgap. Tighter control of both fabrication and assembly is therefore required.

CHAPTER 6

Conclusion and perspectives

6.1 Summary

The objective of this thesis was to investigate periodic lattice structures, composed of beam assemblies, for the design of robust structural components capable of filtering different types of elastic waves in relatively low-frequency ranges. This work was motivated by a targeted application: the redesign of an aircraft cabin seat rail, which must support passenger seats while limiting the transmission of vibrations to the occupants.

The first chapter introduced the application case and the associated design constraints. In the aerospace field, vibration-related issues must be addressed while limiting additional mass. This motivates the development of multifunctional components, in which an existing structural element is redesigned to provide an additional vibration mitigation function. In this context, the seat rail appears as a particularly relevant candidate. It is a key vibration transmission path between the aircraft floor and the passenger seats, while not being a primary load-bearing component for the global structural integrity of the aircraft. It can therefore be redesigned to incorporate a filtering function, provided that its mechanical role of supporting the seats and occupants is preserved. Lattice-type structures were selected for this purpose because they combine low mass, high stiffness, and geometrical periodicity. This periodicity can generate bandgaps through Bragg scattering, thereby preventing elastic-wave propagation over specific frequency ranges. Since the vibrations transmitted to the seats involve several wave polarizations, the objective was to design an absolute filter, defined here as a structure exhibiting overlapping bandgaps for all relevant elastic-wave families within the targeted frequency range.

The second chapter focused on the development of computational and analysis tools for one-dimensional periodic networks made of three-dimensional beam assemblies. The proposed approach relies on the modeling of a unit cell using beam spectral elements, combined with Floquet–Bloch periodic boundary conditions at the cell boundaries. This semi-analytical formulation makes it possible to solve the dispersion relation of complex architected structures efficiently and at low computational cost. It therefore enables the rapid evaluation of many configurations and facilitates the exploration of the geometric design space. However, the large number of degrees of freedom inherent

to lattice structures leads to dense dispersion diagrams, whose interpretation can quickly become difficult. To address this issue, a symmetry-based method was introduced. It allows the eigenvalue problem to be factorized into four independent subproblems associated with distinct wave families. This decomposition establishes a direct link between the geometric parameters of the unit cell and the characteristics of the polarized Bragg bandgaps. As a result, the design of overlapping bandgaps becomes more accessible, making it possible to construct absolute vibration filters in a systematic way. These tools were then used to design a first absolute filter, which was manufactured by polymer additive manufacturing and experimentally evaluated.

The third chapter assessed the compromise between the attenuation performance provided by Bragg bandgaps and the associated loss of specific stiffness. A sandwich architecture was investigated, in which both the skins and the core contribute to the filtering behavior. The numerical tools developed in Chapter 2 were extended by incorporating plate spectral elements and by modeling the coupling between beam and plate components. This study showed that generating low-frequency absolute Bragg bandgaps generally requires strong modifications of the structural wave propagation properties, which can significantly reduce specific stiffness and lead to highly compliant structures. In this context, the sandwich configuration provides an attractive design lever. It allows the use of skins with favorable filtering properties, although they may have limited bending stiffness, while the lattice core contributes to recovering part of the global bending stiffness. The filtering performance can therefore be largely preserved while improving the structural efficiency. Nevertheless, the study also highlighted a fundamental limitation of Bragg-based filters: their characteristic frequency is scale-dependent. Lowering the bandgap frequency requires either increasing the unit-cell size, which reduces compactness, or decreasing the phase velocity, which generally leads to a substantial loss of stiffness.

The fourth chapter addressed locally resonant bandgaps. It focused on the periodic integration of local resonators into waveguides in order to generate subwavelength attenuation bands. Starting from an idealized mass–spring model representing a simple waveguide supporting a single propagating wave, analytical relationships were derived to clarify the trade-off between the mass added by the resonators and the resulting attenuation performance. This analysis was carried out for undamped and damped resonators, as well as for the nonlinear case in which the resonators operate over large deformation ranges. The results provided a physical understanding of the key design parameters and useful reference trends for the design of real filters. The study was then extended to beam-lattice waveguides using the spectral model developed in Chapter 2, with resonant elements targeting a single wave polarization. The comparison with the simplified model showed that, in the undamped case, the mass–spring model accurately captures the main trends and the optimal design parameters. In contrast, for damped finite chains, the evanescent and weakly propagating modes described by the spectral model play a major role in the attenuation levels and must be accounted for. Experimental validation on an additively manufactured prototype confirmed these trends, while also highlighting the limitations of the concept in nonlinear operating regimes. Overall, this chapter proposed a design methodology for locally resonant periodic filters and clarified the influence of mass ratio, damping, finite-size effects, and nonlinearities on the filtering performance.

The fifth chapter built on these developments to design an absolute locally resonant filter. Five resonators were integrated into a cubic lattice unit cell in order to generate polarized locally resonant bandgaps for the four wave families identified in Chapter 2. This strategy makes it possible to tune the resonators and the lattice geometry so as to obtain a structure combining high stiffness with a subwavelength absolute bandgap. However, the compromise between attenuation performance and added mass was found to be less favorable than for the polarized filter investigated in Chapter 4. This limitation is mainly due to a non-optimal distribution of the effective resonant mass among the different wave families, suggesting that alternative resonator configurations could further improve the performance. The concept was then implemented in a demonstrator representative, at reduced scale, of the aircraft cabin seat-rail application. Its performance was investigated through finite-element simulations and experimental validation after manufacturing and assembly. The experimental results, however, did not fully confirm the expected numerical performance. Significant discrepancies were observed between the numerical model and the manufactured structure, mainly due to large assembly tolerances. These tolerances led to a more compliant structure than expected and introduced clearance at the interfaces, effects that were not included in the numerical model.

The progression followed throughout the thesis, from the definition of the application case to the design and experimental assessment of absolute vibration filters, led to several methodological and technological contributions. These contributions are summarized in Table 6.1.

Taken together, these contributions show that the work carried out in this thesis is not limited to the design of a specific demonstrator. It also provides a broader methodological framework for analyzing, interpreting, and designing periodic elastic-wave filters based on lattice structures. The following conclusion therefore draws the main lessons from this work, emphasizing both the potential of the proposed approaches and the limitations that must still be overcome before considering their integration into realistic aeronautical structures.

6.2 Conclusion

This thesis developed a set of theoretical, numerical, and experimental tools for the design of periodic vibration filters based on lattice structures. The work demonstrated that periodic architected components can be used to control the propagation of elastic waves and to generate either Bragg or locally resonant bandgaps. In particular, the concept of an absolute filter was investigated as a means of attenuating several wave polarizations within a common frequency range, which is a key requirement for the targeted aircraft seat-rail application.

A first major outcome of this work is the development of efficient semi-analytical models for periodic beam and beam–plate lattice structures. These models provide direct access to dispersion properties while remaining computationally affordable. The introduction of symmetry-based decompositions further improves the interpretation of complex dispersion diagrams and enables a more systematic design of polarized and absolute bandgaps. These tools are therefore well suited for the preliminary design and optimization of periodic elastic-wave filters.

A second important result is the clarification of the main design compromises governing such

Chapter	Main contribution	Outcome
Chapter 1	Definition of the application case and design objectives for a multifunctional aircraft seat rail.	Identification of the seat rail as a relevant structural component for integrating an elastic-wave filtering function while preserving load-bearing capability.
Chapter 2	Development of a spectral-element and Floquet–Bloch model for periodic beam-lattice waveguides.	Efficient computation and interpretation of dispersion diagrams, including a symmetry-based decomposition into polarized wave families.
Chapter 3	Extension of the spectral formulation to beam–plate sandwich structures.	Quantification of the trade-off between low-frequency absolute Bragg bandgaps and specific stiffness, and identification of sandwich architectures as a possible stiffness-recovery strategy.
Chapter 4	Analysis and design of polarized locally resonant periodic filters.	Derivation of analytical design trends, clarification of the influence of mass ratio, damping, finite-size effects, and nonlinearities, and experimental validation on an additively manufactured prototype.
Chapter 5	Design of an absolute locally resonant lattice filter.	Proposal of a stiff subwavelength absolute filter concept, numerical and experimental assessment on a reduced-scale seat-rail demonstrator, and identification of manufacturing and assembly limitations.

Table 6.1: Main contributions of the thesis.

structures. Bragg-based filters can provide robust attenuation but are strongly constrained by scale effects. Lowering the bandgap frequency generally requires either increasing the unit-cell size or reducing the phase velocity, both of which can be detrimental to compactness and stiffness. Locally resonant filters offer a promising alternative because they can generate subwavelength bandgaps. However, their performance depends strongly on the added resonant mass, damping, finite-size effects, and, in some cases, nonlinear behavior. For absolute locally resonant filters, the distribution of the effective resonant mass among the different wave families becomes a critical design parameter.

The thesis also showed that translating these concepts into experimental demonstrators remains challenging. Additive manufacturing offers a relevant route for producing complex lattice structures, but the agreement between numerical predictions and experimental results is highly sensitive to manufacturing accuracy, assembly tolerances, interface clearances, and local compliance effects. These aspects must be carefully controlled and included in the modeling strategy before such filters can be considered for integration into realistic aeronautical structures.

Overall, this work provides a methodological framework for the design of multifunctional periodic structures combining load-bearing capability and vibration filtering. It demonstrates the potential of lattice-based and locally resonant architectures for generating absolute bandgaps, while also identifying the technological limitations that must be overcome. Further improvements are still required to increase the maturity of the proposed solutions, particularly regarding resonator architecture, mass distribution, manufacturing accuracy, interface modeling, and full-scale validation. These aspects constitute natural directions for future work toward the development of an integrated aircraft seat-rail vibration filter.

6.3 Perspectives

6.3.1 Promising configuration: 2-DOF resonators

The next step is to further improve the current design in order to enhance its filtering performance and simplify the assembly process. To this end, alternative configurations should be investigated. A particularly promising option is the configuration shown in Fig. 6.1c), in which four two-degree-of-freedom resonators are placed on the outer faces of the lattice cube. On each face, the primary resonator is polarized along the x-axis, while the secondary resonator is polarized along either the y- or z-axis. This arrangement provides a more favorable distribution of the effective resonant mass among the different wave families.

A preliminary computation presented in figure. 6.1a) compares the ratio between the transmitted and input acceleration norms for two types of five-cell filters. The result for the current configuration (see figure. 6.1b) , is plotted in red, whereas the result for the new configuration incorporating two-degree-of-freedom resonators (see figure. 6.1c), is plotted in blue. Both configurations were designed to have the same total mass and the same lower edge of the absolute bandgap. The results suggest that the new configuration (blue) provides both improved attenuation performance and a wider attenuation bandwidth, although a dedicated study is still required to confirm and generalize this trend.

In addition, this configuration (see figure. 6.1c.1 and c.2) would simplify both the fabrication and

assembly of the prototype, since it eliminates internal faces. The four outer faces of the final multi-cell beam could then be manufactured as single parts and assembled afterward, either by welding in the case of a metallic structure or by tongue and groove joints in the case of polymer manufacturing. This would avoid assembling the cells one by one and would therefore reduce assembly-related uncertainties.

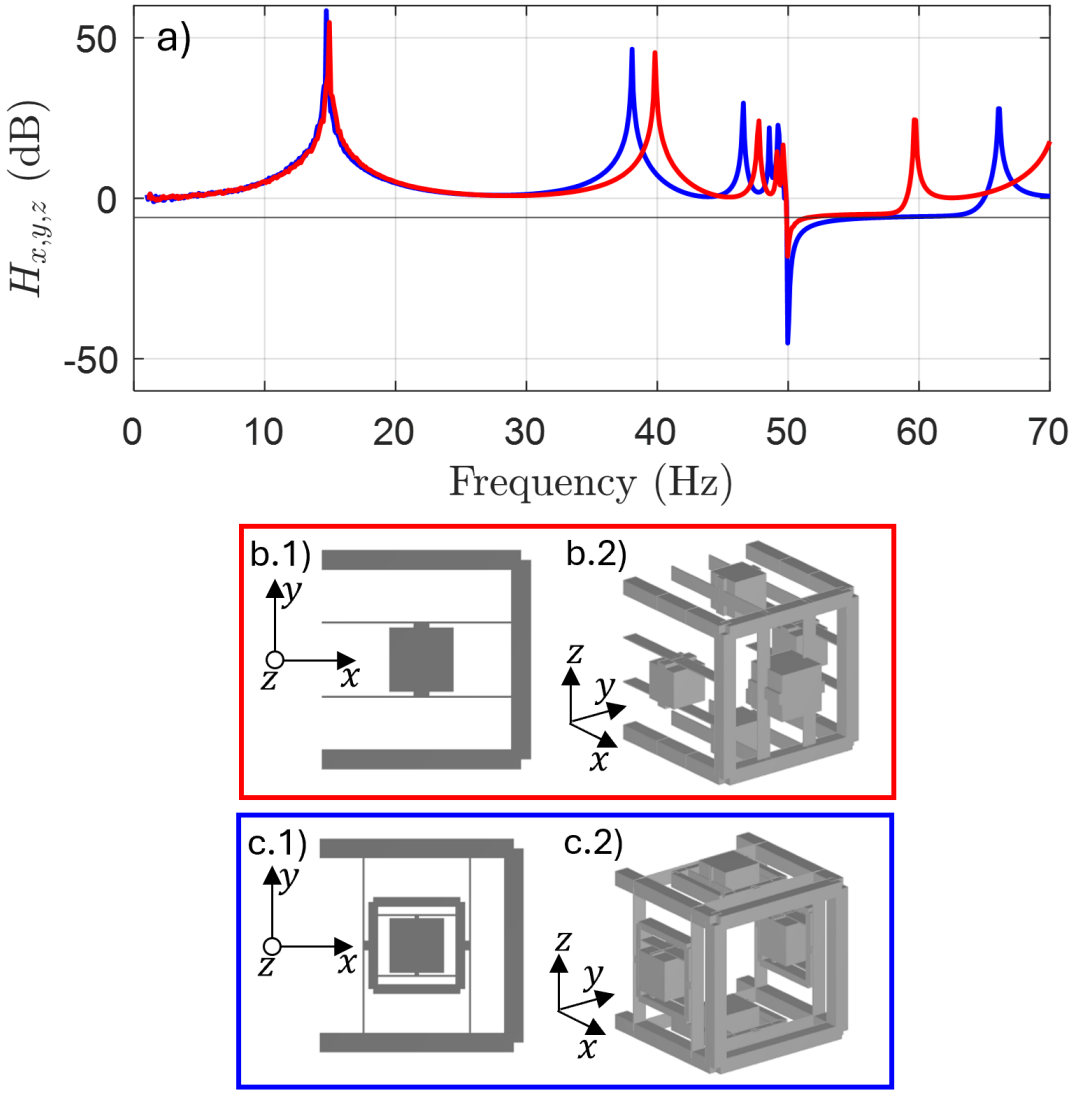

Figure 6.1: Alternative multi-resonator layouts for the cubic beam-lattice unit cell and preliminary numerical comparison. (a) Transmitted-to-input acceleration norm ratio for five-cell filters : actual configuration (red) and new configuration (blue). (b) Actual configuration with five single-degree-of-freedom resonators: two z-oriented resonators, two y-oriented resonators, and one internal x-oriented resonator. (c) New configuration with four external two-degree-of-freedom resonators: on each face, a primary resonator polarized along x is coupled to a secondary resonator polarized along y or z.

6.3.2 The filtering periodic lattice waveguide as a cable HUB

Another possible improvement to the actual filtering rail would be to add a third functionality by using it as a cable hub. In an aircraft, the underfloor area contains an extensive network of cables supplying power and signals to the various onboard electronic systems, including the many sensors distributed throughout the structure. The new rail configuration proposed here is a lattice waveguide with a hollow cross-section, which could therefore also serve as a cable-routing channel. These cables could be periodically attached to the transverse beams of the waveguide.

The intrinsic damping of the cables could help reduce the additional resonant peaks appearing around the bandgap generated by the resonators, without significantly degrading the attenuation performance within the targeted frequency range. More broadly, it may also be worth investigating the interaction between the nonlinear dynamic behavior of the cables and wave propagation in the filter. Similar ideas have already been explored in previous studies, where non-structural components such as cables were used as a means of vibration control in structures developed for aerospace and space applications [221, 222].

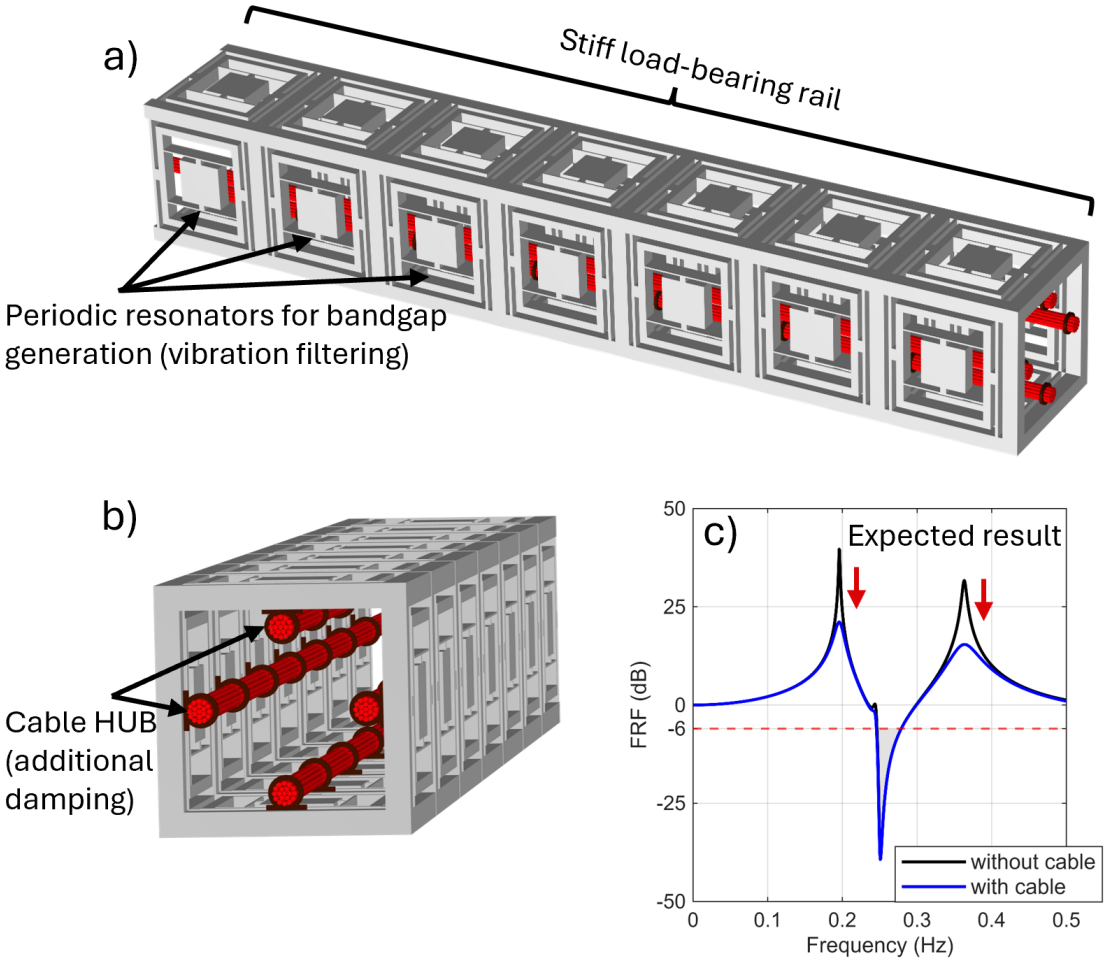

Figure 6.2: Three-functional passenger seat rail prototype: (1) a load-bearing rail enabled by its lattice architecture, (2) a rail capable of filtering elastic waves through the integration of periodically distributed resonators, and (3) a cable-routing rail, where the cables may provide additional damping and thereby further enhance the vibration filtering performance.

6.3.3 Controlling resonator nonlinearities

A final research direction would be to investigate more thoroughly the operating domains of resonators in their nonlinear regime. As shown in the chapter 4, resonator nonlinearities directly affect resonant bandgaps and can therefore strongly influence the filtering performance. It would be particularly interesting to study different types of nonlinearity in order to control their effects and potentially improve attenuation. For instance, softening nonlinearities [223–225] could be exploited to shift the bandgaps toward lower frequencies without increasing the added mass. Impact nonlinearities could also be considered, as they are able to transfer energy across the frequency spectrum [226–228], in particular toward higher frequencies, where Bragg bandgaps can be more easily opened in the waveguide without significantly degrading its stiffness.

For both cases, figures. 6.3 illustrates possible design concepts for exploiting nonlinear effects in local resonators. Figure 6.3a) shows a configuration intended to generate a softening geometric nonlinearity through the inclined slender beams supporting the resonating mass. Figure 6.3b) presents a design based on impact nonlinearity, in which the displacement of the mass is constrained between two stops so that resonance induces repeated impacts. Another possible implementation is shown in Fig. 6.3c), where the impact mechanism is produced by a ball embedded inside the resonator mass.

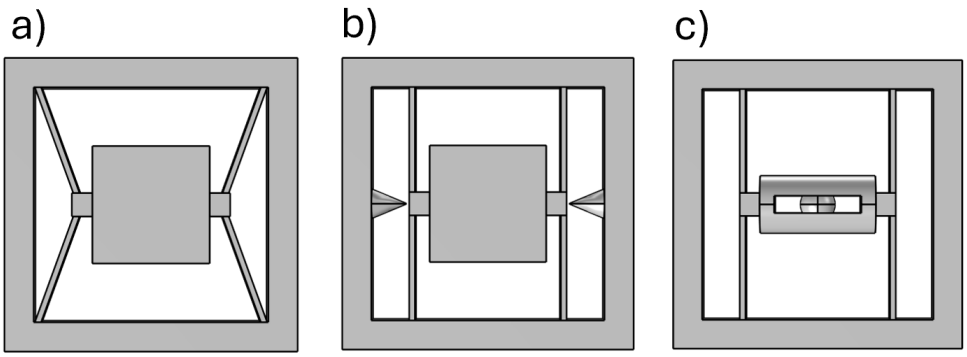

Figure 6.3: Concepts for exploiting nonlinear effects in local resonators. (a) Example of a resonator designed to exhibit a softening geometric nonlinearity through inclined slender supporting beams. (b) Example of an impact-based resonator, in which the mass displacement is limited by two stops, leading to repeated impacts under resonance. (c) Alternative impact-based concept relying on a ball embedded within the resonator mass.

Appendices

A Spectral beam matrices

$$\mathbf{D} = \begin{bmatrix}
1 & 0 & 0 & 0 & 0 & 0 & 1 & 0 & 0 & 0 & 0 & 0 \\
0 & 1 & 0 & 0 & 0 & 1 & 0 & 1 & 0 & 0 & 0 & 1 \\
0 & 0 & 1 & 0 & 1 & 0 & 0 & 0 & 1 & 0 & 1 & 0 \\
0 & 0 & 0 & 1 & 0 & 0 & 0 & 0 & 0 & 1 & 0 & 0 \\
0 & 0 & \beta_{3\mathrm{t}} & 0 & -\beta_{3\mathrm{t}} & 0 & 0 & 0 & \beta_{3\mathrm{e}} & 0 & -\beta_{3\mathrm{e}} & 0 \\
0 & \beta_{2\mathrm{t}} & 0 & 0 & 0 & -\beta_{2\mathrm{t}} & 0 & \beta_{2\mathrm{e}} & 0 & 0 & 0 & -\beta_{2\mathrm{e}} \\
D_{7,1} & 0 & 0 & 0 & 0 & 0 & D_{7,7} & 0 & 0 & 0 & 0 & 0 \\
0 & D_{8,2} & 0 & 0 & 0 & D_{8,6} & 0 & D_{8,8} & 0 & 0 & 0 & D_{8,12} \\
0 & 0 & D_{9,3} & 0 & D_{9,5} & 0 & 0 & 0 & D_{9,9} & 0 & D_{9,11} & 0 \\
0 & 0 & 0 & D_{10,4} & 0 & 0 & 0 & 0 & 0 & D_{10,10} & 0 & 0 \\
0 & 0 & D_{11,3} & 0 & D_{11,5} & 0 & 0 & 0 & D_{11,9} & 0 & D_{11,11} & 0 \\
0 & D_{12,2} & 0 & 0 & 0 & D_{12,6} & 0 & D_{12,8} & 0 & 0 & 0 & D_{12,12}
\end{bmatrix}$$

$$\begin{aligned}
D_{7,1} &= \mathrm{e}^{-Lk_u\mathrm{i}} & D_{7,7} &= \mathrm{e}^{Lk_u\mathrm{i}} & D_{8,2} &= \mathrm{e}^{-Lk_{2\mathrm{t}}\mathrm{i}} \\
D_{8,6} &= \mathrm{e}^{Lk_{2\mathrm{t}}\mathrm{i}} & D_{8,8} &= \mathrm{e}^{-Lk_{2\mathrm{e}}\mathrm{i}} & D_{8,12} &= \mathrm{e}^{Lk_{2\mathrm{e}}\mathrm{i}} \\
D_{9,3} &= \mathrm{e}^{-Lk_{3\mathrm{t}}\mathrm{i}} & D_{9,5} &= \mathrm{e}^{Lk_{3\mathrm{t}}\mathrm{i}} & D_{9,9} &= \mathrm{e}^{-Lk_{3\mathrm{e}}\mathrm{i}} \\
D_{9,11} &= \mathrm{e}^{Lk_{3\mathrm{e}}\mathrm{i}} & D_{10,4} &= \mathrm{e}^{-Lk_\theta\mathrm{i}} & D_{10,10} &= \mathrm{e}^{Lk_\theta\mathrm{i}} \\
D_{11,3} &= \beta_{3\mathrm{t}}\mathrm{e}^{-Lk_{3\mathrm{t}}\mathrm{i}} & D_{11,5} &= -\beta_{3\mathrm{t}}\mathrm{e}^{Lk_{3\mathrm{t}}\mathrm{i}} & D_{11,9} &= \beta_{3\mathrm{e}}\mathrm{e}^{-Lk_{3\mathrm{e}}\mathrm{i}} \\
D_{11,11} &= -\beta_{3\mathrm{e}}\mathrm{e}^{Lk_{3\mathrm{e}}\mathrm{i}} & D_{12,2} &= \beta_{2\mathrm{t}}\mathrm{e}^{-Lk_{2\mathrm{t}}\mathrm{i}} & D_{12,6} &= -\beta_{2\mathrm{t}}\mathrm{e}^{Lk_{2\mathrm{t}}\mathrm{i}} \\
D_{12,8} &= \beta_{2\mathrm{e}}\mathrm{e}^{-Lk_{2\mathrm{e}}\mathrm{i}} & D_{12,12} &= -\beta_{2\mathrm{e}}\mathrm{e}^{Lk_{2\mathrm{e}}\mathrm{i}}
\end{aligned}$$

$$\mathbf{F} = \begin{bmatrix}
F_{1,1} & 0 & 0 & 0 & 0 & 0 & F_{1,7} & 0 & 0 & 0 & 0 & 0 \\
0 & F_{2,2} & 0 & 0 & 0 & F_{2,6} & 0 & F_{2,8} & 0 & 0 & 0 & F_{2,12} \\
0 & 0 & F_{3,3} & 0 & F_{3,5} & 0 & 0 & 0 & F_{3,9} & 0 & F_{3,11} & 0 \\
0 & 0 & 0 & F_{4,4} & 0 & 0 & 0 & 0 & 0 & F_{4,10} & 0 & 0 \\
0 & 0 & F_{5,3} & 0 & F_{5,5} & 0 & 0 & 0 & F_{5,9} & 0 & F_{5,11} & 0 \\
0 & F_{6,2} & 0 & 0 & 0 & F_{6,6} & 0 & F_{6,8} & 0 & 0 & 0 & F_{6,12} \\
F_{7,1} & 0 & 0 & 0 & 0 & 0 & F_{7,7} & 0 & 0 & 0 & 0 & 0 \\
0 & F_{8,2} & 0 & 0 & 0 & F_{8,6} & 0 & F_{8,8} & 0 & 0 & 0 & F_{8,12} \\
0 & 0 & F_{9,3} & 0 & F_{9,5} & 0 & 0 & 0 & F_{9,9} & 0 & F_{9,11} & 0 \\
0 & 0 & 0 & F_{10,4} & 0 & 0 & 0 & 0 & 0 & F_{10,10} & 0 & 0 \\
0 & 0 & F_{11,3} & 0 & F_{11,5} & 0 & 0 & 0 & F_{11,9} & 0 & F_{11,11} & 0 \\
0 & F_{12,2} & 0 & 0 & 0 & F_{12,6} & 0 & F_{12,8} & 0 & 0 & \mathbf{0} & F_{12,12}
\end{bmatrix}$$

$$
\begin{aligned}
F_{1,1} &= AEk_u\mathrm{i} & F_{1,7} &= -AEk_u\mathrm{i} & F_{2,2} &= AG\kappa\left(\beta_{2\mathrm{t}} + k_{2\mathrm{t}}\mathrm{i}\right)\\
F_{2,6} &= -AG\kappa\left(\beta_{2\mathrm{t}} + k_{2\mathrm{t}}\mathrm{i}\right) & F_{2,8} &= AG\kappa\left(\beta_{2\mathrm{e}} + k_{2\mathrm{e}}\mathrm{i}\right) & F_{2,12} &= -AG\kappa\left(\beta_{2\mathrm{e}} + k_{2\mathrm{e}}\mathrm{i}\right)\\
F_{3,3} &= AG\kappa\left(\beta_{3\mathrm{t}} + k_{3\mathrm{t}}\mathrm{i}\right) & F_{3,5} &= -AG\kappa\left(\beta_{3\mathrm{t}} + k_{3\mathrm{t}}\mathrm{i}\right) & F_{3,9} &= AG\kappa\left(\beta_{3\mathrm{e}} + k_{3\mathrm{e}}\mathrm{i}\right)\\
F_{3,11} &= -AG\kappa\left(\beta_{3\mathrm{e}} + k_{3\mathrm{e}}\mathrm{i}\right) & F_{4,4} &= GI_1k_\theta\mathrm{i} & F_{4,10} &= -GI_1k_\theta\mathrm{i}\\
F_{5,3} &= \beta_{3\mathrm{t}}EI_2k_{3\mathrm{t}}\mathrm{i} & F_{5,5} &= \beta_{3\mathrm{t}}EI_2k_{3\mathrm{t}}\mathrm{i} & F_{5,9} &= \beta_{3\mathrm{e}}EI_2k_{3\mathrm{e}}\mathrm{i}\\
F_{5,11} &= \beta_{3\mathrm{e}}EI_2k_{3\mathrm{e}}\mathrm{i} & F_{6,2} &= \beta_{2\mathrm{t}}EI_3k_{2\mathrm{t}}\mathrm{i} & F_{6,6} &= \beta_{2\mathrm{t}}EI_3k_{2\mathrm{t}}\mathrm{i}\\
F_{6,8} &= \beta_{2\mathrm{e}}EI_3k_{2\mathrm{e}}\mathrm{i} & F_{6,12} &= \beta_{2\mathrm{e}}EI_3k_{2\mathrm{e}}\mathrm{i}
\end{aligned}
$$

$$
\begin{aligned}
F_{7,1} &= -AEk_u\mathrm{e}^{-Lk_ui}\mathrm{i} & F_{7,7} &= AEk_u\mathrm{e}^{Lk_ui}\mathrm{i}\\
F_{8,2} &= -AG\kappa\left(\beta_{2\mathrm{t}}\mathrm{e}^{-Lk_{2\mathrm{t}}\mathrm{i}} + k_{2\mathrm{t}}\mathrm{e}^{-Lk_{2\mathrm{t}}\mathrm{i}}\mathrm{i}\right) & F_{8,6} &= AG\kappa\left(\beta_{2\mathrm{t}}\mathrm{e}^{Lk_{2\mathrm{t}}\mathrm{i}} + k_{2\mathrm{t}}\mathrm{e}^{Lk_{2\mathrm{t}}\mathrm{i}}\mathrm{i}\right)\\
F_{8,8} &= -A\,G\,\kappa\,\left(\beta_{2\mathrm{e}}\,\mathrm{e}^{-L\,k_{2\mathrm{e}}\mathrm{i}} + k_{2\mathrm{e}}\,\mathrm{e}^{-L\,k_{2\mathrm{e}}\mathrm{i}}\mathrm{i}\right) & F_{8,12} &= A\,G\,\kappa\,\left(\beta_{2\mathrm{e}}\,\mathrm{e}^{L\,k_{2\mathrm{e}}\mathrm{i}} + k_{2\mathrm{e}}\,\mathrm{e}^{L\,k_{2\mathrm{e}}\mathrm{i}}\mathrm{i}\right)\\
F_{9,3} &= -A\,G\,\kappa\,\left(\beta_{3\mathrm{t}}\,\mathrm{e}^{-L\,k_{3\mathrm{t}}\mathrm{i}} + k_{3\mathrm{t}}\,\mathrm{e}^{-L\,k_{3\mathrm{t}}\mathrm{i}}\mathrm{i}\right) & F_{9,5} &= A\,G\,\kappa\,\left(\beta_{3\mathrm{t}}\,\mathrm{e}^{L\,k_{3\mathrm{t}}\mathrm{i}} + k_{3\mathrm{t}}\,\mathrm{e}^{L\,k_{3\mathrm{t}}\mathrm{i}}\mathrm{i}\right)\\
F_{9,9} &= -A\,G\,\kappa\,\left(\beta_{3\mathrm{e}}\,\mathrm{e}^{-L\,k_{3\mathrm{e}}\mathrm{i}} + k_{3\mathrm{e}}\,\mathrm{e}^{-L\,k_{3\mathrm{e}}\mathrm{i}}\mathrm{i}\right) & F_{9,11} &= A\,G\,\kappa\,\left(\beta_{3\mathrm{e}}\,\mathrm{e}^{L\,k_{3\mathrm{e}}\mathrm{i}} + k_{3\mathrm{e}}\,\mathrm{e}^{L\,k_{3\mathrm{e}}\mathrm{i}}\mathrm{i}\right)\\
F_{10,4} &= -\mathrm{i}G\,I_1\,k_\theta\,\mathrm{e}^{-L\,k_\theta\mathrm{i}} & F_{10,10} &= \mathrm{i}G\,I_1\,k_\theta\,\mathrm{e}^{L\,k_\theta\mathrm{i}}\\
F_{11,3} &= -\mathrm{i}\beta_{3\mathrm{t}}\,E\,I_2\,k_{3\mathrm{t}}\,\mathrm{e}^{-L\,k_{3\mathrm{t}}\mathrm{i}} & F_{11,5} &= -\mathrm{i}\beta_{3\mathrm{t}}\,E\,I_2\,k_{3\mathrm{t}}\,\mathrm{e}^{L\,k_{3\mathrm{t}}\mathrm{i}}\\
F_{11,9} &= -\mathrm{i}\beta_{3\mathrm{e}}\,E\,I_2\,k_{3\mathrm{e}}\,\mathrm{e}^{-L\,k_{3\mathrm{e}}\mathrm{i}} & F_{11,11} &= -\mathrm{i}\beta_{3\mathrm{e}}\,E\,I_2\,k_{3\mathrm{e}}\,\mathrm{e}^{L\,k_{3\mathrm{e}}\mathrm{i}}\\
F_{12,2} &= -\mathrm{i}\beta_{2\mathrm{t}}\,E\,I_3\,k_{2\mathrm{t}}\,\mathrm{e}^{-L\,k_{2\mathrm{t}}\mathrm{i}} & F_{12,6} &= -\mathrm{i}\beta_{2\mathrm{t}}\,E\,I_3\,k_{2\mathrm{t}}\,\mathrm{e}^{L\,k_{2\mathrm{t}}\mathrm{i}}\\
F_{12,8} &= -\mathrm{i}\beta_{2\mathrm{e}}\,E\,I_3\,k_{2\mathrm{e}}\,\mathrm{e}^{-L\,k_{2\mathrm{e}}\mathrm{i}} & F_{12,12} &= -\mathrm{i}\beta_{2\mathrm{e}}\,E\,I_3\,k_{2\mathrm{e}}\,\mathrm{e}^{L\,k_{2\mathrm{e}}\mathrm{i}}
\end{aligned}
$$

$$k_u = \omega\sqrt{\frac{\rho}{E}} \qquad k_\Theta = \omega\sqrt{\frac{\rho}{G}}$$

$$k_{2\mathrm{t}} = \frac{k_{\mathrm{F}2}}{\sqrt{2}}\sqrt{\eta_2k_{\mathrm{F}2}^2 + \sqrt{\eta_2^2k_{\mathrm{F}2}^4 + 4\left(1 - \eta_{21}k_G^4\right)}}$$

$$k_{2\mathrm{e}} = \frac{k_{\mathrm{F}2}}{\sqrt{2}}\sqrt{\eta_2k_{\mathrm{F}2}^2 - \sqrt{\eta_2^2k_{\mathrm{F}2}^4 + 4\left(1 - \eta_{21}k_G^4\right)}}$$

$$k_{3\mathrm{t}} = \frac{k_{\mathrm{F}3}}{\sqrt{2}}\sqrt{\eta_3k_{\mathrm{F}3}^2 + \sqrt{\eta_3^2k_{\mathrm{F}3}^4 + 4\left(1 - \eta_{31}k_G^4\right)}}$$

$$k_{3\mathrm{e}} = \frac{k_{\mathrm{F}3}}{\sqrt{2}}\sqrt{\eta_3k_{\mathrm{F}3}^2 - \sqrt{\eta_3^2k_{\mathrm{F}3}^4 + 4\left(1 - \eta_{31}k_G^4\right)}}$$

$k_{\mathrm{F}2} = \sqrt{\omega}\left(\rho A/EI_3\right)^{1/4}, \eta_2 = I_3/A + EI_3/(\kappa GA)$, $\eta_{21} = I_3/A$. $k_{\mathrm{F}3} = \sqrt{\omega}\left(\rho A/EI_2\right)^{1/4}, \eta_3 = I_2/A + EI_2/(\kappa GA)$, $\eta_{31} = I_2/A$.

B Beam orientation

The rotation matrix $\mathbf{T}_c$ is constructed through three successive rotations that align the global coordinate system $(\mathbf{x}, \mathbf{y}, \mathbf{z})$ with the local coordinate system $(\mathbf{e}_1, \mathbf{e}_2, \mathbf{e}_3)$. The first rotation is around the **z**-axis, the second rotation is around the **y**-axis, and the third rotation is around the **x**-axis to align the section's coordinate system with the $\mathbf{e}_2$ and $\mathbf{e}_3$ axes. The angles of the first and second rotations are determined using the coordinates g_x, g_y, and g_z. The third rotation is defined by an angle Ψ depending on the section's orientation. In our case, with cylindrical symmetry of the section, $\Psi = 0$. The multiplication of these three successive rotations yields the following rotation matrix:

$$\mathbf{T}_c = \begin{bmatrix} \hat{g_x} & \hat{g_y} & \hat{g_z} \\ \frac{-\hat{g_y}\cos\Psi - \hat{g_x}\hat{g_z}\sin\Psi}{Q} & \frac{\hat{g_x}\cos\Psi - \hat{g_y}\hat{g_z}\sin\Psi}{Q} & Q\sin\Psi \\ \frac{\hat{g_y}\sin\Psi - \hat{g_x}\hat{g_z}\cos\Psi}{Q} & \frac{-\hat{g_x}\sin\Psi - \hat{g_y}\hat{g_z}\cos\Psi}{Q} & Q\cos\Psi \end{bmatrix} \tag{B.1}$$

Where $\hat{g_x} = \frac{g_x}{\sqrt{g_x^2+g_y^2+g_z^2}}$, $\hat{g_y} = \frac{g_y}{\sqrt{g_x^2+g_y^2+g_z^2}}$, $\hat{g_z} = \frac{g_z}{\sqrt{g_x^2+g_y^2+g_z^2}}$ and $Q = \sqrt{1-\hat{g_z}}$

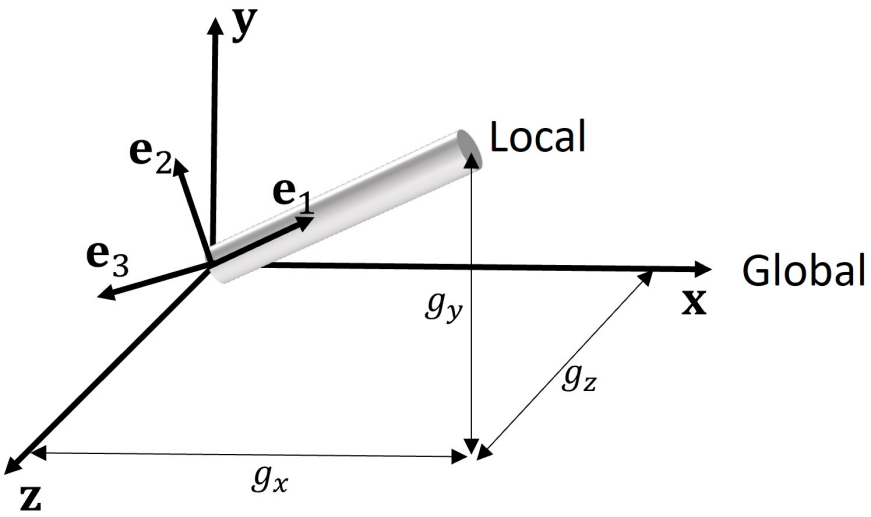

Figure B.1: Direction cosines for an 3D oriented beam

C Symmetry-based condensation

Applying periodic conditions leads to the dynamic stiffness matrix $\mathbf{S}_p$, which is linked to the displacement vector $\mathbf{d}_p$. The displacement vector is decomposed as:

$$\mathbf{d}_p = \begin{bmatrix} \mathbf{d}_p^{y^+} \\ \mathbf{d}_p^{y^-} \\ \mathbf{d}_p^{\mathrm{y0}} \end{bmatrix}$$

where:

- $\mathbf{d}_p^{y^+}$ corresponds to the degrees of freedom of nodes at $y > 0$
- $\mathbf{d}_p^{y^-}$ corresponds to the degrees of freedom of nodes at $y < 0$
- $\mathbf{d}_p^{\mathrm{y0}}$ corresponds to the degrees of freedom of nodes at $y = 0$

Each displacement vector contains six degrees of freedom per node:

$$\mathbf{d}_p^{y^+} = \begin{bmatrix} \mathbf{U}_1^{y^+} & \mathbf{U}_2^{y^+} & \mathbf{U}_3^{y^+} & \mathbf{\Theta}_1^{y^+} & \mathbf{\Theta}_2^{y^+} & \mathbf{\Theta}_3^{y^+} \end{bmatrix}^T$$

$$\mathbf{d}_p^{y^-} = \begin{bmatrix} \mathbf{U}_1^{y^-} & \mathbf{U}_2^{y^-} & \mathbf{U}_3^{y^-} & \mathbf{\Theta}_1^{y^-} & \mathbf{\Theta}_2^{y^-} & \mathbf{\Theta}_3^{y^-} \end{bmatrix}^T$$

$$\mathbf{d}_p^{\mathrm{y0}} = \begin{bmatrix} \mathbf{U}_1^{\mathrm{y0}} & \mathbf{U}_2^{\mathrm{y0}} & \mathbf{U}_3^{\mathrm{y0}} & \mathbf{\Theta}_1^{\mathrm{y0}} & \mathbf{\Theta}_2^{\mathrm{y0}} & \mathbf{\Theta}_3^{\mathrm{y0}} \end{bmatrix}^T$$

where $\mathbf{U}_i^{y^+}$ and $\mathbf{\Theta}_i^{y^+}$ are vectors of size $1 \times n_y$, with n_y being the number of nodes at $y > 0$. Similarly, $\mathbf{U}_i^{\mathrm{y0}}$ is a vector of size $1 \times n_{\mathrm{y0}}$, where n_{y0} is the number of nodes at $y = 0$.

—

The symmetry conditions are:

$$\mathbf{U}_1^{y^+} = \mathbf{U}_1^{y^-}, \quad \mathbf{U}_2^{y^+} = -\mathbf{U}_2^{y^-}, \quad \mathbf{U}_3^{y^+} = \mathbf{U}_3^{y^-},$$

$$\mathbf{\Theta}_1^{y^+} = -\mathbf{\Theta}_1^{y^-}, \quad \mathbf{\Theta}_2^{y^+} = \mathbf{\Theta}_2^{y^-}, \quad \mathbf{\Theta}_3^{y^+} = -\mathbf{\Theta}_3^{y^-}$$

These conditions define the transformation matrix:

$$\mathbf{T}_y^S = \begin{bmatrix} \mathbf{I}_{y^+} & \mathbf{0} \\ \mathbf{C}_y & \mathbf{0} \\ \mathbf{0} & \mathbf{I}_{\mathrm{y0}} \end{bmatrix}$$

where:

$$\mathbf{C}_y = \begin{bmatrix} \mathbf{I}_{n_y} & \mathbf{0} & \mathbf{0} & \mathbf{0} & \mathbf{0} & \mathbf{0} \\ \mathbf{0} & -\mathbf{I}_{n_y} & \mathbf{0} & \mathbf{0} & \mathbf{0} & \mathbf{0} \\ \mathbf{0} & \mathbf{0} & \mathbf{I}_{n_y} & \mathbf{0} & \mathbf{0} & \mathbf{0} \\ \mathbf{0} & \mathbf{0} & \mathbf{0} & -\mathbf{I}_{n_y} & \mathbf{0} & \mathbf{0} \\ \mathbf{0} & \mathbf{0} & \mathbf{0} & \mathbf{0} & \mathbf{I}_{n_y} & \mathbf{0} \\ \mathbf{0} & \mathbf{0} & \mathbf{0} & \mathbf{0} & \mathbf{0} & -\mathbf{I}_{n_y} \end{bmatrix}$$

with $\mathbf{I}_{y+}$, $\mathbf{I}_{y0}$ and $\mathbf{I}_{ny}$ identities matrices of size respectively $6n_y \times 6n_y$, $n_{y0} \times n_{y0}$ and $n_y \times n_y$

The condensed symmetric matrix is:

$$\mathbf{S}_p^S = \left(\mathbf{T}_y^S\right)^T \mathbf{S}_p \mathbf{T}_y^S$$

For the antisymmetric case, the transformation is:

$$\mathbf{T}_y^A = \begin{bmatrix} \mathbf{I}_y^+ & \mathbf{0} \\ -\mathbf{C}_y & \mathbf{0} \\ \mathbf{0} & \mathbf{I}_{y0} \end{bmatrix}$$

The condensed antisymmetric matrix is:

$$\mathbf{S}_p^A = \left(\mathbf{T}_y^A\right)^T \mathbf{S}_p \mathbf{T}_y^A$$

After obtaining $\mathbf{S}_p^S$ and $\mathbf{S}_p^A$, we define the remaining nodes positioned at $z > 0$, $z < 0$, and $z = 0$:

$$\mathbf{d}_p^y = \begin{bmatrix} \mathbf{d}_p^{y,z^+} \\ \mathbf{d}_p^{y,z^-} \\ \mathbf{d}_p^{y,z_0} \end{bmatrix}$$

This allows us to condense the problem into four symmetry cases:

$$\mathbf{S}_p^{\mathrm{SS}} = \left(\mathbf{T}_z^S\right)^T \mathbf{S}_p^S \mathbf{T}_z^S, \quad \mathbf{S}_p^{\mathrm{SA}} = \left(\mathbf{T}_z^A\right)^T \mathbf{S}_p^S \mathbf{T}_z^A$$

$$\mathbf{S}_p^{\mathrm{AS}} = \left(\mathbf{T}_z^S\right)^T \mathbf{S}_p^A \mathbf{T}_z^S, \quad \mathbf{S}_p^{\mathrm{AA}} = \left(\mathbf{T}_z^A\right)^T \mathbf{S}_p^A \mathbf{T}_z^A$$

where:

$$\mathbf{T}_z^S = \begin{bmatrix} \mathbf{I}_z^+ & \mathbf{0} \\ \mathbf{C}_z & \mathbf{0} \\ \mathbf{0} & \mathbf{I}_{z0} \end{bmatrix}, \quad \mathbf{T}_z^A = \begin{bmatrix} \mathbf{I}_z^+ & \mathbf{0} \\ -\mathbf{C}_z & \mathbf{0} \\ \mathbf{0} & \mathbf{I}_{z0} \end{bmatrix}$$

$$\mathbf{C}_z = \begin{bmatrix} \mathbf{I}_{n_z} & \mathbf{0} & \mathbf{0} & \mathbf{0} & \mathbf{0} & \mathbf{0} \\ \mathbf{0} & \mathbf{I}_{n_z} & \mathbf{0} & \mathbf{0} & \mathbf{0} & \mathbf{0} \\ \mathbf{0} & \mathbf{0} & -\mathbf{I}_{n_z} & \mathbf{0} & \mathbf{0} & \mathbf{0} \\ \mathbf{0} & \mathbf{0} & \mathbf{0} & -\mathbf{I}_{n_z} & \mathbf{0} & \mathbf{0} \\ \mathbf{0} & \mathbf{0} & \mathbf{0} & \mathbf{0} & -\mathbf{I}_{n_z} & \mathbf{0} \\ \mathbf{0} & \mathbf{0} & \mathbf{0} & \mathbf{0} & \mathbf{0} & \mathbf{I}_{n_z} \end{bmatrix}$$

D Full complex solution corresponding to Figure 2.12

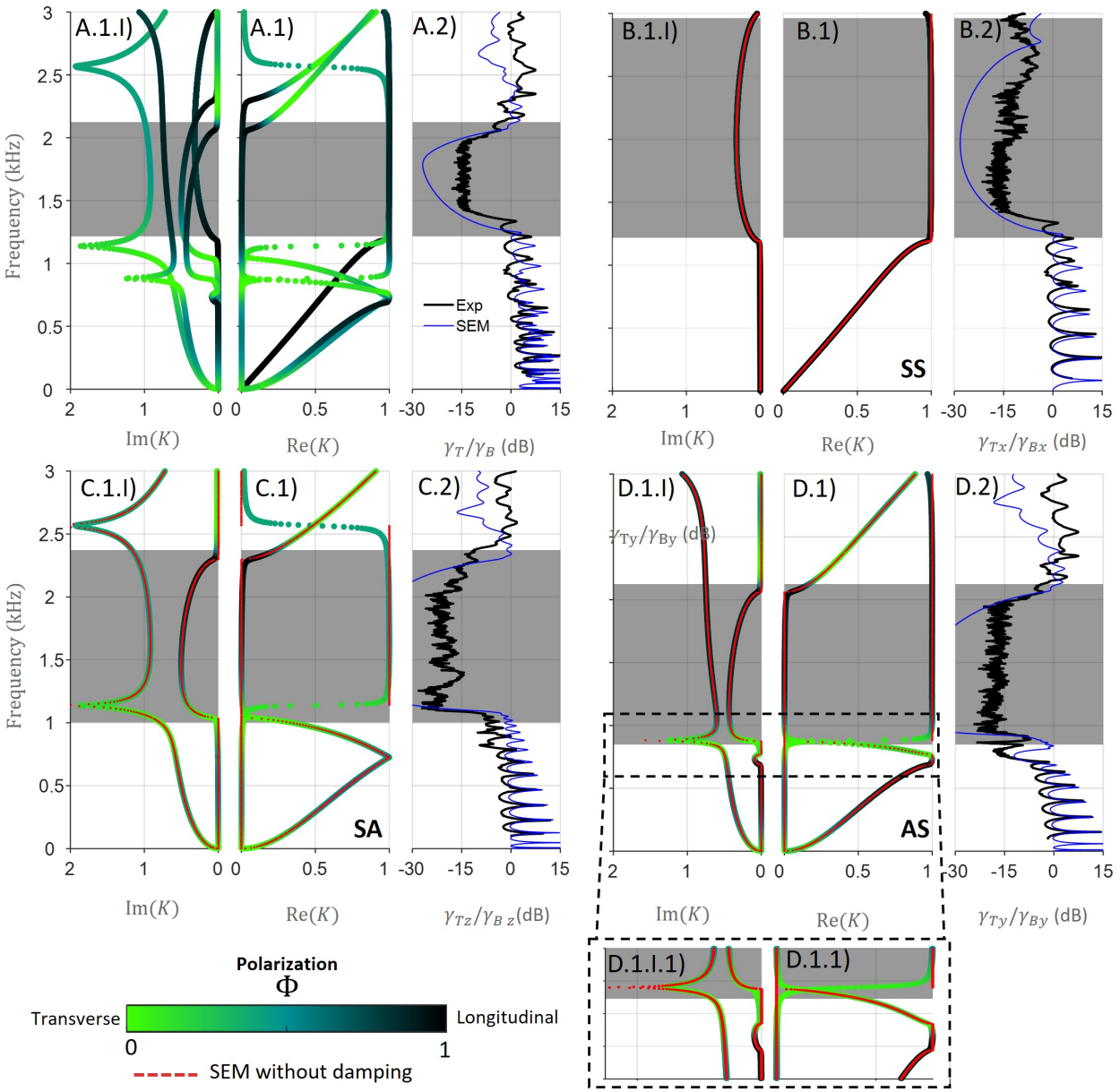

Figure D.1: Full complex dispersion of figure 2.12 (including the imaginary part of the wave vector) and frequency responses for the unit cell S_3 in the presence of damping: (A.1), (B.1), (C.1), and (D.1) display the real part of the complex wavenumber K computed for a complex Young's modulus $E = 3.2(1 + 0.011\mathrm{i})$ GPa (colored points) and a purely real one $E = 3.2$ GPa (red points). These results are identical to those shown in Figure 12. (A.1.I), (B.1.I), (C.1.I), and (D.1.I) display the imaginary part of the complex wavenumber. (D.1.I.1) and (D.1.1) provide close-up views of Figures D.1.I and D.1, respectively, highlighting the bandgap broadening induced by material damping. (A.2), (B.2), (C.2), and (D.2) present the frequency responses of the γ_T/γ_B ratio, obtained from the SEM model (blue curves) and from experimental measurements (black curves), for excitations along the **x**, **z**, and **y** directions.

E Spectral formulation of a free-edge plate element

As shown in Figure E.1, consider a thin rectangular plate with dimensions $a \times b$ and thickness h made of an isotropic material with Young's modulus E, density ρ and Poisson's ratio ν. The figure defines the orientation and sign conventions for translations, rotations, forces and moments. The formulation is divided into two parts, assuming two decoupled deformations: (i) out-of-plane bending ($U_z,\ \Phi_x,\ \Phi_y$ with $V_x,\ V_y,\ M_x,\ M_y$) and (ii) in-plane motion ($U_x,\ U_y$ with $N_x,\ N_y,\ N_{xy}$). This section derives the dynamic stiffness matrix at the four free edges of the plate. This form allows the boundary conditions to be applied a posteriori and enables assembly with other spectral elements (plates, beams).

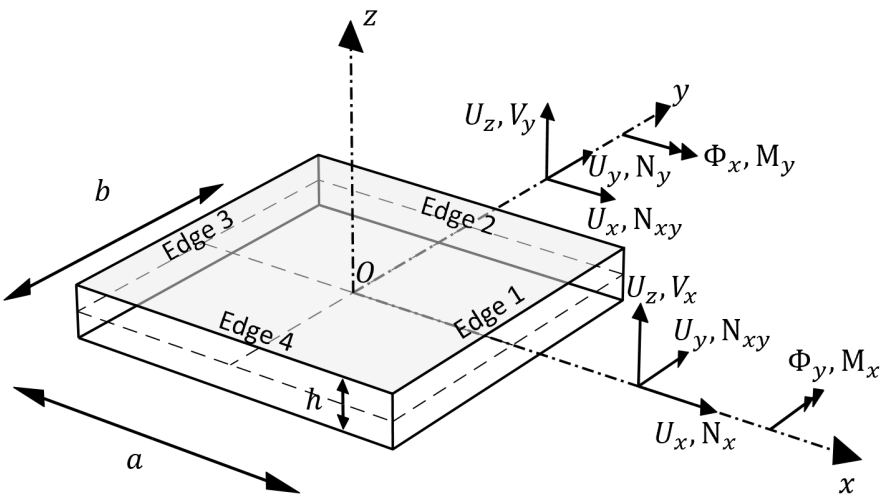

Figure E.1: Coordinate system and notation for translations, rotations, forces, and moments of a thin plate.

Out-of-plane motion

Governing equations

We adopt the Kirchhoff–Love thin-plate approximation, for which the transverse displacement u_z satisfies the biharmonic equation

$$\frac{\partial^4 u_z}{\partial x^4} + 2\,\frac{\partial^4 u_z}{\partial x^2\,\partial y^2} + \frac{\partial^4 u_z}{\partial y^4} - \frac{\rho\,h}{D}\,\frac{\partial^2 u_z}{\partial t^2} = 0, \qquad D = \frac{E h^3}{12(1-\nu^2)}. \tag{E.1}$$

Assuming time-harmonic motion of the form $u_z(x,y,t) = U_z(x,y)\,\mathrm{e}^{\mathrm{i}\omega t}$, where ω denotes the angular frequency, this equation reduces to

$$\frac{\partial^4 U_z}{\partial x^4} + 2\,\frac{\partial^4 U_z}{\partial x^2 \partial y^2} + \frac{\partial^4 U_z}{\partial y^4} - k^4\,U_z = 0, \qquad k^4 = \frac{\rho h\,\omega^2}{D}. \tag{E.2}$$

The associated rotations, shear forces, and bending moments per unit length are defined as

$$\begin{aligned}
&\Phi_y = -\frac{\partial U_z}{\partial x}, \qquad \Phi_x = \frac{\partial U_z}{\partial y}, \\
&V_x = -D\left(\frac{\partial^3 U_z}{\partial x^3} + (2-\nu)\,\frac{\partial^3 U_z}{\partial x\,\partial y^2}\right), \quad V_y = -D\left(\frac{\partial^3 U_z}{\partial y^3} + (2-\nu)\,\frac{\partial^3 U_z}{\partial x^2\,\partial y}\right), \\
&M_x = -D\left(\frac{\partial^2 U_z}{\partial x^2} + \nu\,\frac{\partial^2 U_z}{\partial y^2}\right), \quad M_y = -D\left(\frac{\partial^2 U_z}{\partial y^2} + \nu\,\frac{\partial^2 U_z}{\partial x^2}\right).
\end{aligned} \tag{E.3}$$

Generalized Gorman superposition method

The solution of the free-edge plate problem associated with (E.2) is nontrivial due to the simultaneous enforcement of free boundary conditions along all four edges. Following Gorman's superposition principle, in its generalized form [204, 205], the transverse displacement is decomposed as the sum of two auxiliary fields,

$$U_z(x,y) = U_{z_1}(x,y) + U_{z_2}(x,y), \tag{E.4}$$

each satisfying the governing equation while enforcing complementary subsets of boundary conditions.

The first subproblem U_{z_1} enforces sliding and shear-free conditions on edges 2 and 4, namely $\partial U_z/\partial y = 0$ and $V_y = 0$, while edges 1 and 3 remain free. Introducing a truncation order M_t for transverse bending, U_{z_1} is expanded using a centered Lévy series along the y direction,

$$U_{z_1}(x,y) = \sum_{m=0}^{M_t} X_m(x)\,\cos\!\left(\frac{m\pi y}{b} + \frac{m\pi}{2}\right). \tag{E.5}$$

Substitution of (E.5) into (E.2) yields, for each truncation index m, the fourth-order ordinary differential equation

$$\frac{\mathrm{d}^4 X_m}{\mathrm{d}x^4} - 2\left(\frac{m\pi}{b}\right)^2 \frac{\mathrm{d}^2 X_m}{\mathrm{d}x^2} + \left[\left(\frac{m\pi}{b}\right)^4 - k^4\right] X_m = 0. \tag{E.6}$$

Introducing the characteristic quantities

$$\beta_{1m} = \sqrt{k^2 + \frac{m^2\pi^2}{b^2}}, \qquad \gamma_{1m} = \sqrt{\frac{m^2\pi^2}{b^2} - k^2},$$

the general solution reads

$$X_m(x) = A_{1m}\,\mathrm{e}^{\beta_{1m}x} + B_{1m}\,\mathrm{e}^{-\beta_{1m}x} + C_{1m}\,\mathrm{e}^{\gamma_{1m}x} + D_{1m}\,\mathrm{e}^{-\gamma_{1m}x}, \tag{E.7}$$

where A_{1m}, B_{1m}, C_{1m}, and D_{1m} are integration constants.

By symmetry, the second subproblem U_{z_2} enforces sliding and shear-free conditions on edges 1

and 3, while edges 2 and 4 remain free. Its expression is written as

$$U_{z_2}(x,y) = \sum_{m=0}^{M_t} Y_m(y)\,\cos\!\left(\frac{m\pi x}{a} + \frac{m\pi}{2}\right), \tag{E.8}$$

leading to the analogous solution

$$Y_m(y) = A_{2m}\,\mathrm{e}^{\beta_{2m}y} + B_{2m}\,\mathrm{e}^{-\beta_{2m}y} + C_{2m}\,\mathrm{e}^{\gamma_{2m}y} + D_{2m}\,\mathrm{e}^{-\gamma_{2m}y}, \tag{E.9}$$

with

$$\beta_{2m} = \sqrt{k^2 + \frac{m^2\pi^2}{a^2}}, \qquad \gamma_{2m} = \sqrt{\frac{m^2\pi^2}{a^2} - k^2}.$$

Matrix formulation

The following section introduces a matrix formulation that allows the above analytical solutions to be recast into a compact dynamic stiffness representation suitable for numerical assembly and coupling with other spectral elements.

Edge displacement and force vectors. The out-of-plane kinematic and static quantities are first collected into edge-wise vectors, evaluated at the four plate boundaries ($x = \pm a/2,\ y = \pm b/2$). The generalized displacement vector is defined as

$$\mathbf{q}^{\text{out}} = \begin{bmatrix} U_z^1 \\ \Phi_y^1 \\ U_z^2 \\ \Phi_x^2 \\ U_z^3 \\ \Phi_y^3 \\ U_z^4 \\ \Phi_x^4 \end{bmatrix} = \begin{bmatrix} U_z(\frac{a}{2}, y) \\ \Phi_y(\frac{a}{2}, y) \\ U_z(x, \frac{b}{2}) \\ \Phi_x(x, \frac{b}{2}) \\ U_z(-\frac{a}{2}, y) \\ \Phi_y(-\frac{a}{2}, y) \\ U_z(x, -\frac{b}{2}) \\ \Phi_x(x, -\frac{b}{2}) \end{bmatrix}. \tag{E.10}$$

Similarly, the corresponding shear forces and bending moments per unit length are grouped as

$$\mathbf{Q}^{\text{out}} = \begin{bmatrix} V_x^1 \\ M_x^1 \\ V_y^2 \\ M_y^2 \\ V_x^3 \\ M_x^3 \\ V_y^4 \\ M_y^4 \end{bmatrix} = \begin{bmatrix} V_x(\frac{a}{2}, y) \\ M_x(\frac{a}{2}, y) \\ V_y(x, \frac{b}{2}) \\ M_y(x, \frac{b}{2}) \\ -V_x(-\frac{a}{2}, y) \\ -M_x(-\frac{a}{2}, y) \\ -V_y(x, -\frac{b}{2}) \\ -M_y(x, -\frac{b}{2}) \end{bmatrix}. \tag{E.11}$$

The sign convention ensures that all forces and moments are oriented outward, normal to each

plate edge.

Modal truncation of edge fields. Using the generalized Gorman superposition, the transverse displacement field is expressed as a finite sum of separable solutions indexed by a truncation parameter $m = 0, \ldots, M_t$. Each truncation contributes eight modal coefficients, grouped as

$$\mathbf{C}_m^{\text{out}} = \left[A_{1m},\ B_{1m},\ C_{1m},\ D_{1m},\ A_{2m},\ B_{2m},\ C_{2m},\ D_{2m}\right]^T.$$

The complete modal coefficient vector is obtained by stacking all truncations,

$$\mathbf{C}^{\text{out}} = \begin{bmatrix} \mathbf{C}_0^{\text{out}} \\ \mathbf{C}_1^{\text{out}} \\ \vdots \\ \mathbf{C}_{M_t}^{\text{out}} \end{bmatrix} \in \mathbb{C}^{8(M_t+1)}.$$

For a given truncation m, the corresponding edge displacement and force fields can be written as

$$\mathbf{q}_m^{\text{out}}(s) = \mathbf{D}_m(s)\,\mathbf{C}_m^{\text{out}}, \qquad \mathbf{Q}_m^{\text{out}}(s) = \mathbf{F}_m(s)\,\mathbf{C}_m^{\text{out}},$$

where s denotes the curvilinear coordinate along the considered edge. The matrices $\mathbf{D}_m(s)$ and $\mathbf{F}_m(s)$ contain the analytical expressions resulting from the Lévy solutions and explicitly depend on s through trigonometric functions in x or y.

By superposition of all truncations, the complete edge fields read

$$\mathbf{q}^{\text{out}}(s) = \mathbf{D}(s)\,\mathbf{C}^{\text{out}}, \qquad \mathbf{Q}^{\text{out}}(s) = \mathbf{F}(s)\,\mathbf{C}^{\text{out}}, \tag{E.12}$$

with

$$\mathbf{D}(s) = \left[\mathbf{D}_0(s)\ \mathbf{D}_1(s)\ \cdots\ \mathbf{D}_{M_t}(s)\right], \qquad \mathbf{F}(s) = \left[\mathbf{F}_0(s)\ \mathbf{F}_1(s)\ \cdots\ \mathbf{F}_{M_t}(s)\right].$$

At this stage, the edge variables remain continuous functions of the spatial coordinate s.

Kevorkian–Pascal projection onto generalized edge variables. To eliminate the spatial dependence and obtain a finite-dimensional description, the Kevorkian–Pascal projection [209] is applied. For each projection order $n = 0, \ldots, M_t$, the generalized displacement and force coefficients are defined as

$$\hat{\mathbf{q}}_n^{\text{out}} = \frac{2}{L}\int_s \mathbf{H}_n^{\text{out}}(s)\,\mathbf{q}^{\text{out}}(s)\,\mathrm{d}s, \qquad \hat{\mathbf{Q}}_n^{\text{out}} = \frac{2}{L}\int_s \mathbf{H}_n^{\text{out}}(s)\,\mathbf{Q}^{\text{out}}(s)\,\mathrm{d}s, \tag{E.13}$$

where L denotes the length of the considered edge.

The projection matrix $\mathbf{H}_n^{\text{out}} = \operatorname{diag}(h_{1,n}, \ldots, h_{8,n})$ contains the appropriate trigonometric basis functions,

$$h_{j,n} = \begin{cases} \cos\!\left(\frac{n\pi y}{b} + \frac{n\pi}{2}\right), & j \in \{1,2,5,6\}, \\ \cos\!\left(\frac{n\pi x}{a} + \frac{n\pi}{2}\right), & j \in \{3,4,7,8\}, \end{cases} \qquad n > 0,$$

with $h_{j,0} = 1/2$ enforcing the Kevorkian–Pascal normalization for the rigid ($n = 0$) mode.

Construction of the projected matrices. Substituting the expressions of $\mathbf{q}^{\text{out}}(s)$ and $\mathbf{Q}^{\text{out}}(s)$ into (E.13) yields

$$\hat{\mathbf{q}}_n^{\text{out}} = \hat{\mathbf{D}}_n^{\text{out}}\,\mathbf{C}^{\text{out}}, \qquad \hat{\mathbf{Q}}_n^{\text{out}} = \hat{\mathbf{F}}_n^{\text{out}}\,\mathbf{C}^{\text{out}},$$

with

$$\hat{\mathbf{D}}_n^{\text{out}} = \frac{2}{L}\int_s \mathbf{H}_n^{\text{out}}(s)\,\mathbf{D}(s)\,\mathrm{d}s, \qquad \hat{\mathbf{F}}_n^{\text{out}} = \frac{2}{L}\int_s \mathbf{H}_n^{\text{out}}(s)\,\mathbf{F}(s)\,\mathrm{d}s.$$

Each block $\hat{\mathbf{D}}_n^{\text{out}}$ and $\hat{\mathbf{F}}_n^{\text{out}}$ captures the coupling between the projection order n and all truncation orders $m = 0, \ldots, M_t$.

By stacking the projected quantities for all n, one obtains

$$\hat{\mathbf{q}}^{\text{out}} = \hat{\mathbf{D}}^{\text{out}}\,\mathbf{C}^{\text{out}}, \qquad \hat{\mathbf{Q}}^{\text{out}} = \hat{\mathbf{F}}^{\text{out}}\,\mathbf{C}^{\text{out}}. \tag{E.14}$$

Out-of-plane dynamic stiffness matrix. Eliminating the modal coefficient vector $\mathbf{C}^{\text{out}}$ finally yields the out-of-plane dynamic stiffness relation

$$\hat{\mathbf{Q}}^{\text{out}} = \mathbf{K}^{\text{out}}\,\hat{\mathbf{q}}^{\text{out}}, \qquad \mathbf{K}^{\text{out}} = \hat{\mathbf{F}}^{\text{out}}\big(\hat{\mathbf{D}}^{\text{out}}\big)^{-1}, \tag{E.15}$$

where $\mathbf{K}^{\text{out}} \in \mathbb{C}^{8(M_t+1)\times 8(M_t+1)}$.

In-plane motion

Governing equations

The in-plane displacements (u_x, u_y) of a thin isotropic plate satisfy the coupled membrane equations

$$\begin{cases} \dfrac{\partial^2 u_x}{\partial x^2} + a_1\dfrac{\partial^2 u_x}{\partial y^2} + a_2\dfrac{\partial^2 u_y}{\partial x\partial y} - \dfrac{\rho h}{B}\dfrac{\partial^2 u_x}{\partial t^2} = 0, \\ \dfrac{\partial^2 u_y}{\partial y^2} + a_1\dfrac{\partial^2 u_y}{\partial x^2} + a_2\dfrac{\partial^2 u_x}{\partial x\partial y} - \dfrac{\rho h}{B}\dfrac{\partial^2 u_y}{\partial t^2} = 0, \end{cases} \tag{E.16}$$

where $B = \dfrac{Eh}{1-\nu^2}$, $a_1 = \dfrac{1-\nu}{2}$, and $a_2 = \dfrac{1+\nu}{2}$.

Assuming time-harmonic motion of the form $u_{x,y}(x, y, t) = U_{x,y}(x, y)\,\mathrm{e}^{\mathrm{i}\omega t}$, Eq. (E.16) reduces to

$$\begin{cases} \dfrac{\partial^2 U_x}{\partial x^2} + a_1\dfrac{\partial^2 U_x}{\partial y^2} + a_2\dfrac{\partial^2 U_y}{\partial x\partial y} + \dfrac{\rho h}{B}\,\omega^2\,U_x = 0, \\ \dfrac{\partial^2 U_y}{\partial y^2} + a_1\dfrac{\partial^2 U_y}{\partial x^2} + a_2\dfrac{\partial^2 U_x}{\partial x\partial y} + \dfrac{\rho h}{B}\,\omega^2\,U_y = 0. \end{cases} \tag{E.17}$$

The associated in-plane stress resultants per unit length are defined as

$$N_x = B\left(\frac{\partial U_x}{\partial x} + \nu\frac{\partial U_y}{\partial y}\right), \quad N_y = B\left(\nu\frac{\partial U_x}{\partial x} + \frac{\partial U_y}{\partial y}\right), \quad N_{xy} = B\,a_1\left(\frac{\partial U_x}{\partial y} + \frac{\partial U_y}{\partial x}\right). \tag{E.18}$$

Generalized Gorman superposition method

Following the generalized superposition approach introduced by Gorman and later extended to in-plane dynamics, the solution of (E.17) is constructed as the sum of two auxiliary fields associated with orthogonal coordinate directions,

$$U_x = U_{x_1} + U_{x_2}, \qquad U_y = U_{y_1} + U_{y_2}. \tag{E.19}$$

The first auxiliary field enforces sliding-type boundary conditions along the horizontal edges and is expanded using Lévy-type trigonometric functions in the y direction,

$$\begin{cases} U_{x_1}(x,y) = \displaystyle\sum_{m=1}^{M_i} P_{1m}(x)\, \cos\!\left(\frac{m\pi y}{b} + \frac{m\pi}{2}\right), \\ U_{y_1}(x,y) = \displaystyle\sum_{m=1}^{M_i} Q_{1m}(x)\, \sin\!\left(\frac{m\pi y}{b} + \frac{m\pi}{2}\right), \end{cases} \tag{E.20}$$

where M_i denotes the truncation order for in-plane motion.

By symmetry, the second auxiliary field is expanded along the x direction,

$$\begin{cases} U_{x_2}(x,y) = \displaystyle\sum_{m=1}^{M_i} P_{2m}(y)\, \sin\!\left(\frac{m\pi x}{a} + \frac{m\pi}{2}\right), \\ U_{y_2}(x,y) = \displaystyle\sum_{m=1}^{M_i} Q_{2m}(y)\, \cos\!\left(\frac{m\pi x}{a} + \frac{m\pi}{2}\right). \end{cases} \tag{E.21}$$

Substitution of these expressions into (E.17) yields, for each truncation index $m \geq 1$, two coupled systems of second-order ordinary differential equations,

$$\begin{cases} P''_{1m} + \alpha_1 Q'_{1m} + \alpha_2 P_{1m} = 0, \\ Q''_{1m} + \alpha_3 P'_{1m} + \alpha_4 Q_{1m} = 0, \end{cases} \qquad \begin{cases} P''_{2m} + \gamma_1 Q'_{2m} + \gamma_2 P_{2m} = 0, \\ Q''_{2m} + \gamma_3 P'_{2m} + \gamma_4 Q_{2m} = 0, \end{cases} \tag{E.22}$$

where $k_x = m\pi/a$, $k_y = m\pi/b$, $G = Eh/[2(1+\nu)]$ and the coefficients :

$$\alpha_1 = a_2 k_y \qquad \alpha_2 = (\rho h/B)\omega^2 - a_1 k_y^2 \tag{E.23}$$

$$\alpha_3 = -(a_2/a_1)k_y \qquad \alpha_4 = (\rho h/G)\omega^2 - (1/a1)k_y^2 \tag{E.24}$$

$$\gamma_1 = -(a_2/a_1)k_x \qquad \gamma_2 = (\rho h/G)\omega^2 - (1/a_1)k_x^2 \tag{E.25}$$

$$\gamma_3 = a_2 k_x \qquad \gamma_4 = (\rho h/B)\omega^2 - a_1 k_x^2 \tag{E.26}$$

Elimination of one displacement component in each block leads to a fourth-order ordinary differential equation whose characteristic equation admits two distinct pairs of roots. Accordingly, each in-plane Lévy term $m \geq 1$ gives rise to four exponential waves along the corresponding longitudinal direction.

The resulting general solutions for the first block are written as

$$\begin{aligned} P_{1m}(x) &= A_{1m}^{\text{in}} e^{\lambda_{11}x} + B_{1m}^{\text{in}} e^{-\lambda_{11}x} + C_{1m}^{\text{in}} e^{\lambda_{12}x} + D_{1m}^{\text{in}} e^{-\lambda_{12}x}, \\ Q_{1m}(x) &= \eta_{11} A_{1m}^{\text{in}} e^{\lambda_{11}x} + \eta_{12} B_{1m}^{\text{in}} e^{-\lambda_{11}x} + \eta_{13} C_{1m}^{\text{in}} e^{\lambda_{12}x} + \eta_{14} D_{1m}^{\text{in}} e^{-\lambda_{12}x}, \end{aligned} \tag{E.27}$$

With :

$$\begin{aligned} Z_{11} &= \alpha_2 - \alpha_3\alpha_1 + \alpha_4 \qquad Z_{12} = \alpha_2\alpha_4 \\ \Delta_1 &= Z_{11}^2 - 4Z_{12} \\ \lambda_{11} &= \sqrt{0.5(-Z_{11} + \sqrt{\Delta_1})} \qquad \lambda_{12} = \sqrt{0.5(-Z_{11} - \sqrt{\Delta_1})} \\ \eta_{11} &= (1/(\alpha_1\alpha_4))(\lambda_{11}^3 + \alpha_2\lambda_{11} - \alpha_3\alpha_1\lambda_{11}) \qquad \eta_{12} = -\eta_{11} \\ \eta_{13} &= (1/(\alpha_1\alpha_4))(\lambda_{12}^3 + \alpha_2\lambda_{12} - \alpha_3\alpha_1\lambda_{12}) \qquad \eta_{14} = -\eta_{13} \end{aligned} \tag{E.28}$$

Analogous expressions are derived for the second block (P_{2m}, Q_{2m}) along the y direction:

$$\begin{aligned} P_{2m}(x) &= A_{2m}^{\text{in}} \eta_{21} e^{\lambda_{21}y} + B_{2m}^{\text{in}} \eta_{22} e^{-\lambda_{21}y} + C_{2m}^{\text{in}} \eta_{23} e^{\lambda_{22}y} + D_{2m}^{\text{in}} \eta_{24} e^{-\lambda_{22}y}, \\ Q_{2m}(x) &= A_{2m}^{\text{in}} e^{\lambda_{21}x} + B_{2m}^{\text{in}} e^{-\lambda_{21}x} + C_{2m}^{\text{in}} e^{\lambda_{22}x} + D_{2m}^{\text{in}} e^{-\lambda_{22}x}, \end{aligned} \tag{E.29}$$

with :

$$\begin{aligned} Z_{21} &= \gamma_2 - \gamma_3\gamma_1 + \gamma_4 \qquad Z_{22} = \gamma_2\gamma_4 \\ \Delta_2 &= Z_{21}^2 - 4Z_{22} \\ \lambda_{21} &= \sqrt{0.5(-Z_{21} + \sqrt{\Delta_2})} \qquad \lambda_{22} = \sqrt{0.5(-Z_{21} - \sqrt{\Delta_2})} \\ \eta_{21} &= (1/(\gamma_2\gamma_3))(\lambda_{21}^3 + \gamma_4\lambda_{21} - \gamma_1\gamma_3\lambda_{21}) \qquad \eta_{22} = -\eta_{21} \\ \eta_{23} &= (1/(\gamma_2\gamma_3))(\lambda_{22}^3 + \gamma_4\lambda_{22} - \gamma_1\gamma_3\lambda_{22}) \qquad \eta_{24} = -\eta_{23} \end{aligned} \tag{E.30}$$

At low frequencies, to avoid numerical discrepancies λ_{11}, λ_{12}, λ_{21} and λ_{22} can be reduce to :

$$\begin{aligned} \lambda_{11} &\approx \sqrt{k_y^2 - (\rho h/B)\omega^2} \qquad \lambda_{12} \approx \sqrt{k_y^2 - (\rho h/G)\omega^2} \\ \lambda_{21} &\approx \sqrt{k_x^2 - (\rho h/B)\omega^2} \qquad \lambda_{22} \approx \sqrt{k_x^2 - (\rho h/G)\omega^2} \end{aligned} \tag{E.31}$$

For the rigid in-plane mode $m = 0$, the transverse wavenumbers vanish ($k_x = k_y = 0$), so that all coupling terms proportional to k_x or k_y in Eq. (E.22) cancel. The governing equations therefore decouple into two independent second-order ordinary differential equations, describing pure longitudinal membrane motion along the x and y directions, respectively,

$$P_{10}''(x) + \frac{\rho h}{B}\,\omega^2\, P_{10}(x) = 0, \qquad Q_{20}''(y) + \frac{\rho h}{B}\,\omega^2\, Q_{20}(y) = 0. \tag{E.32}$$

The associated characteristic equation admits a single pair of roots $\pm\lambda_0$, with

$$\lambda_0 = \sqrt{-\frac{\rho h}{B}\omega^2}\,, \tag{E.33}$$

so that the corresponding displacement fields reduce to

$$P_{10}(x) = A_{10}^{\text{in}}\,\mathrm{e}^{\lambda_0 x} + B_{10}^{\text{in}}\,\mathrm{e}^{-\lambda_0 x}, \qquad Q_{20}(y) = A_{20}^{\text{in}}\,\mathrm{e}^{\lambda_0 y} + B_{20}^{\text{in}}\,\mathrm{e}^{-\lambda_0 y}. \tag{E.34}$$

In contrast with the $m \geq 1$ case, where the coupling between U_x and U_y leads to a fourth-order differential equation and four exponential waves per truncation index, the rigid mode $m = 0$ therefore involves only two longitudinal exponential waves.

Matrix formulation

The in-plane dynamic stiffness matrix is derived following the same three-step procedure as for the out-of-plane case: (i) definition of edge-wise displacement and force vectors, (ii) modal truncation of the in-plane Lévy solutions, and (iii) projection onto a finite set of generalized edge variables using the Kevorkian–Pascal projection.

Edge displacement and force vectors. The in-plane kinematic quantities are first collected into edge-wise displacement vectors, evaluated at the four plate boundaries ($x = \pm a/2,\ y = \pm b/2$). The generalized in-plane displacement vector is defined as

$$\mathbf{q}^{\text{in}} = \begin{bmatrix} U_x^1 \\ U_y^1 \\ U_x^2 \\ U_y^2 \\ U_x^3 \\ U_y^3 \\ U_x^4 \\ U_y^4 \end{bmatrix} = \begin{bmatrix} U_x(\frac{a}{2}, y) \\ U_y(\frac{a}{2}, y) \\ U_x(x, \frac{b}{2}) \\ U_y(x, \frac{b}{2}) \\ U_x(-\frac{a}{2}, y) \\ U_y(-\frac{a}{2}, y) \\ U_x(x, -\frac{b}{2}) \\ U_y(x, -\frac{b}{2}) \end{bmatrix}. \tag{E.35}$$

Similarly, the corresponding membrane force resultants per unit length are grouped as

$$\mathbf{Q}^{\text{in}} = \begin{bmatrix} N_x^1 \\ N_{\text{xy}}^1 \\ N_{\text{xy}}^2 \\ N_y^2 \\ N_x^3 \\ N_{\text{xy}}^3 \\ N_{\text{xy}}^4 \\ N_y^4 \end{bmatrix} = \begin{bmatrix} N_x(\frac{a}{2}, y) \\ N_{\text{xy}}(\frac{a}{2}, y) \\ N_{\text{xy}}(x, \frac{b}{2}) \\ N_y(x, \frac{b}{2}) \\ -N_x(-\frac{a}{2}, y) \\ -N_{\text{xy}}(-\frac{a}{2}, y) \\ -N_{\text{xy}}(x, -\frac{b}{2}) \\ -N_y(x, -\frac{b}{2}) \end{bmatrix}. \tag{E.36}$$

The sign convention ensures that all force resultants are oriented outward, normal to each plate edge.

Modal truncation of in-plane fields. The in-plane displacement field is expressed using the generalized Lévy formulation, leading to two coupled displacement components (U_x, U_y). For each truncation order $m \geq 1$, the solution involves four exponential waves per Lévy block and eight modal coefficients. The special case $m = 0$ corresponds to uncoupled rigid-like in-plane motion and contributes only four independent coefficients.

All in-plane modal coefficients are collected into the vector

$$\mathbf{C}^{\text{in}} = \begin{bmatrix} \mathbf{C}_0^{\text{in}} \\ \mathbf{C}_1^{\text{in}} \\ \vdots \\ \mathbf{C}_{M_i}^{\text{in}} \end{bmatrix},$$

where $\mathbf{C}_0^{\text{in}}$ contains four coefficients associated with the $m = 0$ solution, while each $\mathbf{C}_m^{\text{in}}$ $(m \geq 1)$ contains eight coefficients associated with the coupled Lévy waves.

For a given truncation m, the corresponding in-plane edge displacement and force fields can be written as

$$\mathbf{q}_m^{\text{in}}(s) = \mathbf{D}_m^{\text{in}}(s)\, \mathbf{C}_m^{\text{in}}, \qquad \mathbf{Q}_m^{\text{in}}(s) = \mathbf{F}_m^{\text{in}}(s)\, \mathbf{C}_m^{\text{in}},$$

where s denotes the curvilinear coordinate along the considered edge. The matrices $\mathbf{D}_m^{\text{in}}(s)$ and $\mathbf{F}_m^{\text{in}}(s)$ contain the analytical expressions of the Lévy solutions and depend explicitly on s through sine and cosine functions in x or y.

By superposition of all truncations, the continuous in-plane edge fields read

$$\mathbf{q}^{\text{in}}(s) = \mathbf{D}^{\text{in}}(s)\, \mathbf{C}^{\text{in}}, \qquad \mathbf{Q}^{\text{in}}(s) = \mathbf{F}^{\text{in}}(s)\, \mathbf{C}^{\text{in}}, \tag{E.37}$$

with

$$\mathbf{D}^{\text{in}}(s) = \left[\mathbf{D}_0^{\text{in}}(s)\ \mathbf{D}_1^{\text{in}}(s)\ \cdots\ \mathbf{D}_{M_i}^{\text{in}}(s)\right], \qquad \mathbf{F}^{\text{in}}(s) = \left[\mathbf{F}_0^{\text{in}}(s)\ \mathbf{F}_1^{\text{in}}(s)\ \cdots\ \mathbf{F}_{M_i}^{\text{in}}(s)\right].$$

At this stage, the edge variables remain continuous functions of the spatial coordinate s.

Kevorkian–Pascal projection onto generalized edge variables. To eliminate the spatial dependence and obtain a finite-dimensional representation, the Kevorkian–Pascal projection is applied. For each projection order $n = 0, \ldots, M_i$, the generalized in-plane displacement and force coefficients are defined as

$$\hat{\mathbf{q}}_n^{\text{in}} = \frac{2}{L} \int_s \mathbf{H}_n^{\text{in}}(s)\, \mathbf{q}^{\text{in}}(s)\, \mathrm{d}s, \qquad \hat{\mathbf{Q}}_n^{\text{in}} = \frac{2}{L} \int_s \mathbf{H}_n^{\text{in}}(s)\, \mathbf{Q}^{\text{in}}(s)\, \mathrm{d}s, \tag{E.38}$$

where the definitions of L and $\mathrm{d}s$ are identical to those used in the out-of-plane formulation.

The projection matrix $\mathbf{H}_n^{\text{in}} = \mathrm{diag}(h_{1,n}^{\text{in}}, \ldots, h_{8,n}^{\text{in}})$ contains the in-plane trigonometric basis

functions,

$$
\begin{aligned}
h^{\text{in}}_{1,n} &= h^{\text{in}}_{5,n} = \cos\!\left(\tfrac{n\pi y}{b} + \tfrac{n\pi}{2}\right),\\
h^{\text{in}}_{2,n} &= h^{\text{in}}_{6,n} = \sin\!\left(\tfrac{n\pi y}{b} + \tfrac{n\pi}{2}\right),\\
h^{\text{in}}_{3,n} &= h^{\text{in}}_{7,n} = \sin\!\left(\tfrac{n\pi x}{a} + \tfrac{n\pi}{2}\right),\\
h^{\text{in}}_{4,n} &= h^{\text{in}}_{8,n} = \cos\!\left(\tfrac{n\pi x}{a} + \tfrac{n\pi}{2}\right), \qquad n > 0.
\end{aligned}
$$

For the rigid in-plane mode $n = 0$, the Kevorkian–Pascal normalization yields

$$
\mathbf{H}^{\text{in}}_0 = \frac{1}{2}\begin{bmatrix}
1 & 0 & 0 & 0 & 0 & 0 & 0 & 0\\
0 & 0 & 0 & 1 & 0 & 0 & 0 & 0\\
0 & 0 & 0 & 0 & 1 & 0 & 0 & 0\\
0 & 0 & 0 & 0 & 0 & 0 & 0 & 1
\end{bmatrix},
$$

which preserves orthonormality and avoids spurious scaling of the rigid contribution.

Construction of the projected matrices. Substituting the expressions of $\mathbf{q}^{\text{in}}(s)$ and $\mathbf{Q}^{\text{in}}(s)$ into (E.38) leads to

$$
\hat{\mathbf{q}}^{\text{in}}_n = \hat{\mathbf{D}}^{\text{in}}_n\,\mathbf{C}^{\text{in}}, \qquad \hat{\mathbf{Q}}^{\text{in}}_n = \hat{\mathbf{F}}^{\text{in}}_n\,\mathbf{C}^{\text{in}},
$$

with

$$
\hat{\mathbf{D}}^{\text{in}}_n = \frac{2}{L}\int_s \mathbf{H}^{\text{in}}_n(s)\,\mathbf{D}^{\text{in}}(s)\,\mathrm{d}s, \qquad \hat{\mathbf{F}}^{\text{in}}_n = \frac{2}{L}\int_s \mathbf{H}^{\text{in}}_n(s)\,\mathbf{F}^{\text{in}}(s)\,\mathrm{d}s.
$$

By stacking the projected quantities for all n, one obtains

$$
\hat{\mathbf{q}}^{\text{in}} = \hat{\mathbf{D}}^{\text{in}}\,\mathbf{C}^{\text{in}}, \qquad \hat{\mathbf{Q}}^{\text{in}} = \hat{\mathbf{F}}^{\text{in}}\,\mathbf{C}^{\text{in}}. \tag{E.39}
$$

In-plane dynamic stiffness matrix. Eliminating the internal modal coefficient vector $\mathbf{C}^{\text{in}}$ finally yields the in-plane dynamic stiffness relation

$$
\hat{\mathbf{Q}}^{\text{in}} = \mathbf{K}^{\text{in}}\,\hat{\mathbf{q}}^{\text{in}}, \qquad \mathbf{K}^{\text{in}} = \hat{\mathbf{F}}^{\text{in}}\big(\hat{\mathbf{D}}^{\text{in}}\big)^{-1}, \tag{E.40}
$$

where $\mathbf{K}^{\text{in}} \in \mathbb{C}^{(8M_i+4)\times(8M_i+4)}$.

Plate dynamic stiffness formulation

The dynamic stiffness matrix of the plate is denoted by $\mathbf{K}^P$ and relates the generalized boundary displacements to the associated generalized forces. It is initially assembled in the following block-diagonal form:

$$
\mathbf{K}^P\hat{\mathbf{q}}^P = \begin{bmatrix}
\mathbf{K}^{\text{out}} & \mathbf{0}\\
\mathbf{0} & \mathbf{K}^{\text{in}}
\end{bmatrix}\begin{bmatrix}
\hat{\mathbf{q}}^{\text{out}}\\
\hat{\mathbf{q}}^{\text{in}}
\end{bmatrix} = \begin{bmatrix}
\hat{\mathbf{Q}}^{\text{out}}\\
\hat{\mathbf{Q}}^{\text{in}}
\end{bmatrix} \equiv \hat{\mathbf{Q}}^P. \tag{E.41}
$$

F Plate–beam coupling formulation

The plate–beam coupling methodology builds upon a dynamic formulation inspired by the work of Li et al. [208], which addresses plate–spring coupling. Figure F.1 introduces the coordinate system and the sign conventions adopted for the forces, moments, rotations, and displacements involved in the coupling between the beam subsystem and the plate.

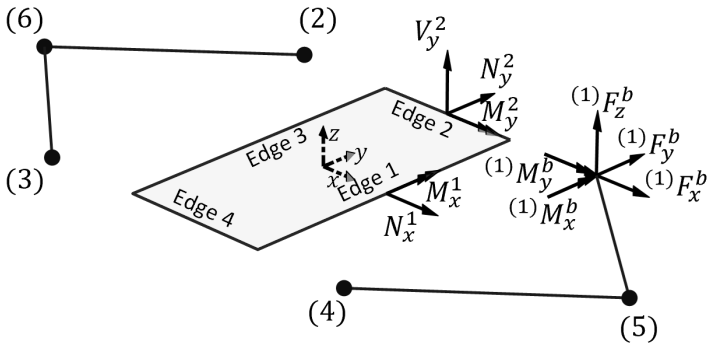

Figure F.1: (a) Coordinate system and notation of the displacements and forces involved in the coupling between plate edges 1 and 2 and beam node 1. (b) Schematic representation of the complete plate–beam assembly.

For coupling purposes, the plate degrees of freedom are reorganized edge-wise. The plate dynamic equilibrium is therefore rewritten as

$$\mathbf{K}^P \begin{bmatrix} \hat{\mathbf{q}}_1^P \\ \hat{\mathbf{q}}_2^P \\ \hat{\mathbf{q}}_3^P \\ \hat{\mathbf{q}}_4^P \end{bmatrix} = \begin{bmatrix} \hat{\mathbf{Q}}_1^P \\ \hat{\mathbf{Q}}_2^P \\ \hat{\mathbf{Q}}_3^P \\ \hat{\mathbf{Q}}_4^P \end{bmatrix}, \tag{F.1}$$

where $\hat{\mathbf{q}}_j^P, \hat{\mathbf{Q}}_j^P \in \mathbb{C}^L$ denote the generalized displacement and force vectors associated with plate edge j. The number of retained modal coefficients is

$$L = (2M_i + 1) + 2(M_t + 1).$$

Each edge vector is defined as

$$\begin{aligned}
\hat{\mathbf{q}}_1^P &= \begin{bmatrix} \mathbf{U}_x^1 & \mathbf{U}_y^1 & \mathbf{U}_z^1 & \mathbf{\Phi}_y^1 \end{bmatrix}^T, \quad \hat{\mathbf{Q}}_1^P = \begin{bmatrix} \mathbf{N}_x^1 & \mathbf{N}_{xy}^1 & \mathbf{V}_x^1 & \mathbf{M}_x^1 \end{bmatrix}^T, \\
\hat{\mathbf{q}}_2^P &= \begin{bmatrix} \mathbf{U}_x^2 & \mathbf{U}_y^2 & \mathbf{U}_z^2 & \mathbf{\Phi}_x^2 \end{bmatrix}^T, \quad \hat{\mathbf{Q}}_2^P = \begin{bmatrix} \mathbf{N}_{xy}^2 & \mathbf{N}_y^2 & \mathbf{V}_y^2 & \mathbf{M}_y^2 \end{bmatrix}^T, \\
\hat{\mathbf{q}}_3^P &= \begin{bmatrix} \mathbf{U}_x^3 & \mathbf{U}_y^3 & \mathbf{U}_z^3 & \mathbf{\Phi}_y^3 \end{bmatrix}^T, \quad \hat{\mathbf{Q}}_3^P = \begin{bmatrix} \mathbf{N}_x^3 & \mathbf{N}_{xy}^3 & \mathbf{V}_x^3 & \mathbf{M}_x^3 \end{bmatrix}^T, \\
\hat{\mathbf{q}}_4^P &= \begin{bmatrix} \mathbf{U}_x^4 & \mathbf{U}_y^4 & \mathbf{U}_z^4 & \mathbf{\Phi}_x^4 \end{bmatrix}^T, \quad \hat{\mathbf{Q}}_4^P = \begin{bmatrix} \mathbf{N}_{xy}^4 & \mathbf{N}_y^4 & \mathbf{V}_y^4 & \mathbf{M}_y^4 \end{bmatrix}^T.
\end{aligned} \tag{F.2}$$

Beam subsystem

The beam assembly is described by a dynamic stiffness matrix $\mathbf{K}^b$, obtained from an assembled spectral beam-element formulation detailed in [194]. The nodal equilibrium of the beam system reads

$$\mathbf{K}^b \begin{bmatrix} {}^{(1)}\mathbf{d}^b \\ {}^{(2)}\mathbf{d}^b \\ {}^{(3)}\mathbf{d}^b \\ {}^{(4)}\mathbf{d}^b \\ {}^{(5)}\mathbf{d}^b \\ {}^{(6)}\mathbf{d}^b \end{bmatrix} = \begin{bmatrix} {}^{(1)}\mathbf{F}^b \\ {}^{(2)}\mathbf{F}^b \\ {}^{(3)}\mathbf{F}^b \\ {}^{(4)}\mathbf{F}^b \\ {}^{(5)}\mathbf{F}^b \\ {}^{(6)}\mathbf{F}^b \end{bmatrix}. \tag{F.3}$$

The four plate corners are defined as

$$C_1 = (1,2), \quad C_2 = (2,3), \quad C_3 = (3,4), \quad C_4 = (4,1),$$

where each corner $C_c = (j_v, j_h)$ corresponds to the intersection of a vertical edge $j_v \in \{1,3\}$ and a horizontal edge $j_h \in \{2,4\}$, located at $(x_c, y_c) \in \{\pm a/2\} \times \{\pm b/2\}$.

At each corner, five degrees of freedom are retained:

$${}^{(c)}\mathbf{d}^b = \left[{}^{(c)}U_x^b,\ {}^{(c)}U_y^b,\ {}^{(c)}U_z^b,\ {}^{(c)}\Theta_x^b,\ {}^{(c)}\Theta_y^b \right]^T,$$

with the associated force vector

$${}^{(c)}\mathbf{F}^b = \left[{}^{(c)}F_x^b,\ {}^{(c)}F_y^b,\ {}^{(c)}F_z^b,\ {}^{(c)}M_y^b,\ {}^{(c)}M_x^b \right]^T.$$

The rotation Θ_z is neglected in the coupling model.

Continuity conditions at the corners

The kinematic coupling between the plate and the beam is enforced at the four plate corners. At each corner, continuity of displacements and rotations is imposed between the beam node and the corresponding plate edge expansions evaluated at the corner coordinates.

We detail the construction for corner $C_1 = (1,2)$, which corresponds to the intersection of edge 1 (vertical edge at $x = +a/2$) and edge 2 (horizontal edge at $y = +b/2$). The coordinates of this corner are therefore

$$(x_1, y_1) = \left(+\tfrac{a}{2}, +\tfrac{b}{2} \right).$$

Kinematic continuity at corner C_1

The continuity of motion requires that the beam displacements and rotations coincide with the plate displacement fields evaluated at the corner. Using the cosine-based modal expansions introduced for

the plate edges, this condition reads

$$
\begin{aligned}
{}^{(1)}U_x^b &= \sum_{n=0}^{M} U_{x,n}^1 \cos\!\left(\tfrac{n\pi y_1}{b} + \tfrac{n\pi}{2}\right), \quad {}^{(1)}U_y^b = \sum_{n=0}^{M} U_{y,n}^2 \cos\!\left(\tfrac{n\pi x_1}{a} + \tfrac{n\pi}{2}\right), \\
{}^{(1)}U_z^b &= \sum_{n=0}^{M} U_{z,n}^2 \cos\!\left(\tfrac{n\pi x_1}{a} + \tfrac{n\pi}{2}\right), \quad {}^{(1)}\Theta_y^b = \sum_{n=0}^{M} \Phi_{y,n}^1 \cos\!\left(\tfrac{n\pi y_1}{b} + \tfrac{n\pi}{2}\right), \\
{}^{(1)}\Theta_x^b &= \sum_{n=0}^{M} \Phi_{x,n}^2 \cos\!\left(\tfrac{n\pi x_1}{a} + \tfrac{n\pi}{2}\right).
\end{aligned}
$$

These relations can be compactly expressed in matrix form as

$$
{}^{(1)}\hat{\mathbf{d}}^{\,b} = \mathbf{T}_{d1}\,\hat{\mathbf{q}}^{P}, \qquad \mathbf{T}_{d1} \in \mathbb{C}^{5\times 4L},
$$

where the transformation matrix $\mathbf{T}_{d1}$ extracts the contributions of edges 1 and 2 only:

$$
\mathbf{T}_{d1} = \Big[\, \underbrace{\mathbf{C}_{dy}(y_1)}_{5\times L} \;\; \underbrace{\mathbf{C}_{dx}(x_1)}_{5\times L} \;\; \mathbf{0} \;\; \mathbf{0} \Big].
$$

Evaluation matrices

The matrices $\mathbf{C}_{dy}$ and $\mathbf{C}_{dx}$ evaluate the plate modal basis functions at the corner coordinates. They are defined as

$$
\mathbf{C}_{dy}(y) = \begin{bmatrix} \mathbf{H}_{dy}(y) & \mathbf{0} & \mathbf{0} & \mathbf{0} \\ \mathbf{0} & \mathbf{0} & \mathbf{0} & \mathbf{0} \\ \mathbf{0} & \mathbf{0} & \mathbf{0} & \mathbf{0} \\ \mathbf{0} & \mathbf{0} & \mathbf{0} & \mathbf{H}_{dy}(y) \\ \mathbf{0} & \mathbf{0} & \mathbf{0} & \mathbf{0} \end{bmatrix}, \qquad \mathbf{C}_{dx}(x) = \begin{bmatrix} \mathbf{0} & \mathbf{0} & \mathbf{0} & \mathbf{0} \\ \mathbf{0} & \mathbf{H}_{dx}(x) & \mathbf{0} & \mathbf{0} \\ \mathbf{0} & \mathbf{0} & \mathbf{H}_{dx}(x) & \mathbf{0} \\ \mathbf{0} & \mathbf{0} & \mathbf{0} & \mathbf{H}_{dx}(x) \\ \mathbf{0} & \mathbf{0} & \mathbf{0} & \mathbf{0} \end{bmatrix}.
$$

The row vectors $\mathbf{H}_{dy}$ and $\mathbf{H}_{dx}$ collect the cosine basis functions evaluated at the corresponding coordinate:

$$
\begin{aligned}
\mathbf{H}_{dy}(y) &= \Big[\, 1,\; \cos\!\left(\tfrac{\pi y}{b} + \tfrac{\pi}{2}\right),\; \ldots,\; \cos\!\left(\tfrac{M\pi y}{b} + \tfrac{M\pi}{2}\right) \,\Big], \\
\mathbf{H}_{dx}(x) &= \Big[\, 1,\; \cos\!\left(\tfrac{\pi x}{a} + \tfrac{\pi}{2}\right),\; \ldots,\; \cos\!\left(\tfrac{M\pi x}{a} + \tfrac{M\pi}{2}\right) \,\Big].
\end{aligned}
$$

Extension to the four corners

The same construction applies to the three remaining corners, yielding the following transformation matrices:

$$
\begin{aligned}
\mathbf{T}_{d2} &= \big[\, \mathbf{0},\; \mathbf{C}_{dx}(x_2),\; \mathbf{C}_{dy}(y_2),\; \mathbf{0} \,\big], \\
\mathbf{T}_{d3} &= \big[\, \mathbf{0},\; \mathbf{0},\; \mathbf{C}_{dy}(y_3),\; \mathbf{C}_{dx}(x_3) \,\big], \\
\mathbf{T}_{d4} &= \big[\, \mathbf{C}_{dy}(y_4),\; \mathbf{0},\; \mathbf{0},\; \mathbf{C}_{dx}(x_4) \,\big].
\end{aligned}
$$

Collecting the displacement constraints at the four corners, the vector of constrained beam degrees of freedom reads

$$\mathbf{d}_c^b = \begin{bmatrix} {}^{(1)}\hat{\mathbf{d}}^b \\ {}^{(2)}\hat{\mathbf{d}}^b \\ {}^{(3)}\hat{\mathbf{d}}^b \\ {}^{(4)}\hat{\mathbf{d}}^b \end{bmatrix} = \underbrace{\begin{bmatrix} \mathbf{T}_{d1} \\ \mathbf{T}_{d2} \\ \mathbf{T}_{d3} \\ \mathbf{T}_{d4} \end{bmatrix}}_{\mathbf{T}_d \in \mathbb{C}^{24\times 4L}} \hat{\mathbf{q}}^P.$$

Projection of efforts

The forces and moments exerted by the beam at each corner are transferred to the plate edges through a projection onto the plate modal basis. This operation ensures energetic consistency between the discrete beam forces and the continuous plate edge expansions.

The projection relies on the Kevorkian–Pascal procedure, which consists in expanding a point load applied at a given curvilinear coordinate onto the modal basis used to describe the edge fields.

General projection principle

Consider a scalar force f^b applied at position s_c along a line segment of length L, parameterized by the curvilinear coordinate $s \in [-L/2, L/2]$. Its projection onto a modal basis

$$\{h_0(s), h_1(s), \ldots, h_N(s)\}$$

is defined as

$$\hat{f}_n = \frac{2}{L} \int_{-L/2}^{L/2} \delta(s - s_c)\, f^b\, h_n(s)\, \mathrm{d}s = \frac{2}{L}\, f^b\, h_n(s_c),$$

where $\delta(\cdot)$ denotes the Dirac distribution. This expression directly yields the modal coefficients associated with the point force.

Projection at corner C_1

We now apply this procedure to corner C_1, located at $(x_1, y_1) = (+a/2, +b/2)$. At this corner, the beam exerts a force vector ${}^{(1)}\mathbf{F}^b$ that must be distributed onto edges 1 and 2 of the plate.

Projection onto edge 1. Edge 1 is a vertical edge of length b, parameterized by the coordinate $s = y$. The axial force and bending moment applied by the beam are projected as

$$\hat{N}_{x,n}^{b,1} = \frac{2}{b}\, {}^{(1)}F_x^b\, h_{1,n}^{\text{in}}(y_1), \qquad \hat{M}_{x,n}^{b,1} = \frac{2}{b}\, {}^{(1)}M_x^b\, h_{2,n}^{\text{out}}(y_1).$$

Projection onto edge 2. Edge 2 is a horizontal edge of length a, parameterized by $s = x$. The transverse force, axial force, and bending moment are projected as

$$\hat{N}_{y,n}^{b,2} = \frac{2}{a}\, {}^{(1)}F_y^b\, h_{4,n}^{\text{in}}(x_1), \qquad \hat{V}_{y,n}^{b,2} = \frac{2}{a}\, {}^{(1)}F_z^b\, h_{3,n}^{\text{out}}(x_1), \qquad \hat{M}_{y,n}^{b,2} = \frac{2}{a}\, {}^{(1)}M_y^b\, h_{4,n}^{\text{out}}(x_1).$$

Matrix form of the projected forces

The projected force vector associated with corner C_1 is assembled as

$$ {}^{(1)}\hat{\mathbf{Q}}^b = \begin{bmatrix} {}^{(1)}\hat{\mathbf{N}}_x^{b,1} \\ {}^{(1)}\hat{\mathbf{V}}_y^{b,2} \\ {}^{(1)}\hat{\mathbf{M}}_x^{b,1} \\ {}^{(1)}\hat{\mathbf{N}}_y^{b,2} \\ {}^{(1)}\hat{\mathbf{M}}_y^{b,2} \end{bmatrix} = \mathbf{T}_{f1}\, {}^{(1)}\mathbf{F}^b, \qquad \mathbf{T}_{f1} \in \mathbb{C}^{2L\times 5}. $$

The projection operator $\mathbf{T}_{f1}$ can be written as

$$ \mathbf{T}_{f1} = \begin{bmatrix} \mathbf{C}_{fy}(y_1) & \mathbf{C}_{fx}(x_1) \end{bmatrix}^T, $$

where the matrices $\mathbf{C}_{fy}$ and $\mathbf{C}_{fx}$ collect the contributions associated with edges 1 and 2, respectively.

Projection matrices

The matrices $\mathbf{C}_{fy}$ and $\mathbf{C}_{fx}$ are defined as

$$ \mathbf{C}_{fy}(y) = \begin{bmatrix} \mathbf{H}_{fy}(y) & \mathbf{0} & \mathbf{0} & \mathbf{0} \\ \mathbf{0} & \mathbf{0} & \mathbf{0} & \mathbf{0} \\ \mathbf{0} & \mathbf{0} & \mathbf{0} & \mathbf{0} \\ \mathbf{0} & \mathbf{0} & \mathbf{0} & \mathbf{H}_{fy}(y) \\ \mathbf{0} & \mathbf{0} & \mathbf{0} & \mathbf{0} \end{bmatrix}, \qquad \mathbf{C}_{fx}(x) = \begin{bmatrix} \mathbf{0} & \mathbf{0} & \mathbf{0} & \mathbf{0} \\ \mathbf{0} & \mathbf{H}_{fx}(x) & \mathbf{0} & \mathbf{0} \\ \mathbf{0} & \mathbf{0} & \mathbf{H}_{fx}(x) & \mathbf{0} \\ \mathbf{0} & \mathbf{0} & \mathbf{0} & \mathbf{H}_{fx}(x) \\ \mathbf{0} & \mathbf{0} & \mathbf{0} & \mathbf{0} \end{bmatrix}. $$

The modal evaluation vectors are given by

$$ \mathbf{H}_{fy}(y) = \frac{2}{b}\Big[\, \tfrac{1}{2},\ \cos\!\big(\tfrac{\pi y}{b} + \tfrac{\pi}{2}\big),\ \ldots,\ \cos\!\Big(\tfrac{M\pi y}{b} + \tfrac{M\pi}{2}\Big)\, \Big], $$

$$ \mathbf{H}_{fx}(x) = \frac{2}{a}\Big[\, \tfrac{1}{2},\ \cos\!\big(\tfrac{\pi x}{a} + \tfrac{\pi}{2}\big),\ \ldots,\ \cos\!\big(\tfrac{M\pi x}{a} + \tfrac{M\pi}{2}\big)\, \Big]. $$

Extension to the four corners

The same projection procedure applies to the remaining corners, leading to the following operators:

$$ \mathbf{T}_{f2} = \begin{bmatrix} \mathbf{C}_{fx}(x_2) & \mathbf{C}_{fy}(y_2) \end{bmatrix}^T, \qquad \mathbf{T}_{f3} = \begin{bmatrix} \mathbf{C}_{fy}(y_3) & \mathbf{C}_{fx}(x_3) \end{bmatrix}^T, \qquad \mathbf{T}_{f4} = \begin{bmatrix} \mathbf{C}_{fy}(y_4) & \mathbf{C}_{fx}(x_4) \end{bmatrix}^T. $$

Collecting the contributions of the four corners, the global vector of projected beam forces reads

$$\hat{\mathbf{Q}}^b = \underbrace{\begin{bmatrix} \mathbf{T}_{f1} & & & \\ & \mathbf{T}_{f2} & & \\ & & \mathbf{T}_{f3} & \\ & & & \mathbf{T}_{f4} \end{bmatrix}}_{\mathbf{T}_F \in \mathbb{C}^{8L \times 20}} \mathbf{F}_c^b,$$

where

$$\mathbf{F}_c^b = \begin{bmatrix} {}^{(1)}\mathbf{F}^b \\ {}^{(2)}\mathbf{F}^b \\ {}^{(3)}\mathbf{F}^b \\ {}^{(4)}\mathbf{F}^b \end{bmatrix}.$$

Equilibrium of forces and moments

The coupling between the plate and the beam is completed by enforcing the equilibrium of forces and moments along each plate edge. For a given edge, the generalized forces carried by the plate must balance the contributions transferred from the two beam corners connected to that edge.

The global vector of projected beam forces $\hat{\mathbf{Q}}^b$ is ordered edge-wise as

$$\hat{\mathbf{Q}}^b = \begin{bmatrix} {}^{(1)}\hat{\mathbf{Q}}^{b,1} \\ {}^{(1)}\hat{\mathbf{Q}}^{b,2} \\ {}^{(2)}\hat{\mathbf{Q}}^{b,2} \\ {}^{(2)}\hat{\mathbf{Q}}^{b,3} \\ {}^{(3)}\hat{\mathbf{Q}}^{b,3} \\ {}^{(3)}\hat{\mathbf{Q}}^{b,4} \\ {}^{(4)}\hat{\mathbf{Q}}^{b,1} \\ {}^{(4)}\hat{\mathbf{Q}}^{b,4} \end{bmatrix} \in \mathbb{C}^{8L},$$

where ${}^{(c)}\hat{\mathbf{Q}}^{b,j}$ denotes the contribution of corner C_c projected onto edge j.

Equilibrium conditions

For each plate edge, equilibrium of generalized forces and moments is enforced by summing the plate contribution and the two adjacent beam contributions. This yields the following set of equations:

$$\hat{\mathbf{Q}}_1^P + {}^{(1)}\hat{\mathbf{Q}}^{b,1} + {}^{(4)}\hat{\mathbf{Q}}^{b,1} = \mathbf{0}, \qquad \hat{\mathbf{Q}}_2^P + {}^{(1)}\hat{\mathbf{Q}}^{b,2} + {}^{(2)}\hat{\mathbf{Q}}^{b,2} = \mathbf{0},$$

$$\hat{\mathbf{Q}}_3^P + {}^{(2)}\hat{\mathbf{Q}}^{b,3} + {}^{(3)}\hat{\mathbf{Q}}^{b,3} = \mathbf{0}, \qquad \hat{\mathbf{Q}}_4^P + {}^{(3)}\hat{\mathbf{Q}}^{b,4} + {}^{(4)}\hat{\mathbf{Q}}^{b,4} = \mathbf{0}.$$

Matrix formulation

Introducing the stacked plate force vector

$$\hat{\mathbf{Q}}^P = \begin{bmatrix} \hat{\mathbf{Q}}_1^P \\ \hat{\mathbf{Q}}_2^P \\ \hat{\mathbf{Q}}_3^P \\ \hat{\mathbf{Q}}_4^P \end{bmatrix} \in \mathbb{C}^{4L},$$

the equilibrium conditions can be written compactly as

$$\hat{\mathbf{Q}}^P + \mathbf{T}_e\, \hat{\mathbf{Q}}^b = \mathbf{0},$$

where $\mathbf{T}_e \in \mathbb{C}^{4L\times 8L}$ is a Boolean assembly matrix that maps the projected beam forces onto the corresponding plate edges:

$$\mathbf{T}_e = \begin{bmatrix} \mathbf{I}_L & \mathbf{0} & \mathbf{0} & \mathbf{0} & \mathbf{0} & \mathbf{0} & \mathbf{I}_L & \mathbf{0} \\ \mathbf{0} & \mathbf{I}_L & \mathbf{0} & \mathbf{I}_L & \mathbf{0} & \mathbf{0} & \mathbf{0} & \mathbf{0} \\ \mathbf{0} & \mathbf{0} & \mathbf{I}_L & \mathbf{0} & \mathbf{I}_L & \mathbf{0} & \mathbf{0} & \mathbf{0} \\ \mathbf{0} & \mathbf{0} & \mathbf{0} & \mathbf{0} & \mathbf{0} & \mathbf{I}_L & \mathbf{0} & \mathbf{I}_L \end{bmatrix}.$$

This operator ensures that each plate edge receives the contributions of the two beam corners connected to it, with consistent sign conventions.

Complete assembly of the coupled system

Introducing the augmented vector of unknowns

$$\begin{bmatrix} \hat{\mathbf{q}}^P \\ {}^{(5)}\mathbf{d}^b \\ {}^{(6)}\mathbf{d}^b \end{bmatrix},$$

which gathers the plate boundary degrees of freedom and the unconstrained beam nodal degrees of freedom, the coupled system can be written as

$$\left(\underbrace{\begin{bmatrix} \mathbf{K}^P & \mathbf{0} & \mathbf{0} \\ \mathbf{0} & \mathbf{0} & \mathbf{0} \\ \mathbf{0} & \mathbf{0} & \mathbf{0} \end{bmatrix}}_{\text{augmented plate contribution}} + \underbrace{\begin{bmatrix} \mathbf{T}_e & \mathbf{0} & \mathbf{0} \\ \mathbf{0} & \mathbf{I} & \mathbf{0} \\ \mathbf{0} & \mathbf{0} & \mathbf{I} \end{bmatrix} \begin{bmatrix} \mathbf{T}_F & \mathbf{0} & \mathbf{0} \\ \mathbf{0} & \mathbf{I} & \mathbf{0} \\ \mathbf{0} & \mathbf{0} & \mathbf{I} \end{bmatrix} \mathbf{K}^b \begin{bmatrix} \mathbf{T}_d & \mathbf{0} & \mathbf{0} \\ \mathbf{0} & \mathbf{I} & \mathbf{0} \\ \mathbf{0} & \mathbf{0} & \mathbf{I} \end{bmatrix}}_{\text{beam contribution}} \right) \begin{bmatrix} \hat{\mathbf{q}}^P \\ {}^{(5)}\mathbf{d}^b \\ {}^{(6)}\mathbf{d}^b \end{bmatrix} = \mathbf{0}.$$

This compact expression defines the global dynamic stiffness matrix of the coupled plate–beam system,

$$\mathbf{K}^{Pb} \in \mathbb{C}^{(4L+12)\times(4L+12)},$$

which fully accounts for kinematic continuity, force projection, and equilibrium at the plate–beam interface.

The formulation is exact within the adopted spectral truncation and provides a modular framework suitable for assembling complex plate–beam architectures.

Bibliography

[1] A. Hall, T. Mayer, I. Wuggetzer, and P. R. N. Childs. "Future Aircraft Cabins and Design Thinking: Optimisation vs. Win-Win Scenarios". In: *Propulsion and Power Research* 2.2 (June 2013), pp. 85–95. ISSN: 2212-540X. DOI: 10.1016/j.jppr.2013.04.001.

[2] J. Bouwens, S. H.-v. Mastrigt, and P. Vink. "Ranking of Human Senses in Relation to Different In-flight Activities Contributing to the Comfort Experience of Airplane Passengers". In: *International Journal of Aviation, Aeronautics, and Aerospace* 5.2 (Apr. 2018). ISSN: 2374-6793. DOI: 10.15394/ijaaa.2018.1228.

[3] T. Kletschkowski. "Some Insights in Active Control of Noise and Vibration in Aircraft Cabins". In: *Noise Theory and Practice* 6.4 (22) (2020), pp. 11–21. ISSN: 2412-8627. DOI: 20.500.12738/10681.

[4] M. Gorji-Bandpy and M. Azimi. "Airframe Noise Sources and Reduction Technologies in Aircraft". In: *Noise & Vibration Worldwide* 43.9 (Oct. 2012), pp. 29–36. ISSN: 0957-4565. DOI: 10.1260/0957-4565.43.9.29.

[5] J. S. Mixson and C. A. Powell. "Review of Recent Research on Interior Noise of Propeller Aircraft". In: *Journal of Aircraft* (May 2012). DOI: 10.2514/3.45229.

[6] M. Sadeghian and M. Gorji-Bandpy. "Investigation All Types of Aircraft Noises: Review Paper". In: *American Journal of Science, Engineering and Technology* 5.1 (2020), p. 33. ISSN: 2578-8345. DOI: 10.11648/j.ajset.20200501.14.

[7] J. F. Unruh. "Structure-Borne Noise Control for Propeller Aircraft". In: *Journal of Aircraft* (May 2012). DOI: 10.2514/3.45654.

[8] M. D. Rao. "Recent Applications of Viscoelastic Damping for Noise Control in Automobiles and Commercial Airplanes". In: *Journal of Sound and Vibration*. 2001 India-USA Symposium on Emerging Trends in Vibration and Noise Engineering 262.3 (May 2003), pp. 457–474. ISSN: 0022-460X. DOI: 10.1016/S0022-460X(03)00106-8.

[9] A. Grewal, D. G. Zimcik, L. Hurtubise, and B. Leigh. "Active Cabin Noise and Vibration Control for Turboprop Aircraft Using Multiple Piezoelectric Actuators". In: *Journal of Intelligent Material Systems and Structures* 11.6 (June 2000), pp. 438–447. ISSN: 1045-389X. DOI: 10.1106/VYJR-2UGX-UD2F-DAHX.

[10] P. Ma, H. Wang, D. Li, S. Yuan, and X. Fan. “Passive Acoustic Liners for Aero-Engine Noise Control: A Review”. In: *Mechanics of Advanced Materials and Structures* (Nov. 2024). ISSN: 1537-6494.

[11] C. Blech and S. C. Langer. *Aircraft cabin noise reduction by means of acoustic black holes*. Text. Institute of Noise Control Engineering, 2017.

[12] N. J. Mansfield and G. Aggarwal. “Whole-Body Vibration Experienced by Pilots, Passengers and Crew in Fixed-Wing Aircraft: A State-of-the-Science Review”. In: *Vibration* 5.1 (Mar. 2022), pp. 110–120. ISSN: 2571-631X. DOI: 10.3390/vibration5010007.

[13] M. A. Bellmann and H. Remmers. “Evaluation of Vibration Perception in Passenger Vehicles and Aircrafts”. In: *Acta Acust* 89 (2003), S11.

[14] L. Krause, S. Van De Par, and S. Töpken. “Pleasantness Ratings for Vertical Whole-Body Vibration on an Aircraft Seat and Relevant Body Parts Involved”. In: *Applied Acoustics* 207 (May 2023), p. 109330. ISSN: 0003682X. DOI: 10.1016/j.apacoust.2023.109330.

[15] I. Hostens and H. Ramon. “Descriptive Analysis of Combine Cabin Vibrations and Their Effect on the Human Body”. In: *Journal of Sound and Vibration*. First International ISMA Workshop on Noise and Vibration in Agricultural and Biological Engineering 266.3 (Sept. 2003), pp. 453–464. ISSN: 0022-460X. DOI: 10.1016/S0022-460X(03)00578-9.

[16] S. Griffiths, J. M. Uratani, A. Ríos-Galván, J. M. Andresen, and M. Mercedes Maroto-Valer. “Green Flight Paths: A Catalyst for Net-Zero Aviation by 2050”. In: *Energy & Environmental Science* 17.24 (2024), pp. 9425–9434. DOI: 10.1039/D4EE02472A.

[17] R. M. A. Valdés and V. F. G. Comendador. “Strategies and Economics for Decarbonizing Aviation by 2050”. In: *Accelerating Sustainable Aviation Initiatives: Technology, Markets and Social Issues*. Ed. by L. M. Braga da Costa Campos. Cham: Springer Nature Switzerland, 2025, pp. 227–265. ISBN: 978-3-031-73993-4. DOI: 10.1007/978-3-031-73993-4_7.

[18] F. C. Barbosa. *Open Rotor Engine Technology Review – A Tool for Efficiency*. Tech. rep. 2020-36-0108. SAE Technical Paper, Mar. 2021. DOI: 10.4271/2020-36-0108.

[19] A. Seitz, D. Schmitt, and S. Donnerhack. “Emission Comparison of Turbofan and Open Rotor Engines under Special Consideration of Aircraft and Mission Design Aspects”. In: *The Aeronautical Journal* 115.1168 (June 2011), pp. 351–360. ISSN: 0001-9240, 2059-6464. DOI: 10.1017/S000192400000587X.

[20] H. Scheel. *Next Generation Aircraft - A Challenge for Interior Acoustics Developments*. https://ince.publisher.ingentaconnect.com/content/ince/incecp/2016/00000253/00000004/art00089. Text. Aug. 2016.

[21] F. Caputo, M. Manzo, D. Perfetto, A. D. Luca, L. D. Palma, A. Chiariello, and F. D. Caprio. “Numerical Drop Test of a Full Composite Fuselage Section Having Two Components of Velocity”. In: *Procedia Structural Integrity*. AIAS 2019 International Conference on Stress

Analysis 24 (Jan. 2019), pp. 788–799. ISSN: 2452-3216. DOI: 10.1016/j.prostr.2020.02.070.

[22] G. SenGupta. *Vibration of Periodic Structures*. Elsevier, Oct. 2023. ISBN: 978-0-323-99023-3.

[23] G. Mitrou, N. Ferguson, and J. Renno. "Wave Transmission through Two-Dimensional Structures by the Hybrid FE/WFE Approach". In: *Journal of Sound and Vibration* 389 (Feb. 2017), pp. 484–501. ISSN: 0022460X. DOI: 10.1016/j.jsv.2016.09.032.

[24] T. Tamir. "Beam and Waveguide Couplers". In: *Integrated Optics*. Berlin, Heidelberg: Springer, 1975, pp. 83–137. DOI: 10.1007/BFb0103619.

[25] R. Langley and K. Heron. "Elastic Wave Transmission through Plate/Beam Junctions". In: *Journal of Sound and Vibration* 143.2 (Dec. 1990), pp. 241–253. ISSN: 0022460X. DOI: 10.1016/0022-460X(90)90953-W.

[26] P. Hagedorn and G. Spelsberg-Korspeter, eds. *Active and Passive Vibration Control of Structures*. Vol. 558. CISM International Centre for Mechanical Sciences. Vienna: Springer, 2014. ISBN: 978-3-7091-1820-7 978-3-7091-1821-4. DOI: 10.1007/978-3-7091-1821-4.

[27] A. M. Baz. *Active and Passive Vibration Damping*. John Wiley & Sons, Apr. 2019. ISBN: 978-1-118-48192-9.

[28] H. Elahi, K. Munir, M. Eugeni, M. Abrar, A. Khan, A. Arshad, and P. Gaudenzi. "A Review on Applications of Piezoelectric Materials in Aerospace Industry". In: *Integrated Ferroelectrics* 211.1 (Oct. 2020), pp. 25–44. ISSN: 1058-4587. DOI: 10.1080/10584587.2020.1803672.

[29] M. Brahem, M. Chouchane, and A. Amamou. "Active Vibration Control of a Rotor Bearing System Using Flexible Piezoelectric Patch Actuators". In: *Journal of Intelligent Material Systems and Structures* 31.10 (June 2020), pp. 1284–1297. ISSN: 1045-389X. DOI: 10.1177/1045389X20916804.

[30] P. Shivashankar and S. Gopalakrishnan. "Review on the Use of Piezoelectric Materials for Active Vibration, Noise, and Flow Control". In: *Smart Materials and Structures* 29.5 (Mar. 2020), p. 053001. ISSN: 0964-1726. DOI: 10.1088/1361-665X/ab7541.

[31] J. A. B. Gripp and D. A. Rade. "Vibration and Noise Control Using Shunted Piezoelectric Transducers: A Review". In: *Mechanical Systems and Signal Processing* 112 (Nov. 2018), pp. 359–383. ISSN: 0888-3270. DOI: 10.1016/j.ymssp.2018.04.041.

[32] A. Spadoni, M. Ruzzene, and K. Cunefare. "Vibration and Wave Propagation Control of Plates with Periodic Arrays of Shunted Piezoelectric Patches". In: *Journal of Intelligent Material Systems and Structures* 20.8 (May 2009), pp. 979–990. ISSN: 1045-389X. DOI: 10.1177/1045389X08100041.

[33] Y. T. Choi and N. M. Wereley. "Adaptively Tunable Magnetorheological Elastomer-Based Vibration Absorber for a Propeller Aircraft Seat". In: *AIP Advances* 12.3 (Mar. 2022), p. 035332. ISSN: 2158-3226. DOI: 10.1063/9.0000323.

[34] Z. R. Wani, M. Tantray, E. Noroozinejad Farsangi, N. Nikitas, M. Noori, B. Samali, and T. Yang. “A Critical Review on Control Strategies for Structural Vibration Control”. In: *Annual Reviews in Control* 54 (2022), pp. 103–124. ISSN: 13675788. DOI: 10.1016/j.arcontrol.2022.09.002.

[35] J. H. Lee, H. Y. Kim, K. H. Kim, M. H. Kim, and S. W. Lee. “Control of a Hybrid Active-Passive Vibration Isolation System”. In: *Journal of Mechanical Science and Technology* 31.12 (Dec. 2017), pp. 5711–5719. ISSN: 1976-3824. DOI: 10.1007/s12206-017-1112-2.

[36] M. A. Trindade and A. Benjeddou. “Hybrid Active-Passive Damping Treatments Using Viscoelastic and Piezoelectric Materials: Review and Assessment”. In: *Journal of Vibration and Control* 8.6 (June 2002), pp. 699–745. ISSN: 1077-5463. DOI: 10.1177/1077546029186.

[37] J. D. Kemp and R. L. Clark. “Optimal Hybrid Active/Passive Vibration Control Design”. In: *Smart Structures and Materials 2002: Modeling, Signal Processing, and Control*. Vol. 4693. SPIE, July 2002, pp. 440–450. DOI: 10.1117/12.475240.

[38] M. H. El Ouni, M. Abdeddaim, S. Elias, and N. B. Kahla. “Review of Vibration Control Strategies of High-Rise Buildings”. In: *Sensors (Basel, Switzerland)* 22.21 (Nov. 2022), p. 8581. ISSN: 1424-8220. DOI: 10.3390/s22218581.

[39] N. Sarkar, T. Konar, and A. (Ghosh. “Passive Vibration Control Techniques for Offshore Structures under Different Environmental Loading: A Review”. In: *Ocean Engineering* 320 (Mar. 2025), p. 120296. ISSN: 0029-8018. DOI: 10.1016/j.oceaneng.2025.120296.

[40] Z. Shu, R. You, and Y. Zhou. “Viscoelastic Materials for Structural Dampers: A Review”. In: *Construction and Building Materials* 342 (Aug. 2022), p. 127955. ISSN: 0950-0618. DOI: 10.1016/j.conbuildmat.2022.127955.

[41] H. Zhang, A. Li, Y. Su, G. Xu, and B. Sha. “Viscoelastic Dampers for Civil Engineering Structures: A Systematic Review of Constructions, Materials, and Applications”. In: *Journal of Building Engineering* 96 (Nov. 2024), p. 110597. ISSN: 2352-7102. DOI: 10.1016/j.jobe.2024.110597.

[42] C. Cai, H. Zheng, and G. Liu. “Vibration Analysis of a Beam with PCLD Patch”. In: *Applied Acoustics* 65.11 (Nov. 2004), pp. 1057–1076. ISSN: 0003682X. DOI: 10.1016/j.apacoust.2004.05.004.

[43] A. G. Cunha-Filho, A. M. G. de Lima, M. V. Donadon, and L. S. Leão. “Flutter Suppression of Plates Using Passive Constrained Viscoelastic Layers”. In: *Mechanical Systems and Signal Processing*. Special Issue from ICEDyn 2015 79 (Oct. 2016), pp. 99–111. ISSN: 0888-3270. DOI: 10.1016/j.ymssp.2016.02.025.

[44] S. Jaisee, F. Yue, and Y. H. Ooi. “A State-of-the-Art Review on Passive Friction Dampers and Their Applications”. In: *Engineering Structures* 235 (May 2021), p. 112022. ISSN: 0141-0296. DOI: 10.1016/j.engstruct.2021.112022.

[45] P. M. Calvi and G. M. Calvi. “Historical Development of Friction-Based Seismic Isolation Systems”. In: *Soil Dynamics and Earthquake Engineering* 106 (Mar. 2018), pp. 14–30. ISSN: 0267-7261. DOI: 10.1016/j.soildyn.2017.12.003.

[46] J. Yuan, C. Gastaldi, E. Denimal Goy, and B. Chouvion. “Friction Damping for Turbomachinery: A Comprehensive Review of Modelling, Design Strategies, and Testing Capabilities”. In: *Progress in Aerospace Sciences* 147 (May 2024), p. 101018. ISSN: 0376-0421. DOI: 10.1016/j.paerosci.2024.101018.

[47] L. Fournier, L. Sanches, S. Foucaud, and G. Michon. “Dynamic Modeling and Experimental Analysis of Aerospace Equipment Attached Using Reclosable Fasteners”. In: *Journal of Spacecraft and Rockets* 61.6 (2024), pp. 1711–1722. ISSN: 0022-4650. DOI: 10.2514/1.A36074.

[48] M. Berardengo, G. E. P. Della Porta, S. Manzoni, and M. Vanali. “Adaptive multi-modal tuned mass dampers based on shape memory alloys: Design and validation”. In: *Sensors and Instrumentation, Aircraft/Aerospace, Energy Harvesting & Dynamic Environments Testing, Volume 7*. Ed. by C. Walber and S. Manzoni. Springer, 2020, pp. 151–161. DOI: 10.1007/978-3-030-12676-6_14.

[49] P. C. Jain, A. Mukherjee, and Y. Krishna. “Tuned mass dampers for flight vehicle components subjected to rocket noise”. In: *Aerospace Science and Technology* 15 (2011), pp. 175–182. DOI: 10.1016/j.ast.2010.11.004.

[50] K. Yang, Y. Zhang, H. Ding, T. Yang, and L.-Q. Chen. “Nonlinear energy sink for whole-spacecraft vibration reduction”. In: *Journal of Vibration and Acoustics* 139.2 (2017), p. 021011. DOI: 10.1115/1.4035377.

[51] W.-Y. Zhang, M.-Q. Niu, and L.-Q. Chen. “Vibration reduction of a Timoshenko beam with multiple parallel nonlinear energy sinks”. In: *Applied Sciences* 12.18 (2022), p. 9008. DOI: 10.3390/app12189008.

[52] G. Habib and F. Romeo. “Comparative Analysis of NES and TMD Performance via High-Dimensional Invariant Manifolds”. In: *IUTAM Symposium on Exploiting Nonlinear Dynamics for Engineering Systems*. Springer International Publishing, 2020, pp. 143–153. DOI: 10.1007/978-3-030-23692-2_13.

[53] Y.-P. Xiong, K.-J. Song, and X. Ai. “Influence of Flexible Foundation on Isolator Wave Effects”. In: *Shock and Vibration* 3.1 (1996), p. 878674. ISSN: 1875-9203. DOI: 10.3233/SAV-1996-3107.

[54] G. L. Hermsdorf, S. A. Szilagyi, S. Rösch, and E. Schäffer. “High Performance Passive Vibration Isolation System for Optical Tables Using Six-Degree-of-Freedom Viscous Damping Combined with Steel Springs”. In: *Review of Scientific Instruments* 90.1 (Jan. 2019), p. 015113. ISSN: 0034-6748, 1089-7623. DOI: 10.1063/1.5060707.

[55] E. Davoodi, P. Safarpour, M. Pourgholi, and M. Khazaee. “Design and Evaluation of Vibration Reducing Seat Suspension Based on Negative Stiffness Structure”. In: *Proceedings of the Institution of Mechanical Engineers, Part C: Journal of Mechanical Engineering Science* 234.21 (Nov. 2020), pp. 4171–4189. ISSN: 0954-4062, 2041-2983. DOI: 10.1177/0954406220921203.

[56] J. Shu, E. He, Y. Li, and C. Zhang. “The Quasi-Zero Stiffness Seat Vibration Isolator Design to Improve Cockpit Vibration Comfort”. In: *Journal of Vibration Engineering & Technologies* 12.4 (Apr. 2024), pp. 5999–6014. ISSN: 2523-3939. DOI: 10.1007/s42417-023-01232-9.

[57] A. Banerjee, R. Das, and E. P. Calius. “Waves in Structured Mediums or Metamaterials: A Review”. In: *Archives of Computational Methods in Engineering* 26.4 (Sept. 2019), pp. 1029–1058. ISSN: 1886-1784. DOI: 10.1007/s11831-018-9268-1.

[58] A. Banerjee and K. K. Bera. *An Introduction to Waves in Mechanical Periodic Structures and Metamaterials*. CRC Press, Dec. 2025. ISBN: 978-1-040-75989-9.

[59] A. Palermo, S. Krödel, A. Marzani, and C. Daraio. “Engineered Metabarrier as Shield from Seismic Surface Waves”. In: *Scientific Reports* 6.1 (Dec. 2016), p. 39356. ISSN: 2045-2322. DOI: 10.1038/srep39356.

[60] Muhammad and C. W. Lim. “From Photonic Crystals to Seismic Metamaterials: A Review via Phononic Crystals and Acoustic Metamaterials”. In: *Archives of Computational Methods in Engineering* 29.2 (Mar. 2022), pp. 1137–1198. ISSN: 1886-1784. DOI: 10.1007/s11831-021-09612-8.

[61] C. P. Jisha, S. Nolte, and A. Alberucci. “Geometric Phase in Optics: From Wavefront Manipulation to Waveguiding”. In: *Laser & Photonics Reviews* 15.10 (2021), p. 2100003. ISSN: 1863-8899. DOI: 10.1002/lpor.202100003.

[62] Z. Xu. “Rainbow Trapping with Long Oscillation Lifetimes in Gradient Magnetoinductive Metasurfaces”. In: *Physical Review Applied* 12.2 (2019). DOI: 10.1103/PhysRevApplied.12.024043.

[63] A. Colombi, S. Guenneau, P. Roux, and R. V. Craster. “Transformation Seismology: Composite Soil Lenses for Steering Surface Elastic Rayleigh Waves”. In: *Scientific Reports* 6.1 (Apr. 2016), p. 25320. ISSN: 2045-2322. DOI: 10.1038/srep25320.

[64] S. Yang, X. Zhou, and Y.-F. Wang. “Tunable Band Gap and Wave Guiding in Periodic Grid Structures with Thermal Sensitive Materials”. In: *Composite Structures* 290 (June 2022), p. 115536. ISSN: 0263-8223. DOI: 10.1016/j.compstruct.2022.115536.

[65] M. Thota and K. W. Wang. “Tunable Waveguiding in Origami Phononic Structures”. In: *Journal of Sound and Vibration* 430 (Sept. 2018), pp. 93–100. ISSN: 0022-460X. DOI: 10.1016/j.jsv.2018.05.031.

[66] M. S. Kushwaha, P. Halevi, L. Dobrzynski, and B. Djafari-Rouhani. "Acoustic Band Structure of Periodic Elastic Composites". In: *Physical Review Letters* 71.13 (Sept. 1993), pp. 2022–2025. DOI: 10.1103/PhysRevLett.71.2022.

[67] C. Wang, X. Yao, G. Wu, and L. Tang. "Complete Vibration Band Gap Characteristics of Two-Dimensional Periodic Grid Structures". In: *Composite Structures* 274 (Oct. 2021), p. 114368. ISSN: 02638223. DOI: 10.1016/j.compstruct.2021.114368.

[68] R. Prasad and A. Sarkar. "Broadband Vibration Isolation for Rods and Beams Using Periodic Structure Theory". In: *Journal of Applied Mechanics* 86.021004 (Dec. 2018). ISSN: 0021-8936. DOI: 10.1115/1.4042011.

[69] I. Newton. "Principia—Book II, Imprimatur S". In: *Pepys, Reg. Soc. Præses, London* (1686).

[70] J. W. S. B. Rayleigh. "The theory of sound". In: 2 (1896).

[71] L. Brillouin. "Wave propagation in periodic structures". In: (1946).

[72] C. Kittel, P. McEuen, and P. McEuen. "Introduction to solid state physics, 8 wiley". In: *New York* (1976).

[73] S. Rytov. "Acoustical properties of a thinly laminated medium". In: *Sov. Phys. Acoust* 2.1 (1956), pp. 68–80.

[74] C.-T. Sun, J. D. Achenbach, and G. Herrmann. "Continuum Theory for a Laminated Medium". In: *Journal of Applied Mechanics* 35.3 (Sept. 1968), pp. 467–475. ISSN: 0021-8936. DOI: 10.1115/1.3601237.

[75] E. Yablonovitch. "Inhibited Spontaneous Emission in Solid-State Physics and Electronics". In: *Physical Review Letters* 58.20 (May 1987), pp. 2059–2062. DOI: 10.1103/PhysRevLett.58.2059.

[76] R. L. Chern, C. C. Chang, C. C. Chang, and R. R. Hwang. "Large Full Band Gaps for Photonic Crystals in Two Dimensions Computed by an Inverse Method with Multigrid Acceleration". In: *Physical Review E* 68.2 (Aug. 2003), p. 026704. ISSN: 1063-651X, 1095-3787. DOI: 10.1103/PhysRevE.68.026704.

[77] M. M. Sigalas. "Elastic and acoustic wave band structure". In: *Journal of sound and vibration* 158.2 (1992), pp. 377–382.

[78] Z. Liu, X. Zhang, Y. Mao, Y. Y. Zhu, Z. Yang, C. T. Chan, and P. Sheng. "Locally Resonant Sonic Materials". In: *Science* 289.5485 (Sept. 2000), pp. 1734–1736. DOI: 10.1126/science.289.5485.1734.

[79] F. Bloch. "Über die Quantenmechanik der Elektronen in Kristallgittern". In: *Zeitschrift für Physik* 52.7 (July 1929), pp. 555–600. ISSN: 0044-3328. DOI: 10.1007/BF01339455.

[80] M. I. Hussein, M. J. Leamy, and M. Ruzzene. "Dynamics of Phononic Materials and Structures: Historical Origins, Recent Progress, and Future Outlook". In: *Applied Mechanics Reviews* 66.040802 (May 2014). ISSN: 0003-6900. DOI: 10.1115/1.4026911.

[81] M. S. Kushwaha. “Classical Band Structure of Periodic Elastic Composites”. In: *International Journal of Modern Physics B* 10.09 (Apr. 1996), pp. 977–1094. ISSN: 0217-9792. DOI: 10.1142/S0217979296000398.

[82] Y. K. Lin and T. J. McDaniel. “Dynamics of Beam-Type Periodic Structures”. In: *Journal of Engineering for Industry* 91.4 (Nov. 1969), pp. 1133–1141. ISSN: 0022-0817. DOI: 10.1115/1.3591761.

[83] R. Esquivel-Sirvent and G. H. Cocoletzi. “Band Structure for the Propagation of Elastic Waves in Superlattices”. In: *The Journal of the Acoustical Society of America* 95.1 (Jan. 1994), pp. 86–90. ISSN: 0001-4966. DOI: 10.1121/1.408301.

[84] W. X. Zhong and F. W. Williams. “On the Direct Solution of Wave Propagation for Repetitive Structures”. In: *Journal of Sound and Vibration* 181.3 (Mar. 1995), pp. 485–501. ISSN: 0022-460X. DOI: 10.1006/jsvi.1995.0153.

[85] L. Junyi and D. S. Balint. “An Inverse Method to Determine the Dispersion Curves of Periodic Structures Based on Wave Superposition”. In: *Journal of Sound and Vibration* 350 (Aug. 2015), pp. 41–72. ISSN: 0022-460X. DOI: 10.1016/j.jsv.2015.03.041.

[86] A. Safaeinili and D. E. Chimenti. “Floquet Analysis of Guided Waves in Periodically Layered Composites”. In: *The Journal of the Acoustical Society of America* 98.4 (Oct. 1995), pp. 2336–2342. ISSN: 0001-4966. DOI: 10.1121/1.413281.

[87] A. M. B. Braga and G. Herrmann. “Floquet Waves in Anisotropic Periodically Layered Composites”. In: *The Journal of the Acoustical Society of America* 91.3 (Mar. 1992), pp. 1211–1227. ISSN: 0001-4966. DOI: 10.1121/1.402505.

[88] E. López Olazagasti, G. H. Cocoletzi, and W. Luis Mochán. “Optical Properties of Bimetallic Superlattices”. In: *Solid State Communications* 78.1 (Apr. 1991), pp. 9–12. ISSN: 0038-1098. DOI: 10.1016/0038-1098(91)90799-2.

[89] J.-L. Tsai, H.-H. Huang, and C. T. Sun. “Multi-Displacement Continuum Model for Discrete Systems”. In: *International Journal of Mechanical Sciences* 52.12 (Dec. 2010), pp. 1767–1771. ISSN: 0020-7403. DOI: 10.1016/j.ijmecsci.2010.09.010.

[90] T. F. Krauss and R. M. De La Rue. “Photonic Crystals in the Optical Regime — Past, Present and Future”. In: *Progress in Quantum Electronics* 23.2 (Mar. 1999), pp. 51–96. ISSN: 0079-6727. DOI: 10.1016/S0079-6727(99)00004-X.

[91] J. D. Joannopoulos, S. G. Johnson, J. N. Winn, and R. D. Meade. *Photonic Crystals: Molding the Flow of Light - Second Edition*. Princeton University Press, Nov. 2019. ISBN: 978-1-4008-2824-1. DOI: 10.1515/9781400828241.

[92] R. Martínez-Sala, J. Sancho, J. V. Sánchez, V. Gómez, J. Llinares, and F. Meseguer. “Sound Attenuation by Sculpture”. In: *Nature* 378.6554 (Nov. 1995), pp. 241–241. ISSN: 0028-0836, 1476-4687. DOI: 10.1038/378241a0.

[93] M. Sigalas, M. S. Kushwaha, E. N. Economou, M. Kafesaki, I. E. Psarobas, and W. Steurer. "Classical Vibrational Modes in Phononic Lattices: Theory and Experiment". In: *Zeitschrift für Kristallographie - Crystalline Materials* 220.9-10 (Oct. 2005), pp. 765–809. ISSN: 2196-7105, 2194-4946. DOI: 10.1524/zkri.2005.220.9-10.765.

[94] J. Liu, H. Guo, and T. Wang. "A Review of Acoustic Metamaterials and Phononic Crystals". In: *Crystals* 10.4 (Apr. 2020), p. 305. ISSN: 2073-4352. DOI: 10.3390/cryst10040305.

[95] C. Croënne, E. J. S. Lee, H. Hu, and J. H. Page. "Band Gaps in Phononic Crystals: Generation Mechanisms and Interaction Effects". In: *AIP Advances* 1.4 (Dec. 2011), p. 041401. ISSN: 2158-3226. DOI: 10.1063/1.3675797.

[96] Y. Xu, X. Zhou, W. Wang, L. Wang, F. Peng, and B. Li. "On Natural Frequencies of Non-Uniform Beams Modulated by Finite Periodic Cells". In: *Physics Letters A* 380.40 (Sept. 2016), pp. 3278–3283. ISSN: 0375-9601. DOI: 10.1016/j.physleta.2016.07.057.

[97] M. Ruzzene and A. Baz. "Control of Wave Propagation in Periodic Composite Rods Using Shape Memory Inserts". In: *Journal of Vibration and Acoustics* 122.2 (June 1999), pp. 151–159. ISSN: 1048-9002. DOI: 10.1115/1.568452.

[98] F. Romeo and A. Luongo. "Vibration Reduction in Piecewise Bi-Coupled Periodic Structures". In: *Journal of Sound and Vibration* 268.3 (Nov. 2003), pp. 601–615. ISSN: 0022-460X. DOI: 10.1016/S0022-460X(03)00375-4.

[99] A. S. Phani, J. Woodhouse, and N. A. Fleck. "Wave Propagation in Two-Dimensional Periodic Lattices". In: *The Journal of the Acoustical Society of America* 119.4 (Apr. 2006), pp. 1995–2005. ISSN: 0001-4966, 1520-8524. DOI: 10.1121/1.2179748.

[100] D. M. Mead. "WAVE PROPAGATION IN CONTINUOUS PERIODIC STRUCTURES: RESEARCH CONTRIBUTIONS FROM SOUTHAMPTON, 1964–1995". In: *Journal of Sound and Vibration* 190.3 (Feb. 1996), pp. 495–524. ISSN: 0022-460X. DOI: 10.1006/jsvi.1996.0076.

[101] G. Sen Gupta. "Natural Flexural Waves and the Normal Modes of Periodically-Supported Beams and Plates". In: *Journal of Sound and Vibration* 13.1 (Sept. 1970), pp. 89–101. ISSN: 0022-460X. DOI: 10.1016/S0022-460X(70)80082-7.

[102] A. Hvatov and S. Sorokin. "Free Vibrations of Finite Periodic Structures in Pass- and Stop-Bands of the Counterpart Infinite Waveguides". In: *Journal of Sound and Vibration* 347 (July 2015), pp. 200–217. ISSN: 0022460X. DOI: 10.1016/j.jsv.2015.03.003.

[103] A. Pelat, T. Gallot, and F. Gautier. "On the Control of the First Bragg Band Gap in Periodic Continuously Corrugated Beam for Flexural Vibration". In: *Journal of Sound and Vibration* 446 (Apr. 2019), pp. 249–262. ISSN: 0022460X. DOI: 10.1016/j.jsv.2019.01.029.

[104] E. Manconi and B. Mace. "Veering and Strong Coupling Effects in Structural Dynamics". In: *Journal of Vibration and Acoustics* 139.2 (Apr. 2017), p. 021009. ISSN: 1048-9002, 1528-8927. DOI: 10.1115/1.4035109.

[105] Z.-Q. Ni, Y. Zhang, L.-H. Jiang, and L. Han. "Bending Vibration Band Structure of Phononic Crystal Beam by Modified Transfer Matrix Method". In: *International Journal of Modern Physics B* 28.15 (June 2014), p. 1450093. ISSN: 0217-9792. DOI: 10.1142/S0217979214500933.

[106] G. Carta and M. Brun. "Bloch–Floquet Waves in Flexural Systems with Continuous and Discrete Elements". In: *Mechanics of Materials* 87 (Aug. 2015), pp. 11–26. ISSN: 0167-6636. DOI: 10.1016/j.mechmat.2015.03.004.

[107] Y. Lu and A. Srivastava. *Combining Plane Wave Expansion and Variational Techniques for Fast Phononic Computations*. May 2017. DOI: 10.48550/arXiv.1603.06873.

[108] V. F. Dal Poggetto and A. L. Serpa. "Flexural Wave Band Gaps in a Ternary Periodic Metamaterial Plate Using the Plane Wave Expansion Method". In: *Journal of Sound and Vibration* 495 (Mar. 2021), p. 115909. ISSN: 0022-460X. DOI: 10.1016/j.jsv.2020.115909.

[109] I. A. Veres, T. Berer, and O. Matsuda. "Complex Band Structures of Two Dimensional Phononic Crystals: Analysis by the Finite Element Method". In: *Journal of Applied Physics* 114.8 (Aug. 2013), p. 083519. ISSN: 0021-8979. DOI: 10.1063/1.4819209.

[110] C. W. Zhou, J. P. Lainé, M. N. Ichchou, and A. M. Zine. "Wave Finite Element Method Based on Reduced Model for One-Dimensional Periodic Structures". In: *International Journal of Applied Mechanics* 07.02 (Apr. 2015), p. 1550018. ISSN: 1758-8251. DOI: 10.1142/S1758825115500180.

[111] A. Khelif, B. Aoubiza, S. Mohammadi, A. Adibi, and V. Laude. "Complete Band Gaps in Two-Dimensional Phononic Crystal Slabs". In: *Physical Review E* 74.4 (Oct. 2006), p. 046610. ISSN: 1539-3755, 1550-2376. DOI: 10.1103/PhysRevE.74.046610.

[112] X. Zhang, Z. Liu, Y. Liu, and F. Wu. "Elastic Wave Band Gaps for Three-Dimensional Phononic Crystals with Two Structural Units". In: *Physics Letters A* 313.5 (July 2003), pp. 455–460. ISSN: 0375-9601. DOI: 10.1016/S0375-9601(03)00807-7.

[113] Y.-F. Wang, Y.-S. Wang, and X.-X. Su. "Large Bandgaps of Two-Dimensional Phononic Crystals with Cross-like Holes". In: *Journal of Applied Physics* 110.11 (Dec. 2011), p. 113520. ISSN: 0021-8979. DOI: 10.1063/1.3665205.

[114] F. Lucklum and M. J. Vellekoop. "Bandgap Engineering of Three-Dimensional Phononic Crystals in a Simple Cubic Lattice". In: *Applied Physics Letters* 113.20 (Nov. 2018), p. 201902. ISSN: 0003-6951. DOI: 10.1063/1.5049663.

[115] C. Jiu-Jiu, Q. Bo, and C. Jian-Chun. "Complete Band Gaps for Lamb Waves in Cubic Thin Plates with Periodically Placed Inclusions". In: *Chinese Physics Letters* 22.7 (July 2005), p. 1706. ISSN: 0256-307X. DOI: 10.1088/0256-307X/22/7/040.

[116] F. Meseguer, M. Holgado, D. Caballero, N. Benaches, J. Sánchez-Dehesa, C. López, and J. Llinares. "Rayleigh-Wave Attenuation by a Semi-Infinite Two-Dimensional Elastic-Band-

Gap Crystal". In: *Physical Review B* 59.19 (May 1999), pp. 12169–12172. DOI: 10.1103/PhysRevB.59.12169.

[117] Y. Tanaka and S.-i. Tamura. "Surface Acoustic Waves in Two-Dimensional Periodic Elastic Structures". In: *Physical Review B* 58.12 (Sept. 1998), pp. 7958–7965. DOI: 10.1103/PhysRevB.58.7958.

[118] N. Khan, A. Riccio, M. Pelliccione, P. Franciosa, and D.-M. Morabito. "A systematic review of design for additive manufacturing of aerospace lattice structures: Current trends and future directions". In: *Progress in Aerospace Sciences* 146 (2024), p. 100816. DOI: 10.1016/j.paerosci.2023.100816.

[119] S. Li, Z. Ma, Y. Deng, and D. Zhou. "A Comprehensive Review on Energy-Absorbing Mechanical Metamaterials". In: *Composites Part B* 276 (2025), p. 110966. DOI: 10.1016/j.compositesb.2023.110966.

[120] L. Gao, Y. Lin, and R. Qi. "Additive manufacturing and lattice design for thermal management". In: *Applied Thermal Engineering* 233 (2023), p. 121727. DOI: 10.1016/j.applthermaleng.2023.121727.

[121] J. Liu, M. Xu, R. Zhang, X. Zhang, and W. Xi. "Progress of Porous/Lattice Structures Applied in Thermal Management Technology of Aerospace Applications". In: *Aerospace* 9.12 (2022), p. 827. DOI: 10.3390/aerospace9120827.

[122] E. Dalpadulo, M. Pollon, A. Vergnano, and F. Leali. "Design for Additive Manufacturing of Lattice Structures for Functional Integration of Thermal Management and Shock Absorption". In: *Journal of Manufacturing and Materials Processing* 9.1 (2025), p. 24. DOI: 10.3390/jmmp9010024.

[123] C. Pan, Y. Han, and J. Lu. "Design and Optimization of Lattice Structures: A Review". In: *Applied Sciences* 10.18 (2020), p. 6374. DOI: 10.3390/app10186374.

[124] M. Bedoya, S. Rodriguez, O. Moreno, S. Lucas, M. Zimmermann, and J. Llorca. "Cellular Structures Analysis Under Compression Test". In: *Polymers* 17.11 (2023), p. 1476. DOI: 10.3390/polym17111476.

[125] H. Feng, C. Cai, X. Ruan, H. Jin, and Y. Hu. "Mechanical Properties Regulation of Invar36 Alloy Metastructures Printed by Selective Laser Melting". In: *Metals* 15.6 (2025), p. 1275. DOI: 10.3390/met15061275.

[126] R. Sindhu, C. W. Lim, H.-T. J. Li, and Z. Zhao. "Lightweight architected lattice phononic crystals with broadband and multiband vibration mitigation characteristics". In: *Extreme Mechanics Letters* 41 (2020), p. 100994. DOI: 10.1016/j.eml.2020.100994.

[127] M. Benedetti, A. du Plessis, R. O. Ritchie, M. Dallago, N. Razavi, and F. Berto. "Architected cellular materials: A review on their mechanical properties towards fatigue-tolerant design and fabrication". In: *Materials Science and Engineering: R: Reports* 144 (2021), p. 100606. DOI: 10.1016/j.mser.2021.100606.

[128] H. Shi, K. Zhang, X. Liu, H. Liu, H. Peng, and Z. Deng. "Vibration Suppression of a Meta-Structure with Hybridization of Kresling Origami and Waterbomb-Based Origami". In: *Composite Structures* 334 (Apr. 2024), p. 117964. ISSN: 0263-8223. DOI: 10.1016/j.compstruct.2024.117964.

[129] X. Liu, K. Zhang, H. Shi, F. Hong, H. Liu, and Z. Deng. "Origami-Inspired Metamaterial with Compression–Twist Coupling Effect for Low-Frequency Vibration Isolation". In: *Mechanical Systems and Signal Processing* 208 (Feb. 2024), p. 111076. ISSN: 0888-3270. DOI: 10.1016/j.ymssp.2023.111076.

[130] X. N. Liu, G. L. Huang, and G. K. Hu. "Chiral Effect in Plane Isotropic Micropolar Elasticity and Its Application to Chiral Lattices". In: *Journal of the Mechanics and Physics of Solids* 60.11 (Nov. 2012), pp. 1907–1921. ISSN: 0022-5096. DOI: 10.1016/j.jmps.2012.06.008.

[131] H.-y. Yang, S.-l. Cheng, X.-f. Li, Q. Yan, B. Wang, Y.-j. Xin, Y.-t. Sun, Q. Ding, H. Yan, Y.-j. Li, and Q.-x. Zhao. "Study on Bandgap and Vibration Attenuation Mechanism of Novel Chiral Lattices". In: *Physica B: Condensed Matter* 651 (Feb. 2023), p. 414596. ISSN: 0921-4526. DOI: 10.1016/j.physb.2022.414596.

[132] K. Zhang, P. Zhao, C. Zhao, F. Hong, and Z. Deng. "Study on the Mechanism of Band Gap and Directional Wave Propagation of the Auxetic Chiral Lattices". In: *Composite Structures* 238 (Apr. 2020), p. 111952. ISSN: 0263-8223. DOI: 10.1016/j.compstruct.2020.111952.

[133] P. Zhao, K. Zhang, L. Qi, and Z. Deng. "3D Chiral Mechanical Metamaterial for Tailored Band Gap and Manipulation of Vibration Isolation". In: *Mechanical Systems and Signal Processing* 180 (Nov. 2022), p. 109430. ISSN: 0888-3270. DOI: 10.1016/j.ymssp.2022.109430.

[134] W. Ding, T. Chen, C. Chen, D. Chronopoulos, and J. Zhu. "A Three-Dimensional Twisted Phononic Crystal with Omnidirectional Bandgap Based on Inertial Amplification by Utilizing Translation-Rotation Coupling". In: *Journal of Sound and Vibration* 541 (Dec. 2022), p. 117307. ISSN: 0022460X. DOI: 10.1016/j.jsv.2022.117307.

[135] F. He, Y. Zhang, D. Qian, and G. Wei. "Band Gap Properties of a Curved Phononic Crystal Truss Structure". In: *Acta Mechanica* 236.3 (Mar. 2025), pp. 2193–2209. ISSN: 1619-6937. DOI: 10.1007/s00707-025-04266-0.

[136] Muhammad, C. Lim, J. T. Li, and Z. Zhao. "Lightweight Architected Lattice Phononic Crystals with Broadband and Multiband Vibration Mitigation Characteristics". In: *Extreme Mechanics Letters* 41 (Nov. 2020), p. 100994. ISSN: 23524316. DOI: 10.1016/j.eml.2020.100994.

[137] Y. Chen, L. Yang, J. Lou, J. Wang, M. Filippi, E. Carrera, and X. Fang. "Bio-Inspired Elastic Metamaterial by B-form DNA: Programmable Dual Helix Structures for Low-Frequency Longitudinal Wave Prohibition". In: *Composite Structures* 360 (Apr. 2025), p. 118986. ISSN: 0263-8223. DOI: 10.1016/j.compstruct.2025.118986.

[138] Y. Chen, F. Qian, L. Zuo, F. Scarpa, and L. Wang. "Broadband and Multiband Vibration Mitigation in Lattice Metamaterials with Sinusoidally-Shaped Ligaments". In: *Extreme*

Mechanics Letters 17 (Nov. 2017), pp. 24–32. ISSN: 23524316. DOI: 10.1016/j.eml.2017.09.012.

[139] Y.-F. Wang, Y.-S. Wang, and C. Zhang. "Bandgaps and Directional Propagation of Elastic Waves in 2D Square Zigzag Lattice Structures". In: *Journal of Physics D: Applied Physics* 47.48 (Nov. 2014), p. 485102. ISSN: 0022-3727. DOI: 10.1088/0022-3727/47/48/485102.

[140] S. Gonella and M. Ruzzene. "Analysis of In-Plane Wave Propagation in Hexagonal and Re-Entrant Lattices". In: *Journal of Sound and Vibration* 312.1 (Apr. 2008), pp. 125–139. ISSN: 0022-460X. DOI: 10.1016/j.jsv.2007.10.033.

[141] Z. Guo, J. Wen, D. Yu, G. Hu, and Y. Yang. "Widening the Band Gaps of Hourglass Lattice Truss Core Sandwich Structures for Broadband Vibration Suppression". In: *Journal of Vibration and Acoustics* 145.061002 (Oct. 2023). ISSN: 1048-9002. DOI: 10.1115/1.4063443.

[142] V. Gupta, R. K. Munian, and B. Bhattacharya. "Dispersion Analysis of the Hourglass-Shaped Periodic Shell Lattice Structure". In: *International Journal of Solids and Structures* 254–255 (Nov. 2022), p. 111931. ISSN: 0020-7683. DOI: 10.1016/j.ijsolstr.2022.111931.

[143] S. Kim, H. Hong, J. Jeong, W. Kim, W. Kim, G. Sim, J. Lee, and S. S. Kim. "Optimization of 3D Printed Truss *Meta*-Structure for Structural Performance and Switchable Vibration Attenuation". In: *Composites Part A: Applied Science and Manufacturing* 193 (June 2025), p. 108845. ISSN: 1359-835X. DOI: 10.1016/j.compositesa.2025.108845.

[144] X. Chen, Y. Wei, S. Jiang, Z. Guo, Y. Han, C. Zhao, and T. Li. "Broadband Vibration Reduction of Single-Beam Honeycomb Metamaterial with Tunable Bandgap Characteristics". In: *Journal of Vibration Engineering & Technologies* 13.1 (Jan. 2025), p. 28. ISSN: 2523-3939. DOI: 10.1007/s42417-024-01612-9.

[145] Z.-Y. Li, T.-X. Ma, Y.-Z. Wang, F.-M. Li, and C. Zhang. "Vibration Isolation by Novel Meta-Design of Pyramid-Core Lattice Sandwich Structures". In: *Journal of Sound and Vibration* 480 (Aug. 2020), p. 115377. ISSN: 0022460X. DOI: 10.1016/j.jsv.2020.115377.

[146] L. Sun, J. Li, and Y. Xiao. "BROAD AND LOW FREQUENCY BANDGAP IN TRUSS CORE SANDWICH BEAM". In: *Mechanics of Solids* 56.3 (May 2021), pp. 421–429. ISSN: 1934-7936. DOI: 10.3103/S0025654421030122.

[147] L. Li, J. Wu, F. Yang, P. Li, G. Lu, H. Fan, J. Zhao, N. Zhang, and Q. Yang. "Mechanisms of Low-Frequency Bandgap Formation and Energy Absorption of Three-Dimensional Nested Hybrid Lattice Structures". In: *Composites Part B: Engineering* 291 (Feb. 2025), p. 112045. ISSN: 1359-8368. DOI: 10.1016/j.compositesb.2024.112045.

[148] G. Aguzzi, C. Kanellopoulos, R. Wiltshaw, R. V. Craster, E. N. Chatzi, and A. Colombi. "Octet Lattice-Based Plate for Elastic Wave Control". In: *Scientific Reports* 12.1 (Jan. 2022), p. 1088. ISSN: 2045-2322. DOI: 10.1038/s41598-022-04900-0.

[149] T. Delpero, S. Schoenwald, A. Zemp, and A. Bergamini. "Structural Engineering of Three-Dimensional Phononic Crystals". In: *Journal of Sound and Vibration* 363 (Feb. 2016), pp. 156–165. ISSN: 0022460X. DOI: 10.1016/j.jsv.2015.10.033.

[150] G.-L. Yu and H.-W. Miao. "On Vibration Isolation of Sandwich Plate with Periodic Hollow Tube Core". In: *Journal of Sandwich Structures & Materials* (2017). DOI: 10.1177/1099636217707933.

[151] Z.-J. Wu, F.-M. Li, and C. Zhang. "Vibration Band-Gap Properties of Three-Dimensional Kagome Lattices Using the Spectral Element Method". In: *Journal of Sound and Vibration* 341 (Apr. 2015), pp. 162–173. ISSN: 0022460X. DOI: 10.1016/j.jsv.2014.12.038.

[152] J. F. Doyle. "Wave Propagation in Structures". In: *Wave Propagation in Structures: An FFT-Based Spectral Analysis Methodology*. Ed. by J. F. Doyle. New York, NY: Springer US, 1989, pp. 126–156. ISBN: 978-1-4684-0344-2. DOI: 10.1007/978-1-4684-0344-2_6.

[153] M. Mellmann, E. Perras, and C. Zhang. "Computation of the Elastic Wave Band Structures and Transmission in Pre-Deformed Periodic Frame Structures by SEM". In: *Forum Acusticum*. Lyon, France, Dec. 2020, pp. 1117–1123. DOI: 10.48465/fa.2020.0358.

[154] B. Kumar, A. Banerjee, R. Das, and B. Manna. "Frequency Dependent Effective Modulus of Square Grid Lattice Using Spectral Element Method". In: *Mechanics of Materials* 184 (Sept. 2023), p. 104695. ISSN: 01676636. DOI: 10.1016/j.mechmat.2023.104695.

[155] B. R. Mace, D. Duhamel, M. J. Brennan, and L. Hinke. "Finite Element Prediction of Wave Motion in Structural Waveguides". In: *The Journal of the Acoustical Society of America* 117.5 (Apr. 2005), pp. 2835–2843. ISSN: 0001-4966. DOI: 10.1121/1.1887126.

[156] M. C. Messner, M. I. Barham, M. Kumar, and N. R. Barton. "Wave Propagation in Equivalent Continuums Representing Truss Lattice Materials". In: *International Journal of Solids and Structures* 73–74 (Nov. 2015), pp. 55–66. ISSN: 00207683. DOI: 10.1016/j.ijsolstr.2015.07.023.

[157] A. Gross, P. Pantidis, K. Bertoldi, and S. Gerasimidis. "Correlation between Topology and Elastic Properties of Imperfect Truss-Lattice Materials". In: *Journal of the Mechanics and Physics of Solids* 124 (Mar. 2019), pp. 577–598. ISSN: 0022-5096. DOI: 10.1016/j.jmps.2018.11.007.

[158] C. Yilmaz and G. M. Hulbert. "Dynamics of Locally Resonant and Inertially Amplified Lattice Materials". In: *Dynamics of Lattice Materials*. John Wiley & Sons, Ltd, 2017. Chap. 11, pp. 233–258. ISBN: 978-1-118-72958-8. DOI: 10.1002/9781118729588.ch11.

[159] Y. Xiao, S. Wang, Y. Li, and J. Wen. "Closed-Form Bandgap Design Formulas for Beam-Type Metastructures". In: *Mechanical Systems and Signal Processing* 159 (Oct. 2021), p. 107777. ISSN: 08883270. DOI: 10.1016/j.ymssp.2021.107777.

[160] Z. Guo, G. Hu, V. Sorokin, L. Tang, X. Yang, and J. Zhang. "Low-Frequency Flexural Wave Attenuation in Metamaterial Sandwich Beam with Hourglass Lattice Truss Core". In: *Wave*

Motion 104 (July 2021), p. 102750. ISSN: 01652125. DOI: 10.1016/j.wavemoti.2021.102750.

[161] K. H. Matlack, A. Bauhofer, S. Krödel, A. Palermo, and C. Daraio. "Composite 3D-printed Metastructures for Low-Frequency and Broadband Vibration Absorption". In: *Proceedings of the National Academy of Sciences* 113.30 (July 2016), pp. 8386–8390. DOI: 10.1073/pnas.1600171113.

[162] J. Liu and S. Li. "A Novel 3D-Printed Negative-Stiffness Lattice Structure with Internal Resonance Characteristics and Tunable Bandgap Properties". In: *Materials (Basel, Switzerland)* 16.24 (Dec. 2023), p. 7669. ISSN: 1996-1944. DOI: 10.3390/ma16247669.

[163] W. Jiang, M. Yin, Q. Liao, L. Xie, and G. Yin. "Three-Dimensional Single-Phase Elastic Metamaterial for Low-Frequency and Broadband Vibration Mitigation". In: *International Journal of Mechanical Sciences* 190 (Jan. 2021), p. 106023. ISSN: 00207403. DOI: 10.1016/j.ijmecsci.2020.106023.

[164] J. Chu, G. Zhou, X. Liang, H. Liang, Z. Yang, and T. Chen. "A Metamaterial for Low-Frequency Vibration Damping". In: *Materials Today Communications* 36 (Aug. 2023), p. 106464. ISSN: 2352-4928. DOI: 10.1016/j.mtcomm.2023.106464.

[165] X. An, X. Yuan, and H. Fan. "Meta-Kagome Lattice Structures for Broadband Vibration Isolation". In: *Engineering Structures* 277 (Feb. 2023), p. 115403. ISSN: 0141-0296. DOI: 10.1016/j.engstruct.2022.115403.

[166] X. An, H. Fan, and C. Zhang. "Elastic Wave and Vibration Bandgaps in Planar Square Metamaterial-Based Lattice Structures". In: *Journal of Sound and Vibration* 475 (June 2020), p. 115292. ISSN: 0022-460X. DOI: 10.1016/j.jsv.2020.115292.

[167] X. An, C. Lai, W. He, and H. Fan. "Three-Dimensional Meta-Truss Lattice Composite Structures with Vibration Isolation Performance". In: *Extreme Mechanics Letters* 33 (Nov. 2019), p. 100577. ISSN: 2352-4316. DOI: 10.1016/j.eml.2019.100577.

[168] W. Elmadih, D. Chronopoulos, W. P. Syam, I. Maskery, H. Meng, and R. K. Leach. "Three-Dimensional Resonating Metamaterials for Low-Frequency Vibration Attenuation". In: *Scientific Reports* 9.1 (Aug. 2019), p. 11503. ISSN: 2045-2322. DOI: 10.1038/s41598-019-47644-0.

[169] Y. Liu, Y. Jin, Y. Yang, W. Yang, Z. Tong, and Y. Li. "Lightweight Continuous Carbon Fiber Reinforced Composite Truss Beam Metastructure with Cruciform Resonators for Vibration Attenuation". In: *Composites Part A: Applied Science and Manufacturing* 201 (Feb. 2026), p. 109408. ISSN: 1359835X. DOI: 10.1016/j.compositesa.2025.109408.

[170] J. S. Jensen. "Phononic band gaps and vibrations in one- and two-dimensional mass–spring structures". In: *Journal of Sound and Vibration* 266.5 (Oct. 2003), pp. 1053–1078. ISSN: 0022-460X. DOI: 10.1016/S0022-460X(02)01629-2.

[171] D. Yu, Y. Liu, G. Wang, L. Cai, and J. Qiu. "Low Frequency Torsional Vibration Gaps in the Shaft with Locally Resonant Structures". In: *Physics Letters A* 348.3 (Jan. 2006), pp. 410–415. ISSN: 0375-9601. DOI: 10.1016/j.physleta.2005.08.067.

[172] A. Banerjee, S. Adhikari, and M. I. Hussein. "Inertial Amplification Band-Gap Generation by Coupling a Levered Mass with a Locally Resonant Mass". In: *International Journal of Mechanical Sciences* 207 (Oct. 2021), p. 106630. ISSN: 00207403. DOI: 10.1016/j.ijmecsci.2021.106630.

[173] S. Taniker and C. Yilmaz. "Phononic Gaps Induced by Inertial Amplification in BCC and FCC Lattices". In: *Physics Letters A* 377.31 (Oct. 2013), pp. 1930–1936. ISSN: 0375-9601. DOI: 10.1016/j.physleta.2013.05.022.

[174] C. Yilmaz, G. M. Hulbert, and N. Kikuchi. "Phononic Band Gaps Induced by Inertial Amplification in Periodic Media". In: *Physical Review B* (2007). DOI: 10.1103/PhysRevB.76.054309.

[175] Q. Lin, J. Zhou, K. Wang, D. Xu, G. Wen, and Q. Wang. "Three-Dimensional Quasi-Zero-Stiffness Metamaterial for Low-Frequency and Wide Complete Band Gap". In: *Composite Structures* 307 (Mar. 2023), p. 116656. ISSN: 02638223. DOI: 10.1016/j.compstruct.2022.116656.

[176] Q. Lin, J. Zhou, K. Wang, D. Xu, G. Wen, Q. Wang, and C. Cai. "Low-Frequency Locally Resonant Band Gap of the Two-Dimensional Quasi-Zero-Stiffness Metamaterials". In: *International Journal of Mechanical Sciences* 222 (May 2022), p. 107230. ISSN: 0020-7403. DOI: 10.1016/j.ijmecsci.2022.107230.

[177] C. Cai, J. Zhou, L. Wu, K. Wang, D. Xu, and H. Ouyang. "Design and Numerical Validation of Quasi-Zero-Stiffness Metamaterials for Very Low-Frequency Band Gaps". In: *Composite Structures* 236 (Mar. 2020), p. 111862. ISSN: 02638223. DOI: 10.1016/j.compstruct.2020.111862.

[178] Y. Gao, L. Wang, W. Sun, K. Wu, and H. Hu. "Ultrawide Bandgap in Metamaterials via Coupling of Locally Resonant and Bragg Bandgaps". In: *Acta Mechanica* 233.2 (Feb. 2022), pp. 477–493. ISSN: 1619-6937. DOI: 10.1007/s00707-021-03122-1.

[179] H. Sheng, M.-X. He, J. Zhao, C. T. Kam, Q. Ding, and H. P. Lee. "The ABH-based Lattice Structure for Load Bearing and Vibration Suppression". In: *International Journal of Mechanical Sciences* 252 (Aug. 2023), p. 108378. ISSN: 0020-7403. DOI: 10.1016/j.ijmecsci.2023.108378.

[180] A. Pelat, F. Gautier, S. C. Conlon, and F. Semperlotti. "The Acoustic Black Hole: A Review of Theory and Applications". In: *Journal of Sound and Vibration* 476 (June 2020), p. 115316. ISSN: 0022460X. DOI: 10.1016/j.jsv.2020.115316.

[181] J. Li, X. Fan, and F. Li. "Numerical and Experimental Study of a Sandwich-like Metamaterial Plate for Vibration Suppression". In: *Composite Structures* 238 (Apr. 2020), p. 111969. ISSN: 02638223. DOI: 10.1016/j.compstruct.2020.111969.

[182] C. Li, Z. Chen, and Y. Jiao. "Vibration and Bandgap Behavior of Sandwich Pyramid Lattice Core Plate with Resonant Rings". In: *Materials* 16.7 (Jan. 2023), p. 2730. ISSN: 1996-1944. DOI: 10.3390/ma16072730.

[183] C. C. Claeys, K. Vergote, P. Sas, and W. Desmet. "On the Potential of Tuned Resonators to Obtain Low-Frequency Vibrational Stop Bands in Periodic Panels". In: *Journal of Sound and Vibration* 332.6 (Mar. 2013), pp. 1418–1436. ISSN: 0022-460X. DOI: 10.1016/j.jsv.2012.09.047.

[184] L. Van Belle, C. Claeys, E. Deckers, and W. Desmet. "The Impact of Damping on the Sound Transmission Loss of Locally Resonant Metamaterial Plates". In: *Journal of Sound and Vibration* 461 (Nov. 2019), p. 114909. ISSN: 0022460X. DOI: 10.1016/j.jsv.2019.114909.

[185] C. Claeys, N. G. Rocha de Melo Filho, L. Van Belle, E. Deckers, and W. Desmet. "Design and Validation of Metamaterials for Multiple Structural Stop Bands in Waveguides". In: *Extreme Mechanics Letters*. Frontiers in Mechanical Metamaterials 12 (Apr. 2017), pp. 7–22. ISSN: 2352-4316. DOI: 10.1016/j.eml.2016.08.005.

[186] W. Jiang, G. Yin, L. Xie, and M. Yin. "Multifunctional 3D Lattice Metamaterials for Vibration Mitigation and Energy Absorption". In: *International Journal of Mechanical Sciences* 233 (Nov. 2022), p. 107678. ISSN: 0020-7403. DOI: 10.1016/j.ijmecsci.2022.107678.

[187] Y. Zhang, D. Yu, and J. Wen. "Study on the Band Gaps of Phononic Crystal Pipes with Alternating Materials in the Radial and Axial Directions". In: *Extreme Mechanics Letters*. Frontiers in Mechanical Metamaterials 12 (Apr. 2017), pp. 2–6. ISSN: 2352-4316. DOI: 10.1016/j.eml.2016.10.005.

[188] J. Plisson, A. Pelat, F. Gautier, V. R. Garcia, and T. Bourdon. "Experimental Evidence of Absolute Bandgaps in Phononic Crystal Pipes". In: *Applied Physics Letters* 116.20 (May 2020), p. 201902. ISSN: 0003-6951. DOI: 10.1063/5.0007532.

[189] P. Zhao, K. Zhang, F. Hong, and Z. Deng. "Tacticity-Based One-Dimensional Chiral Equilateral Lattice for Tailored Wave Propagation and Design of Elastic Wave Logic Gate". In: *Journal of Sound and Vibration* 521 (Mar. 2022), p. 116671. ISSN: 0022-460X. DOI: 10.1016/j.jsv.2021.116671.

[190] A. Bergamini, M. Miniaci, T. Delpero, D. Tallarico, B. Van Damme, G. Hannema, I. Leibacher, and A. Zemp. "Tacticity in Chiral Phononic Crystals". In: *Nature Communications* 10.1 (Oct. 2019), p. 4525. ISSN: 2041-1723. DOI: 10.1038/s41467-019-12587-7.

[191] K. Fujita, M. Tomoda, O. B. Wright, and O. Matsuda. "Perfect Acoustic Bandgap Metabeam Based on a Quadruple-Mode Resonator Array". In: *Applied Physics Letters* 115.8 (Aug. 2019), p. 081905. ISSN: 0003-6951, 1077-3118. DOI: 10.1063/1.5117283.

[192] H. Lamb. “On waves in an elastic plate”. In: *Proceedings of the Royal Society of London. Series A, Containing Papers of a Mathematical and Physical Character* 93.648 (Jan. 1997), pp. 114–128. DOI: 10.1098/rspa.1917.0008.

[193] D. Royer and E. Dieulesaint. *Elastic Waves in Solids I: Free and Guided Propagation*. en. Berlin: Springer Science & Business Media, Nov. 1999. ISBN: 978-3-540-65932-7. DOI: 10.1002/9781119902942.

[194] T. Bonneval, M. Lanoy, R. Tanays, L. Sanches, G. Michon, and A. Pelat. “Dispersion analysis in a 3D lattice elastic waveguide for the design of an absolute filter”. en. In: *Journal of Sound and Vibration* 617 (Nov. 2025), p. 119314. ISSN: 0022460X. DOI: 10.1016/j.jsv.2025.119314.

[195] U. Lee. *Spectral Element Method in Structural Dynamics*. en. Singapore: John Wiley & Sons, July 2009. ISBN: 978-0-470-82375-0. DOI: 10.1002/9780470823767.

[196] S. S. Antman. “The Theory of Rods”. en. In: *Linear Theories of Elasticity and Thermoelasticity: Linear and Nonlinear Theories of Rods, Plates, and Shells*. Ed. by C. Truesdell. Berlin, Heidelberg: Springer, 1973, pp. 641–703. ISBN: 978-3-662-39776-3. DOI: 10.1007/978-3-662-39776-3_6.

[197] R. A. Anderson. “Flexural Vibrations in Uniform Beams According to the Timoshenko Theory”. In: *Journal of Applied Mechanics* 20.4 (June 2021), pp. 504–510. ISSN: 0021-8936. DOI: 10.1115/1.4010755.

[198] M. Collet, M. Ouisse, M. Ruzzene, and M. N. Ichchou. “Floquet–Bloch decomposition for the computation of dispersion of two-dimensional periodic, damped mechanical systems”. In: *International Journal of Solids and Structures* 48.20 (2011), pp. 2837–2848. DOI: 10.1016/j.ijsolstr.2011.06.002.

[199] D. Huntington and C. Lyrintzis. “Improvements to and Limitations of Latin Hypercube Sampling”. In: *Probabilistic Engineering Mechanics* 13.4 (Oct. 1998), pp. 245–253. ISSN: 02668920. DOI: 10.1016/S0266-8920(97)00013-1.

[200] Y. Li and H. Wu. “A Clustering Method Based on K-Means Algorithm”. In: *Physics Procedia* 25 (2012), pp. 1104–1109. ISSN: 18753892. DOI: 10.1016/j.phpro.2012.03.206.

[201] L. Van Belle, C. Claeys, E. Deckers, and W. Desmet. “On the Impact of Damping on the Dispersion Curves of a Locally Resonant Metamaterial: Modelling and Experimental Validation”. In: *Journal of Sound and Vibration* 409 (Nov. 2017), pp. 1–23. ISSN: 0022460X. DOI: 10.1016/j.jsv.2017.07.045.

[202] H. Zi, Y. Li, M. Hu, F. Zhu, and L. Zhu. “Flexural wave bandgap and isolation characteristics of vibration and sound in periodic sandwich plates”. en. In: *Chinese Journal of Ship Research* 18.2 (Apr. 2023), pp. 81–89. ISSN: 1673-3185. DOI: 10.19693/j.issn.1673-3185.02462.

[203] M. Ruzzene, L. Mazzarella, P. Tsopelas, and F. Scarpa. “Wave Propagation in Sandwich Plates with Periodic Auxetic Core”. EN. In: *Journal of Intelligent Material Systems and Structures* 13.9 (Sept. 2002), pp. 587–597. ISSN: 1045-389X. DOI: 10.1106/104538902031865.

[204] Z. Wei, X. Yin, S. Yu, and W. Wu. "Dynamic stiffness formulation for transverse and in-plane vibration of rectangular plates with arbitrary boundary conditions based on a generalized superposition method". en. In: *International Journal of Mechanics and Materials in Design* 17.1 (Mar. 2021), pp. 119–135. ISSN: 1573-8841. DOI: 10.1007/s10999-020-09515-9.

[205] D. Gorman. "Free vibration analysis of the completely free rectangular plate by the method of superposition". en. In: *Journal of Sound and Vibration* 57.3 (Apr. 1978), pp. 437–447. ISSN: 0022460X. DOI: 10.1016/0022-460X(78)90322-X.

[206] D. Gorman. "Free in-plane vibration analysis of rectangular plates by the method of superposition". en. In: *Journal of Sound and Vibration* 272.3-5 (May 2004), pp. 831–851. ISSN: 0022460X. DOI: 10.1016/S0022-460X(03)00421-8.

[207] M. Nefovska-Danilovic and M. Petronijevic. "In-plane free vibration and response analysis of isotropic rectangular plates using the dynamic stiffness method". In: *Computers & Structures* 152 (May 2015), pp. 82–95. ISSN: 0045-7949. DOI: 10.1016/j.compstruc.2015.02.001.

[208] Z. Li, G. Jin, Y. Chen, T. Ye, B. Zhang, T. Yang, and P. Li. "Unified vibration modeling of shell and plate structures with resonators". In: *International Journal of Mechanical Sciences* 287 (Feb. 2025), p. 109921. ISSN: 0020-7403. DOI: 10.1016/j.ijmecsci.2025.109921.

[209] S. Kevorkian and M. Pascal. "AN ACCURATE METHOD FOR FREE VIBRATION ANALYSIS OF STRUCTURES WITH APPLICATION TO PLATES". en. In: *Journal of Sound and Vibration* 246.5 (Oct. 2001), pp. 795–814. ISSN: 0022460X. DOI: 10.1006/jsvi.2001.3709.

[210] M. A. Campana, M. Ouisse, E. Sadoulet-Reboul, M. Ruzzene, S. Neild, and F. Scarpa. "Impact of non-linear resonators in periodic structures using a perturbation approach". In: *Mechanical Systems and Signal Processing* 135 (Jan. 2020), p. 106408. ISSN: 0888-3270. DOI: 10.1016/j.ymssp.2019.106408.

[211] A. H. Nayfeh and D. T. Mook. *Nonlinear Oscillations*. New York: John Wiley & Sons, 1979. ISBN: 978-0471121428.

[212] A. F. Vakakis. "Nonlinear Normal Modes (NNMs) and Their Applications in Vibration Theory: An Overview". In: *Mechanical Systems and Signal Processing* 11.1 (1997), pp. 3–22. DOI: 10.1006/mssp.1996.0108.

[213] H. B. Keller. "Numerical solution of bifurcation and nonlinear eigenvalue problems". In: *SIAM Journal on Scientific and Statistical Computing* 7 (1977), pp. 157–175.

[214] M. Peeters, R. Viguié, G. Sérandour, G. Kerschen, and J.-C. Golinval. "Nonlinear normal modes, Part II: Toward a practical computation using numerical continuation techniques". In: *Mechanical Systems and Signal Processing* 23.1 (2009). Special Issue: Non-linear Structural Dynamics, pp. 195–216. ISSN: 0888-3270. DOI: https://doi.org/10.1016/j.ymssp.2008.04.003.

[215] A. F. Vakakis, O. Gendelman, L. A. Bergman, D. M. McFarland, G. Kerschen, and Y. S. Lee. *Nonlinear Targeted Energy Transfer in Mechanical and Structural Systems*. Berlin: Springer, 2008. DOI: 10.1007/978-1-4020-9130-8.

[216] G. Theocharis, N. Boechler, and C. Daraio. "Nonlinear Periodic Phononic Structures and Granular Crystals". In: *Acoustic Metamaterials and Phononic Crystals*. Ed. by P. A. Deymier. Berlin, Heidelberg: Springer Berlin Heidelberg, 2013, pp. 217–251. ISBN: 978-3-642-31232-8. DOI: 10.1007/978-3-642-31232-8_7.

[217] M. I. Hussein, M. J. Leamy, and M. Ruzzene. "Dynamics of phononic materials and structures: Historical origins, recent progress, and future outlook". In: *Applied Mechanics Reviews* 66.4 (2014), p. 040802. DOI: 10.1115/1.4026911.

[218] A. Ogasawara, K. Fujita, M. Tomoda, O. Matsuda, and O. B. Wright. "Wave-canceling acoustic metarod architected with single material building blocks". In: *Applied Physics Letters* 116.24 (June 2020), p. 241904. ISSN: 0003-6951. DOI: 10.1063/5.0011319.

[219] Y. Li, Y. Xiao, J. Guo, Z. Zhu, and J. Wen. "Single-phase metabeam for three-directional broadband vibration suppression". In: *International Journal of Mechanical Sciences* 234 (Nov. 2022), p. 107683. ISSN: 0020-7403. DOI: 10.1016/j.ijmecsci.2022.107683.

[220] G. Ma, C. Fu, G. Wang, P. del Hougne, J. Christensen, Y. Lai, and P. Sheng. "Polarization bandgaps and fluid-like elasticity in fully solid elastic metamaterials". en. In: *Nature Communications* 7.1 (Nov. 2016), p. 13536. ISSN: 2041-1723. DOI: 10.1038/ncomms13536.

[221] X. Cadiot, L. Sanches, A. Hot, A. Mouysset, and G. Michon. "Dynamic Base Excitation of a Satellite Cable Harness: Modeling and Experiments". In: *Journal of Spacecraft and Rockets* 59.6 (2022), pp. 2206–2209. ISSN: 0022-4650. DOI: 10.2514/1.A35529.

[222] J. Loukota, J.-C. Passieux, A. Lucchetti, and G. Michon. "Modeling of Nonstructural Components in the Dynamic Behavior of Aeronautical Structures". In: *Journal of Aircraft* 54.1 (2017), pp. 85–93. ISSN: 0021-8669. DOI: 10.2514/1.C033777.

[223] W. Jiao. "Opening and Closing a Bandgap via Alternating Softening and Hardening Nonlinearities". In: *Physical Review B* 111.21 (June 2025), p. 214308. ISSN: 2469-9950, 2469-9969. DOI: 10.1103/qf3q-11hl.

[224] J. Zhao, H. Zhou, K. Yi, I. Kovacic, and R. Zhu. "Ultra-Broad Bandgap Induced by Hybrid Hardening and Softening Nonlinearity in Metastructure". In: *Nonlinear Dynamics* 111.19 (Oct. 2023), pp. 17687–17707. ISSN: 1573-269X. DOI: 10.1007/s11071-023-08808-w.

[225] J. Zhao, I. Kovacic, and R. Zhu. "Wideband Vibration Attenuation of a Metamaterial Beam via Integrated Hardening and Softening Nonlinear Resonators". In: *Nonlinear Dynamics* 113.18 (Sept. 2025), pp. 23903–23920. ISSN: 1573-269X. DOI: 10.1007/s11071-024-10402-7.

[226] M. A. Al-Sheyyab and M. A. Bukhari. "Unlocking Targeted Energy Transfer in Phononic Lattices: Exploring Local Vibro-Impact Nonlinearity in Multiple Local Resonator Metamate-

rials". In: *IFAC-PapersOnLine*. The 4th Modeling, Estimation, and Control Conference – 2024 58.28 (Jan. 2024), pp. 228–233. ISSN: 2405-8963. DOI: 10.1016/j.ifacol.2024.12.039.

[227] J. Jin, H. Kim, H.-I. Koh, and J. Park. "Railway Noise Reduction by Periodic Tuned Particle Impact Damper with Bounce and Pitch-Coupled Vibration Modes". In: *Composite Structures* 284 (Mar. 2022), p. 115230. ISSN: 0263-8223. DOI: 10.1016/j.compstruct.2022.115230.

[228] H. Li, M. Sécail-Géraud, A. Pelat, F. Gautier, and C. Touzé. "Experimental Evidence of Energy Transfer and Vibration Mitigation in a Vibro-Impact Acoustic Black Hole". In: *Applied Acoustics* 182 (Nov. 2021), p. 108168. ISSN: 0003-682X. DOI: 10.1016/j.apacoust.2021.108168.

List of Publications

Published journal article

T. Bonneval, M. Lanoy, R. Tanays, L. Sanches, G. Michon, and A. Pelat, "Dispersion analysis in a 3D lattice elastic waveguide for the design of an absolute filter," *Journal of Sound and Vibration*, vol. 617, p. 119314, 2025. DOI: 10.1016/j.jsv.2025.119314.

Journal article under publication

T. Bonneval, M. Lanoy, R. Tanays, G. Michon, and A. Pelat, "Analysis of the trade-off between bending stiffness and absolute bandgap width based on the dispersion relations of a periodic lattice sandwich beam," *Journal of Sound and Vibration*, under publication.

Conference communications

T. Bonneval, M. Lanoy, R. Tanays, G. Michon, and A. Pelat, "Implementation and experimental study of a periodic vibration filter," *International Conference on Wave Mechanics and Vibrations (ICOWP)*, Lisbon, Portugal, September 3, 2025.

T. Bonneval, M. Lanoy, G. Michon, and A. Pelat, "Performance of a periodic absolute vibration filter in a sandwich structure," *SURVISHNO*, Paris, France, May 22, 2025.

T. Bonneval, M. Lanoy, G. Michon, and A. Pelat, "Design of vibrational filters based on 3D lattice material elongated structure," *INTER-NOISE and NOISE-CON Congress and Conference Proceedings*, vol. 270, pp. 4603–4610, 2024. DOI: 10.3397/IN_2024_3484

T. Bonneval, M. Lanoy, R. Tanays, G. Michon, and A. Pelat, "Designing absolute bandgaps in networks of beams using the Spectral Element Method combined with a genetic optimization algorithm," *International Congress on Artificial Materials for Novel Wave Phenomena (Metamaterials)*, Crete, Greece, September 14, 2023.

T. Bonneval, M. Lanoy, R. Tanays, G. Michon, and A. Pelat, "Morphing design of networks of beams to maximize absolute bandgaps using the Spectral Element Method," *Metamaterials, Photonic Crystals and Plasmonics Conference (META)*, Paris, France, July 20, 2023.

RÉPUBLIQUE FRANÇAISE
Liberté
Égalité
Fraternité

Université de Toulouse

Titre : Conception de filtres vibratoires absolus par le design de guides d'ondes lattices périodiques.

Mots clés : métamatériau, filtre, vibration, structure treillis

Résumé : Le confort des passagers constitue un enjeu majeur dans la conception des cabines d'avion. Parmi les différentes sources d'inconfort, les vibrations transmises par la structure occupent une place importante, en particulier celles dues au balourd des turbines, généralement situées sous les ailes. Ces vibrations se propagent à travers la structure de la cabine jusqu'aux sièges et peuvent altérer sensiblement le confort perçu. Cette problématique devient encore plus critique avec l'émergence de nouvelles architectures de propulsion, comme les open rotors, dont les vitesses de rotation plus faibles déplacent les excitations vers des fréquences plus basses, précisément dans la gamme où le corps humain est le plus sensible. En cas d'exposition prolongée, ces vibrations peuvent engendrer, au-delà de l'inconfort, des effets néfastes sur la santé.

Cette thèse porte sur l'atténuation de la transmission vibratoire au sein de la cabine d'un aéronef, plus précisément au niveau du rail supportant les sièges passagers, qui constitue un chemin de transmission critique. En raison de la complexité des sous-ensembles traversés, cette transmission conduit à une excitation multipolarisée. L'objectif est de concevoir ce rail de façon à préserver ses performances statiques tout en lui conférant une fonction de filtrage vibratoire absolu, indépendante de la polarisation de l'excitation. L'approche repose sur le développement de structures lattices, c'est-à-dire d'architectures périodiques formées d'un réseau de poutres, offrant un excellent compromis entre masse et rigidité. Employées comme guides d'ondes, ces structures périodiques peuvent générer des bandes interdites, c'est-à-dire des plages de fréquences dans lesquelles les ondes élastiques ne se propagent plus. Deux mécanismes physiques sont exploités : les interférences de Bragg, liées à la périodicité de la structure, et les résonances locales, obtenues par l'ajout de résonateurs capables de localiser l'énergie vibratoire autour de leur fréquence propre et d'en limiter la propagation.

L'ambition de ce travail est ainsi de développer un filtre vibratoire absolu, efficace à basse fréquence et compatible avec les contraintes industrielles de l'aéronautique. La démarche combine conception, modélisation, optimisation et validation expérimentale. Elle aboutit à la fabrication et à la caractérisation expérimentale, à l'échelle laboratoire, d'un démonstrateur représentatif de l'application visée, afin d'évaluer concrètement le potentiel de cette approche pour les futures cabines d'avion.

Title: Conception of absolute vibration filters through the design of periodic lattice waveguides.

Key words: metamaterial, filter, vibration, lattice structure

Abstract: Passenger comfort is a major issue in aircraft cabin design. Among the various sources of discomfort, structure-borne vibrations play an important role, particularly those caused by turbine imbalance, with the engines generally located beneath the wings. These vibrations propagate through the cabin structure to the seats and can significantly affect perceived comfort. This issue becomes even more critical with the emergence of new propulsion architectures, such as open rotors, whose lower rotational speeds shift the dominant excitations toward lower frequencies, precisely within the range to which the human body is most sensitive. Under prolonged exposure, such vibrations may cause not only discomfort but also adverse health effects.

This thesis focuses on mitigating vibration transmission within an aircraft cabin, more specifically through the rail supporting the passenger seats, which constitutes a critical transmission path. Owing to the complexity of the substructures crossed by the vibrations, this transmission results in a multi-polarized excitation. The objective is to design this rail so as to preserve its static performance while endowing it with an absolute vibration-filtering function, independent of the polarization of the excitation. The proposed approach is based on the development of lattice structures, that is, periodic architectures made of a network of beams, offering an excellent compromise between mass and stiffness. When used as waveguides, these periodic structures can generate band gaps, that is, frequency ranges in which elastic waves can no longer propagate. Two physical mechanisms are exploited: Bragg interference, related to the structural periodicity, and local resonances, obtained by adding resonators capable of localizing vibrational energy around their natural frequency and limiting its propagation.

The ambition of this work is therefore to develop an absolute vibration filter that is effective at low frequencies and compatible with the industrial constraints of aeronautics. The methodology combines design, modeling, optimization, and experimental validation. It leads to the fabrication and experimental characterization, at laboratory scale, of a demonstrator representative of the targeted application, in order to assess concretely the potential of this approach for future aircraft cabins.